

The Pennsylvania State University
The Graduate School
Department of Materials Science and Engineering

MORPHOLOGY AND TRANSPORT IN IONIC MEMBRANES

A Dissertation in
Materials Science and Engineering
by
Melanie Lisa Disabb-Miller

© 2013 Melanie Lisa Disabb-Miller

Submitted in Partial Fulfillment
of the Requirements
for the Degree of

Doctor of Philosophy

December 2013

**The dissertation of Melanie Lisa Disabb-Miller was reviewed and approved*
by the following:**

Michael A. Hickner
Associate Professor of Materials Science and Engineering Dissertation
Advisor, Chair of Committee

Ralph H. Colby
Professor of Materials Science and Engineering and Chemical Engineering

James Runt
Professor of Polymer Science

Enrique D. Gomez
Assistant Professor of Chemical Engineering

Suzanne Mohny
Professor of Materials Science and Engineering and Electrical Engineering
Chair, Intercollege Graduate Degree Program in Materials Science and
Engineering

***Signatures are on file in the Graduate School.**

ABSTRACT

Ion-containing polymers for fuel cell membranes have been studied to determine the chemical structure and ion content relationship to membrane water uptake, conductivity, and morphology. Random and block copolymer proton exchange membranes (PEMs) and anion exchange membranes (AEMs) with unique properties, such as diblock and triblock copolymers, superacidic moieties, and charge-delocalized polymer-tethered Ru-complex based cations, were investigated, and new metrics were developed to analyze fundamental ion transport behavior in these polymers. The morphology of the polymer systems was examined using small angle x-ray scattering (SAXS), small angle neutron scattering (SANS), and transmission electron microscopy (TEM). By studying a number of different ion-conducting systems using multiple techniques and deep analysis of structure-property relationships, a more complete picture of the property landscape of these materials was developed.

Model diblock and unique triblock copolymer systems with center-functionalized blocks based on poly(styrene), PS, and poly(hexyl methacrylate), PHMA, were synthesized via atom transfer radical polymerization (ATRP). The PS block was functionalized for backbone-independent comparisons of PEM and AEM water uptake and conductivity to provide insight in how the properties of PEMs and AEMs compare and aid in further AEM development. The ratio of the mobile ion diffusion coefficients and dilute solution ion diffusivity (D/D_0) was developed as a new metric, allowing for accurate comparison of polymer systems with different ion moieties and contents. Subsequently, it was determined that block copolymer PEMs and AEMs demonstrate the same barriers to ion transport if the mobility of the charge carrier is considered.

Solution and membrane morphology was correlated for the PS-PHMA membrane systems using SAXS, SANS and TEM techniques. Two additional polymer systems incorporating unique Ru-complex-based and superacid ionic groups were investigated, as well. The effect of cross-link density on water uptake and conductivity was studied for bis(terpyridine) ruthenium-based AEMs with the new metrics to compare the conductivity of various AEM counterions. Finally, the conductivity, water uptake, and morphology of superacid random and block copolymer PEMs were explored. The perfluorosulfonic acid groups in these polymers led to enhanced conductivity over the alkyl and aryl sulfonic acid groups.

Through this research, new insight was gained into the fundamental associations between water and ions in polymer membranes. These methods were applied to membranes with a wide variety of ionic groups and random and block copolymer PEM and AEM systems, with the goal to aid in the development and design of ion-conductive materials for a wide variety of applications with enhanced performance.

TABLE OF CONTENTS

Table of Figures	viii
Table of Tables	xiv
List of Symbols and Acronyms	xv
Acknowledgements	xxiii
Chapter 1 Introduction and Literature Review	1
1.1. Background and Motivation	1
1.2. Important Membrane Characteristics	4
1.3. Current Status of Proton and Anion Exchange Membranes	7
1.3.1 Proton Exchange Membranes	7
1.3.2 Anion Exchange Membranes	10
1.4. Ion Transport	12
1.4.1 Non-Aqueous and Aqueous Dynamics	12
1.4.2 Ion Transport Mechanisms in Pure Water	14
1.4.3 Water-Ion Interactions in Polymers	16
1.4.4 Ion Transport Metrics	17
1.5. Block Copolymers	20
1.5.1 Block Copolymer Overview	20
1.5.2 Block Copolymer PEMs and AEMs	23
1.5.3 Control of Block Copolymer Morphology	25
1.5.4 Diblock and Triblock Copolymers	27
1.6. AEMs with Alternative Cations	28
1.7. References	29
Chapter 2 Experimental Methods	35
2.1. Introduction	35
2.2. Synthesis and Functionalization of Poly(hexyl methacrylate)-Poly(styrene)- Based Block Copolymers	35
2.2.1 Atom Transfer Radical Polymerization	36
2.2.2 Functionalization for PEMs	37
2.2.3 Functionalization for AEMs	38
2.2.4 Membrane Fabrication	39
2.3. Additional Materials	39
2.3.1 Poly(vinyl benzyl chloride)-Poly(styrene)-Based Block Copolymers	40
2.3.2 Bis(terpyridine) Ruthenium-Based AEMs	41
2.3.3 Superacid PEMs	41
2.4. Polymer Characterization	41
2.4.1 Size Exclusion Chromatography	42
2.4.2 Nuclear Magnetic Resonance Spectroscopy	42
2.4.3 Differential Scanning Calorimetry	43
2.5. Membrane Characterization	43

2.5.1	Conductivity Measurements	44
2.5.2	Water Uptake Measurements	45
2.5.3	Small and Intermediate Angle X-ray Scattering	46
2.5.4	Small Angle Neutron Scattering	47
2.5.5	Transmission Electron Microscopy	47
2.6.	References	48
Chapter 3	Ion Motion in Anion and Proton-Conducting Triblock Copolymers.....	49
3.1.	Introduction	49
3.2.	Experimental.....	52
3.2.1	Polymer Synthesis and Membrane Preparation	52
3.2.2	Characterization	56
3.3.	Results and Discussion	58
3.4.	Conclusions	71
3.5.	References	72
Chapter 4	Solution Morphology of Triblock Copolymers.....	75
4.1.	Introduction	75
4.2.	Experimental.....	78
4.2.1	Polymer Synthesis	78
4.2.2	Solution and Membrane Preparation	79
4.3.	Instrumentation.....	80
4.4.	Results and Discussion	80
4.5.	Conclusions	93
4.6.	References	94
Chapter 5	Organization and Conductivity of Analogous Diblock and Triblock Ion Conductors.....	96
5.1.	Introduction	96
5.2.	Experimental.....	99
5.2.1	Polymer Synthesis and Membrane Preparation	99
5.2.2	Characterization	101
5.3.	Results and Discussion	103
5.4.	Conclusions	109
5.5.	References	110
Chapter 6	Morphology and Conductivity of Poly(styrene)-Based Anion Exchange Membranes.....	112
6.1.	Introduction	112
6.2.	Experimental.....	114
6.3.	Results and Discussion	116
6.4.	Conclusions	129
6.5.	References	129

Chapter 7	Water Uptake and Ion Mobility in Cross-Linked Bis(terpyridine) Ruthenium-Based Anion Exchange Membranes	132
7.1.	Introduction	132
7.2.	Experimental Methods.....	138
7.2.1	Polymer Synthesis and Membrane Preparation	138
7.2.2	Characterization	139
7.3.	Results and Discussion of BTP-R1	141
7.4.	Results and Discussion of BTP-R2	148
7.5.	Conclusions	158
7.6.	References	159
Chapter 8	Scattering of Superacid Proton Exchange Membranes.....	161
8.1.	Introduction	161
8.2.	Experimental.....	163
8.2.1	Random Copolymer PEMs	163
8.2.2	Triblock Copolymer PEMs.....	163
8.3.	Results and Discussion of the Random Copolymer PEMs.....	164
8.4.	Results and Discussion of the Superacid Triblock Copolymer PEMs.....	172
8.5.	Conclusions	176
8.6.	References	176
Chapter 9	Summary and Future Research Directions	179
9.1.	Summary and Conclusions	179
9.1.1	Ion Motion in Anion and Proton-Conducting Triblock Copolymers.....	179
9.1.2	Solution Morphology of Triblock and Diblock Copolymers.....	181
9.1.3	Organization and Conductivity of Analogous Diblock and Triblock Ion Conductors.....	182
9.1.4	Morphology and Conductivity of Poly(styrene)-Based Anion Exchange Membranes	183
9.1.5	Water Uptake and Ion Mobility in Cross-Linked Bis(terpyridine) Ruthenium-Based Anion Exchange Membranes	184
9.1.6	Scattering of Superacid Proton Exchange Membranes.....	185
9.2.	Directions for Future Research.....	185
9.3.	References	188
Appendix A	Ion Motion in Anion and Proton-Conducting Triblock Copolymers.....	191
A.1	Determination of Triblock Copolymer Molecular Weight.....	191
A.2	Polymer Functionalization.....	193
A.3	Characterization.....	195
Appendix B	Organization and Conductivity of Analogous Diblock and Triblock Ion Conductors.....	197
B.1	Polymer characterization by SEC and NMR.....	197
B.2	Sulfonation of the Block Copolymers	203

TABLE OF FIGURES

Figure 1.1 Schematic of a fuel cell with the polymer electrolyte membrane shown in blue, the catalyst shown in gray, and the gas diffusion layers (GDLs) shown in black for (a) proton exchange membrane (PEM) fuel cells and (b) anion exchange membrane (AEM) fuel cells.....	2
Figure 1.2. Schematics depicting the hopping (Grotthuss) and vehicle mechanisms of proton transport in pure water. Hydrogen atoms are blue, and oxygen atoms are red. ^{14,60}	15
Figure 1.3. Schematic depicting polymer chains for a homopolymer, AB random copolymer, AB diblock copolymer, ABA triblock copolymer, and AB graft copolymer. Polymer A is represented by blue beads, and polymer B is represented by red beads.	21
Figure 1.4. Phase diagram for an AB diblock copolymer (top) and cartoons of (a) lamellar, (b) gyroid, (c) cylindrical, and (d) spherical morphologies. ^{74,75}	22
Figure 1.5. Transmission electron micrographs of (a) PS- <i>g</i> -PSSA and (b) PS- <i>r</i> -PSSA. The greater phase separation of the graft copolymer contributes to the higher conductivity shown in (c). ⁴⁵	24
Figure 1.6. (a) Small angle x-ray scattering curves of poly(styrene- <i>b</i> -(4-vinyl pyridine)) in a mixed dioxane/tetrahydrofuran/ <i>N,N</i> -dimethylformamide solution, and (b) a scanning electron microscope image of the top surface of the membrane cast from the 15 wt % solution. ⁸⁸	27
Figure 1.7. Configurations of lamellar AB diblock and ABA triblock copolymers. The diblock chains do not form bridges or loops, but the triblock chains are capable of demonstrating both configurations. ⁹⁰	28
Figure 2.1. Generalized ATRP reaction showing the rates of activation (k_{act}), deactivation (k_{deact}), and propagation (k_p). P_n and P_n^\bullet are the propagating species and radical. ¹²	36
Figure 2.2. Sulfonation scheme of the PHMA- <i>b</i> -PS- <i>b</i> -PHMA triblock copolymer, depicting functionalization for PEMs.	38
Figure 2.3. Two-step scheme to produce QA-functionalized PHMA- <i>b</i> -PS- <i>b</i> -PHMA for AEMs. A chloromethylation step ⁵ was followed by conversion to QA groups via trimethylamine.	39
Figure 2.4. Schematic of the cell used for conductivity measurements of free-standing membranes, ¹¹ with (1) securing screws, (2) Teflon [®] blocks, (3), stainless steel electrodes, (4) equilibration windows, and (5) the membrane.	45
Figure 3.1. Sulfonation and quaternization routes of the PHMA- <i>b</i> -PS- <i>b</i> -PHMA triblock copolymer.....	55

- Figure 3.2. Reaction rates of chloromethylation using the method developed by Avram, et al.²⁴ The stoichiometric ratios published by Avram, et al.,²⁴ a 1:3:3 ratio of polymer sites to be functionalized:paraformaldehyde:chlorotrimethylsilane and 0.2 mol% tin (IV) chloride are represented by (□). Other stoichiometric ratios shown are 1:3:3 and 0.6 mol % catalyst (○), 1:9:9 and 0.6 mol % catalyst (△), 1:9:9 and 0.2 mol % catalyst (◇), and 1:60:3 and 0.2 mol % catalyst (▽). The maximum degree of functionalization of the poly(styrene) block attainable before degradation was approximately 53 mol %.60
- Figure 3.3. Conductivity versus hydration number of P-1.2-H (■), P-1.6-H (●), P-2.3-H (▲), A-1.1-HCO₃ (▽), A-1.2-Cl (□), A-1.7-Cl (○), and A-2.0-Cl (△).62
- Figure 3.4. The diffusion coefficient as a function of hydration number of P-1.2-H (■), P-1.6-H (●), P-2.3-H (▲), A-1.2-Cl (□), A-1.7-Cl (○), and A-2.0-Cl (△) at (a) all hydration numbers, and (b) at low levels of hydration.64
- Figure 3.5. The ratio of the diffusion coefficient, D, to the dilute solution diffusivity, D₀ as a function of hydration number for P-1.2-H (■), P-1.6-H (●), P-2.3-H (▲), A-1.2-Cl (□), A-1.7-Cl (○), and A-2.0-Cl (△).66
- Figure 3.6. Sensitivity of change in log σ to RH of P-1.2-1.6-2.3-H (■) and A-1.2-1.7-2.0-Cl (□).67
- Figure 3.7. SAXS patterns of (a) PEMs and (b) AEMs. Arrows indicate primary and secondary scattering peaks.68
- Figure 3.8. Bright field TEM images of the microtomed cross-section of membranes (a) P-1.6-H and (b) A-1.7-Cl. The spherical domains shown are on the order of 20 nm. The morphologies for the PEM and AEM are comparable, which supports the similar D/D₀ ratios for the materials.71
- Figure 4.1. Chemical structures of the (a) PHMA-*b*-PS-*b*-PHMA triblock copolymers with tethered sulfonate (PEM) or quaternary ammonium (AEM) moieties and (b) PHMA-*b*-PS diblock copolymer with tethered sulfonate moieties (PEM).79
- Figure 4.2. Transmission electron microscopy, TEM, images of (a) unfunctionalized PHMA-*b*-PS-*b*-PHMA, (b) P-1.2-H, (c) P-1.6-H, and (d) P-2.3-H.83
- Figure 4.3. Transmission electron microscopy, TEM, images of (a) A-1.2-Cl, (b) A-1.7-Cl, and (c) A-2.0-Cl.84
- Figure 4.4. Diagram of some of the parameters used in the polydisperse core-shell model, left, and a cartoon of the PHMA-*b*-PS-*b*-PHMA TB-1 micelles, right.85
- Figure 4.5. Illustration of the model fit (solid black line) to SANS data (dotted colored line) of A-2.0-Cl for 1 wt % solution, 10 wt % solution, and dry membrane.86
- Figure 4.6. Schematic depicting the size (in nm) of the core (white, red, or green) and shell (blue) for the particles in the 1 wt % solutions, 10 wt % solutions, and dry

membrane according to the fit to the NIST polydisperse core-shell model with a hard sphere structure factor.	87
Figure 4.7. The core polydispersity is plotted as a function of weight percent polymer. As the polymer concentration increases, the particle cores became less polydisperse.	88
Figure 4.8. The proposed solution to membrane morphology transition is shown from left to right, with snapshots of the 1 wt % solution, the 10 wt % solution, and of the final membrane.	88
Figure 4.9. Illustration of the model fit (solid black line) to SANS data (dotted colored line) of DB-1.1-H for 0.1, 1, 10, and 20 wt % solutions.	91
Figure 4.10. Schematic depicting the size (in nm) of the core (white) and shell (blue or green) for the particles in the 0.1, 1, 10, and 20 wt % according to the fit to the NIST polydisperse core-shell model with a hard sphere structure factor.	92
Figure 4.11. The core polydispersity of the diblock and triblock copolymers in solution is plotted as a function of weight percent polymer. As the polymer concentration increases, the particle cores became less polydisperse.	93
Figure 5.1. A diagram depicting the formation of bridges and loops within a lamellar ABA triblock copolymer and the lack of such formation in an analogous AB diblock copolymer, left; ²⁰ a cartoon depicting AB diblock copolymer chains created from “cutting” an ABA triblock copolymer in half, right.	97
Figure 5.2. Chemical structures of the (a) PHMA- <i>b</i> -PS- <i>b</i> -PHMA triblock copolymer with tethered sulfonate (PEM) moieties and (b) PHMA- <i>b</i> -PS diblock copolymer with tethered sulfonate moieties (PEM). The cartoons depict the diblock copolymer was designed with a molecular weight such that it was as if the triblock copolymer chain had been cut in half.	103
Figure 5.3. Comparison of the (a) water uptake and (b) hydration number of diblock (DB) and triblock (TB) PEMs as a function of ion content.	105
Figure 5.4. The conductivity of the membranes increased with RH and hydration number ...	107
Figure 5.5. Small angle x-ray scattering (SAXS) patterns for (a) diblock and (b) triblock copolymer PEMs. Primary peaks are indicated by q*.	108
Figure 6.1. Conductivity at 30 °C of block and random QA-functionalized multiblock copoly(arylene ether) AEMs. The block copolymers exhibit higher conductivity than the random copolymers. ²³	114
Figure 6.2. Chemical structures of (a) QA PVBC- <i>ran</i> -PS, and (b) QA PVBC- <i>b</i> -PS.	116
Figure 6.3. For a given IEC, the (■) QA PVBC- <i>b</i> -PS copolymers were more hydrated than the (○) QA PVBC- <i>ran</i> -PS copolymers at 95% RH, shown by (a) increased water uptake, wu, and (b) increased hydration number, λ , as function of IEC.	119

- Figure 6.4. The conductivity, σ , of the (■) QA PVBC-*b*-PS and (○) QA PVBC-*ran*-PS copolymers at 95% RH, shown as a function of (a) IEC, and (b) hydration number, λ 121
- Figure 6.5. Mobile ion diffusivity, D , at 95% RH of the (■) QA PVBC-*b*-PS and (○) QA PVBC-*ran*-PS copolymers. 122
- Figure 6.6. The ratio of diffusivity, D , to dilute solution, D_0 , at 95% RH is shown for the (■) QA PVBC-*b*-PS and (○) QA PVBC-*ran*-PS copolymers. Both block and random copolymer AEMs are well below the ideal value of unity for D/D_0 123
- Figure 6.7. Small angle xray scattering (SAXS) patterns for (a) QA PVBC-*b*-PS copolymers (—) B-1.06, (—) B-1.41, (—) B-1.59, (—) B-1.78, (—) B-2.09, and (b) QA PVBC-*ran*-PS copolymers (—) R-1.43, (—) R-1.84, and (—) R-2.05. The block copolymers AEMs showed primary scattering peaks, indicated with q , while the random copolymer AEMs did not show any ordering. 127
- Figure 6.8. Relationship between D , the interdomain spacing calculated from SAXS and $(N_{QA\ VBC})^{2/3}$. The pseudo-linear relationship is in agreement with the Semenov equation, except for the outlier of B-1.78. 128
- Figure 7.1. Schematic of the argon-purged conductivity setup. Argon is bubbled through water before and during the conductivity measurement. 140
- Figure 7.2. First iteration of monomers polymerized by Grubbs' second generation catalyst into resulting chemical structure overlayed on optical image of a membrane, BTP-R1. 142
- Figure 7.3. Humidity dependence of conductivity and water uptake for the AEM with monomer:DCPD = 1:2. 143
- Figure 7.4. Decline in conductivity of the hydroxide form AEMs during conductivity measurements; (top) kept under Ar blanket for up to 3 h, (bottom) left open to atmosphere after 3 h. Conductivities were measured with samples exposed to liquid water at 30 °C. 144
- Figure 7.5. Change in hydroxide conductivity upon exposure of the samples to 1 M KOH for 2 h. Conductivities were measured with samples exposed to liquid water at 30 °C. 145
- Figure 7.6. Impact of temperature on conductivity for the membranes (a) in the HCO_3^- form and (b) in the Cl^- form. 146
- Figure 7.7. The difference in conductivity at 30 °C between membranes in the Cl^- form and in the HCO_3^- form as a function of water uptake. 148
- Figure 7.8. Monomers polymerized by Grubbs' second generation catalyst into resulting chemical structure overlayed on optical image of a membrane, BTP-R2. 149

- Figure 7.9. Conductivity of membranes as a function of hydration number in the (a) chloride form and (b) bicarbonate form for (■) [DCPD]:[M+COD] = 1:1, (●) [DCPD]:[M+COD] = 2:1, and (▲) [DCPD]:[M+COD] = 5:1. The maximum conductivity occurred at a hydration number of approximately 50 and 125 for membranes in chloride form and bicarbonate form, respectively. 151
- Figure 7.10. The role of ion concentration on membrane conductivity for membranes in the chloride form with [DCPD]:[M+COD] ratios of (■) 1:1, (●) 2:1, and (▲) 5:1. The IEC and hydration number of the membranes are denoted next to the corresponding symbols. 152
- Figure 7.11. Hydration number decreased as ion concentration increases for membranes in chloride form with [DCPD]:[M+COD] ratios of (■) 1:1, (●) 2:1, and (▲) 5:1. 153
- Figure 7.12. Ratio of the diffusion coefficient, D , to the dilute solution diffusivity, D_0 , as a function of hydration number for membranes in the (a) chloride form and (b) bicarbonate form, with [DCPD]:[M+COD] ratios of (■) 1:1, (●) 2:1, and (▲) 5:1. The higher D/D_0 ratio for the bicarbonate ions signifies that the bicarbonate diffusion coefficient in the samples was closer to the dilute solution diffusivity of bicarbonate ions. 156
- Figure 7.13. Ion transport properties of membranes in the bicarbonate form, for Ru (II) complex-based membranes with [DCPD]:[M+COD] ratios of (■) 1:1, (■) 2:1, and (■) 5:1; BTMA-based tetramethyl bisphenol membranes with (●) 100, (●) 80, (●) 60, and (●) 40 mol % tetramethyl bisphenol;⁶ (▲) imidazolium-based poly(fluorenyl ether ketone sulfone) membrane;⁸ and phosphonium-based bromomethylated poly(2,6-dimethyl-1,4-phenylene oxide) membranes with (▼) 20%, (▼) 34%, (▼) 57%, and (▼) 90% degree of functionalization,³⁵ where (a) depicts bicarbonate conductivity as a function of hydration number, and (b) illustrates the ratio of the diffusion coefficient, D , to the dilute solution diffusivity, D_0 , as a function of hydration number. 157
- Figure 8.1. Chemical structures of sulfonated poly(sulfone), PSU, and poly(styrene), PS. The perfluorosulfonate, aryl sulfonate, and alkyl sulfonate groups are shown as S_1 , S_2 , and S_3 , respectively. 165
- Figure 8.2. Intermediate angle x-ray scattering (IAXS) patterns of dry 200-PSU (top)* and 40-sPS (bottom) membranes. The sPS membranes scatter more strongly than do the PSU membranes. *Adapted from Chang, Y., et al. *Polymer Chemistry* 2013, 4, 272–281. 168
- Figure 8.3. Small angle neutron scattering (SANS) patterns of hydrated 135-PSU (top) and 30-sPS (bottom) membranes. The primary scattering peak is denoted by q . The overall scattering of the membranes is similar. 170
- Figure 8.4. The swelling of the membranes calculated from $(d_{\text{SANS}} - d_{\text{IAXS}})/d_{\text{IAXS}}$ increased with the ion content of the membranes. 171

Figure 8.5. Chemical structure of the perfluorosulfonated (S_1) PHMA- <i>b</i> -PS- <i>b</i> -PHMA triblock copolymers.....	172
Figure 8.6. Small angle x-ray scattering (SAXS) patterns of (a) 43-PS and (b) 68-PS superacid triblock copolymer PEMs. The primary scattering peak is denoted by q^* or q	174
Figure A.1. Size exclusion chromatograph for the styrene macroinitiator (—) and the PHMA- <i>b</i> -PS- <i>b</i> -PHMA triblock copolymer (---).....	192
Figure A.2. ^1H NMR spectra for poly(styrene) macroinitiator in deuterated chloroform. The inset shows the peaks associated with the benzyl bromide endgroups.	192
Figure A.3. ^1H NMR spectra for PHMA- <i>b</i> -PS- <i>b</i> -PHMA in deuterated chloroform.....	193
Figure A.4. ^1H NMR spectra for the sulfonated triblock copolymer, PHMA- <i>b</i> -sPS- <i>b</i> -PHMA, in deuterated N,N-dimethylformamide.....	194
Figure A.5. ^1H NMR spectra for the quaternary ammonium functionalized triblock copolymer, PHMA- <i>b</i> -qaPS- <i>b</i> -PHMA, in deuterated N,N-dimethylformamide.....	195
Figure A.6 DSC data for the unfunctionalized triblock copolymer (---), compared to (a) quaternary ammonium functionalized triblock copolymers A-1.2-Cl (---), A-1.7-Cl (---), A-2.0-Cl (---); and (b) sulfonated triblock copolymers P-1.2-H (---), P-1.5-H (---), P-2.3-H (---). The T_g for the PHMA (---) block and the PS block (—) of the polymer were calculated using TA Instruments Universal Analysis software and is marked on the curves.	196
Figure B.1. Size exclusion chromatograph for the styrene macroinitiator (—) and the PHMA- <i>b</i> -PS diblock copolymer (---).	198
Figure B.2. Size exclusion chromatograph for the styrene macroinitiator (—) and the PHMA- <i>b</i> -PS- <i>b</i> -PHMA triblock copolymer (---).....	198
Figure B.3. ^1H NMR spectra for poly(styrene) monofunctional macroinitiator in deuterated chloroform. The inset shows the peaks associated with the benzyl bromide end groups.....	199
Figure B.4. ^1H NMR spectra for PHMA- <i>b</i> -PS in deuterated chloroform.	200
Figure B.5. ^1H NMR spectra for poly(styrene) difunctional macroinitiator in deuterated chloroform. The inset shows the peaks associated with the benzyl bromide end groups.....	201
Figure B.6. ^1H NMR spectra for PHMA- <i>b</i> -PS- <i>b</i> -PHMA in deuterated chloroform.....	202

TABLE OF TABLES

Table 3.1. Polymer sample parameters and properties.	61
Table 3.2. Hydrated ion concentration and calculated diffusion coefficients from conductivity measurements and dilute solution ^a	66
Table 3.3. Interdomain spacing for the PHMA- <i>b</i> -PS- <i>b</i> -PHMA samples as a function of ion content.	70
Table 4.1. Interdomain spacings of the PHMA- <i>b</i> -PS- <i>b</i> -PHMA TB-1	81
Table 4.2. Interdomain spacings of PHMA- <i>b</i> -PS and PHMA- <i>b</i> -PS- <i>b</i> -PHMA (TB-2).....	89
Table 5.1. Polymer Membrane Characteristics and Properties	104
Table 6.1. Attributes of QA functionalized diblock and random copolymer AEMs	117
Table 6.2. Properties of QA functionalized diblock and random copolymer AEMss	118
Table 6.3. Concentration and Calculated Diffusion Coefficients from Conductivity Measurements and Dilute Solution	124
Table 7.1. Chemical structure, conductivity, and hydration number of several BTMA-containing polymers used as AEMs.	137
Table 7.2. BTP-R1 membrane properties with various M:DCPD ratios	142
Table 7.3. BTP-R2 membrane sample parameters and properties	149
Table 8.1. Random Copolymer Membrane Parameters and Properties	166
Table 8.2. Superacid (S ₁) Triblock Copolymer Membrane Parameters and Properties.....	173
Table 8.3. Number of Repeat Units and Values of N ^{2/3}	175
Table A.1. Conditions for sulfonation of the PHMA- <i>b</i> -PS- <i>b</i> -PHMA triblock copolymer.	194
Table B.1. Sulfonation Reaction Conditions	203

LIST OF SYMBOLS AND ACRONYMS

Symbols

\AA	Angstrom
A	Cross-sectional area
$-b-$	Block copolymer
B	Constant
$^{\circ}\text{C}$	Degrees Celsius
c	Concentration
$[]$	Concentration
χ	Interaction parameter
$-co-$	Copolymer
cm	Centimeters
δ	Solubility parameter
d	Interdomain spacing
D	Diffusion coefficient
D_0	Dilute solution diffusivity
D/D_0	Diffusivity ratio
E_a	Activation energy
F	Faraday's constant
f	Fraction
g	Gram
$-g-$	Graft copolymer

H^+	Proton
1H	Proton
Hz	Hertz
K	Kelvin
J	Joules
k	Rate
k_B	Boltzmann constant
kg	Kilogram
kJ	Kilojoules
λ	Hydration number
L	Length between electrodes
M	Molar
M_{H_2O}	Mass of water
m	Mass of sample
mg	Milligram
MHz	Megahertz
mL	Milliliter
M_n	Number-average molecular weight
mS	MilliSiemens
μ	Mobility
μ'	Effective mobility
μm	Micrometer
N	Degree of polymerization or number of repeat units
nm	Nanometer
Ω	Ohms

%	Percent
π	Pi
ρ	Density
P_n	Propagating species
pK_a	Acid dissociation constant
q	Ion charge
q	Scattering vector
- r -	Random copolymer
®	Registered trademark
R	Membrane resistance
R	Universal gas constant
r	Radius
σ	Conductivity
σ_0	Conductivity at infinite temperature
s	Second
T	Temperature
T_0	Vogel temperature
T_g	Glass transition temperature
X_{v-H_2O}	Volume-based water uptake
V	Volts
V	Volume
V_r	Reference volume
z	Valence charge

Abbreviations

AC	Alternating current
AEM	Anion exchange membrane
AIBN	2,2'-Azobis(2-methylpropionitrile)
Ar	Argon
ATRP	Atom transfer radical polymerization
au	Arbitrary units
BPSH	Poly(bisphenol sulfone)
bpy	2,2'-Bipyridyl
BTMA	Benzyltrimethylammonium
BTP	Bis(terpyridine)
Br	Bromine
C	Carbon
CCD	Charge-coupled device
CDTB	Cumyl diththiobenzoate
(CH ₂ O) _n	Paraformaldehyde
Cl	Chloride
COD	Cylcooctadiene
Cu	Copper
<i>d</i>	Deuterium
d	Days
d-DMF	Deuterated N,N-dimethylformamide
D ₂ O	Deuterium oxide
DB	Diblock

DCPD	Dicyclopentadiene
DF	Degree of functionalization
DMF	N,N-dimethylformamide
exp	Exponential
FC	Fuel cell
G2	Second generation catalyst
GDL	Gas diffusion layers
GPC	Gel permeation chromatogram
h	Hours
H	Hydrogen
HCO ₃	Bicarbonate
H ₂ SO ₄	Sulfuric acid
HMA	Hexylmethacrylate
HPLC	High-performance liquid chromatography
IAXS	Intermediate angle x-ray scattering
IEC	Ion exchange capacity
K	Potassium
M	Monomer
Me	Methyl
MEA	Membrane electrode assembly
MeOH	Methanol
meq	Milliequivalents
min	Minutes
mol	Moles
N	Nitrogen

Na	Sodium
NCNR	National Institute of Standards and Technology Center for Neutron Research
NIST	National Institute of Standards and Technology
nm	Not measured
NMR	Nuclear magnetic resonance
O	Oxygen
OH	Hydroxide
ORNL	Oak Ridge National Laboratory
PDI	Polydispersity index
PEM	Proton exchange membrane
PFG	Pulsed field gradient
PFSA	Perfluorosulfonic acid-containing polymer
PHMA	Poly(hexyl methacrylate)
PMB	Poly(methylbutylene)
PMDETA	N,N,N',N',N''-pentamethyldiethylenetriamine
ppm	Parts per million
PS	Poly(styrene)
PSS	Poly(styrene sulfonate)
PSSA	Poly(styrene sulfonate)
PSU	Poly(sulfone)
PVBC	Poly(vinyl benzyl chloride)
QA	Quaternary ammonium
RAFT	Reversible addition-fragmentation chain-transfer polymerization
RH	Relative humidity
RI	Refractive index

ROMP	Ring-opening metathesis polymerization
Ru	Ruthenium
S	Siemens
S	Sulfur
S ₁	Perfluorosulfonate group
S ₂	Aryl sulfonate group
S ₃	Alkyl sulfonate group
SANS	Small angle neutron scattering
SAXS	Small angle x-ray scattering
SDAPP	Sulfonated poly(phenylene)
SEC	Size exclusion chromatography
SEM	Scanning electron microscopy
SLD	Scattering length density
SnCl ₄	Tin chloride
SO ₃ H	Sulfonate
sPEEK	Sulfonated poly(ether ether ketone ketone)
sPS	Sulfonated poly(styrene)
TB	Triblock
TEM	Transmission electron microscopy
TGA	Thermogravimetric analysis
THF	Tetrahydrofuran
VFT	Vogel-Fulcher-Tammann
WAXS	Wide angle x-ray scattering
w/w	Weight/weight basis
wt	Weight

wu Water uptake

ACKNOWLEDGEMENTS

I would like to thank my advisor, Dr. Michael Hickner for support, guidance, and tutelage during my time at Penn State. The day I received the phone call from Dr. Hickner, asking me if I wanted to work on fuel cells was the day I mentally joined the group, and I have loved my research since my first steps into the lab at Penn State. Dr. Hickner has encouraged me when I needed it, pushed me to surpass the limits I set for myself, and helped me when I was at a loss. Most of all, Dr. Hickner has made me a better scientist by cultivating the researcher within me and teaching me to trust myself, and I am truly grateful for his influence on my career.

I am also thankful for our collaborators, as they provided me with materials and discussion for significant portions of my thesis, particularly Dr. Gregory Tew and Dr. Chulsung Bae and their groups, as well as our Oak Ridge National Laboratory collaborator Dr. Lilin He. I consider myself fortunate to have such a pertinent committee, and I am indebted to Dr. James Runt, Dr. Ralph Colby, and Dr. Enrique Gomez. They have posed valid questions and have provided redirection for my work, and I would not be as confident in my research had it not been for their guidance. I have been privileged to have been exposed to wonderful educators and scientists during my path to Penn State, and I must acknowledge their influence on my choice to pursue math and science research through Materials Science and Engineering and my love for polymers. All of this would not have been possible without my funding sources, ARO W911NF-08-1-0282 and ARPA-E DE-AR0000121.

The Hickner Group, past and present, has been my extended family at Penn State, and I would be remiss to exclude them. They have acted as close friends, problem-solvers, teachers, and occasionally challengers. It is not always easy to argue science, and we have had heated discussions, but I knew I could always rely on my fellow groupmates to help and support me. I am particularly grateful for Tomonori Saito, Brian Chaloux, Kyle Bryson, Stephanie Petrina, Romesh Patel, Xie He, Sarah Black, Doug Kushner, and Geoff Geise. Tomonori, Brian, and Kyle

taught me most of my polymer chemistry knowledge, and I fondly remember the days when we all shared one hood and only two or three hotplates. Since then, they have continued to provide support and help me when I need it, especially Brian and Tomonori. Stephanie, Romesh, and Xie He were the vocal and scientific graduate student leaders in the group when I first started, and I appreciate their guidance and friendship. I was overjoyed when Stephanie moved into 26 Steidle, and I was no longer the only female in that office. Sarah, Doug, and Geoff have been of great help during the later phases of my work, helping me organize my thoughts and encouraging me to finish. Outside of the Hickner Group, I would like to thank Greg Tudryn for his assistance, especially on scattering, Kyle Hart for his eternal optimism, and Lauren Abbott, who was a strong sounding board, sanity check, lunch mate, and is a good friend.

I would like to thank my family, particularly Joel, Michele, Alexander, Ethan, Peter, Molly, and Sam, and Grandma Lu, who have loved me unconditionally, fostered the nerd in me, and supported me in all of my endeavors. I owe my leadership skills to them, as well as my inquisitive nature and overall nerdiness. They are a huge part of who I am today, and I cannot thank them enough, especially my parents, for all the opportunities they have given me. Finally, I would like to thank my wonderful, loving, thoughtful, and caring husband and best friend, Mike. I do not know if I could have made it through graduate school without his support. I also appreciate the support of his family, who has always accepted me. Although Mike often thought I was crazy for going back to graduate school, he gave up the city he loved to marry me and move to State College. He has encouraged me, supported me mentally and physically, and made sure I was nourished and at least a little rested. Mike has spent countless hours in the lab so I would not be alone when I had to run reactions and experiments into the wee hours of the morning, even though he was not the one in graduate school. I am forever thankful for his sacrifice, friendship, love, patience, and support, as well as the hopes and dreams for life after Penn State.

Chapter 1

Introduction and Literature Review

1.1. Background and Motivation

Current global energy demands are increasing along with fossil fuel costs, requiring new sources of energy. Means of alternative energy production are being explored as an answer to this problem, and new materials are being developed to attain the goal of moving beyond fossil fuels as our predominant energy supply. Ion-containing polymers have been of interest for use in lithium batteries and as electrolytes for solar hydrogen generators, water electrolyzers, and fuel cell membranes. The conductivity, stability, and cost of these polymer electrolytes are still below the desired values for widespread industry use, and improving their performance commands deep comprehension of the phenomena controlling the ion conductivity of polymeric materials, including polymer and solvent dynamical processes and the concentration of charge carriers within the material. The conductivity of polymer electrolytes such as poly(ethylene oxide) used in lithium batteries depends on the long-range segmental motion of the polymer, which is temperature dependent and described by the Vogel - Fulcher - Tammann (VFT) relaxation dynamics of the polymer chain segments. Polymer fuel cell membranes, the focus of this dissertation, also demonstrate increased ion conductivity with temperature, but the conductivity is extremely dependent on the hydration of the membranes and the conductivity process is thermally activated as described by Arrhenius kinetics, which signals that water dynamics controls the ion conductivity of hydrated materials.¹⁻³

Fuel cell devices electrochemically convert the chemical energy of a fuel, such as hydrogen or methanol, into electrical energy.⁴ For polymer electrolyte membrane fuel cells operated using hydrogen as the fuel, the only chemical byproduct is water, and applications include providing energy for vehicles and for stationary and portable devices. Compared to other fuel cells that operate at temperatures between 200-800 °C, polymer electrolyte membrane fuel cells operate at relatively lower temperatures 60-120 °C, and typically have higher power density and lower cost than fuel cells that operate at higher temperatures.^{2,5} Schematics of proton exchange membrane (PEM) and anion exchange membrane (AEM) fuel cells are shown below in Figure 1.1. A polymer electrolyte membrane fuel cell device consists of an anode and a cathode, responsible for oxidation and reduction reactions; gas diffusion layers (GDLs); catalyst layers; and a polymer electrolyte membrane. The PEM or AEM acts as a separator for the reactants and as an ion conductor between the electrodes.

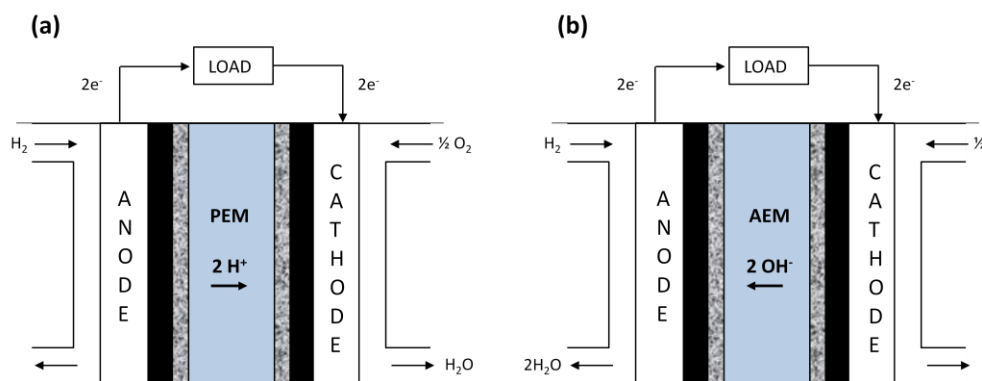


Figure 1.1 Schematic of a fuel cell with the polymer electrolyte membrane shown in blue, the catalyst shown in gray, and the gas diffusion layers (GDLs) shown in black for (a) proton exchange membrane (PEM) fuel cells and (b) anion exchange membrane (AEM) fuel cells.

Polymer fuel cell membranes (shown in Figure 1.1) should be as thin as possible to allow for efficient proton or anion transport, but thick enough to provide separation between the anode

and cathode of the fuel cell. To be considered for widespread use, a fuel cell membrane must possess high ionic conductivity, good thermal and hydrolytic stability, low fuel crossover, adequate water uptake with minimal swelling, low cost, and easy incorporation into membrane electrode assemblies (MEAs).^{4,6,7} Increasing the thickness of the polymer electrolyte membrane lengthens the lifetime of the fuel cell, but it also increases the cost of the device.⁵ Currently, proton exchange membranes (PEMs) require precious metal catalysts, such as platinum, for fuel cell operation; anion exchange membranes (AEMs) do not have this demand. However, the next generation of AEMs will have to be more stable under alkaline conditions and demonstrate improved conductivity.^{1,2,6,8} Advances in this technology would have a significant impact on the transportation industry if performance increased with cost reduction, but cost-performance trade-offs must be considered. Most major automakers have active fuel cell projects, as fuel cell efficiency is more than double the efficiency of internal combustion engines.⁹

In addition to the high cost of PEM fuel cells due to precious metal catalysts or expensive membranes such as Nafion[®], the lifetime of these fuel cells is too short. Exposure to fuel and air impurities can inhibit electrode charge-transfer processes and alter water and gas transport of the GDLs, reducing PEM fuel cell performance. To better gauge PEM fuel cell durability, load cycling, start/stop cycling, and exposure to changing temperature and relative humidity experiments are an active area of PEM fuel cell research.^{4,10} Although AEM fuel cells do not require noble metal catalysts, the conductivity of AEMs is lower than PEMs due to the decreased diffusion coefficient of the hydroxide ions associated with AEMs, compared to the protons associated with PEMs. Further decrease in conductivity occurs if the hydroxide ions reaction with carbon dioxide and convert to bicarbonate ions, which have an even lower diffusion coefficient. Additionally, AEMs are not currently stable at the high pH required for fuel cell operation; the stability of quaternary ammonium, phosphonium, and sulfonium groups in basic conditions needs improvement and is under investigation.^{2,6}

The interaction of water with PEMs and AEMs is critical to the performance of fuel cells; proton and anion conductivity depend on water content. Reducing the relative humidity (RH) dramatically decreases the membrane conductivity and can damage the membrane. Yet, liquid water can flood the porous GDLs, which can lead to breakdown of the fuel cell. The amount of water in a fuel cell must be carefully regulated, but fuel cell membranes must also maintain high conductivity at low levels of hydration.^{1,11} There is a need for fundamental knowledge to allow for gains in understanding fuel cell operation mechanisms, but it is extremely difficult to simultaneously investigate *in situ* and *operando* water transport in fuel cells. Although investigation of the MEA is important, it is also critical to understand the water sorption and transport properties of the polymer electrolyte membrane.⁹ This work focuses on investigating the connections between polymer hydration, morphology, and conductivity in polymer electrolyte membranes.

1.2. Important Membrane Characteristics

To properly research polymer electrolyte membranes and compare the performance of one membrane against others, specific characteristics are commonly analyzed and need to be considered as a set of information to gain insight into the different levels of membrane performance. Instead of using degree of functionalization to account for the ion content in membranes, which is difficult to use to evaluate different membrane systems on an equal basis, a gravimetric ion exchange capacity (IEC) is calculated in units of milliequivalents of ion per gram of dry polymer. The IEC serves as a consistent quantity to assess ion content independent of the polymer system; a membrane with an IEC of $2.0 \text{ meq}\cdot\text{g}^{-1}$, contains twice as many ions as a membrane with an IEC of $1.0 \text{ meq}\cdot\text{g}^{-1}$, regardless of the specific polymer or ion used. The water

uptake (wu) of a polymer or membrane is typically reported as a weight percent, shown in equation 1.1, but this does not account for the ion content of the polymer.

$$\text{wu (\%)} = \left(\frac{m_{\text{hyd}} - m_0}{m_0} \right) \times 100 \quad (1.1)$$

where m_{hyd} is the hydrated sample mass and m_0 is the mass of the dry sample.

From the IEC and water uptake, the conducting ion concentration can be computed from equation 1.2, below.

$$c = 0.001 \cdot \frac{\rho \cdot \text{IEC}}{1 + 0.01 X_{\text{v-H}_2\text{O}}} \quad (1.2)$$

where c is the moles of ions per cm^3 of polymer, ρ is the polymer density, IEC is the milliequivalents of ion per gram polymer, and $X_{\text{v-H}_2\text{O}}$ is the volume-based water uptake.¹²

The wu of a membrane is often converted to a hydration number (λ), which is the number of water molecules per mobile ion (see equation 1.3).

$$\lambda = \left(\frac{m_{\text{RH}} - m_0}{m_0} \right) \cdot \left(\frac{1000}{M_{\text{H}_2\text{O}} \cdot \text{IEC}} \right) \quad (1.3)$$

where m_{RH} is the sample mass at a given relative humidity, RH; m_0 is the mass of the dry sample; $M_{\text{H}_2\text{O}}$ is 18.02 g, the molecular mass of water; and IEC is the ion exchange capacity with units of milliequivalents of ions per gram of polymer.

Finally, the ionic conductivity (σ) is determined from a measurement of the membrane resistance, illustrated by equation 1.4. The units of σ are Siemens per centimeter, $\text{S}\cdot\text{cm}^{-1}$, or milliSiemens per centimeter.

$$\sigma = \frac{L}{R \cdot A} \quad (1.4)$$

where L is the length between electrodes, R is the resistance of the membrane, and A is the cross-sectional area of the membrane. The conductivity can be used to determine the effective proton mobility of the ion, which includes contributions from acid dissociation, tortuosity, and the proximity of acid groups to one another.¹³ These terms are related by equation 1.5, below:

$$\sigma_{\text{H}^+} = F[-\text{SO}_3\text{H}]\mu'_{\text{H}^+} \quad (1.5)$$

where σ_{H^+} is the measured conductivity, F is Faraday's constant, $[-\text{SO}_3\text{H}]$ is the acid concentration, and μ'_{H^+} is the effective proton mobility.¹³ These symbols and parameters will be used frequently to discuss the performance of PEMs and AEMs and compare and contrast different polymeric systems.

There are a few other key membrane parameters such as water self-diffusion coefficient,^{14–16} dilute solution diffusivity,¹⁷ and interdomain spacing and ionic phase morphology.^{18–23} These terms will be introduced throughout the thesis, where needed. It is thought that the interplay of ionic group concentration, hydration number, and morphology ultimately determine the conductivity of the material, and it is helpful to have measurements of these key parameters in understanding membrane properties from a fundamental level.

1.3. Current Status of Proton and Anion Exchange Membranes

1.3.1 Proton Exchange Membranes

In the past few decades, PEM development has been an active area of research, and the membranes are being integrated into commercial fuel cells. To serve as a successful PEM, a membrane must demonstrate thermal stability and high proton conductivity at low levels of hydration, and it must also be robust to survive the cycling that occurs during fuel cell operation. Improving the ion exchange capacity, IEC, the number of ions per gram of polymer, without compromising the membrane toughness is necessary. To minimize PEM swelling, the number of water molecules per ion, or hydration number λ (equation 1.3), must also be a point of focus and must be kept low enough to not plasticize the polymer greatly, yet some water is required for effective ion conductivity. Finally, the overall durability and cost of perfluorinated PEMs is a barrier to widespread use, especially since PEM fuel cells currently require precious metal catalysts because of their acidic environment.^{1,3,4,10}

Random copolymer PEMs with sulfonate groups distributed statistically along the polymer backbone have demonstrated potential for use in fuel cells, and poly(perfluorosulfonic acid)-based membranes lead the field with trademarked Nafion[®], Aquivion[®], Flemion[®], and 3M ionomer polymers. Nafion[®], in particular, developed by DuPont, has been extensively studied and used as a benchmark for comparison for new polymer electrolytes. In an effort to design polymers with similar performance, the morphology of Nafion[®] has been an active area of research. The early Gierke model suggested that the main substructure of Nafion[®] was water-filled nanochannels lined with functional groups, based on small angle and wide angle x-ray scattering measurements. The model depicted clusters of inverted micelles on the order of

4 nm, connected by channels that were approximately 1 nm in size.^{24,25} However, the Gierke model did not take into account the crystallinity of the perfluorocarbon backbone or the chemical structure of the polymer on the phase-separated morphology, and this model has been considered inadequate in light of more extensive scattering and hydration studies. Although there is not agreement on the exact morphology of Nafion[®], current accepted models include ionic clusters that form rod-like micelles or form cylindrical or ribbon-like aggregates that bundle^{26,27} and inverted-micelle cylinders that also form bundles.²⁸ The newer models relate the ionomer peak from small angle x-ray scattering data to the distances between aggregates and use wide angle x-ray scattering data to provide data on sub-aggregate structural details and account for the ion-ion interactions, crystallinity, and long-aspect ratio structures observed in Nafion[®].^{26,27,29,30}

Nafion[®] has been compared to other PEMs to determine the bases for the high performance of Nafion[®]. In relationship to sulfonated poly(ether ether ketone ketone), sPEEKK, Nafion[®] was found to have wider, more direct and separated channels that interconnected, with ions in close proximity channels while the channels in sPEEKK were narrow, branched, with less connectivity, further separation between ions, and dead ends. As hydration increased, the conductivity increased for both membranes, but at low levels of hydration, the conductivity of Nafion[®] was less reduced than the conductivity of sPEEKK. Further of note was the effect of water on the mechanical and transport properties of the membranes; with excessive swelling, the membranes lost mechanical integrity, and conductivity decreased due to ion dilution.¹⁵ The morphology of Nafion[®] was imaged by transmission electron microscopy (TEM) and compared to the morphology of sulfonated poly(phenylene), SDAPP. The images illustrated the larger ionic domains of Nafion[®], which led to higher water diffusion and ion transport. The smaller domains and less-pronounced phase separation of SDAPP were believed to be the origin of the lower conductivity in those membranes.³¹ However, the high conductivity of Nafion[®] is paired with

undesirable high methanol crossover in fuel cell operation, as well as low stability at temperatures above 80 °C.^{3,10}

Polymers with aromatic backbones, such as poly(imides), poly(phenylenes), poly(sulfones), and poly(ketones) have also shown promise.^{1,3,4,7,32–34} Poly(imide) fuel cell membranes from six-member rings have demonstrated long lifetimes and high performance, as the stability is greater than poly(imide) backbones containing five-member rings.³⁵ In contrast to Nafion[®], poly(imides) have stiff backbones and low methanol permeability. Nevertheless, poly(imides) have lower conductivity than Nafion[®] and many other PEMs, but are making advances in that area.^{34,36} Sulfonated poly(phenylenes), such as SDAPP, also have stiff backbones, leading to high glass transition temperatures (T_g) and desirable mechanical properties. Although the conductivity of SDAPP membranes is appreciable, it is less than Nafion[®] and poly(sulfone) membranes for a given IEC and λ .^{31,33} Poly(arylene ether sulfones) have been studied extensively as fuel cell membranes due to their promising thermal stability, high conductivity, and low methanol permeability. Of particular interest are poly(bisphenol sulfones), BPSH, membranes, which have demonstrated conductivities higher than Nafion[®]; however, the IEC values of the BPSH membranes were also higher. It is believed that BPSH membranes possess less phase separation and fewer interconnected ionic domains, which lowers conductivity and methanol permeability by greater confinement of water. The synthesis of these membranes has improved to allow for design of hydrophilic or hydrophobic blocks, enhancing the durability and conductivity of the membranes.^{36–39} Sulfonated poly(arylene ether ketone) membranes exhibited similar conductivity as Nafion[®] and higher Young's modulus than the benchmark membrane.⁴⁰ By blending sulfonated poly(arylene ether ketones) with poly(benzimidazole) to ionically crosslink the poly(ketone) and by doping the polymer with heteropolyacids that are strong Bronsted acids, the swelling and resistance of the membranes decreased.⁴¹ This suggests that other PEMs comprised of a single homopolymer may also benefit from combination with

other substituents. Also, ion-containing block copolymers have exhibited higher conductivity than their random copolymer counterparts and will be discussed later for use as PEMs and AEMs.^{2,42-48}

1.3.2 Anion Exchange Membranes

The first alkaline fuel cells used an aqueous solution of potassium hydroxide as the electrolyte, hydrogen gas as fuel, and operated at temperatures ranging from 50-200 °C. However, the liquid electrolytes are susceptible to carbon dioxide poisoning, causing the formation of precipitates and reduced performance. Instead, polymer membranes have been seen as an alternative electrolyte for ion conduction, leading to increased interest in AEM fuel cells. Unlike PEM fuel cells and their need for precious metal catalysts, fuel cells based on AEMs can leverage cheaper catalyst metals due the alkaline environment during fuel cell operation. However, AEMs are less stable and must demonstrate improved conductivity to be viewed as true competition to PEMs in the fuel cell market.^{1,2,5,6}

Developed by the Tokuyama Soda Company of Japan, the earliest AEMs were poly(chloropropene) crosslinked by divinylbenzene and functionalized with quaternary ammonium groups using triethylamine.² Since then, many other random copolymers, such as poly(sulfones),^{49,50} poly(phenylene oxides),⁵¹⁻⁵³ poly(ketones),⁵⁴ poly(tetrafluoroethylene),⁵⁵ and poly(styrene-*b*-ethylene-*co*-butylene-*b*-styrene) have been used to produce AEMs. Quaternary ammonium, QA, functionalized poly(arylene ether sulfone) membranes with side chain pendant functional groups demonstrated lower water uptake than Nafion[®] and a conventional poly(arylene ether sulfone), but the hydroxide conductivity was also lower for the majority of the membranes tested.⁴⁹ Bromination of a benzylmethyl poly(sulfone) with subsequent amination before and after membrane casting led another series of QA poly(arylene

ether sulfone) membranes. The membranes that were in QA form before being cast exhibited higher conductivity for a given IEC than those converted after casting. The higher conductivity of the first set of membranes was attributed to ionic interactions of the QA groups during the casting process.⁵⁰ Brominated poly(phenylene oxide) was reacted with dimethylethanolamine to produce AEMs that had high ion exchange potential. By controlling the concentration of dimethylethanolamine and the reaction temperature, AEMs with lower w_u and higher conductivity have been developed.⁵¹ Comb-shaped, QA-functionalized poly(phenylene oxide) membranes demonstrated comparable conductivity and lower w_u than analogous, non-comb-shaped poly(phenylene oxide) membranes. Membranes from the comb-shaped polymer showed a morphology consisting of hydrophilic-hydrophobic domain phase separation with interconnected hydrophilic domains, which accounted for the higher conductivity.⁵² Continued development of this class of polymers through variation of the length of the alkyl side chain allowed for tunable properties; the polymer with the longest side chain showed lower w_u and higher conductivity.⁵³ A quaternized cardo poly(ether ketone) membrane with minimal ion content had low water and methanol uptake while exhibiting high conductivity for the IEC. In fact, the overall water and methanol uptake of the AEM was similar to a membrane cast from the unfunctionalized polymer.⁵⁴ To research Nafion[®]-based AEMs, membranes were cast from poly(tetrafluoroethylene) backbones functionalized with different cationic moieties. The membranes demonstrated reasonable conductivity values for their IEC and their overall thermal and chemical stability was promising, but the AEMs had large w_u and λ values.⁵⁵ Comparatively, the hydrocarbon backbone poly(styrene-*b*-ethylene-*co*-butylene-*b*-styrene) was functionalized with QA for use as an AEMs. Penetrating channels were observed in an image of the membrane cross-section, and the overall morphology was uniform. Again, thermal stability was adequate, but the membrane demonstrated low conductivity and high w_u for the IEC.⁵⁶ AEMs continue to improve, and block copolymer AEMs will be discussed in Section 1.4. At this point, it is not

known what the key strategies are for improved AEM performance, but by studying the relationships between fixed ion concentration, water diffusion, morphology, and ion conductivity, promising directions in the field can be identified.

1.4. Ion Transport

1.4.1 Non-Aqueous and Aqueous Dynamics

Ion conduction in polymers can occur through either non-aqueous mechanisms in dry systems or aqueous dynamics in hydrated polymers. The important material contributions governing the conduction vary with the mechanism. For non-aqueous conductors, such as polymers for lithium ion batteries, the ion dynamics are dominated by the polymer segmental properties, such as T_g , the glass transition temperature, and the dielectric constant of the system which drives ion pair separation.

Conductivity values in these systems typically range from $10^{-11} \text{ S}\cdot\text{cm}^{-1}$ to $10^{-3} \text{ S}\cdot\text{cm}^{-1}$. Their temperature dependent conductivity behavior is described by the Vogel-Fulcher-Tammann (VFT) equation, shown below:

$$\ln \sigma = \sigma_0 \exp\left(\frac{-B}{T - T_0}\right) \quad (1.6)$$

where σ is conductivity; σ_0 is the conductivity at infinite temperature; B is a constant; T is temperature; and T_0 is the Vogel temperature, at which point the polymer has essentially no free volume.^{1,57} VFT expressions for the temperature-dependent conductivity are directly linked to

VFT expressions of segmental dynamics and provide a justification for increasing the segmental dynamics of the polymer to increase ion conductivity.

A proton-conducting system of imidazole-terminated ethylene oxide oligomers doped with small amounts of strong acids was designed to function with no liquid solvent. The significant imidazole content and the low T_g of the systems translated into relatively high conductivities. It was determined that 2-10 mol % of acidic groups provided the best structure, which is critical because proton conductivity occurred primarily through structure diffusion, which is intermolecular proton transfer.⁵⁸ The effect of counterion was investigated for poly(phosphazenes), where a doped system was compared to a pure ionomers system. Although the polymer matrix controlled ion diffusion, the mobility of the ions in the doped system was an order of magnitude larger than the ionomeric system, and the activation energy for transport was lower for the doped system. It was concluded that ionomers must have lower glass transition temperatures, create new transport pathways, or decrease the bonding energy between the bound ion and the counterion in order for these systems to be viable.⁵⁷

Comparatively, aqueous conductors rely on water dynamics for conduction, rather than the polymer segmental dynamics as governed by T_g , and typical conductivity values range from $10^{-4} \text{ S}\cdot\text{cm}^{-1}$ to $1 \text{ S}\cdot\text{cm}^{-1}$. Water acts as both a proton donor and a proton acceptor and possesses fast rotational dynamics, allowing for the higher conductivity of hydrated polymers compared to non-aqueous conductors.

The ionic conductivity of these systems is dominated by Arrhenius behavior, as described by equation 1.8 below:

$$\ln \sigma = \ln \sigma_0 \exp\left(\frac{-E_a}{RT}\right) \quad (1.7)$$

where σ is conductivity; σ_0 is the conductivity at infinite temperature; E_a is the activation energy to transport, R is the universal gas constant; and T is temperature.^{1,59} In this case, water motion is thermally activated, so an Arrhenius expression describes the temperature-dependent conductivity behavior of aqueous-conducting systems, and polymer dynamics do not play a role in ion transport. Aside from temperature, the E_a is influenced by the ion content, water uptake, and the water-ion interactions in the polymer. The rest of this section will discuss the mechanisms of aqueous conduction in greater detail.

1.4.2 Ion Transport Mechanisms in Pure Water

Proton transport in pure water has been well-studied and is described as “structure diffusion,” where hydrogen bonds form an Eigen-ion of H_9O_4^+ and break to form a Zundel-ion of H_5O_2^+ . The energy barrier between the two complexes is minimal, so proton diffusion in water is considered to be fast, especially compared to the diffusion of oxygen in water.¹⁵ There are two methods by which protons move through water: hopping or structure diffusion (loosely termed Grotthus) and vehicle mechanisms, as shown in Figure 1.2. For the hopping or structure diffusion method, protons essentially change their associated oxygen nuclei and shuttle through the hydrogen bonds being formed and broken by the water molecules. The atoms in the water molecules themselves are considered to be stationary other than their rattling motion as the

covalent and hydrogen bonds switch in accordance with the motion of the free proton. On the other hand, water molecules and protons move at the same rate during the vehicle mechanism; the water molecules act as a “vehicle” by which the ions are transported.^{14,60}

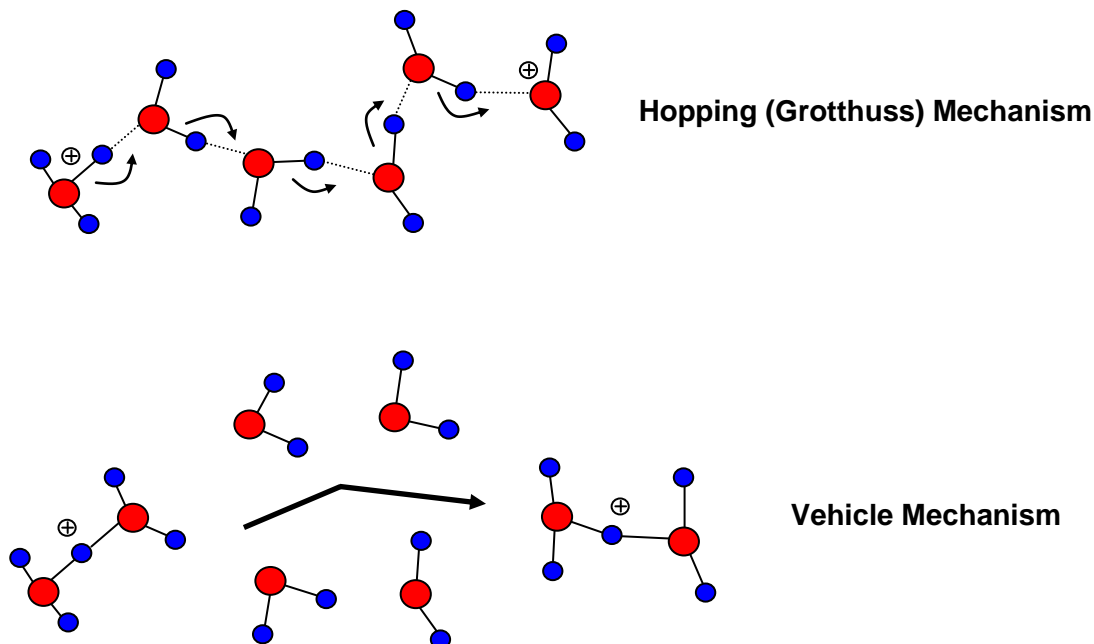


Figure 1.2. Schematics depicting the hopping (Grotthuss) and vehicle mechanisms of proton transport in pure water. Hydrogen atoms are blue, and oxygen atoms are red.^{14,60}

Hydrated hydroxide ions have been considered to be water molecules missing a proton, so the transport of these ions has been regarded as the movement of a “proton hole,” similar to a hole in electronic conduction. Recent studies have shown that hydroxide hydration complexes are different from proton hydration complexes, and the transport mechanism of hydroxide ions is not analogous or fully understood.^{61,62} Protons have localized charges and the bonding of hydronium is highly directional, but hydroxide ions have a more diffuse charge and thus the hydrogen bonding events during hopping transport as not as constrained. This general comparison of the

molecular features of hopping in each system is reflected through the lower diffusion coefficient of hydroxide ions, $20.64 \times 10^8 \text{ m}^2(\text{s}\cdot\text{V})^{-1}$, compared to the diffusion coefficient of protons, $36.23 \times 10^8 \text{ m}^2(\text{s}\cdot\text{V})^{-1}$, both at 298 K. For a hydroxide ion to move, a hydrogen bond in the first solvation shell of the hydroxide ion must be broken, and then a weak hydrogen bond must form between the hydrogen atom of the hydroxide ion and a nearby water molecule. Instead of the tricoordinate complexes formed during proton transport, there is a combination of intermediate tricoordinate, $\text{OH}(\text{H}_2\text{O})_3$, and tetragonal, $\text{OH}(\text{H}_2\text{O})_4$, complexes associated with hydroxide transport. However, the mechanism of hydroxide transport is still not completely clear in water or in polymer membranes.^{61,62}

1.4.3 Water-Ion Interactions in Polymers

Although ion transport in pure water is important to investigate, it is critical to study water-ion interactions in polymers, as the water sorbed into ion conductors does not feature properties that are analogous to bulk water. One aspect of this effort is comparison of proton diffusion in hydrated Nafion[®], calculated from conductivity values, to water self-diffusion coefficients using pulsed field gradient ¹H nuclear magnetic resonance (PFG-NMR) spectroscopy. At low levels of hydration, the proton and water moved at the same rate, indicated by their similar diffusion coefficients and suggesting transport through the vehicle mechanism. However, at high levels of hydration, the diffusion coefficient of the proton in the membrane was larger than the water diffusion coefficient, so the proton in Nafion[®] had faster transport than the translational diffusion of water, which is a signature of proton hopping or Grotthus mechanism.⁶³ The “pores” of fully hydrated Nafion[®] have been modeled to further probe the behavior of water

in an ionic membrane. Towards the center of the model “pores,” the proton diffusion coefficient increased because the friction between the tethered sulfonate groups and the proton decreased.⁶⁴

Relative to other membranes, ion transport in Nafion[®] is more facile. The dielectric constant in hydrated sPEEKK is lower than that of hydrated Nafion[®] because the cation and anion are bound more tightly in sPEEKK and the water is more bound to the polymer (lowering its effective permittivity), even for the same volume fraction of water in the polymer. The observation of a lower effective dielectric constant in sPEEKK is linked to its lower self-diffusion coefficient and greater water-polymer interactions.¹⁵ Another method of correlating differences in ion transport is to compare the activation energy, E_a , for each membrane.⁶⁵ The E_a of Nafion[®] was lower than the E_a of SDAPP, another PEM, probably due to the smaller domains in SDAPP, thus limiting transport and increasing the activation energy of SDAPP.³¹ These comparisons reinforce the position of Nafion[®] as a benchmark membrane for ion transport, but the hydration of the membrane must be monitored. In general, ionic conductivity is thermally activated process, and it increases with water content because there is more mobile water available for ion transport. At a critical point, however, there is sufficient water content such that ion dilution occurs. The conductivity is reduced because of the overall decreased ion concentration.^{65,66}

1.4.4 Ion Transport Metrics

One of the issues hindering the development of PEMs and AEMs is the discrepancy in the methods by which data is measured and reported. Other than the criteria described in Section 1.2, which are not always reported in every case of a new ion-conductive material, there is little consistency in the numbers reported for various PEMs and AEMs. Comparison and evaluation of

these membranes is compromised by this shortcoming, and efforts have been established to improve this inadequacy.

Since the conductivity and hydration of PEMs and AEMs generally increase with ion content, it is difficult to separate these aspects from one another. To compare conductivity values of membranes with different IECs, many researchers have used an IEC-normalized conductivity, calculated as shown below:

$$\sigma_{\text{IEC}} = \frac{\sigma}{\text{IEC}} \quad (1.8)$$

where σ_{IEC} is the IEC-normalized conductivity, σ is the measured conductivity, and IEC is the milliequivalents of ion per gram of polymer.⁶⁷⁻⁶⁹

Although IEC-normalized conductivity provides one method to assess the properties of different membranes, it does not account for differences in ion mobility. This is especially important in comparing the conductivity values for PEMs and AEMs, since the mobility of protons is $362.4 \times 10^{-5} \text{ cm}^2 \cdot \text{V}^{-1} \cdot \text{s}^{-1}$, which is much greater than the mobility of hydroxide ions, $197.6 \times 10^{-5} \text{ cm}^2 \cdot \text{V}^{-1} \cdot \text{s}^{-1}$, bicarbonate ions, $46.4 \times 10^{-5} \text{ cm}^2 \cdot \text{V}^{-1} \cdot \text{s}^{-1}$, and chloride ions, $76.3 \times 10^{-5} \text{ cm}^2 \cdot \text{V}^{-1} \cdot \text{s}^{-1}$, the ions typically used in AEMs.⁷⁰ Mobility-normalized conductivity has been used in this regard, as determined by the equation below:

$$\sigma_n = \frac{\sigma}{\mu_i} \quad (1.9)$$

where σ_n is the normalized conductivity, σ is the measured conductivity, and μ_i is the mobility of the conductive ion.

Mobility-normalized conductivity was calculated to investigate the transport properties of SDAPP PEMs and an QA-poly(sulfone) AEMs. The AEMs demonstrated lower conductivity

than the PEMs at similar IEC and w_u . Difference in mobility accounted for some of the conductivity discrepancies between the PEMs and AEMs, but it was not the only factor. The number of mobile ions was believed to be lower for the AEMs than the PEMs due to the greater dissociation of the protons from the tethered sulfonate groups compared to the hydroxide ions and the tethered quaternary ammonium groups.⁷¹

However, this approach is still limited and does not provide information about the actual transport of the ions or account for ion concentration. To achieve this goal, the diffusion coefficient, of PEMs and AEMs have been calculated from the measured conductivity of the membranes, using the Nernst-Einstein equation and the number density of charge carriers expressed earlier in equation 1.2.¹² This value can be used to calculate the diffusion coefficients of the mobile ions from a form of the Nernst–Einstein equation, below:

$$D = \frac{\sigma \cdot RT}{cz^2F^2} \quad (1.10)$$

where σ is the measured conductivity, R is the ideal gas constant, T is temperature, c is the computed concentration of ions in the hydrated membrane as calculated by equation 1.2, z is valance charge, and F is Faraday’s constant.⁷² This diffusion coefficient is the “effective diffusion coefficient” of the ion because it includes tortuosity implicit in the conductive pathways of the ions. However D is used throughout this work, as tortuosity was not measured or calculated in these systems.

The calculated diffusion constants were compared to the dilute solution diffusivities, D_0 , of the mobile ions, using the dilute solution mobility of each ion as follows:

$$D_0 = \frac{\mu \cdot k_B T}{q} \quad (1.11)$$

where μ is the dilute solution ion mobility, k_B is the Boltzmann constant, T is temperature, and q is the ion charge.¹⁷

The ratio of D/D_0 was compared for PEMs and AEMs derived from the same polymer and was found to be similar as a function of λ for both proton and chloride counterions. Although the conductivity values of the PEMs were greater than the AEMs, it could be attributed to the higher mobility of the protons. The fundamental ion transport in these two materials was comparable, an intriguing result.⁷³

1.5. Block Copolymers

1.5.1 Block Copolymer Overview

Thus far, the majority of PEMs and AEMs described have been homopolymers or random copolymers. However, block copolymer PEMs and AEMs are of particular interest. Complex morphologies are attainable with block copolymers, which can be tuned based on the fraction of each component in the block copolymer.^{74,75} A schematic depicting hypothetical chains of various polymers and copolymers is shown in Figure 1.3, with polymer A represented by blue beads and polymer B represented by red beads.

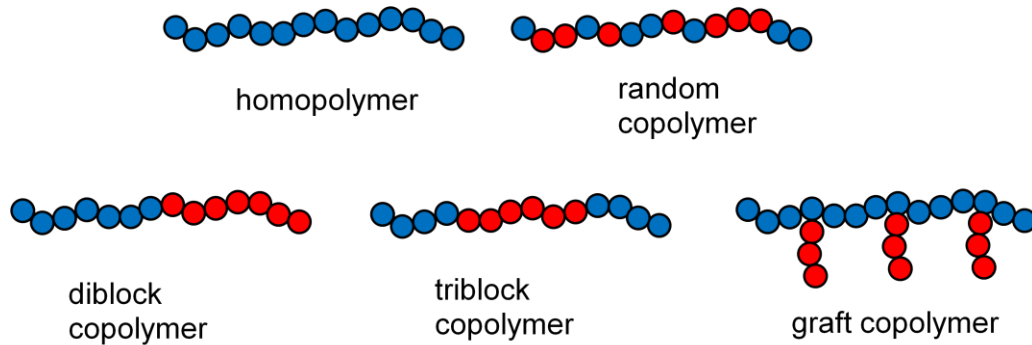


Figure 1.3. Schematic depicting polymer chains for a homopolymer, AB random copolymer, AB diblock copolymer, ABA triblock copolymer, and AB graft copolymer. Polymer A is represented by blue beads, and polymer B is represented by red beads.

The complex morphologies possible with diblock copolymer are controlled by the fraction of each component, f , the interaction parameter, χ , and the number of repeat units, N . Using Flory-Huggins and self-consistent mean field theories, phase diagrams have been calculated to predict the morphology of AB diblock copolymers as a function of the parameters above, see Figure 1.4. The interaction parameter, χ , is calculated from the Hildebrand solubility parameters for polymers A and B, shown by the equation below:

$$\chi = \frac{V_r (\delta_A - \delta_B)^2}{RT} \quad (1.12)$$

where V_r is the reference volume, δ_A and δ_B are the solubility parameters for polymers A and B respectively, R is the ideal gas constant, and T is the temperature.⁷⁶

However, it is important to note that these calculations and diagrams do not take into account the effect of ions on solubility parameters and the interaction parameter. Therefore, it is more challenging to design a specific morphology for ion-containing polymers. Microstructures

observed experimentally by these systems are not predicted by Flory-Huggins parameters, and ion-ion interactions matter.⁷⁷ The next sections will discuss block copolymer PEMs and AEMs and will touch on the unique morphologies demonstrated by these polymers.

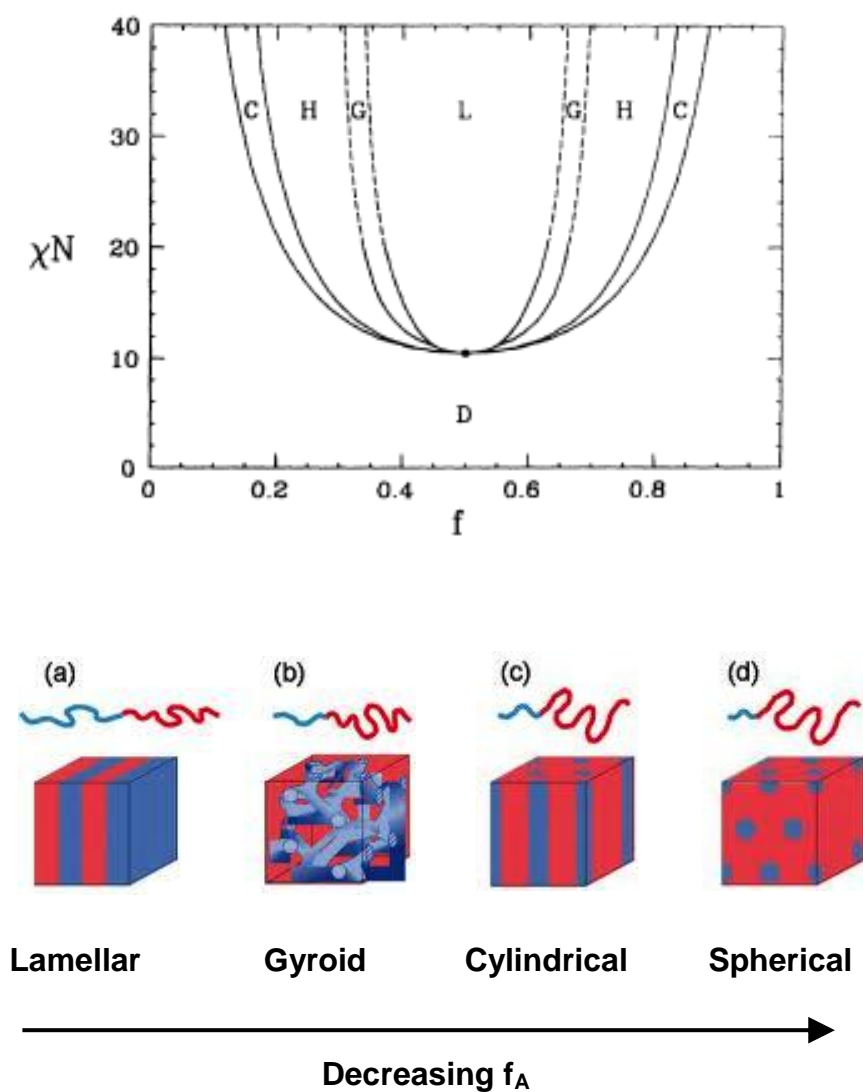


Figure 1.4. Phase diagram for an AB diblock copolymer (top) and cartoons of (a) lamellar, (b) gyroid, (c) cylindrical, and (d) spherical morphologies.^{74,75}

1.5.2 Block Copolymer PEMs and AEMs

Sulfonated block copolymer PEMs have demonstrated higher conductivity than their random copolymer counterparts, partly attributed to morphology differences between the block and random copolymers.^{42,44–46} Poly(styrene)-poly(styrene sulfonate), PS-PSSA, graft and random copolymers were designed by Holdcroft and co-workers to control the morphology and content of the PEMs. The graft copolymer (PS-*g*-PSSA) exhibited higher conductivity and more phase-separated domains than the random copolymer, (PS-*r*-PSSA), as shown in Figure 1.5.⁴⁵ Sulfonated poly([vinylidene difluoride-*co*-hexafluoropropylene]-*b*-styrene) block copolymers were synthesized in an effort to produce strongly phase-separated membranes since the two blocks were incompatible. By increasing the ion content, the conductivity and the phase segregation between blocks increased. The conductivity of these polymers was higher than analogous random copolymers, believed to be due to the increased phase segregation of the block copolymers.^{44,46}

Morphological studies on ion-containing block copolymers have centered on those with fluorinated or aromatic backbones and sulfonic acid pendant groups.⁷⁸ Balsara and co-workers have observed varied morphologies for poly(styrene sulfonate-*b*-methylbutylene), PSS-PMB. For the systems studied, Flory-Huggins and self-consistent mean field theories predicted lamellar morphology, but the ion content present in the polymer led to perforated lamellar, cylindrical, and gyroid microstructures.²² Elabd and co-workers studied poly(styrene-*b*-isobutylene-*b*-styrene) and found that even without long-range order, local lamellar morphologies were present and led to enhanced proton conductivity over randomly sulfonated poly(styrene).⁷⁹ Park and Balsara have also studied the effect of humidity on the order of PSS-PMB, and found that changes in the film morphology occurred more quickly than did changes in conductivity.²³

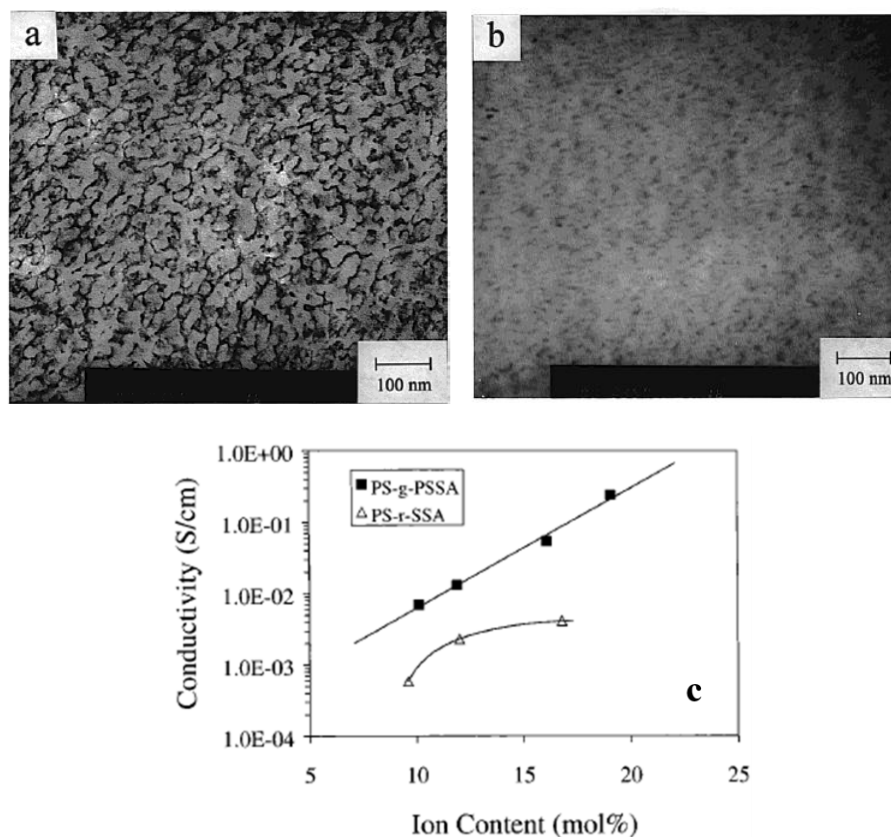


Figure 1.5. Transmission electron micrographs of (a) PS-*g*-PSSA and (b) PS-*r*-PSSA. The greater phase separation of the graft copolymer contributes to the higher conductivity shown in (c).⁴⁵

Block copolymer AEMs are less studied, and it is unclear if they will exhibit the same morphology-conductivity relationships as PEMs. Quaternized block copolymers demonstrated increased mechanical strength compared to randomly-functionalized copolymers, attributed to control of swelling by the non-ionic block.² Hwang and Ohya synthesized QA block copolymers with biphasic morphology that exhibited increased conductivity compared to random copolymers. However, the block copolymers had higher IEC values than the random copolymers.^{2,80} Miyatake established that QA multiblock copoly(arylene ether) fluorene-containing polymers demonstrated higher conductivity than analogous random copolymers.⁴⁸ As the details on AEMs begin to

emerge, it will be interesting to discover if their structure-property relationships will be comparable to PEMs.

1.5.3 Control of Block Copolymer Morphology

The conductivity and hydration of block copolymer PEMs and AEMs are linked to the morphology of the polymers, as described in the previous section. Selecting a particular morphology or altering the morphology of the membranes should modify the properties of the membrane, and subsequently, honing in on the ideal morphology would lead improved membrane performance. Two methods by which block copolymer morphology can be controlled are design of polymer and choice of solvent.

The design of the polymer is perhaps the most crucial of the parameters in that it is necessary to select blocks or grafts that complement one another and also phase segregate. Membranes must be durable, so a brittle polymer such as poly(styrene) has been combined with lower- T_g polymers, such as poly(methyl butylene)²³ and poly(hexyl methacrylate).⁸¹ The phase segregation of Nafion[®] has served as a target for block copolymer membranes, leading to fluorinated graft and block copolymers with discrete domains.^{45,82} The decision to synthesize graft or block copolymers is important since graft copolymer PEMs have smaller channels than diblock copolymer PEMs, leading to reduced ion mobility and lower conductivity in the graft copolymers.⁸³ The degree of polymerization is also a concern; as molecular weight increases, the size of the hydrophilic domain increases, but there is a greater barrier to ordering of the block copolymer during membrane casting.^{84,85} Finally, the ion content in the polymer greatly contributes to the morphology of the membrane, and order-to-disorder transitions in ion-containing block copolymers has been well documented.^{22,78,86}

The solvent used during membrane casting can determine the morphology of the final PEM or AEM. A block copolymer exhibiting ordered lamellar morphology when cast from a polar aprotic solvent can also exhibit disordered morphology when cast from a mixture of polar aprotic and protic solvents, resulting in changes in conductivity.⁸⁵ Co-continuous and continuous microdomains in the direction of transport are the desired morphology for membranes, and they are attainable with correct solvent choice and adequate ion content. Block copolymer membranes that were disordered as cast from a polar solvent demonstrated ordered conductivity and improved conductivity when cast from a polar aprotic solvent.⁷⁹ Choosing to cast an ion-containing block copolymer from a solvent that kinetically traps a random, phase-separated morphology decreases the effective tortuosity of the membrane and facilitates ion transport. This is achieved through careful examination of solubility parameters and subsequent mixing of solvents as necessary.⁴³

Several researchers have taken the next step and observed the evolution of the membrane morphology during the solvent evaporation process. The ordering kinetics of block copolymer films can be monitored through *in-situ* small angle x-ray scattering experiments, where transitions in morphology can be detected as a function of block copolymer concentration.⁸⁷ In addition, the observed morphology can be “set” by using non-solvent-induced phase separation. This process involves monitoring the structural evolution of the membrane as solvent evaporates and then immersing the film into a bath that precipitates the membrane. The resulting film typically consists of uniform pores with an ordered morphology that is consistent with the solution morphology detected *in-situ*, as shown in Figure 1.6.⁸⁸ Through the use of solvent choice and selective precipitation, obtaining the targeted morphology can be a reality.

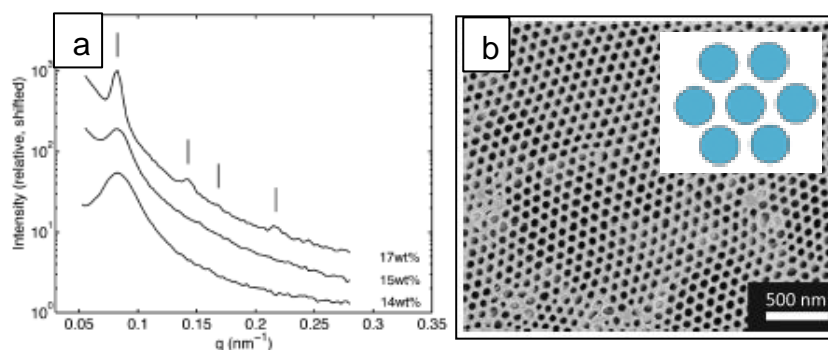


Figure 1.6. (a) Small angle x-ray scattering curves of poly(styrene-*b*-(4-vinyl pyridine)) in a mixed dioxane/tetrahydrofuran/*N,N*-dimethylformamide solution, and (b) a scanning electron microscope image of the top surface of the membrane cast from the 15 wt % solution.⁸⁸

1.5.4 Diblock and Triblock Copolymers

Block copolymers provide advantages over random copolymers in that their chemical structures are tunable, they demonstrate a wide range of targetable morphologies, and they exhibit higher conductivity.⁷⁸ Both diblock and triblock copolymers have been developed for use as fuel cell membranes; diblock copolymers have expressed highly ordered microphase separated morphologies, and triblock copolymers have showed high conductivity at reasonable levels of hydration.^{22,79} Self-consistent field theory has been used to model melts of AB diblock and ABA triblock copolymers.^{89,90} AB diblock copolymers are straightforward systems to research and typically phase separate into A and B blocks, but multiblock copolymers possess additional interactions that enhance material properties. These interactions, bridge and loop configurations, are present in systems such as ABA triblock copolymers. In this example, bridges are formed when the B block bridges two interfaces between the A block, increasing the mechanical strength of the polymer. Likewise, B loops form when both ends of the B blocks are in the same interface, with the A blocks in that same interface, illustrated in Figure 1.7.⁸⁹

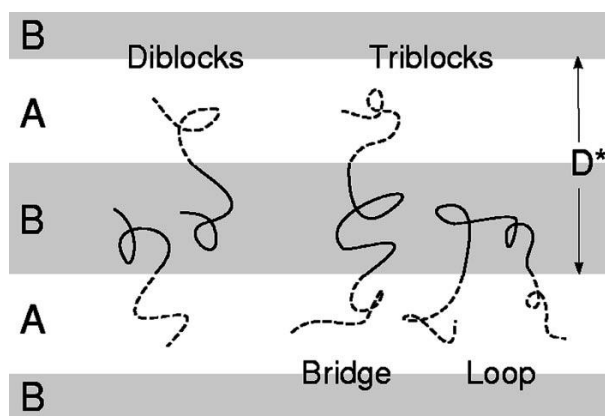


Figure 1.7. Configurations of lamellar AB diblock and ABA triblock copolymers. The diblock chains do not form bridges or loops, but the triblock chains are capable of demonstrating both configurations.⁹⁰

Due to the lack of interpenetrating networks in diblock copolymers, they experience chain pull-out under stress and are believed to swell more than triblock copolymers. The bridges and loops formed by triblock copolymers increase the number of entanglements and the mechanical strength, and bridges have been noted as a critical aspect of thermoplastic elastomers.⁹⁰ One could expect that diblock copolymers might demonstrate higher conductivity than triblock copolymers due to better ordering, increased ion motility, and higher λ . However, if the diblock copolymer swells excessively, the membrane will lose its mechanical integrity. Ion dilution could also occur with high λ , decreasing the conductivity of the membrane. Triblock copolymers may be the better approach for developing viable fuel cell membranes.

1.6. AEMs with Alternative Cations

The AEMs discussed previously have focused on the use of polymers with benzyltrimethylammonium (BTMA) moieties, but there are other cations currently being used in

AEMs. New cations are being sought primarily to increase the stability of AEMs, but the transport ramifications of these structures, must also be studied in depth. Benzyl quaternary phosphonium functionalized poly(sulfone-methylene) AEMs have demonstrated comparable conductivity to BTMA membranes.^{91,92} Low IEC sulfonium-containing poly(sulfones) have also been realized as AEMs; diphenyl(3-methyl-4-methoxyphenyl) tertiary sulfonium cations exhibited more than double the conductivity of ordinary sulfonium-functionalized poly(sulfone).⁶⁸ Although imidazolium cations have also been explored, N-linked 1-methyl imidazolium show decreased conductivity compared to BTMA.⁹³

Cross-linked AEMs have been successful in reducing water uptake and swelling of the membranes while maintaining reasonable conductivity. The conductivity of cross-linked quaternary phosphonium functionalized was consistent with non-cross-linked membranes in both phosphonium and trimethyl ammonium forms.⁶⁹ Ring-opening metathesis polymerization (ROMP) of a phosphonium-functionalized poly(ethylene) produced a membrane with low IEC and reasonable conductivity.⁹⁴ ROMP of a bis(terpyridine)Ru(II) complex-functionalized norbornene with dicyclopentadiene (DCPD) led to the first metal-containing AEMs. The use of the metal Ru(II) complex allowed for two counterions to be involved in ion transport, and the conductivity varied with the monomer to DCPD ratio. Future work in this area will focus on reducing the wu of these membranes while maintaining competitive conductivity.⁹⁵

1.7. References

- (1) Hickner, M. A. *Mater. Today* **2010**, *13*, 34–41.
- (2) Couture, G.; Alaaeddine, A.; Boschet, F.; Ameduri, B. *Prog. Polym. Sci.* **2011**, *36*, 1521–1557.

- (3) Yee, R. S. L.; Rozendal, R. A.; Zhang, K.; Ladewig, B. P. *Chem. Eng. Res. Des.* **2012**, *90*, 950–959.
- (4) Zhang, H.; Shen, P. K. *Chem. Rev.* **2012**, *112*, 2780–832.
- (5) Arges, C. G.; Ramani, V.; Pintauro, P. N. *Electrochem. Soc. Interface* **2010**, 31–35.
- (6) Merle, G.; Wessling, M.; Nijmeijer, K. *J. Memb. Sci.* **2011**, *377*, 1–35.
- (7) Zhang, L.; Chae, S.-R.; Hendren, Z.; Park, J.-S.; Wiesner, M. R. *Chem. Eng. J.* **2012**, *204-206*, 87–97.
- (8) Varcoe, J. R.; Slade, R. C. T. *Fuel Cells* **2005**, *5*, 187–200.
- (9) Deabate, S.; Gebel, G.; Huguet, P.; Morin, A.; Pourcelly, G. *Energy Environ. Sci.* **2012**, *5*, 8824–8847.
- (10) Borup, R.; Meyers, J.; Pivovar, B.; Kim, Y. S.; Mukundan, R.; Garland, N.; Myers, D.; Wilson, M.; Garzon, F.; Wood, D.; Zelenay, P.; More, K.; Stroh, K.; Zawodzinski, T.; Boncella, J.; McGrath, J. E.; Inaba, M.; Miyatake, K.; Hori, M.; Ota, K.; Ogumi, Z.; Miyata, S.; Nishikata, A.; Siroma, Z.; Uchimoto, Y.; Yasuda, K.; Kimijima, K.-I.; Iwashita, N. *Chem. Rev.* **2007**, *107*, 3904–51.
- (11) Manke, I.; Markötter, H.; Tötze, C.; Kardjilov, N.; Grothausmann, R.; Dawson, M.; Hartnig, C.; Haas, S.; Thomas, D.; Hoell, A.; Genzel, C.; Banhart, J. *Adv. Eng. Mater.* **2011**, *13*, 712–729.
- (12) Kim, Y.; Einsla, B.; Sankir, M.; Harrison, W.; Pivovar, B. *Polymer (Guildf)*. **2006**, *47*, 4026–4035.
- (13) Peckham, T. J.; Schmeisser, J.; Rodgers, M.; Holdcroft, S. *J. Mater. Chem.* **2007**, *17*, 3255.
- (14) Kreuer, K. *Solid State Ionics* **1997**, *94*, 55–62.
- (15) Kreuer, K. *J. Memb. Sci.* **2001**, *185*, 29–39.
- (16) Li, J.; Park, J. K.; Moore, R. B.; Madsen, L. A. *Nat. Mater.* **2011**, *10*, 507–11.
- (17) Muthukumar, M. In *Advances in Chemical Physics*; Rice, S. A., Ed.; 2005; Vol. 131, p. 45.
- (18) Mani, S.; Weiss, R. A.; Williams, C. E.; Hahn, S. F. *Macromolecules* **1999**, *32*, 3663.
- (19) Lu, X.; Steckle, W. P.; Weiss, R. A. *Macromolecules* **1993**, *26*, 5876–5884.
- (20) Hiesgen, R. *Electrochim. Acta* **2009**, *55*, 423–429.

- (21) Goswami, M.; Sumpter, B. G.; Huang, T.; Messman, J. M.; Gido, S. P.; Isaacs-Sodeye, A. I.; Mays, J. W. *Soft Matter* **2010**, *6*, 6146.
- (22) Park, M. J.; Balsara, N. P. *Macromolecules* **2008**, *41*, 3678–3687.
- (23) Park, M. J.; Nedoma, A. J.; Geissler, P. L.; Balsara, N. P.; Jackson, A.; Cookson, D. *Macromolecules* **2008**, *41*, 2271–2277.
- (24) Gierke, T. D.; Munn, G. E.; Wilson, F. C. *J. Polym. Sci. Part B Polym. Phys.* **1981**, *19*, 1687–1704.
- (25) Hsu, W. Y.; Gierke, T. D. *J. Memb. Sci.* **1983**, *13*, 307–326.
- (26) Gebel, G. *Polymer (Guildf)*. **2000**, *41*, 5829–5838.
- (27) Gebel, G.; Diat, O. *Fuel Cells* **2005**, 261–276.
- (28) Schmidt-Rohr, K. *Nature* **2007**, 1–15.
- (29) Schmidt-Rohr, K.; Chen, Q. *Nat. Mater.* **2008**, *7*, 75–83.
- (30) Mauritz, K. A.; Moore, R. B. *Chem. Rev.* **2004**, *104*, 4535–85.
- (31) Hickner, M. A.; Fujimoto, C.; Cornelius, C. *Polymer (Guildf)*. **2006**, *47*, 4238–4244.
- (32) Li, Y.; Wang, F.; Yang, J.; Liu, D.; Roy, A.; Case, S.; Lesko, J.; McGrath, J. E. *Polymer (Guildf)*. **2006**, *47*, 4210–4217.
- (33) Fujimoto, C. H.; Hickner, M. A.; Cornelius, C. J.; Loy, D. A. *Macromolecules* **2005**, *38*, 5010–5016.
- (34) Wei, H.; Fang, X. *Polymer (Guildf)*. **2011**, *52*, 2735–2739.
- (35) Aoki, M.; Asano, N.; Miyatake, K.; Uchida, H.; Watanabe, M. *J. Electrochem. Soc.* **2006**, *153*, A1154.
- (36) Hickner, M. A.; Pivovar, B. S. *Fuel Cells* **2005**, *5*, 213–229.
- (37) Wang, F.; Hickner, M.; Kim, Y. S.; Zawodzinski, T. a.; McGrath, J. E. *J. Memb. Sci.* **2002**, *197*, 231–242.
- (38) Lee, H.-S.; Roy, A.; Lane, O.; Dunn, S.; McGrath, J. E. *Polymer (Guildf)*. **2008**, *49*, 715–723.
- (39) Roy, A.; Lee, H.-S.; McGrath, J. E. *Polymer (Guildf)*. **2008**, *49*, 5037–5044.

- (40) Xing, P.; Robertson, G. P.; Guiver, M. D.; Mikhailenko, S. D.; Kaliaguine, S. *Macromolecules* **2004**, *37*, 7960–7967.
- (41) Kerres, J.; Tang, C.-M.; Graf, C. *Ind. Eng. Chem. Res.* **2004**, *43*, 4571–4579.
- (42) Peckham, T. J.; Holdcroft, S. *Adv. Mater.* **2010**, *22*, 4667–4690.
- (43) Isaacs Sodeye, A. I.; Huang, T.; Gido, S. P.; Mays, J. W. *Polymer (Guildf)*. **2011**, *52*, 1963–1970.
- (44) Rubatat, L.; Shi, Z.; Diat, O.; Holdcroft, S.; Frisken, B. J. *Macromolecules* **2006**, *39*, 720–730.
- (45) Ding, J.; Chuy, C.; Holdcroft, S. *Chem. Mater.* **2001**, *13*, 2231–2233.
- (46) Shi, Z.; Holdcroft, S. *Macromolecules* **2005**, *38*, 4193–4201.
- (47) Hwang, G.; Ohya, H. *J. Memb. Sci.* **1998**, *140*, 195–203.
- (48) Tanaka, M.; Fukasawa, K.; Nishino, E.; Yamaguchi, S.; Yamada, K.; Tanaka, H.; Bae, B.; Miyatake, K.; Watanabe, M. *J. Am. Chem. Soc.* **2011**, *133*, 10646–54.
- (49) Li, N.; Zhang, Q.; Wang, C.; Lee, Y. M.; Guiver, M. D. *Macromolecules* **2012**, *45*, 2411–2419.
- (50) Yan, J.; Hickner, M. A. *Macromolecules* **2010**, *43*, 2349–2356.
- (51) Xu, T.; Liu, Z.; Li, Y.; Yang, W. *J. Memb. Sci.* **2008**, *320*, 232–239.
- (52) Li, N.; Yan, T.; Li, Z.; Thurn-Albrecht, T.; Binder, W. H. *Energy Environ. Sci.* **2012**, *5*, 7888.
- (53) Li, N.; Leng, Y.; Hickner, M. A.; Wang, C.-Y. *J. Am. Chem. Soc.* **2013**, *135*, 10124–10133.
- (54) Xiong, Y.; Liu, Q. L.; Zeng, Q. H. *J. Power Sources* **2009**, *193*, 541–546.
- (55) Salerno, H. L. S.; Elabd, Y. A. *J. Appl. Polym. Sci.* **2013**, *127*, 298–307.
- (56) Vinodh, R.; Ilakkiya, A.; Elamathi, S.; Sangeetha, D. *Mater. Sci. Eng. B* **2010**, *167*, 43–50.
- (57) Klein, R. J.; Welna, D. T.; Weikel, A. L.; Allcock, H. R.; Runt, J. **2007**, 3990–3995.
- (58) Schuster, M. F. H.; Meyer, W. H.; Schuster, M.; Kreuer, K. D. *Chem. Mater.* **2004**, *16*, 329–337.

- (59) Hickner, M. A. *J. Polym. Sci. Part B Polym. Phys.* **2012**, *50*, 9–20.
- (60) Kreuer, K.-D. *Chem. Mater.* **1996**, *8*, 610–641.
- (61) Tuckerman, M. E.; Marx, D.; Parrinello, M. *Nature* **2002**, *417*, 925–929.
- (62) Marx, D.; Chandra, A.; Tuckerman, M. E. *Chem. Rev.* **2010**, *110*, 2174–216.
- (63) Zawodzinski, T. A.; Neeman, M.; Sillerud, L. O.; Gottesfeld, S. *J. Phys. Chem.* **1991**, *95*, 6040–6044.
- (64) Paddison, S. J.; Paul, R. *Phys. Chem. Chem. Phys.* **2002**, *4*, 1158–1163.
- (65) Kreuer, K.-D.; Paddison, S. J.; Spohr, E.; Schuster, M. *Chem. Rev.* **2004**, *104*, 4637–4678.
- (66) Gottesfeld, S.; Zawodzinski, T. A. In *Advances in Electrochemical Science and Engineering*; 1997; pp. 195–307.
- (67) Grew, K. N.; Chu, D.; Chiu, W. K. S. *J. Electrochem. Soc.* **2010**, *157*, B1024.
- (68) Zhang, B.; Gu, S.; Wang, J.; Liu, Y.; Herring, A. M.; Yan, Y. *RSC Adv.* **2012**, *2*, 12683.
- (69) Gu, S.; Cai, R.; Yan, Y. *Chem. Commun.* **2011**, *47*, 2856–2858.
- (70) Voet, D.; Voet, J. G. *Biochemistry*; Fourth.; John Wiley & Sons, 2011; p. 45.
- (71) Hibbs, M. R.; Hickner, M. A.; Alam, T. M.; McIntyre, S. K.; Fujimoto, C. H.; Cornelius, C. J. *Chem. Mater.* **2008**, *20*, 2566–2573.
- (72) Walls, H. J.; Fedkiw, P. S.; Zawodzinski, T. A.; Khan, S. A. *J. Electrochem. Soc.* **2003**, *150*, E165–E174.
- (73) Disabb-Miller, M. L.; Johnson, Z. D.; Hickner, M. A. *Macromolecules* **2013**, *46*, 949–956.
- (74) Bates, F. S.; Fredrickson, G. H. *Phys. Today* **1999**, *52*, 32–38.
- (75) Matsen, M. W.; Schick, M. *Phys. Rev. Lett.* **1994**, *72*, 2660–2663.
- (76) Lu, X.; Weiss, R. A. *Macromolecules* **1996**, *29*, 1216–1221.
- (77) Knychala, P.; Banaszak, M.; Park, M. J.; Balsara, N. P. *Macromolecules* **2009**, *42*, 8925–8932.
- (78) Elabd, Y. A.; Hickner, M. A. *Macromolecules* **2011**, *44*, 1–11.
- (79) Elabd, Y. A.; Napadensky, E.; Walker, C. W.; Winey, K. I. *Macromolecules* **2006**, *39*, 399–407.

- (80) Hwang, G.-J.; Ohya, H. *J. Memb. Sci.* **1998**, *149*, 163–169.
- (81) Saito, T.; Moore, H. D.; Hickner, M. A. *Macromolecules* **2010**, *43*, 599–601.
- (82) Isaacs Sodeye, A. I.; Huang, T.; Gido, S. P.; Mays, J. W. *Polymer (Guildf)*. **2011**, *52*, 5393–5396.
- (83) Tsang, E. M. W.; Zhang, Z.; Shi, Z.; Soboleva, T.; Holdcroft, S. *J. Am. Chem. Soc.* **2007**, *129*, 15106–7.
- (84) Park, M. J.; Downing, K. H.; Jackson, A.; Gomez, E. D.; Minor, A. M.; Cookson, D.; Weber, A. Z.; Balsara, N. P. *Nano Lett.* **2007**, *7*, 3547–52.
- (85) Kim, B.; Kim, J.; Jung, B. *J. Memb. Sci.* **2005**, *250*, 175–182.
- (86) Moore, H. D.; Saito, T.; Hickner, M. A. *J. Mater. Chem.* **2010**, *20*, 6316.
- (87) Heinzer, M. J.; Han, S.; Pople, J. A.; Baird, D. G.; Martin, S. M. *Macromolecules* **2012**, *45*, 3471–3479.
- (88) Dorin, R. M.; Marques, D. S.; Sai, H.; Vainio, U.; Phillip, W. A.; Peinemann, K.; Nunes, S. P.; Wiesner, U. *ACS Macro Lett.* **2012**, *1*, 614–617.
- (89) Matsen, M. W. *J. Chem. Phys.* **1995**, *102*, 3884–3887.
- (90) Matsen, M. W.; Thompson, R. B. *J. Chem. Phys.* **1999**, *111*, 7139–7146.
- (91) Gu, S.; Cai, R.; Luo, T.; Chen, Z.; Sun, M.; Liu, Y.; He, G.; Yan, Y. *Angew. Chemie (International Ed.)* **2009**, *48*, 6499–6502.
- (92) Gu, S.; Cai, R.; Luo, T.; Jensen, K.; Contreras, C.; Yan, Y. *ChemSusChem* **2010**, *3*, 555–558.
- (93) Chen, D.; Hickner, M. A. *ACS Appl. Mater. Interfaces* **2012**, *4*, 5775–5781.
- (94) Noonan, K. J. T.; Hugar, K. M.; Kostalik, H. A.; Lobkovsky, E. B.; Abruña, H. D.; Coates, G. W. *J. Am. Chem. Soc.* **2012**, *134*, 18161–18164.
- (95) Zha, Y.; Disabb-Miller, M. L.; Johnson, Z. D.; Hickner, M. A.; Tew, G. N. *J. Am. Chem. Soc.* **2012**, *134*, 4493–4496.

Chapter 2

Experimental Methods

2.1. Introduction

This chapter will introduce the polymers and membranes used for the research in this dissertation and will briefly describe the characterization techniques and experimental methods. Diblock and triblock poly(hexyl methacrylate)-poly(styrene)-based polymers were synthesized and functionalized for PEMs and AEMs. Additional materials include poly(vinyl benzyl chloride)-poly(styrene) block copolymers for AEMs, bis(terpyridine) ruthenium-based AEMs, and superacid PEMs. Characterization methods of the synthesized and functionalized block copolymers will be presented, as well as the techniques used to study the structure and properties of the membranes.

2.2. Synthesis and Functionalization of Poly(hexyl methacrylate)-Poly(styrene)-Based Block Copolymers

This section will discuss the general experimental procedure for the synthesis and functionalization of poly(hexyl methacrylate)-poly(styrene)-based block copolymers. Several batches of poly(hexyl methacrylate)-*b*-poly(styrene)-*b*-poly(styrene), PHMA-*b*-PS-*b*-PHMA, triblock copolymers were synthesized for use as PEMs and AEMs. Using a similar method, a poly(hexyl methacrylate)-*b*-poly(styrene), PHMA-*b*-PS, diblock copolymer was synthesized and

functionalized for use as PEMs. Membranes derived from these polymers form the basis of several in-depth studies.

2.2.1 Atom Transfer Radical Polymerization

Diblock and triblock poly(hexyl methacrylate)-poly(styrene)-based block copolymers were synthesized via atom radical transfer polymerization (ATRP). ATRP relies on a transition metal to act as a catalyst and carrier of a halogen atom in a redox process. The transition metal abstracts a halogen atom, producing the oxidized metal halide and a radical. The radical reacts with the monomer, producing an intermediate radical. The radical and intermediate radical combine, and the reduced transition metal is regenerated for a new cycle.¹ A general ATRP reaction depicting activation, deactivation and propagation rates are depicted in Figure 2.1.

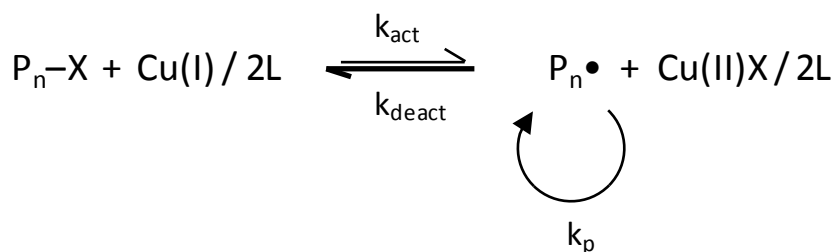


Figure 2.1. Generalized ATRP reaction showing the rates of activation (k_{act}), deactivation (k_{deact}), and propagation (k_p). P_n and $P_n\bullet$ are the propagating species and radical.¹²

For the poly(hexyl methacrylate)-poly(styrene) block copolymer systems described in this work, the poly(styrene) block was grown first and became a macroinitiator for the growth of the poly(hexyl methacrylate). Each monomer was purified through a column of activated alumina

before use. The ligand and catalyst were combined, using a mortar and pestle when applicable, and added to a round-bottom flask. The initiator and monomer were added to the flask, and the vessel was purged with argon. Subsequently, five freeze-pump-thaw cycles were applied to the reaction mixture to remove oxygen from the vessel. The reaction was placed in a heated oil bath to start the reaction. After the appropriate reaction time, the heat to the oil bath was turned off, and the vessel was allowed to cool overnight while stirring. The reaction contents were diluted with tetrahydrofuran (THF) and passed through a filter and an activated alumina column. The polymer was precipitated into methanol (MeOH), washed, dissolved in THF, and precipitated a second time into MeOH. The polymer was filtered, washed with MeOH, and dried in a vacuum oven at 60 °C for two days before characterization. Additional specific reaction conditions will be discussed in the individual chapters pertaining to the block copolymers.

2.2.2 Functionalization for PEMs

The PS block of the PHMA-PS-based diblock and triblock copolymers was postfunctionalized via sulfonation for use as PEMs, shown in Figure 2.2. To produce 25 mL of 1M acetyl sulfate reagent, 1.3 mL of sulfuric acid and 3 mL of acetic anhydride were combined in 20.7 mL of 1,2-dichloroethane, DCE, at 0 °C. The acetyl sulfate reagent was allowed to warm to room temperature and added to a 10% w/w solution of PHMA-PS-based block copolymer in 1,2-dichloroethane, which adequately dissolved the polymer, since the solubility parameters (δ) of the polymers and solvent are close to each other. From literature,²⁻⁴ $\delta_{\text{DCE}} = 19 \text{ (J}\cdot\text{cm}^{-3})^{1/2}$, $\delta_{\text{PS}} = 18.6 \text{ (J}\cdot\text{cm}^{-3})^{1/2}$, and $\delta_{\text{PHMA}} = 17.6 \text{ (J}\cdot\text{cm}^{-3})^{1/2}$.

The degree of functionalization (DF) varied based on the molar equivalents of acetyl sulfate used with respect to the PS block of the polymer used in the reaction and on the reaction

time. The reactions were conducted at 50 °C, under argon. Any addition specific information about the reaction conditions will be discussed in the individual chapters pertaining to the block copolymers.

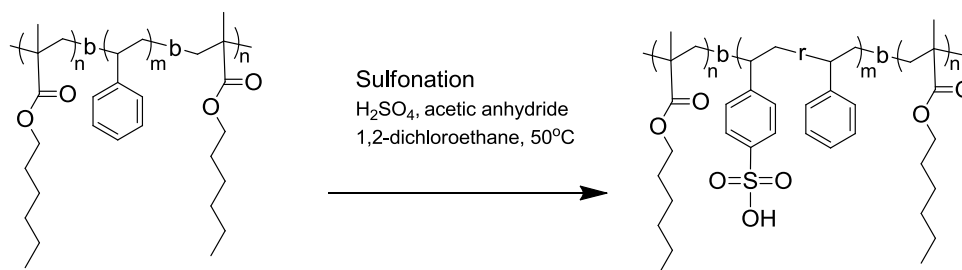


Figure 2.2. Sulfonation scheme of the PHMA-*b*-PS-*b*-PHMA triblock copolymer, depicting functionalization for PEMs.

2.2.3 Functionalization for AEMs

To produce AEMs, the PS block of the PHMA-*b*-PS-*b*-PHMA triblock copolymer was functionalized in two steps, shown in Figure 2.3. The first step was chloromethylation with paraformaldehyde, chlorotrimethylsilane, and a Lewis acid catalyst, SnCl₄, in chloroform.⁵ With respect to PS, different DFs were achieved by varying the reaction time. To convert the chloromethyl groups for quaternary ammonium, the polymer was reacted with three times molar excess of 45 wt % aqueous trimethylamine at room temperature.

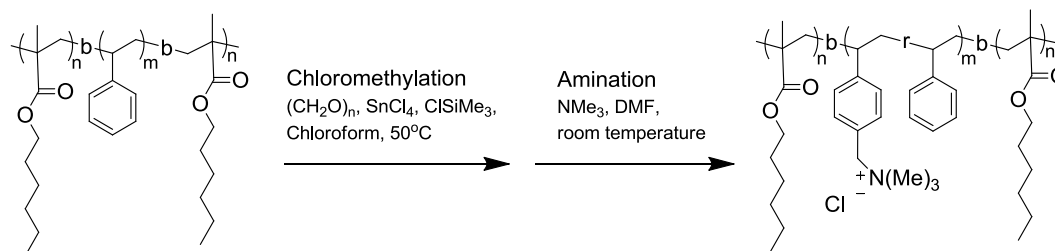


Figure 2.3. Two-step scheme to produce QA-functionalized PHMA-*b*-PS-*b*-PHMA for AEMs. A chloromethylation step⁵ was followed by conversion to QA groups via trimethylamine.

2.2.4 Membrane Fabrication

Films of functionalized PHMA-PS block copolymer were cast from approximately 10% w/w N,N-dimethylformamide (DMF) solutions in poly(tetrafluoroethylene) molds. The molds were covered with a glass plate to allow the polymer solution to evaporate at ambient conditions over a period of two-three 2-3 weeks. The films were subsequently dried *in vacuo* for 24 hours at 40 °C for the AEMs and at 50 °C for the PEMs. The dried films were approximately 150-225 μm thick, as measured by a Mitutoyo IP65 293-344 micrometer.

2.3. Additional Materials

In addition to the PHMA-PS block copolymers discussed in Section 2.2, several other materials for AEMs and PEMs were provided for study. These included random and block poly(vinyl benzyl chloride)-poly(styrene), PVBC-PS, copolymers for AEMs; bis(terpyridine)

ruthenium-based AEMs; and superacid PEMs. The materials were either used as received or modified as described in the following sections.

2.3.1 Poly(vinyl benzyl chloride)-Poly(styrene)-Based Block Copolymers

Random and block poly(vinyl benzyl chloride)-poly(styrene), PVBC-PS, copolymers were synthesized and functionalized for use as AEMs by Kyle Bryson and Professor Michael Hickner at the Pennsylvania State University.⁶ PS-*b*-PVBC block copolymers were synthesized using reversible addition-fragmentation chain-transfer (RAFT) polymerization, with cumyl dithiobenzoate (CDTB) as the chain transfer agent. The PS-PVBC random copolymers were synthesized by mixing styrene and vinyl benzyl chloride monomers in controlled feed ratios with CDTB. 2,2'-Azobis(2-methylpropionitrile), AIBN, was used as the initiator in both systems. The polymers were dissolved in THF, and trimethylamine was added to convert the benzyl chloride moieties to benzyltrimethylammonium.

The QA PVC-PS polymers were too brittle to form free-standing films. Instead, films were dropcast from solutions onto substrates, with the mixed solvent system of n-propanol and toluene. For morphology characterization, the films were dropcast onto Kapton[®] substrates, and pieces of these films were then used for water uptake measurements. To measure conductivity, the polymers were dropcast onto electrodes fabricated by Brian Chaloux of the Pennsylvania State University and of the US Naval Research Laboratory with the assistance of Holly Ricks-Laskowski of the US Naval Research Laboratory. All dropcast films were allowed to dry overnight in ambient conditions.

2.3.2 Bis(terpyridine) Ruthenium-Based AEMs

Bis(terpyridine) ruthenium-based AEMs were synthesized by Yongping Zha, Madhura Pawar, and Professor Greg Tew, of the University of Massachusetts Amherst.⁷ The membranes were synthesized using ring opening metathesis polymerization, ROMP,⁸ and were provided in chloride form. To exchange or verify the counterion associated with the ruthenium (II) complex, membranes were soaked in 1M NaCl, NaHCO₃, or KOH overnight. To rid the membranes of any excess ions, the membranes were then rinsed and soaked in deionized water for at least three hours three separate times.

2.3.3 Superacid PEMs

Random poly(sulfone) and poly(styrene) copolymers with aryl sulfonate, alkyl sulfonate, and perfluorosulfonate groups for use as PEMs were synthesized by Ying Chang and Professor Chulsung Bae of the Rensselaer Polytechnic Institute.^{9,10} The membranes were used as received, with no modification. In addition to the received membranes, two sets of PHMA-*b*-PS-*b*-PHMA triblock copolymers synthesized as described in Section 2.2.1 were sent to Chang and Bae for post-functionalization of the PS block to produce block copolymer superacid PEMs.

2.4. Polymer Characterization

This section will discuss the methods by which the synthesized and functionalized polymers were characterized. Size exclusion chromatography was used to determine the molecular weight of each polymer, along with nuclear magnetic resonance spectroscopy, NMR.

NMR was also used to ascertain the degree of functionalization of the polymers. Finally, differential scanning calorimetry was used to measure the glass transition temperatures of one polymer system.

2.4.1 Size Exclusion Chromatography

To determine the number average molecular weight, M_n , and polydispersity index, PDI, of the PHMA-PS block copolymers, size exclusion chromatography, SEC, was performed on the samples using a Waters gel permeation chromatogram, GPC, which included Waters Breeze software for analysis, a 1515 isocratic HPLC pump, styrogel, and a 2414 RI detector. The unfunctionalized PS macroinitiator and PHMA-PS block copolymers were dissolved in THF for this characterization. The instrument was calibrated with a narrow set of PS standards in THF, which allowed for accurate analysis of the PS macroinitiator. SEC of the PHMA-PS block copolymers did not provide accurate molecular weights, but the PDI could be reported. The M_n of the block copolymers was calculated using nuclear magnetic resonance spectroscopy, discussed in the next section.

2.4.2 Nuclear Magnetic Resonance Spectroscopy

^1H nuclear magnetic resonance, NMR, spectroscopy with a Bruker DRX-400 MHz spectrometer was used to determine the degree of functionalization of the PHMA-PS based block copolymers. The polymers were dried *in vacuo* overnight at room temperature and subsequently dissolved in *d*-chloroform, *d*₆-dimethylsulfoxide, or *d*₇-N,N-dimethylformamide for NMR characterization.

This technique was also used to calculate the M_n of the PHMA-PS based block copolymers. End group analysis of the ^1H NMR spectra of the PS macroinitiator was compared to the M_n determined from SEC, and a scaling factor was calculated to account for non-uniformity with the end groups. Once the PHMA-PS based block copolymer was synthesized, the previous scaling factor and M_n of the PS macroinitiator served as a reference by which to calculate the number of PHMA repeat units, and thus the M_n of the PHMA block(s).

2.4.3 Differential Scanning Calorimetry

Glass transition temperatures, T_g , of the PHMA-*b*-PS-*b*-PHMA triblock copolymers were determined using a TA instruments differential scanning calorimeter, DSC, Q200. Membranes were dried *in vacuo* at 30-50 °C overnight twice and kept in a desiccator to remove water and solvent and maintain the dry state of the membranes. The dry samples were heated under nitrogen at rate of 10 °C·min⁻¹ from -80 °C to 210 °C for the sulfonated polymers and from -80 °C to 210 °C for the quaternary ammonium polymers. T_g values were reported as the transition midpoint during the second or third heating cycle. Residual effects of trapped water or solvent were not observed.

2.5. Membrane Characterization

This section will discuss the methods by which membrane performance was evaluated; techniques to measure conductivity and water uptake and determine membrane morphology will be enumerated.

2.5.1 Conductivity Measurements

Conductivity was measured using AC impedance spectroscopy with a Solartron 1260A Impedance/Gain-Phase Analyzer. The conductivity of free-standing films was obtained using a two-point, in-plane geometry (see Figure 2.4) at frequencies between 1 MHz and 100 Hz¹¹ and calculated from equation 1.3. The conductivity of membranes was measured in one of two environments: controlled relative humidity, RH, and temperature or fully hydrated with controlled temperature. For RH conductivity experiments, the humidity and temperature were controlled using an Espec SH-241 environmental chamber. The temperature was held at 30 °C, and the humidity steps typically used were 20%, 35%, 50%, 75%, and 95%. The real value of the impedance, where the imaginary response was zero, was used as the membrane resistance. Activation energies for ion conduction of samples immersed in liquid water were determined using an Arrhenius activation relationship (equation 2.1) from conductivity measurements at 30 °C, 40 °C, 50 °C, 60 °C, and 70 °C. The logarithm of conductivity versus 1/T was linearly regressed and Arrhenius activation energy was computed from the slope of the best-fit regression.

$$\sigma = \sigma_0 \exp\left(-\frac{E_a}{RT}\right) \quad (2.1)$$

where σ is the measured conductivity, σ_0 is the conductivity prefactor, E_a is the activation energy, R is the ideal gas constant, and T is the temperature in Kelvin. Error in conductivity measurements is believed to be on the order of $1\text{mS}\cdot\text{cm}^{-1}$.

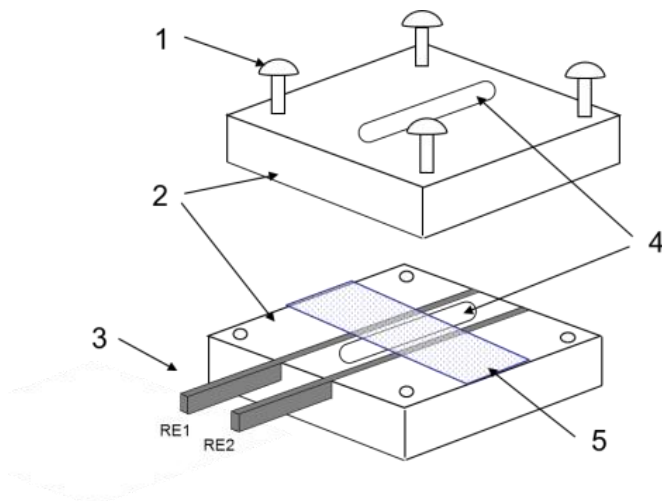


Figure 2.4. Schematic of the cell used for conductivity measurements of free-standing membranes,¹¹ with (1) securing screws, (2) Teflon[®] blocks, (3), stainless steel electrodes, (4) equilibration windows, and (5) the membrane.

2.5.2 Water Uptake Measurements

Water uptake measurements were performed using either relative humidity thermogravimetric analysis, RH-TGA, or immersing the membrane in deionized water to fully hydrate it. Both methods required the use of equations 1.1 and 1.3 for determination of the water uptake and hydration number from the raw data. Membranes were measured in the appropriate counterion forms (proton form for PEMs, and chloride and bicarbonate forms for AEMs). Water uptake in an RH environment was measured using a TA Instruments Q5000SA water vapor sorption microbalance at 30 °C with typical RH steps of 20%, 35%, 50%, 75%, and 95%. For hydrated water measurements, the membranes were fully immersed in deionized water to equilibrate for at least 24 hours before use. Before weighing to determine the hydrated mass, each

membrane was removed from water and lightly blotted with a Kimwipe[®] to remove surface water. The sample was immersed in deionized water to rehydrate it, and the process was repeated for a total of five times. To obtain the dry weight of the membrane, the membrane was dried *in vacuo* at 80 °C for two days and then weighed again.

2.5.3 Small and Intermediate Angle X-ray Scattering

Small angle xray scattering, SAXS, and intermediate angle x-ray scattering (IAXS) patterns were obtained on a Rigaku (formerly Molecular Metrology) instrument with a pinhole camera with Osmic microfocus source and parallel beam optic. The instrument had a Cu target with a 1.452 Å wavelength and also a multiwire detector. Samples were dried *in vacuo* at ambient conditions before being placed in the SAXS chamber. Spectra of the dried films were collected under vacuum at ambient temperature, and typical collection times ranged from 20-60 minutes to achieve a minimum of 300,000 photon counts. Scattering intensities were normalized for background scattering and beam transmission. Interdomain spacings were calculated from equation 2.2 below:

$$d = \frac{2\pi}{q} \quad (2.2)$$

where d is the interdomain spacing and q is the scattering vector in inverse Angstroms. D-spacing values are reported in nm.

2.5.4 Small Angle Neutron Scattering

SANS experiments were performed at the National Institute of Standards and Technology (NIST) Center for Neutron Research (NCNR) on the NG7 30 m SANS and at Oak Ridge National Laboratory on the Spallation Neutron Source on beam line 6, the EQ-SANS diffractometer, or on the High Flux Isotope Reactor on beam line CG2, the general purpose SANS diffractometer. Local contacts were Boualem Hammouda (NIST NCNR), Chris Stanley (ORNL), and Lilin He (ORNL). Lilin He (ORNL) also performed some SANS measurements in collaboration with this work, but all three staff members helped with SANS data reduction and analysis.

For SANS studies, low wt % solutions of the triblock copolymers were made in d_7 -N,N-dimethylformamide. A few drops of d_4 -methanol and d_8 -tetrahydrofuran were added as needed to aid solubility. Dropcast films on aluminum and free-standing membranes were put in the SANS chamber dry or equilibrated in D₂O or under a specific relative humidity for at least 8 h before undergoing neutron scattering experiments. Scattering intensities were normalized for background scattering and beam transmission. Data was fit to models using the NCNR software toolbox add-on in Igor Pro. Interdomain spacings were calculated from equation 2.2.

2.5.5 Transmission Electron Microscopy

Transmission electron microscopy, TEM, images of membrane cross-sections were acquired on a JEOL JEM 1200 EXII microscope equipped with a tungsten emitter operating at 80 kV and a CCD camera with TCL software. Cast membrane samples were cross-sectioned by Missy Hazen of the Huck Institutes of the Life Sciences at the Pennsylvania State University. Membranes were cross-sectioned at -120 °C using a Leica Ultracut UC6 ultramicrotome with

EMFC6 cryo attachment, and the sections were collected on carbon/Formvar-coated grids. All images were of unstained samples.

2.6. References

- (1) Wang, J.-S.; Matyjaszewski, K. *Macromolecules* **1995**, *28*, 7901–7910.
- (2) Lu, X.; Weiss, R. A. *Macromolecules* **1996**, *29*, 1216–1221.
- (3) Hughes, L. J.; Britt, G. E. *J. Appl. Polym. Sci.* **1961**, *5*, 337–348.
- (4) Xu, H.; Song, J.; Tian, T.; Feng, R. *Soft Matter* **2012**, *8*, 3478.
- (5) Avram, E.; Luca, C.; Petrovan, S.; Milhailescu, C. *Polym. Plast. Technol. Eng.* **1996**, *35*, 757–768.
- (6) Bryson, K. C.; Hickner, M. A. Synthesis of novel ion-conducting polymers via reversible addition-fragmentation chain transfer polymerization, Pennsylvania State University, 2010.
- (7) Zha, Y.; Disabb-Miller, M. L.; Johnson, Z. D.; Hickner, M. A.; Tew, G. N. *J. Am. Chem. Soc.* **2012**, *134*, 4493–4496.
- (8) Clark, T. J.; Robertson, N. J.; Kostalik, H. A.; Lobkovsky, E. B.; Mutolo, P. F.; Abruña, H. D.; Coates, G. W. *J. Am. Chem. Soc.* **2009**, *131*, 12888–12889.
- (9) Chang, Y.; Brunello, G. F.; Fuller, J.; Hawley, M.; Kim, Y. S.; Disabb-Miller, M.; Hickner, M. A.; Jang, S. S.; Bae, C. *Macromolecules* **2011**, *44*, 8458–8469.
- (10) Chang, Y.; Brunello, G. F.; Fuller, J.; Disabb-Miller, M. L.; Hawley, M. E.; Kim, Y. S.; Hickner, M. A.; Jang, S. S.; Bae, C. *Polym. Chem.* **2013**, *4*, 272–281.
- (11) Fujimoto, C. H.; Hickner, M. A.; Cornelius, C. J.; Loy, D. A. *Macromolecules* **2005**, *38*, 5010–5016.
- (12) Matyjaszewski, K.; Patten, T. E.; Xia, J. *J. Am. Chem. Soc.* **1997**, *119*, 674–680.

Chapter 3

Ion Motion in Anion and Proton-Conducting Triblock Copolymers

3.1. Introduction

Ion-containing block copolymers are of interest for fuel cell membranes and other electrochemical or water transport applications due to their high degree of phase separation that promotes formation of a connected ionic nanophase and a hydrophobic mechanically reinforcing phase. The size and connectivity of the highly functionalized ionic phase can be controlled to achieve a range of properties by tuning the block copolymer composition and membrane processing.^{1,2} The ability to control the ionic domain structure of fuel cell membranes is a critical aspect of optimizing their properties and boosting their performance. Sulfonated block copolymers have served as model systems to assess the effects of molecular structure and morphological order on proton exchange membrane (PEM) performance, and work in this area may lead to the discovery of novel membranes with better properties than the current state-of-the-art poly(perfluorosulfonic acid)-based materials.³ Currently, sulfonated block copolymers have shown higher proton conductivity than their sulfonated random copolymer counterparts.^{4–8} Now that anion exchange membrane fuel cells (AEMFCs) are becoming viable alternatives to PEM fuel cells (PEMFCs),^{9,10} it is crucial to understand whether block copolymer motifs are able to significantly improve anion exchange membrane (AEM) properties and fundamental investigations are needed to reveal the similarities and differences between AEMs and their more well-studied PEM counterparts.

This chapter is adapted from Disabb-Miller, M. L.; Johnson, Z. D.; Hickner, M. A. *Macromolecules* **2013**, *46*, 949–956.

Typical polymers used in ion-containing block copolymer morphological studies include those with fluorinated or aromatic backbones with sulfonic acid pendant groups.¹ Rubatat and co-workers discovered a sub-phase of ionic aggregates within the lamellar phase of a 17.9-24.3-*b*-8.1-1.9 kg·mol⁻¹ poly([vinylidene difluoride-*co*-hexafluoropropylene]-*b*-styrene) block copolymer.⁶ The proton conductivity of this block copolymer increased with the ion exchange capacity (IEC) if the hydration number was less than 40-50. Above this value of hydration number, however, additional water led to proton dilution, and the conductivity did not show any significant change with additional hydration.⁷ Elabd and co-workers observed enhanced transport in 7.5-*b*-33.8-*b*-7.5 kg·mol⁻¹ poly(styrene-*b*-isobutylene-*b*-styrene) with increased ion content, particularly in comparison to randomly-sulfonated poly(styrene). Small angle x-ray scattering (SAXS) patterns showed anisotropic, lamellar morphologies and at IEC values greater than one, this ordering was disrupted. Yet the high sulfonation of this material still led to enhanced proton conductivity even in membranes lacking long-range order.¹¹

The bulk morphologies of 31.2 kg·mol⁻¹ fluorinated poly(isoprene-*b*-styrene) and fluorinated poly(isoprene-*b*-styrene sulfonate) were investigated by Goswami, et al. and found to vary depending on the volume fraction of the sulfonated block and the casting solvent. Monte Carlo simulations of the sulfonated block copolymer suggest that electrostatic interactions of the charged moieties were responsible for the atypical morphologies.¹² Similarly, the morphology of sulfonated poly(styrene-*b*-methylbutylene) has been extensively studied by Balsara and co-workers for copolymers with number-average molecular weights (M_n) up to 22.3-*b*-21.3 kg·mol⁻¹. For the molecular weights studied and volume fractions of polystyrene between 0.45 and 0.5, non-ionic (conventional) block copolymers are predicted to show lamellar morphology according to Flory-Huggins and self-consistent mean field theories. Yet, Balsara and co-workers observed gyroid, hexagonal, hexagonally-perforated lamellar, and lamellar microstructures for poly(sulfonated styrene-*b*-methylbutylene), PSS-*b*-PMB, that were thermally

reversible and depended on IEC and molecular weight.¹³ They have determined that prediction of the phase behavior of complex copolymer systems, such as PSS-*b*-PMB, should also consider the placement of the sulfonated groups along the chain. Simulations of alternating PSS groups lead to lamellar-like morphologies, while different sized runs of PSS groups intermixed with styrene monomer residues in the sulfonated phase lead to perforated lamellar, cylindrical, and gyroid morphologies.¹⁴ In experimental systems, it is still an open question as to the connectivity of sulfonated and unsulfonated repeat units in the sulfonated phase. Humidity-induced order-to-disorder transitions for the gyroid phase with a domain spacing of 5.2 nm were observed for a PSS-*b*-PMB copolymer with M_n 1.4-1.4 kg·mol⁻¹. This domain spacing was the smallest observed for a block copolymer to date and is likely due to stabilization of the ionic phase because of its high segregation strength.^{15,16,17}

Sulfonated block copolymers have displayed interesting morphological properties compared to conventional, non-ionic block copolymers. However, there have not been many comprehensive studies regarding the phase behavior of quaternary ammonium functionalized block copolymers. Terada, et al. showed that quaternized block copolymers possessed improved mechanical strength compared to randomly functionalized copolymers by controlling the swelling of the membrane through the non-ionic block.¹⁸ Quaternized block copolymers synthesized by Hwang and Ohya had biphasic morphology that showed increased conductivity compared to random copolymers, but the block copolymers also had higher values of IEC. The conductivities of the membranes ranged from 0.15-0.24 S·cm⁻¹, measured in a 2 M solution of KCl, so the salt likely played a major role in the conductivity of these materials.^{18,19} Finally, Miyatake demonstrated that quaternized multiblock copoly(arylene ether) polymers containing fluorene (54-90 kg·mol⁻¹) had higher conductivity than their random copolymer counterparts.²⁰

By comparing the membrane performance of PEMs and AEMs functionalized from the same polymer backbone, we seek to determine the critical factors that control membrane

performance in these types of water-absorbing, single ion conducting membranes. In particular, we aim to establish the key differences in conductivity properties between PEM and AEM block copolymers. Ionic conductivity is the product of the ion mobility, the number of charge carriers, and the charge of the ion. The sulfonated block copolymers were investigated in the H^+ form, while the quaternary ammonium containing block copolymers were probed in the Cl^- or HCO_3^- form. Compared to K^+ with a value of unity in dilute aqueous solution, the dilute solution relative mobility of H^+ is 4.76, while the mobility of Cl^- is 1.04 and HCO_3^- is 0.61.^{21,22} These differences in the intrinsic mobility of the charge-carrying ion must be taken into account to understand the conductivity in AEMs.

Evaluating the conductivity behavior of PEMs and AEMs with the same block copolymer structure will provide new insights into developing more conductive AEMs and link themes in the design of PEMs and AEMs. The goal of this work is to compare the membrane performance of sulfonated and quaternized poly(hexyl methacrylate)-*b*-poly(styrene)-*b*-poly(hexyl methacrylate), PHMA-*b*-PS-*b*-PHMA triblock copolymers to determine the commonalities between ion-conducting block copolymers with mobile cations or anions. In particular, factors contributing to PEM and AEM conductivity and the role of ion mobility are discussed.

3.2. Experimental

3.2.1 Polymer Synthesis and Membrane Preparation

Styrene (Aldrich, 99%) and hexyl methacrylate (HMA, Aldrich, 98%) were passed through an activated alumina column to remove inhibitors prior to use. Copper(I) bromide (CuBr , Fluka, > 98.0%), 2,2'-bipyridyl (bpy, Alfa Aesar, 99%), α,α' -dibromo-p-xylene (Aldrich,

97%), toluene (Mallinckrodt Chemicals, ACS), tetrahydrofuran (THF, Mallinckrodt Chemicals, ACS), methanol (MeOH, Mallinckrodt Chemicals, ACS), dimethylformamide (DMF, Mallinckrodt Chemicals, ACS), dichloroethane (EMD Chemicals, OmniSolv), acetic anhydride (Alfa Aesar, 97+%), sulfuric acid (J.T. Baker, ACS), paraformaldehyde (Alfa Aesar, 97%), chlorotrimethyl silane (Alfa Aesar, 98+%), tin(IV) chloride (SnCl_4 , Acros, 99%, anhydrous), trimethylamine (Alfa Aesar, 45 wt % aqueous), and potassium bicarbonate (Alfa Aesar, 99%) were used as received.

The triblock copolymers were synthesized using atom transfer radical polymerization (ATRP) with the difunctional initiator, α,α' -dibromo-*p*-xylene, as described by Saito, et al.²³ Briefly, a difunctional poly(styrene) macroinitiator was synthesized in the bulk (72.7 g styrene) in a Schlenk flask in the presence of 0.19 g of copper(I) bromide (CuBr), 0.91 g of 2,2'-bipyridyl (bpy), and 0.42 g of α,α' -dibromo-*p*-xylene at 110 °C for 7 h (targeting 50% conversion). The reaction mixture underwent five freeze-pump-thaw cycles under vacuum and Ar before being placed in the oil bath to start the polymerization. After termination of the reaction, approximately 200 mL of THF was added the reaction mixture before the mixture was passed through an activated alumina column and precipitated into methanol. The polymer was filtered and washed with MeOH. The polymer was dissolved in THF before a second precipitation in MeOH. The polymer was filtered and washed again and dried in a vacuum oven at 60 °C for 2 d. This procedure resulted in 20 g of difunctional poly(styrene) ATRP macroinitiator with bromine end groups (see Appendix A for NMR), Br-PS-Br, (approximately 30% conversion). Next, 5 g of the Br-PS-Br was dissolved in 70 mL of toluene with 12 mL of hexylmethacrylate (HMA) in a Schlenk flask. After the addition of 0.05 g of CuBr and 0.11 g of bpy, the flask underwent five freeze-pump-thaw cycles under vacuum and Ar. The flask was placed in an oil bath at 105 °C to start the polymerization of HMA, which proceeded for 24 h. The same post-reaction work-up was used after termination of the reaction. This strategy facilitated synthesis of 9 g (40% conversion)

of a symmetric ABA triblock copolymer with poly(styrene) as the middle block and poly(hexyl methacrylate) as the end blocks. The poly(hexyl methacrylate)-*b*-poly(styrene)-*b*-poly(hexyl methacrylate) (PHMA-*b*-PS-*b*-PHMA) triblock copolymer had a molecular weight of 16.5-*b*-32-*b*-16.5 kg·mol⁻¹, as determined by size exclusion chromatography (SEC) and ¹H NMR spectroscopy (see Appendix A). A single 7 g batch of this triblock copolymer was used for further postmodification with sulfonate or quaternary ammonium groups.

The sulfonated samples were synthesized by post modification of the PHMA-*b*-PS-*b*-PHMA triblock copolymer using acetyl sulfate to selectively functionalize the PS midblock. Sulfuric acid (1.3 mL) and acetic anhydride (3 mL) were combined in 20.7 mL of 1,2-dichloroethane at 0 °C to produce 25 mL of 1M acetyl sulfate reagent. The acetyl sulfate was warmed to room temperature and added to a 10 wt/wt % solution of PHMA-*b*-PS-*b*-PHMA in 1,2-dichloroethane. The degree of sulfonation (DS) depended on the reaction time and the molar equivalents of acetyl sulfate (with respect to PS) present in the reaction. For high degrees of sulfonation, the reagents were added in two batches (see Appendix A for details). All reactions were conducted at 50 °C under argon. The chemical structure of the functionalized triblock copolymer is shown in Figure 3.1 Refer to the Appendix A for ¹H NMR spectrum of sulfonated triblock copolymer.

To obtain the quaternary ammonium functionalized PHMA-*b*-PS-*b*-PHMA, the PS midblock was selectively chloromethylated with paraformaldehyde and chlorotrimethylsilane in the presence of a Lewis acid catalyst, SnCl₄.²⁴ Different extents of functionalization (with respect to PS) were obtained by varying the reaction time. Other routes involving *in-situ* formation of chloromethyl methylether²⁵ led to no reaction, likely due to complexation of the zinc-based Lewis acid catalyst with the methacrylate blocks. Additional details of the chloromethylation reactions will be included in the Results and Discussion section. The chloromethylated polymer was reacted with three times molar excess of 45 wt % aqueous trimethylamine to convert the

chloromethyl groups into quaternary ammonium chloride ions. The chemical structures of the functionalized triblock copolymers are shown in Figure 3.1.

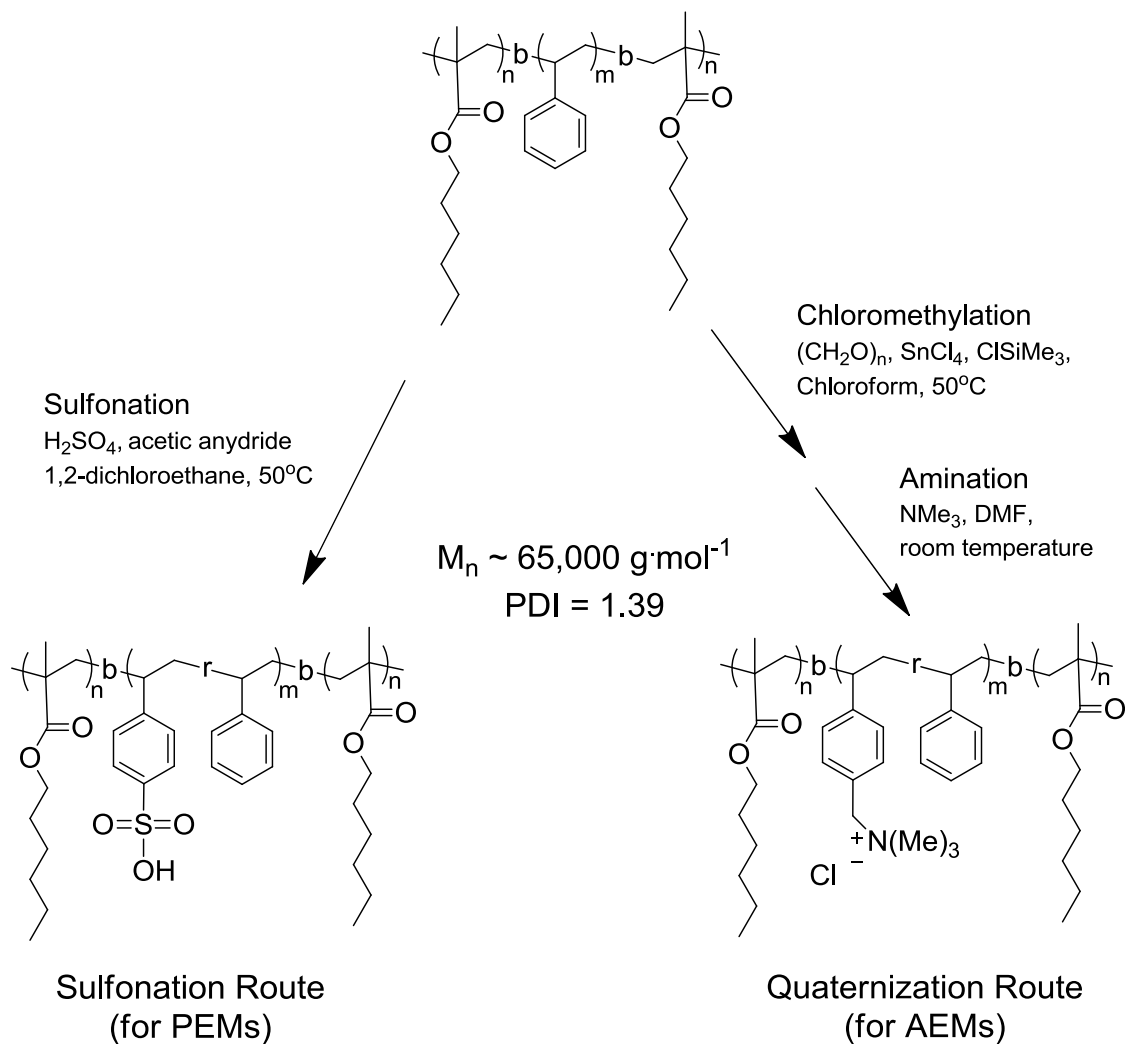


Figure 3.1. Sulfonation and quaternization routes of the PHMA-*b*-PS-*b*-PHMA triblock copolymer.

Films of the functionalized PHMA-*b*-PS-*b*-PHMA triblock copolymers were cast from approximately 10 wt/wt % N,N-dimethylformamide (DMF) solutions in a poly(tetrafluoroethylene) mold at ambient temperature with a glass cover for a period of 2-3 weeks and then dried *in vacuo* for 24 h at 40 °C for the AEMs and at 50 °C for the PEMs. The resulting film thicknesses were approximately 150-225 μm .

In addition to being examined in chloride form, the 1.2 IEC AEM sample was converted to bicarbonate form by soaking in a 0.5 M potassium bicarbonate solution for 48 h. The membrane was rinsed in deionized water for 24 h to remove excess salt and dried before characterization.

3.2.2 Characterization

^1H NMR spectra of the polymers were obtained on a Bruker DRX-400 spectrometer using *d*-chloroform, *d*₈-tetrahydrofuran, or *d*₆-dimethylsulfoxide (Cambridge Isotope) as a solvent. SEC was performed using a Waters gel permeation chromatography system (GPC), which included Waters Breeze software for analysis, a 1515 isocratic HPLC pump, styrogel columns, and a 2414 RI detector. Tetrahydrofuran was used as the eluent at 35 °C, and the GPC was calibrated to a set of narrow polydispersity index (PDI) poly(styrene) standards. Glass transition temperatures (T_g) were determined using a TA Instruments differential scanning calorimeter (DSC) Q200 at a heating rate of 10 °C min⁻¹ under nitrogen from -80 °C to 210 °C for the sulfonated polymers and from -80 °C to 150 °C for the quaternary ammonium polymers. Glass transition temperatures are reported as the transition midpoint during the second or third heating cycle.

SAXS patterns were collected on a Rigaku (formerly Molecular Metrology) instrument with a pinhole camera with Osmic microfocus source and parallel beam optic. The instrument was equipped with a Cu target ($\lambda = 1.542 \text{ \AA}$) and a multiwire area detector. Measurements of the dried films were obtained under vacuum at ambient temperature. Typical collection times ranged from 20-40 min or 300,000 photon counts. Scattering intensities for similar thickness films were normalized for background scattering and beam transmission.

For transmission electron microscopy (TEM) imaging, cast membrane samples were cross-sectioned at $-120 \text{ }^{\circ}\text{C}$ using a Leica Ultracut UC6 ultramicrotome with EMFC6 cryo attachment. The sections were collected on Carbon/Formvar-coated grids. Imaging was performed on a JEOL JEM 1200 EXII microscope equipped with a tungsten emitter operating at 80 kV. Images were recorded on a CCD camera using TCL software. All images were of unstained samples.

Conductivity measurements were performed using AC impedance spectroscopy on a Solartron 1260A Impedance/Gain-Phase Analyzer. The conductivity of free-standing films was measured using a two-point, in-plane geometry at frequencies between 1 MHz and 100 Hz.²⁶ Ion conductivity (σ) was calculated from:

$$\sigma = \frac{L}{R \cdot A} \quad (3.1)$$

where L is the length between electrodes, R is the resistance of the membrane, and A is the cross-sectional area of the membrane. Error in conductivity measurements is believed to be on the order of $1 \text{ mS} \cdot \text{cm}^{-1}$. During the measurements, humidity and temperature were controlled using an Espec SH-241 environmental chamber. The relative humidity varied from 20% to 95%, while the

temperature was held at 30 °C. The real value of the impedance, where the imaginary response is zero, was used as the membrane resistance.

Water uptake ($wu = (mass_{hydrated} - m_0)/m_0$) was measured using a TA Instruments Q5000SA water vapor sorption microbalance at 30 °C between relative humidities of 20% and 95%. The hydration number (λ), or the number of water molecules per ionic group, was calculated from:

$$\lambda = \left(\frac{m_{RH} - m_0}{m_0} \right) \times \left(\frac{1000}{M_{H_2O} \cdot IEC} \right) \quad (3.2)$$

where m_{RH} is the sample mass at a given RH, m_0 is the mass of the dry sample, M_{H_2O} is 18.02 g, the molecular mass of water, and IEC is the ion exchange capacity with units of milliequivalents of ions per gram of polymer.

The activation energy for ion conduction, E_a , was calculated from conductivity measurements with the sample immersed in liquid water between 30 and 70 °C (in 10 °C steps). The logarithm of conductivity versus $1/T$ was linearly regressed, and an Arrhenius activation energy was computed from the slope of the best fit regression.

3.3. Results and Discussion

Optimization of the chloromethylation procedure for functionalization of the PHMA-*b*-PS-*b*-PHMA triblock copolymer proved to be challenging. Chloromethylation of acrylates has resulted in low IEC polymer ($0.12 \text{ mmol} \cdot \text{g}^{-1}$) that is not useful as an ion-conductive membrane.²⁷ Vinylbenzyl chloride and alkyl bromides could not be used in place of the styrene block because benzyl halogens are an initiator for ATRP and therefore cannot be a component of

the monomer or polymer. Likewise, chloromethylation of the styrene block prior to block copolymer synthesis²⁸ would also exclude ATRP as a viable block copolymer synthesis technique. The PHMA-*b*-PS-*b*-PHMA triblock copolymer was chloromethylated via the Wright method, a common chloromethylation method which generates chloromethylmethyl ether *in situ* from dimethoxymethane, thionyl chloride and zinc(II) chloride.²⁵ The resulting polymer had a degree of functionalization (DF) of 3-4 mol % with respect to the moles of PS, yielding an IEC of approximately 0.2 meq·g⁻¹. We attribute the low degree of functionality to coordination of the ZnCl₂ catalyst with the carbonyl groups of the poly(hexyl methacrylate), and adding additional catalyst to compensate for this coordination degraded the polymer.

Instead, the Avram method was used to chloromethylate PHMA-*b*-PS-*b*-PHMA, in which a precursor chloromethylating reagent was formed in chloroform from paraformaldehyde, chlorotrimethyl silane, and SnCl₄.²⁴ To generate the precursor, paraformaldehyde and chlorotrimethylsilane were added to chloroform in a 1:1 molar ratio with 0.2 mol % SnCl₄, with respect to the moles of PS repeat unit. The precursor was stirred overnight under argon at 45 °C before it was cannulated into a 10 wt % solution of polymer in chloroform at 50 °C under argon. The overall molar ratio of polymer to reagents was 1:3:3 (PS:paraformaldehyde:chlorotrimethyl silane). The reaction proceeded at 50 °C until the desired DF was achieved. It is important to note that the maximum DF attained without polymer degradation was approximately 53 mol % of the styrene residues.

Conditions of reagent concentration and reaction time were varied in an effort to increase the DF of the triblock copolymer, but increased reagent concentration and longer reaction times led to polymer degradation. Figure 3.2 depicts the degree of functionalization as a function of reaction time under different chloromethylation conditions. During the reaction, small aliquots of the reaction mixture were removed at specific time intervals, precipitated in methanol rinsed and ^1H NMR spectra were taken. These studies were used as a basis for large-scale chloromethylation. Increasing the scale of the reaction decreased the degree of chloromethylation. The most repeatable results were achieved using fresh catalyst and dry chloroform.

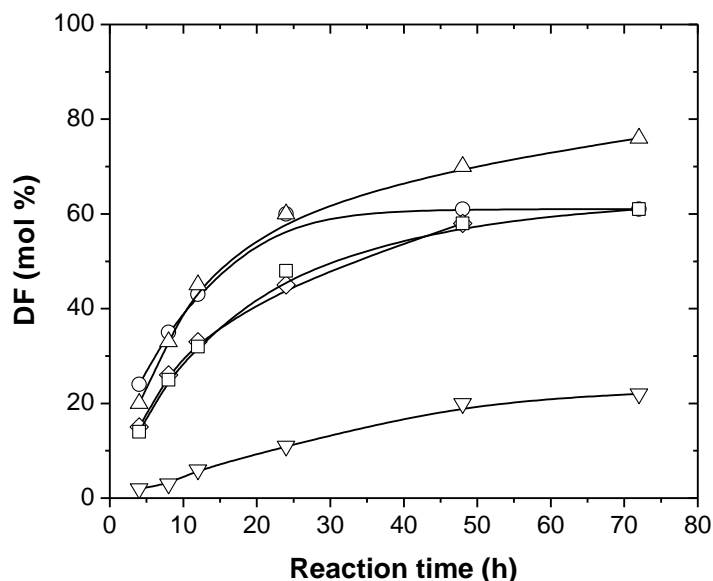


Figure 3.2. Reaction rates of chloromethylation using the method developed by Avram, et al.²⁴ The stoichiometric ratios published by Avram, et al.,²⁴ a 1:3:3 ratio of polymer sites to be functionalized:paraformaldehyde:chlorotrimethylsilane and 0.2 mol% tin (IV) chloride are represented by (□). Other stoichiometric ratios shown are 1:3:3 and 0.6 mol % catalyst (○), 1:9:9 and 0.6 mol % catalyst (△), 1:9:9 and 0.2 mol % catalyst (◇), and 1:60:3 and 0.2 mol % catalyst (▽). The maximum degree of functionalization of the poly(styrene) block attainable before degradation was approximately 53 mol %.

The sample identification of the quaternized and sulfonated polymers synthesized and their membrane properties are shown in Table 3.1. Low, mid, and high-IEC polymers were synthesized for both AEMs and PEMs. The water uptake, hydration number, and conductivity of the sulfonated polymers were higher than those of the quaternized polymers. The counter ions associated with the ionic tethers in PEMs and AEMs contribute to both the conductivity and the water uptake of the membranes. Although water uptake increases with IEC, the sulfonate- H^+ pairs associated with the PEMs have a stronger affinity for water than do the benzyltrimethylammonium- Cl^- pairs associated with the AEMs,²⁹ illustrated by the equivalent water uptake of A-2.0-Cl and the less functionalized sulfonated polymer, P-1.2-H. The 1.1 meq·g⁻¹ IEC AEM showed greater water uptake in the HCO_3^- form compared to lower water uptake in the Cl^- form underscoring the importance of the mobile species in determining the water uptake of the sample.

Table 3.1. Polymer sample parameters and properties.

Sample	DF (%)	IEC (meq·g ⁻¹)	T _g (°C)	wu [†] (%)	λ [†]	σ [†] (mS·cm ⁻¹)	E _a (kJ·mol ⁻¹)
PHMA- <i>b</i> -PS- <i>b</i> -PHMA	0	0	98	21	nm	nm	nm
A-1.1-HCO ₃	28	1.1	nm	39	12	7.1	16
A-1.2-Cl	28	1.2	111	15	7	2.0	26
A-1.7-Cl	42	1.7	113	29	9	4.6	nm
A-2.0-Cl	53	2.0	112	29	8	5.0	nm
P-1.2-H	27	1.2	118	29	14	18.3	15
P-1.6-H	38	1.6	125	46	17	20.9	15
P-2.3-H	61	2.3	175	79	19	50.7	nm

A denotes quaternary ammonium functionalized PHMA-*b*-PS-*b*-PHMA. P denotes sulfonated PHMA-*b*-PS-*b*-PHMA. The IEC is the number in the sample name, and the last letter(s) of the sample name is the counter ion.

† Value for membrane at 95% RH for water uptake (wu), hydration number (λ) and conductivity (σ).

nm denotes measurements that were not obtained.

To understand the role of water sorption on the ionic conductivity of the quaternized and sulfonated PHMA-*b*-PS-*b*-PHMA triblock copolymers, the conductivity was analyzed as a function of hydration number, Figure 3.3. The sulfonated membranes, solid symbols, exhibited the highest conductivity values due to the higher mobility of protons compared to the anionic species.

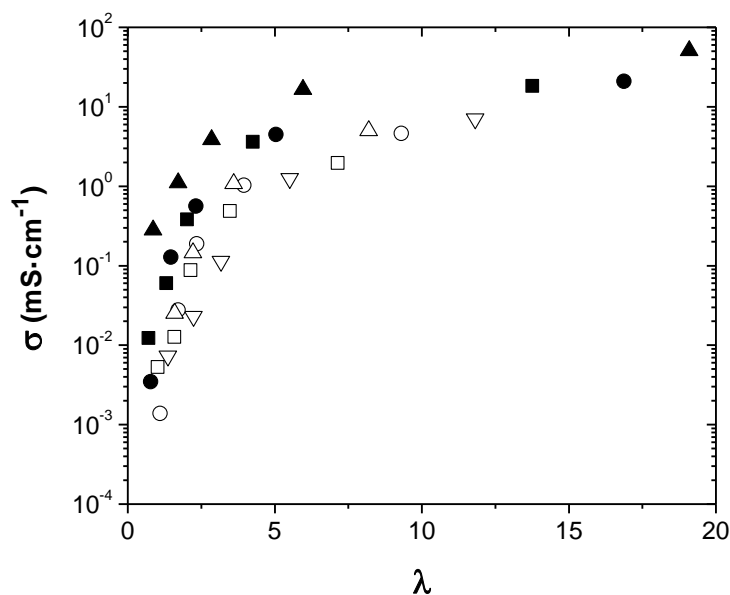


Figure 3.3. Conductivity versus hydration number of P-1.2-H (■), P-1.6-H (●), P-2.3-H (▲), A-1.1-HCO₃ (▽), A-1.2-Cl (□), A-1.7-Cl (○), and A-2.0-Cl (△).

The comparison between the conductivity of the PEMs and the AEMs in Figure 3.3 is biased due to the mobility of the conductive species. To gain insight into the mechanism of conductivity for water-absorbing PEMs and AEMs, the ion diffusion coefficients as a function of hydration were considered.

The diffusion coefficients of the mobile ions for each sample were calculated from the measured conductivity values using a form of the Nernst-Einstein equation and the number density of charge carriers given by:

$$c = 0.001 \times \frac{IEC \times \rho}{1 + 0.01 X_{v-H_2O}} \quad (3.3)$$

where c is the moles of ion per cm^3 of polymer, IEC is the milliequivalents of ion per gram of polymer, ρ is the polymer density, and X_{v-H_2O} is the volume-based water uptake, as opposed to the mass-based water uptake (wu) presented in Table 3.1.³⁰ The densities of the polymers were calculated using the NIST NCNR SLD calculator and weighted linear combinations of pure component densities.³¹

The diffusion coefficients of the mobile ions were calculated from:

$$D = \frac{\sigma RT}{cz^2 F^2} \quad (3.4)$$

where σ is the measured conductivity, R is the ideal gas constant, T is temperature, c is the computed concentration of ions in the hydrated membrane as above, z is valence charge, and F is Faraday's constant.³² Figure 3.4 shows that the PEMs displayed higher diffusion coefficients than the AEMs, which is a reflection of the types of mobile species in each sample. The AEMs had similar diffusivities, regardless of IEC, which could be due to a lack of ion clustering as has been previously observed in quaternary ammonium-containing random copolymers.^{33,34} P-2.3-H had higher diffusivity at low λ than the other PEMs, likely due to a higher ionic density in the highly sulfonated PS phase.

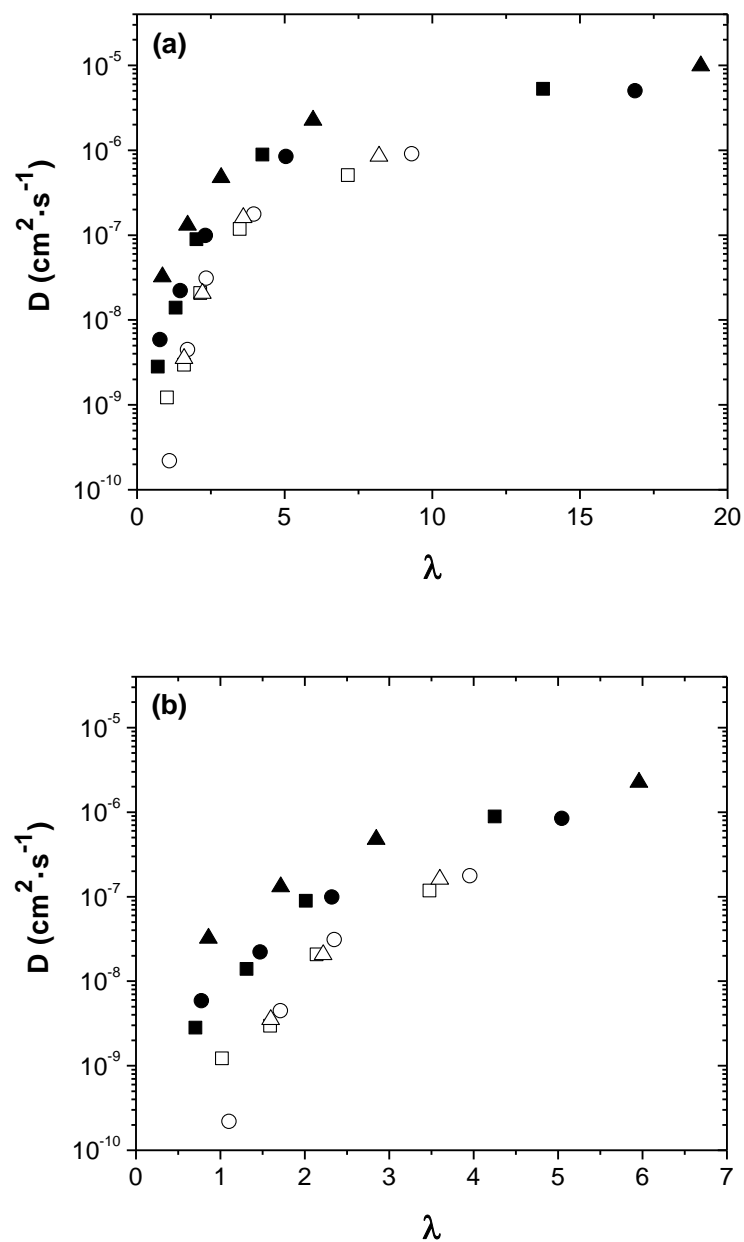


Figure 3.4. The diffusion coefficient as a function of hydration number of P-1.2-H (■), P-1.6-H (●), P-2.3-H (▲), A-1.2-Cl (□), A-1.7-Cl (○), and A-2.0-Cl (△) at (a) all hydration numbers, and (b) at low levels of hydration.

For a more thorough comparison of the factors contributing to the conductivity of the membranes aside from mobile species mobility, the diffusivity ratio between the Nernst-Einstein calculated diffusivities from conductivity measurements (D) and the dilute solution diffusivity of the mobile ion (D_0) are shown in Figure 3.5. The dilute solution diffusivities (see Table 3.2) were calculated from the dilute solution mobilities of the mobile ion using:

$$D_0 = \frac{\mu k_B T}{q} \quad (3.5)$$

where μ is the dilute ion mobility, k_B is the Boltzmann constant, T is temperature, and q is the ion charge.³⁵ The diffusivity ratio, D/D_0 , was similar for AEMs and PEMs as a function of hydration number. This relationship indicates that the mobilities of protons and chloride ions scale similarly with the hydration of the ionic group, which is an interesting result and shows that the hydrophilic phase in each material is able to achieve similar levels of ion mobility. The maximum computed diffusivities at high λ were about an order of magnitude less than the dilute solution diffusivities. It appears that the diffusion coefficients of both mobile, solvated anions and cations were suppressed by the same amount in membranes compared to dilute solution. One of the key goals for optimizing the performance of these materials will be to further decrease the gap between the dilute solution ion diffusivity and the ion diffusivity in the membrane.

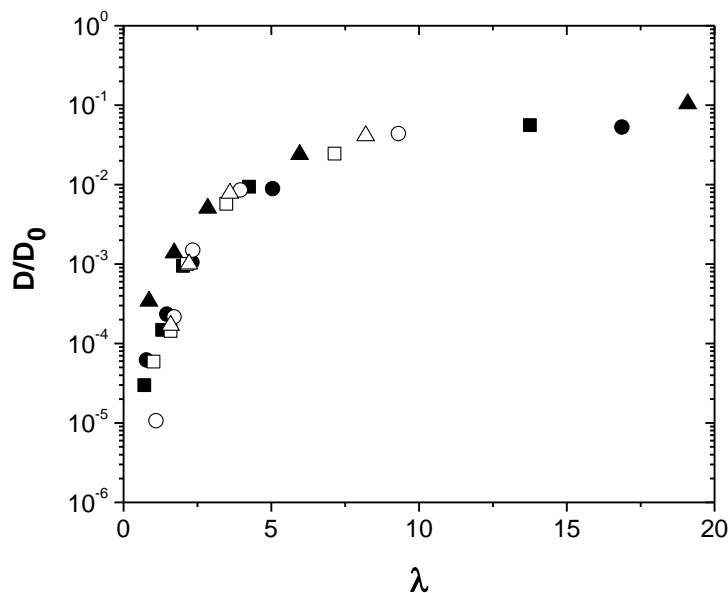


Figure 3.5. The ratio of the diffusion coefficient, D , to the dilute solution diffusivity, D_0 as a function of hydration number for P-1.2-H (■), P-1.6-H (●), P-2.3-H (▲), A-1.2-Cl (□), A-1.7-Cl (○), and A-2.0-Cl (△).

Table 3.2. Hydrated ion concentration and calculated diffusion coefficients from conductivity measurements and dilute solution^a

Sample	c^b (mol·cm ⁻³)	D^b (cm ² ·s ⁻¹)	D_0 (cm ² ·s ⁻¹)	D^b/D_0
A-1.2-Cl	1.0×10^{-3}	5.1×10^{-7}	2.1×10^{-5}	2.4×10^{-2}
A-1.7-Cl	1.4×10^{-3}	9.1×10^{-7}	2.1×10^{-5}	4.3×10^{-2}
A-2.0-Cl	1.6×10^{-3}	8.5×10^{-7}	2.1×10^{-5}	4.1×10^{-2}
P-1.2-H	0.9×10^{-3}	5.3×10^{-6}	9.5×10^{-5}	5.6×10^{-2}
P-1.6-H	1.1×10^{-3}	5.0×10^{-6}	9.5×10^{-5}	5.3×10^{-2}
P-2.3-H	1.4×10^{-3}	9.8×10^{-6}	9.5×10^{-5}	1.0×10^{-1}

^aA denotes quaternary ammonium functionalized PHMA-*b*-PS-*b*-PHMA. P denotes sulfonated PHMA-*b*-PS-*b*-PHMA. The IEC (see Table 3.1) is the number in the sample name. The last letter of the sample name is the counter ion. ^bValue for membrane at 95% RH.

The slope of the change in log conductivity as a function of RH was calculated for various IEC samples to determine how the ion conductivity in AEMs and PEMs respond to decreases in hydration, Figure 3.6. For both AEMs and PEMs, the slope of the log conductivity versus RH curve decreased with an increase in sample IEC. This data demonstrates that as the amount of functionalization of the hydrophilic domains was increased, the materials became less sensitive to hydration. At low IEC, the ionic groups were dispersed within the PS block, and higher hydration numbers are needed to bridge the ionic species. With higher IEC samples, the ionic groups were closer together in the ionic domains and the conductive pathways were not as dependent on high concentrations of water.

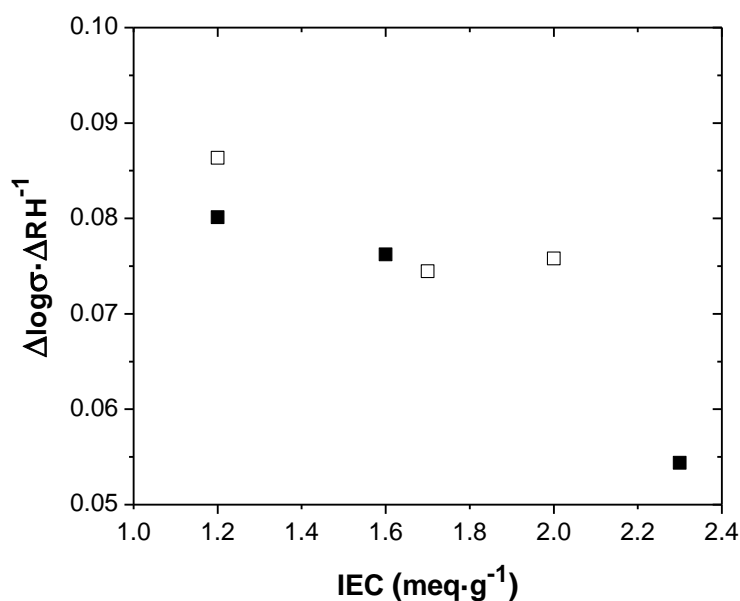


Figure 3.6. Sensitivity of change in log σ to RH of P-1.2-1.6-2.3-H (■) and A-1.2-1.7-2.0-Cl (□).

To understand conductivity differences between the AEMs and PEMs in addition to the ion mobility and ion clustering arguments above, the microphase morphologies of the block

copolymer-based membranes must be considered. The morphology of the sulfonated and quaternary ammonium functionalized PHMA-*b*-PS-*b*-PHMA triblock copolymers were investigated by SAXS, Figure 3.7.

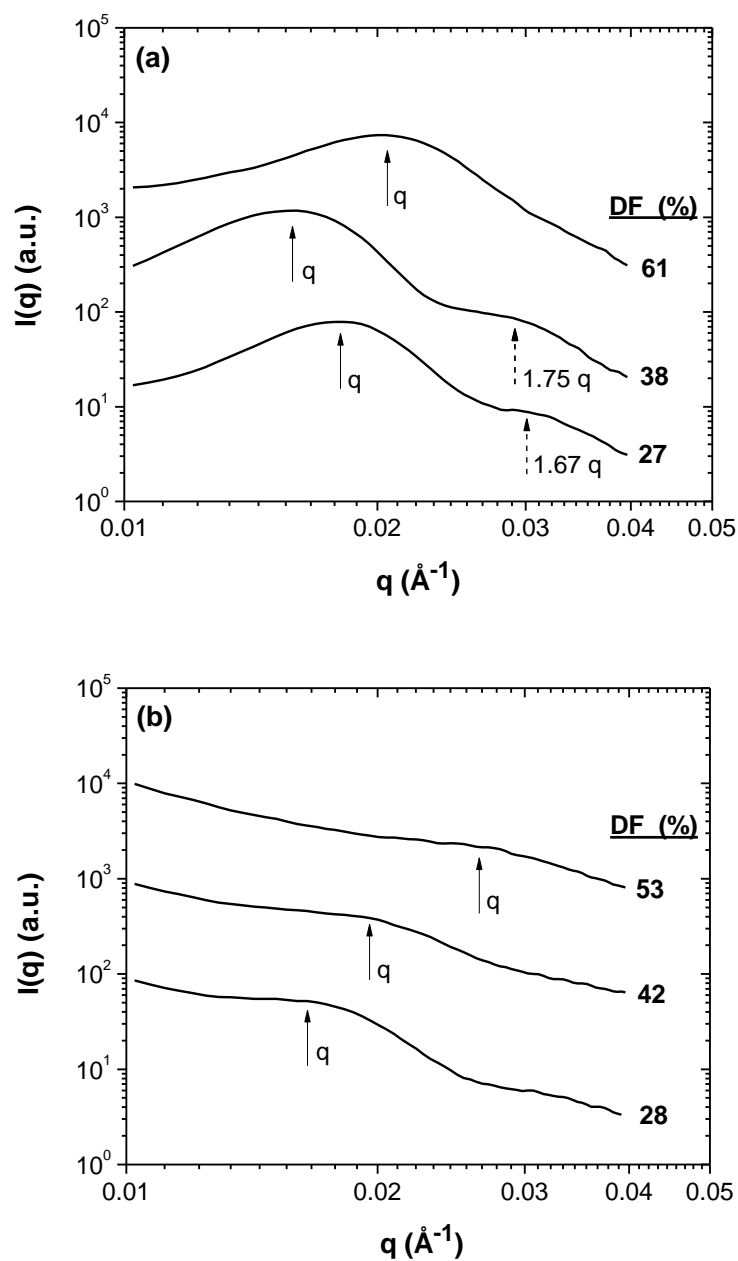


Figure 3.7. SAXS patterns of (a) PEMs and (b) AEMs. Arrows indicate primary and secondary scattering peaks.

The unfunctionalized polymer did not show any ordering, but peaks were present in the SAXS patterns for the proton and chloride forms of the functionalized triblock copolymer. The membranes do not have long-range order as indicated by the absence of higher order peaks in the SAXS patterns. The AEMs showed a consistent decrease in interdomain spacing with increasing DF, but the PEM series did not exhibit a trend. There could be significant kinetic trapping in the case of AEMs, which would lower the interdomain spacing with increased functionalization due to the formation of small phases. The 38% functionalized sample, P-1.6-H, showed a primary scattering peak at a smaller q value than either of the other PEMs. The peaks in the SAXS pattern were fit with Gaussian functions, and the interdomain spacings, listed in Table 3.3, were calculated from the primary peak maxima using $d = 2\pi \cdot q^{-1}$. The interdomain spacing did not seem to depend on the type of functionalization; the sulfonated and quaternary ammonium functionalized samples had similar d -spacings. However, the sulfonated membranes were more ordered than the quaternized membranes, evident from the secondary scattering peaks for P-1.2-H and P-1.6-H. The greater disorder in P-1.6-H may also occur in the AEMs, evident from the magnitude of peaks. The shift to higher q for P-2.3-H may be due to ion-ion interactions or to the larger volume fraction of sulfonate groups compared to styrene monomer residues. The scattering peaks of the PEMs were more well-defined than the scattering peaks of the AEMs, most likely due to the greater solubility parameter difference between hydrophilic and hydrophobic blocks in sulfonate materials compared to polymers functionalized with quaternary ammonium cations. Although no effective solubility parameter measurements exist for quaternary ammonium-tethered moieties, the phase separation in these types of materials has been more difficult to detect than in sulfonated materials. Therefore, there could be more phase mixing between the ionic and hydrophilic domains in the AEMs compared to the distinct phase separation usually noted for sulfonated PEMs.

Table 3.3. Interdomain spacing for the PHMA-*b*-PS-*b*-PHMA samples as a function of ion content.

Sample	DF (mol%)	IEC (meq·g ⁻¹)	Interdomain spacing (nm)
A-1.2-Cl	28	1.2	39
A-1.7-Cl	42	1.7	34
A-2.0-Cl	53	2.0	28
P-1.2-H	27	1.2	35
P-1.6-H	38	1.6	39
P-2.3-H	61	2.3	31

The phase separated morphology of the triblock copolymer membranes is shown in the unstained transmission electron micrographs in Figure 3.8. Both the PEMs and the AEMs exhibited disordered spherical morphology, with ions located in the darker phase exterior to the lighter-colored domains. The spherical domains were approximately 20 nm in size, which corresponds to the secondary scattering peaks shown in Figure 3.7a. The membranes were not annealed; previous work attempting thermal and solvent annealing of a similar system was not successful, likely due to the high molecular weights of these triblock copolymers and the presence of ions that impedes polymer motion and greatly increases the T_g of the ionic phase.

The similar morphology of the PEMs and AEMs shown by TEM and SAXS reveal why the sulfonated and quaternary ammonium-functionalized triblock copolymers have comparable D/D_0 values. As mentioned earlier, the diffusion coefficients of both mobile, solvated anions and cations were suppressed by the same amount in membranes compared to dilute solution, which is explained by the analogous morphologies of P-1.6-H and A-1.7-Cl.

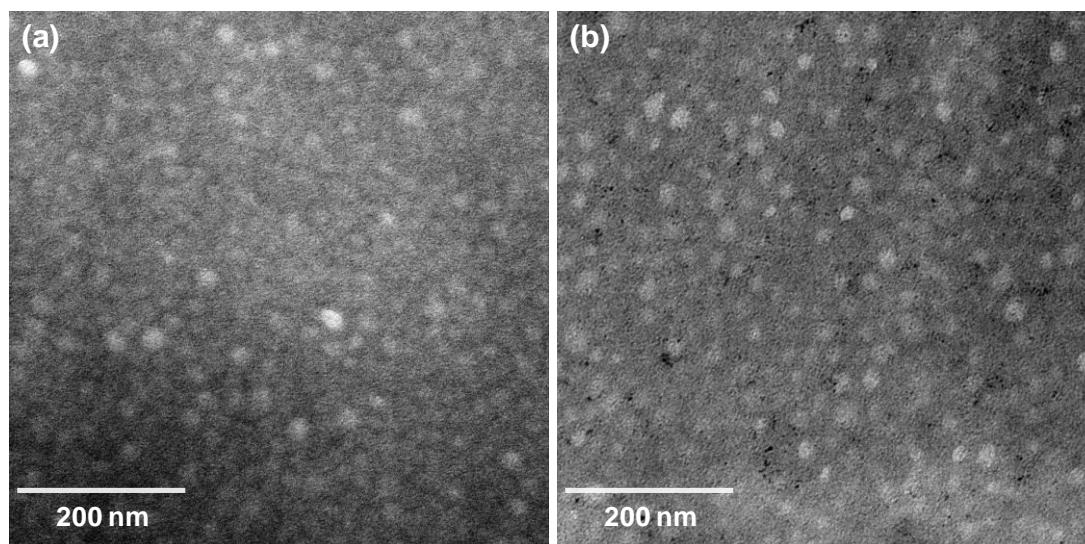


Figure 3.8. Bright field TEM images of the microtomed cross-section of membranes (a) P-1.6-H and (b) A-1.7-Cl. The spherical domains shown are on the order of 20 nm. The morphologies for the PEM and AEM are comparable, which supports the similar D/D_0 ratios for the materials.

3.4. Conclusions

The properties of PEMs and AEMs with identical polymer backbones were compared. PHMA-*b*-PS-*b*-PHMA triblock copolymer was functionalized with sulfonate or quaternary ammonium moieties to produce low, mid, and high-IEC PEMs and AEMs. Chloromethylation of the polymer using the Avram method was employed to achieve a maximum DF of 53 mol %. The in-plane conductivity of the PEMs was greater than that of the AEMs because of high proton mobility, and the PEMs had greater hydration numbers for the same value of RH due to ion pair hydration effects. To remove the bias of ion mobility in the comparison of the AEM and PEM

conductivity, the ratio of D/D_0 was calculated. For a given RH, AEMs and PEMs demonstrated similar values for D/D_0 except for the highest IEC PEM sample at low hydration.

As the IEC of the membranes increased, the sensitivity of the σ on RH decreased, demonstrating that highly functionalized ionic phases are critical to good conductivity properties. In addition, any differences in the membrane performance between AEMs and PEMs cannot be attributed to differences in the morphology of the membranes, as they have similar interdomain spacings and phase separated morphologies. This study has shown that in many respects, AEMs and PEMs of the same polymer backbone have similar properties if ionic mobility is considered and there is sufficient hydration and IEC. At low IEC, it appears that ionic clustering of sulfonate domains may boost conductivity of PEMs compared to AEMs, which will pose a challenge to creating AEMs with high conductivity at low hydration.

3.5. References

- (1) Elabd, Y. A.; Hickner, M. A. *Macromolecules* **2011**, *44*, 1–11.
- (2) Hickner, M. A. *Materials Today* **2010**, *13*, 34–41.
- (3) Yang, Y.; Holdcroft, S. *Fuel Cells* **2005**, *5*, 171–186.
- (4) Peckham, T. J.; Holdcroft, S. *Advanced Materials* **2010**, *22*, 4667–4690.
- (5) Isaacs Sodeye, A. I.; Huang, T.; Gido, S. P.; Mays, J. W. *Polymer* **2011**, *52*, 1963–1970.
- (6) Rubatat, L.; Shi, Z.; Diat, O.; Holdcroft, S.; Frisken, B. J. *Macromolecules* **2006**, *39*, 720–730.
- (7) Shi, Z.; Holdcroft, S. *Macromolecules* **2005**, *38*, 4193–4201.
- (8) Ding, J.; Chuy, C.; Holdcroft, S. *Chemistry of Materials* **2001**, *13*, 2231–2233.
- (9) Varcoe, J. R.; Slade, R. C. T. *Fuel Cells* **2005**, *5*, 187–200.

- (10) Lu, S.; Pan, J.; Huang, A.; Zhuang, L.; Lu, J. *Proceedings of the National Academy of Sciences of the United States of America* **2008**, *105*, 20611–20614.
- (11) Elabd, Y. A.; Napadensky, E.; Walker, C. W.; Winey, K. I. *Macromolecules* **2006**, *39*, 399–407.
- (12) Goswami, M.; Sumpter, B. G.; Huang, T.; Messman, J. M.; Gido, S. P.; Isaacs-Sodeye, A. I.; Mays, J. W. *Soft Matter* **2010**, *6*, 6146.
- (13) Park, M. J.; Balsara, N. P. *Macromolecules* **2008**, *41*, 3678–3687.
- (14) Knychala, P.; Banaszak, M.; Park, M. J.; Balsara, N. P. *Macromolecules* **2009**, *42*, 8925–8932.
- (15) Park, M. J.; Nedoma, A. J.; Geissler, P. L.; Balsara, N. P.; Jackson, A.; Cookson, D. *Macromolecules* **2008**, *41*, 2271–2277.
- (16) Lu, X.; Weiss, R. A. *Macromolecules* **1996**, *29*, 1216–1221.
- (17) Zhou, N. C.; Xu, C.; Burghardt, W. R.; Composto, R. J.; Winey, K. I. *Macromolecules* **2006**, 2373–2379.
- (18) Couture, G.; Alaaeddine, A.; Boschet, F.; Ameduri, B. *Progress in Polymer Science* **2011**, *36*, 1521–1557.
- (19) Hwang, G.-J.; Ohya, H. *Journal of Membrane Science* **1998**, *149*, 163–169.
- (20) Tanaka, M.; Fukasawa, K.; Nishino, E.; Yamaguchi, S.; Yamada, K.; Tanaka, H.; Bae, B.; Miyatake, K.; Watanabe, M. *Journal of the American Chemical Society* **2011**, *133*, 10646–54.
- (21) *Lange's Handbook of Chemistry*; Dean, J. A., Ed.; 15th ed.; McGraw Hill: New York, 1999.
- (22) Vanysek, P. In *CRC Handbook of Chemistry and Physics*; Lide, D. R., Ed.; CRC Press: Boca Raton, 2002.
- (23) Saito, T.; Moore, H. D.; Hickner, M. A. *Macromolecules* **2010**, *43*, 599–601.
- (24) Avram, E.; Luca, C.; Petrovan, S.; Milhailescu, C. *Polymer-Plastics Technology and Engineering* **1996**, *35*, 757–768.
- (25) Wright, M. E.; Toplikar, E. G.; Svejda, S. A. *Macromolecules* **1991**, *24*, 5879–5880.
- (26) Fujimoto, C. H.; Hickner, M. A.; Cornelius, C. J.; Loy, D. A. *Macromolecules* **2005**, *38*, 5010–5016.

- (27) Leena, S.; Kumar, K. S. *The Journal of Peptide Research: Official Journal of the American Peptide Society* **2001**, 58, 117–28.
- (28) Ning, F.; Jiang, M.; Mu, M.; Duan, H.; Xie, J. *Journal of Polymer Science Part A: Polymer Chemistry* **2002**, 40, 1253–1266.
- (29) Erdey-Gruz, T. *Transport Phenomena in Aqueous Solutions*; 1974.
- (30) Kim, Y.; Einsla, B.; Sankir, M.; Harrison, W.; Pivovar, B. *Polymer* **2006**, 47, 4026–4035.
- (31) NIST NCNR Scattering Length Density Calculator
<http://www.ncnr.nist.gov/resources/sldcalc.html>.
- (32) Walls, H. J.; Fedkiw, P. S.; Zawodzinski, T. A.; Khan, S. A. *Journal of The Electrochemical Society* **2003**, 150, E165–E174.
- (33) Hickner, M. A.; Tudryn, G. J.; Alam, T. M.; Hibbs, M. R.; Fujimoto, C. H. *Macromolecular Symposia* **2009**, 279, 59–62.
- (34) Yan, J.; Hickner, M. A. *Macromolecules* **2010**, 43, 2349–2356.
- (35) Muthukumar, M. In *Advances in Chemical Physics*; Rice, S. A., Ed.; 2005; Vol. 131, p. 45.

Chapter 4

Solution Morphology of Triblock Copolymers

4.1. Introduction

Block copolymers are one strategy for next-generation for fuel cell membranes.¹ Complex morphologies are attainable with block copolymers, and block copolymers have shown higher conductivity than random copolymers.²⁻⁴ Many different morphologies have been demonstrated for ionic membranes depending on composition and processing. The coexistence of cylindrical and lamellar morphology was observed by Weber, et al. for a poly(styrene-*b*-4-vinylbenzyl hexylimidazolium bis(trifluoromethanesulfonyl)imide) membrane cast from tetrahydrofuran (THF) with a molecular weight of 31.1 kg·mol⁻¹ and 8.6 mol % ionic liquid. The membrane was annealed at 150 °C for 3 h.⁵ A solvent-cast poly([vinylidene difluoride-co-hexafluoropropylene]-*b*-styrene) with a molecular weight of 17.9 kg·mol⁻¹ and 32 mol% sulfonation had wormlike ionic domains.⁶ Park and Balsara have shown that the morphology of solvent-cast and annealed films of PSS-PMB, poly(styrene sulfonate-*b*-methylbutylene), is dependent on the molecular weight and ion content. Lamellar, gyroid, and hexagonal morphologies were observed for membranes with 21, 32, and 39 mol % sulfonation and molecular weights of 3.1-2.6, 12.1-8.7, 1.8-1.4, kg·mol⁻¹ PSS-PMB, respectively.⁷

The properties of block copolymers in solution are important to the resultant film morphology. Kelley, et al. found the micelle radius of poly(butadiene-*b*-ethylene oxide) with a

molecular weight of $11.2 \text{ kg}\cdot\text{mol}^{-1}$ decreased as the content of THF in the water/THF solution mixture increased. However, the poly(butadiene) micelle core radius, as seen by cryo-transmission electron microscopy (TEM), increased with THF content.⁸ Solvent choice and solution properties become critical for higher molecular weight polymers, as annealing is more difficult for these polymers. The morphology of a 27 mol % sulfonated $118 \text{ kg}\cdot\text{mol}^{-1}$ poly(styrene-*b*-[ethylene-*ran*-butylene]-*b*-styrene) membranes depended on the casting solvent. Cross-sections of membranes cast from THF showed lamellar morphology, while membranes cast from a mixed solvent of methanol and THF were disordered. Kim, et al. believe the addition of even small amounts of methanol (20 vol %) to the casting solvent inhibited the formation of the lamellar structure.⁹ A molecular dynamics simulation of the solvent evaporation process of poly(isoprene-*b*-ethylene oxide) in solution examined the effect of solvent choice on the height of the polymer film; a bead-spring model was used to simulate the polymer in selective and non-selective solvents. When the polymer was evaporated from a solvent selective to poly(ethylene oxide) block, the poly(isoprene) beads were “pushed” from the liquid layer and formed islands on the surface of the polymer film. When a non-selective solvent was used, the evaporated film had a more uniform distribution of the poly(ethylene oxide) and poly(isoprene) beads.¹⁰

Long-range ordering of a cast film occurs during the solvent evaporation process, as determined by Tsige, et al. with the molecular dynamics simulation of the evaporation of solvent from a multiblock copolymer in solution. The relative stiffness of the two blocks also played a role in the final ordering of the film.^{11,12} Heinzer, et al. used small angle x-ray scattering (SAXS) to monitor the evolution of morphology for a poly(styrene-*b*-butadiene) film as the solvent (toluene) evaporated. The primary scattering peak was first observed when the solution was 30 wt % polymer, and the peak became more pronounced as the toluene continued to evaporate. The secondary scattering peak was not observed until approximately 50 wt % polymer, and the ratio of the primary to secondary peaks were consistent with a hexagonal morphology. In this

study, the relative positions of the peaks were constant at all polymer concentrations.¹³ Weisner and co-workers used the combination of self-assembly and non-solvent induced phase separation method to cast a poly(styrene-*b*-4-vinylpyridine) film from a 15 wt % solution of dioxane, THF, and dimethylformamide, and “set” the morphology observed at that concentration. The SAXS pattern of the 15 wt % polymer solution suggested a hexagonal morphology, which was consistent with scanning electron microscopy (SEM) images of the self-assembled top surface of the cast membrane.¹⁴

Sulfonated pentablock copolymers in solution were studied by Winey and co-workers using SAXS. The scattering data of 11 wt % solutions of poly(*t*-butyl styrene-*b*-hydrogenated isoprene-*b*-sulfonated styrene-*b*-hydrogenated isoprene-*b*-*t*-butyl styrene) was fit to the Kinning-Thomas hard sphere model, and the radius of the micelle core and corona were calculated.¹⁵ Small angle neutron scattering (SANS) has also been used to investigate polymers in solution, where the contrast is from differences in nuclear scattering length. For samples with poor x-ray contrast, deuterium can be added to the system to increase the contrast for SANS experiments. Additionally, the slopes of SANS curves vary with the aggregate shape, as shown in the study of Pluronic 85 (poly(ethylene oxide-*b*-propylene oxide-*b*-ethylene oxide)) in deuterium oxide by Hammouda.¹⁶ Solution and membrane morphologies of sulfonated poly(phenylene) were studied by He, et al. Bundles or rodlike aggregates were present in both the polymer in solution and in the dry membranes.¹⁷ Correlating the solution and membrane morphologies is of interest to target specific morphologies and design better fuel cell membranes.

4.2. Experimental

4.2.1 Polymer Synthesis

Two different poly(hexyl methacrylate)-*b*-poly(styrene)-*b*-poly(hexyl methacrylate), PHMA-*b*-PS-*b*-PHMA, triblock copolymers were synthesized using atom transfer radical polymerization (ATRP) with a difunctional initiator, α , α' -dibromo-*p*-xylene, as described by Saito, et al.¹⁸ This strategy facilitated synthesis of a symmetric ABA triblock copolymer with poly(styrene) as the middle block and poly(hexyl methacrylate) as the end blocks. The PHMA-*b*-PS-*b*-PHMA triblock copolymers had molecular weights of 16.5-*b*-30.5-*b*-16.5 and 11.1-*b*-24.8-*b*-11.1 kg·mol⁻¹, as determined by size exclusion chromatography (SEC), calibrated to poly(styrene) standards, and ¹H NMR. A single batch of the first triblock copolymer was used for further postmodification with sulfonate or quaternary ammonium groups, and the second batch was functionalized with only sulfonate groups. The structure of the PHMA-*b*-PS-*b*-PHMA triblock copolymers is shown in Figure 4.1 (a).¹⁹

A poly(hexyl methacrylate)-*b*-poly(styrene), PHMA-*b*-PS, diblock copolymer was synthesized via ATRP with a method similar to the above. However, instead of using a difunctional initiator for synthesis of a difunctional PS macroinitiator, 1-bromoethyl benzene was used to make a monofunctional PS macroinitiator. To polymerize the hexyl methacrylate monomer, copper (I) bromide, CuBr, and N,N,N',N',N''-pentamethyldiethylenetriamine, PMDETA, were used as the catalyst and ligand. The PHMA-*b*-PS diblock copolymer had a molecular weight of 11.2-*b*-10.1 kg·mol⁻¹, as determined by size exclusion chromatography (SEC), calibrated to poly(styrene) standards, and ¹H NMR. The polymer was subsequently

functionalized with sulfonate groups, and the chemical structure of the PHMA-*b*-PS diblock copolymer is shown in Figure 4.1 (b).

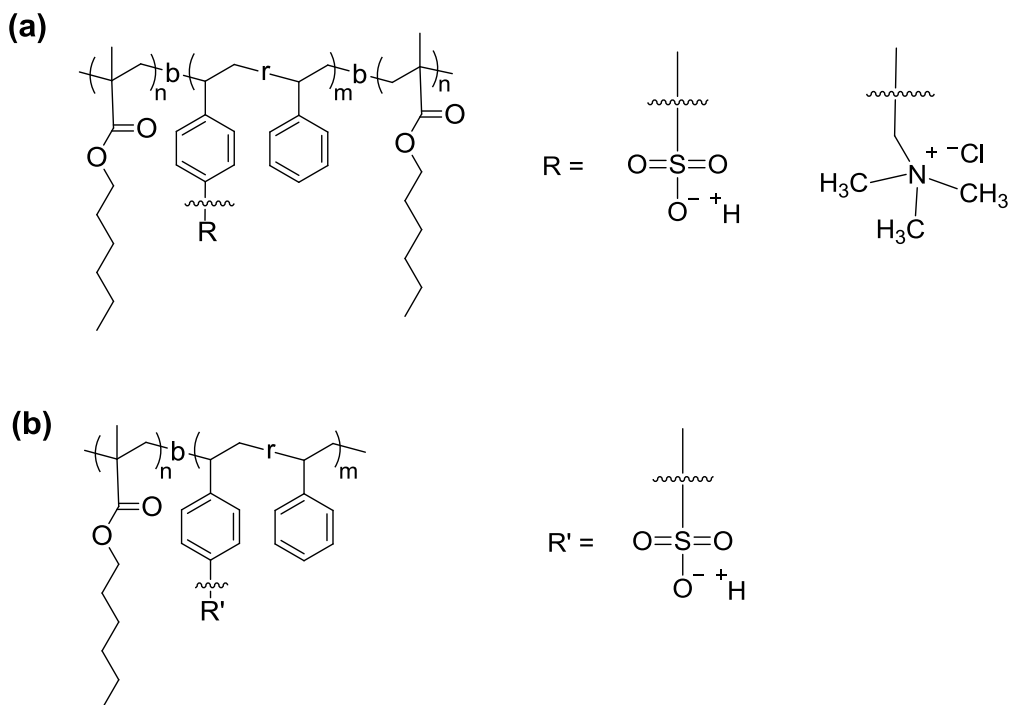


Figure 4.1. Chemical structures of the (a) PHMA-*b*-PS-*b*-PHMA triblock copolymers with tethered sulfonate (PEM) or quaternary ammonium (AEM) moieties and (b) PHMA-*b*-PS diblock copolymer with tethered sulfonate moieties (PEM).

4.2.2 Solution and Membrane Preparation

For SANS studies, 1 and 10 wt % solutions of the 16.5-*b*-30.5-*b*-16.5 kg·mol⁻¹ triblock copolymers were made in *d*₇-N,N-dimethylformamide, d-DMF. For the diblock copolymer and the 11.1-*b*-24.8-*b*-11.1 kg·mol⁻¹ triblock copolymer, 0.1, 1, 10, and 20 wt % solutions were made in d-DMF. A few drops of *d*₄-methanol and *d*₈-tetrahydrofuran were added as needed to aid solubility. Films of the functionalized triblock copolymers were cast from approximately

10 wt % solutions of polymer in N,N-dimethylformamide, DMF. The films were cast in a poly(tetrafluoroethylene) mold at ambient temperature with a glass cover slightly open for a period of 2-3 weeks and then dried *in vacuo* for 24 h at 40 °C for the AEMs and at 50 °C for the PEMs. The resulting film thicknesses were approximately 150-225 μm . When applicable, membranes were equilibrated in D_2O or under a specific relative humidity for at least 8 h before undergoing neutron scattering experiments.

4.3. Instrumentation

^1H NMR spectra of the polymers were obtained on a Bruker DRX-400 spectrometer using *d*-chloroform, *d*₈-tetrahydrofuran, or *d*₆-dimethylsulfoxide (Cambridge Isotope Laboratories) as a solvent. SANS experiments were performed at the NIST Center for Neutron Research (NCNR) on the NG7 30 m SANS and at Oak Ridge National Laboratory on the Spallation Neutron Source on beam line 6, the EQ-SANS diffractometer, or on the High Flux Isotope Reactor on beam line CG2, the general purpose SANS diffractometer.

4.4. Results and Discussion

For ease of reference in this chapter, the 16.5-*b*-30.5-*b*-16.5 $\text{kg}\cdot\text{mol}^{-1}$ PHMA-*b*-PS-*b*-PHMA triblock copolymer will be named TB-1, and the 11.1-*b*-24.8-*b*-11.1 $\text{kg}\cdot\text{mol}^{-1}$ PHMA-*b*-PS-*b*-PHMA triblock copolymer will be named TB-2. Results on the interdomain spacing of the PHMA-*b*-PS-*b*-PHMA TB-1 polymers in the solution state and of the PEM and AEM as a function of relative humidity have been determined from the correlation peak in the

SANS patterns. A case study comparison of TB-2 and the PHMA-*b*-PS diblock copolymer in solution will be discussed later.

Table 4.1 lists the IEC values and interdomain spacings of the TB-1 copolymers in the solution, dry, and hydrated states. From these calculations, where $d = 2\pi/q$, it is evident that the ionic domain size of the polymers changes between solution and dry membrane morphology and under hydration. The interdomain spacing is larger for the 10 wt % polymer solutions than for the membranes, so the domain size changes as the solvent is removed to form a membrane. When humidity is introduced to the ionic samples, the dry membranes swell, increasing the interdomain spacing. At this point, there appears to be no significant differences between the interdomain spacings of the AEMs and the PEMs.

Table 4.1. Interdomain spacings of the PHMA-*b*-PS-*b*-PHMA TB-1

Sample	IEC ($\text{meq}\cdot\text{g}^{-1}$)	D-spacing, 10 wt % in d_7 -DMF (nm)	D-spacing, dry membrane (nm)	D-spacing, hydrated membrane in D_2O (nm)
Non-ionic	0	76	41	--
A-1.2-Cl	1.2	70	39	41
A-1.7-Cl	1.7	56	37	47
A-2.0-Cl	2.0	70	31	44
P-1.2-H	1.2	61	39	40
P-1.6-H	1.6	61	41	47
P-2.3-H	2.3	83	--	--

A denotes quaternary ammonium functionalized PHMA-*b*-PS-*b*-PHMA and P denotes sulfonated PHMA-*b*-PS-*b*-PHMA.

The IEC is the number in the sample name, and the last letter(s) of the sample name is the counterion.

Using the sulfonated PHMA-*b*-PS-*b*-PHMA as a model, the morphology of the dry membrane can be predicted using equation 4.1 below.²⁰

$$\chi = \frac{V}{R \cdot T} (\delta_A - \delta_B)^2 \quad (4.1)$$

where χ is the Flory-Huggins interaction parameter, V is the molar volume, R is the universal gas constant, and δ is the solubility parameter for each component. According to literature, $\delta_{\text{PS}} = 34 \text{ (J}\cdot\text{cm}^{-3})^{1/2}$, $\delta_{\text{PS}} = 18.6 \text{ (J}\cdot\text{cm}^{-3})^{1/2}$, and $\delta_{\text{PHMA}} = 17.6 \text{ (J}\cdot\text{cm}^{-3})^{1/2}$, which were used to calculate χ .^{21,22}

The calculated interaction parameter χ and N , the number of repeat units, were combined with the volume fraction of PS in the triblock copolymer to predict a lamellar morphology according to the ABA triblock copolymer phase diagram published by Matsen and Thompson.²³ However, this interaction parameter considers each component as a homopolymer, and does not consider the arrangement of the ions within the ionic block, so the morphological prediction may be incorrect.²⁴ Experimentally, the ratio of the primary and secondary scattering peaks from the SAXS patterns suggests a hexagonal morphology for the PEM membrane.²⁵ However, unstained cross-sections of the AEMs and PEMs were imaged using transmission electron microscopy, TEM, seen in Chapter 3 and in Figure 4.2 and Figure 4.3, and show a spherical morphology with the ions on the exterior of the domains. The spherical domains are approximately 20 nm in size. The membranes were not annealed; previous work attempting thermal and solvent annealing of a similar system was not successful likely due to the high molecular weights of these triblock copolymers and the presence of ions that impedes polymer motion and increases T_g of the ionic phase greatly.

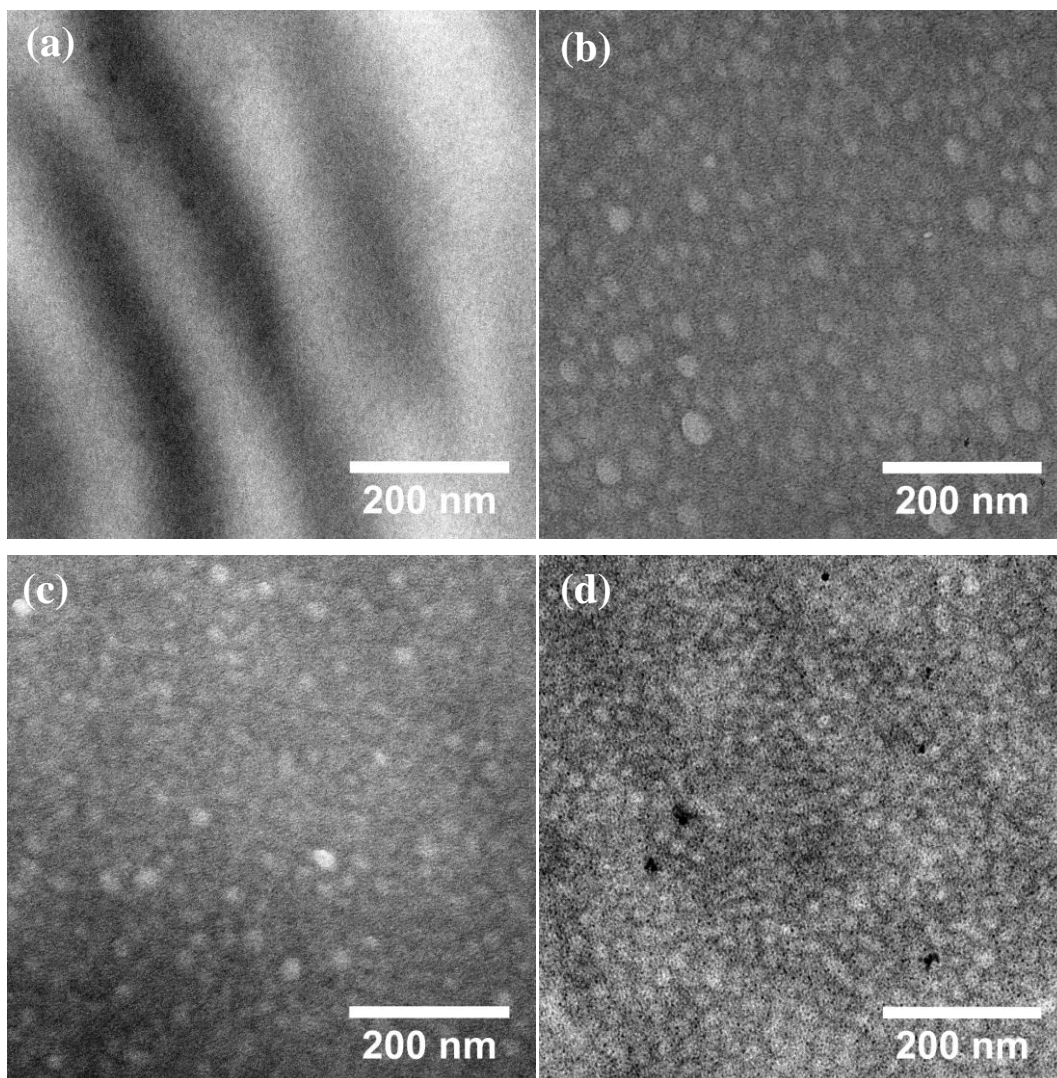


Figure 4.2. Transmission electron microscopy, TEM, images of (a) unfunctionalized PHMA-*b*-PS-*b*-PHMA, (b) P-1.2-H, (c) P-1.6-H, and (d) P-2.3-H.

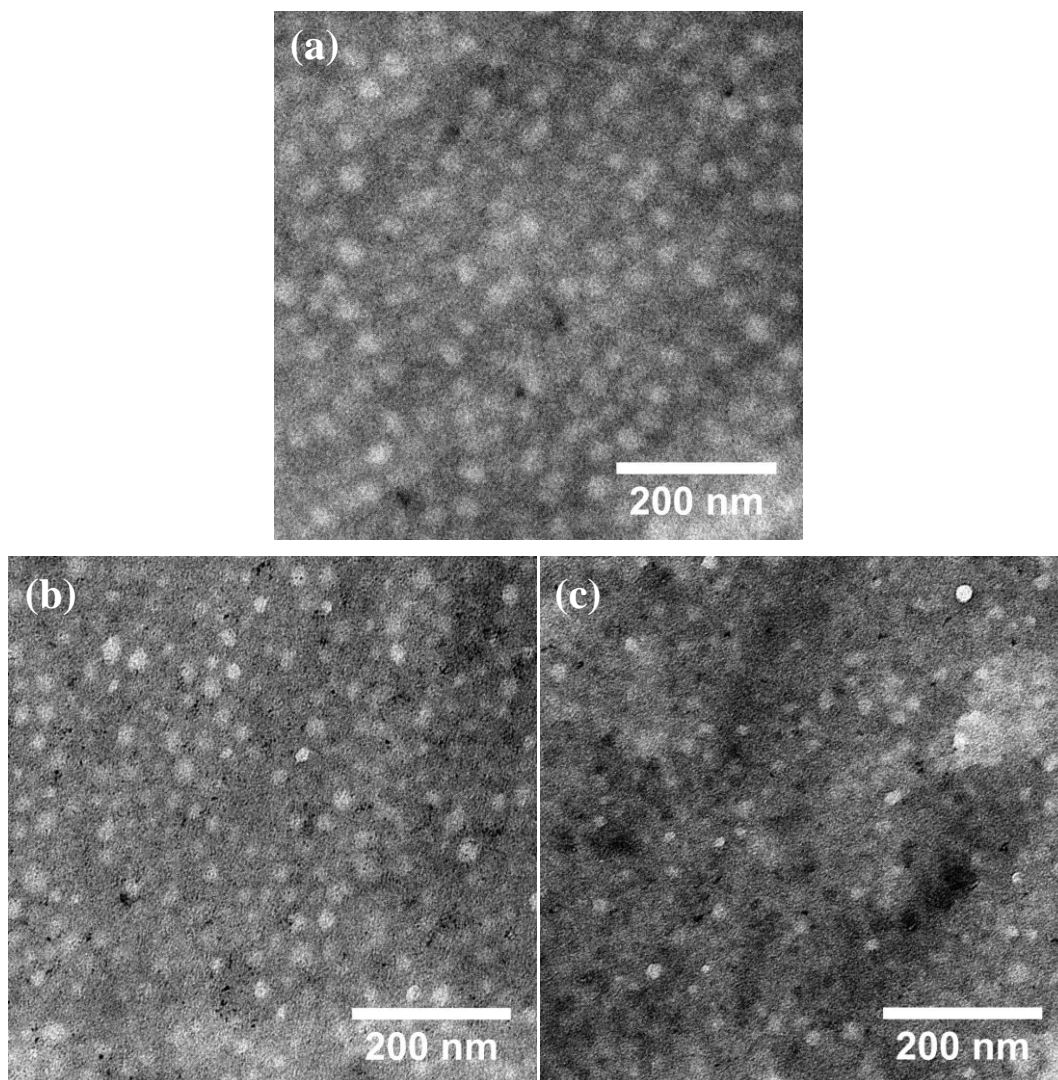


Figure 4.3. Transmission electron microscopy, TEM, images of (a) A-1.2-Cl, (b) A-1.7-Cl, and (c) A-2.0-Cl.

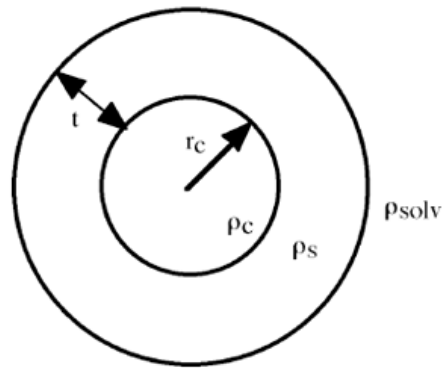
The SANS patterns for the solution and dry membrane experiments were fit to the polydisperse core-shell model with a hard sphere structure factor, developed by the National Institute of Standards and Technology (NIST) Center for Neutron Research (NCNR).²⁶ The hard

sphere structure factor relates the spatial arrangement of the particles to one another. The model function is calculated as:

$$P(q) = \frac{\text{scale}}{V_s} \left[\frac{3V_c(\rho_c - \rho_s)j_1(qr_c)}{qr_c} + \frac{3V_s(\rho_s - \rho_{\text{solv}})j_1(qr_s)}{qr_s} \right]^2 + bkg \quad (4.2)$$

$$\text{where: } j_1(x) = \frac{(\sin x - x \cos x)}{x^2}, r_s = r_c + t, \text{ and } V_i = \left(\frac{4\pi}{3}\right) r_i^3$$

and V_c , V_s and r_c , r_s are the volume and the radius of the core and shell respectively, q is the scattering vector, t is the shell thickness, and ρ_c , ρ_s , ρ_{solv} are the scattering length densities (SLDs) of the core, shell, and solvent respectively, shown in Figure 4.4 with a cartoon of our micelles.



r_c = core radius t = shell thickness
 ρ_c = core scattering length density, SLD
 ρ_s = shell SLD ρ_{solv} = solvent SLD

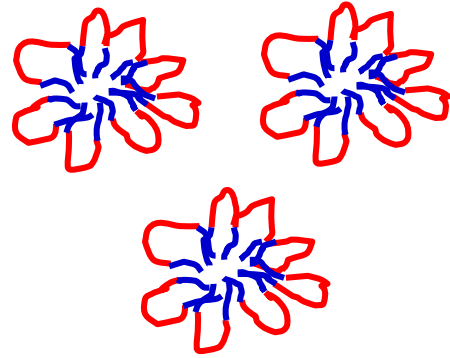


Figure 4.4. Diagram of some of the parameters used in the polydisperse core-shell model, left, and a cartoon of the PHMA-*b*-PS-*b*-PHMA TB-1 micelles, right.

The SANS scattering curves for the 1 wt % solutions, 10 wt % solutions, and dry membranes were fit to the model above using the NIST SANS Macro.²⁶ Calculated values were used as the initial starting values for the volume fraction of polymer and the SLDs. Iterations were performed until there was no change in the chi squared or error. An example of the fit to data of A-2.0-Cl for 1 and 10 wt % solutions and for the dry membrane is shown in Figure 4.5. The dotted line represents the SANS data, and the solid line depicts the model fit.

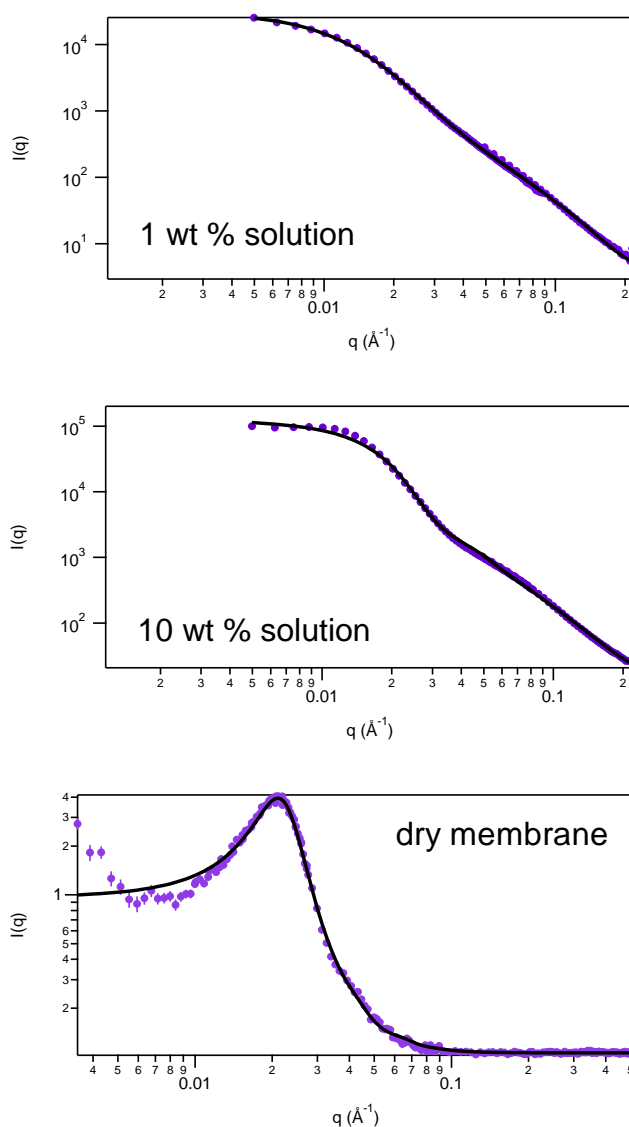


Figure 4.5. Illustration of the model fit (solid black line) to SANS data (dotted colored line) of A-2.0-Cl for 1 wt % solution, 10 wt % solution, and dry membrane.

All samples were fit using this procedure, which determined values the core radius and shell thickness, depicted in Figure 4.6. As the concentration of the polymer was increased, the system with no ions had decreased radius. Overall for the AEMs and PEMs, the core radius increased as the polymer concentration of the solutions increased from 1 wt % to 10 wt % due to more polymer per volume solvent and due to ion aggregation. From the 10 wt % solution to the dense membrane, the shell thickness increased with the solvent evaporation.

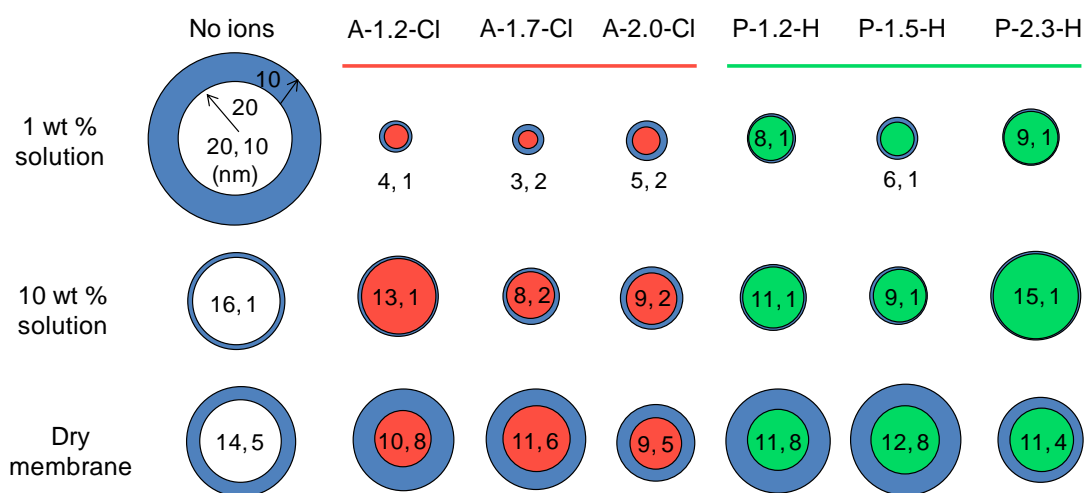


Figure 4.6. Schematic depicting the size (in nm) of the core (white, red, or green) and shell (blue) for the particles in the 1 wt % solutions, 10 wt % solutions, and dry membrane according to the fit to the NIST polydisperse core-shell model with a hard sphere structure factor.

The polydispersity of the micelle cores was also calculated, and as the size of the micelles and polymer content increased, the core polydispersity decreased (Figure 4.7). It is interesting to note that the AEM micelle cores were more polydisperse than the PEM micelle cores in 1 wt % solution. At such low polymer content, the difference is more likely due to polymer-ion interactions and not polymer-solvent interactions.

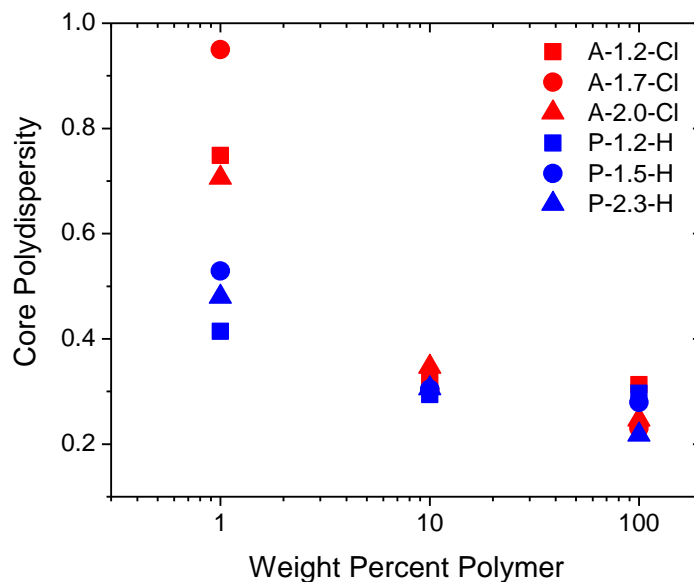


Figure 4.7. The core polydispersity is plotted as a function of weight percent polymer. As the polymer concentration increases, the particle cores became less polydisperse.

A schematic of the overall solution to membrane morphology evolution is depicted in Figure 4.8. For the dry membranes, the final scattering length densities for the core, shell, and solvent were on the same order of magnitude as the calculated initial values, 4×10^{-6} to 5×10^{-6} . The scattering length densities of the 1 wt % and 10 wt % solutions ranged from 1×10^{-3} to 7×10^{-6} and 2×10^{-3} to 1×10^{-5} , respectively.

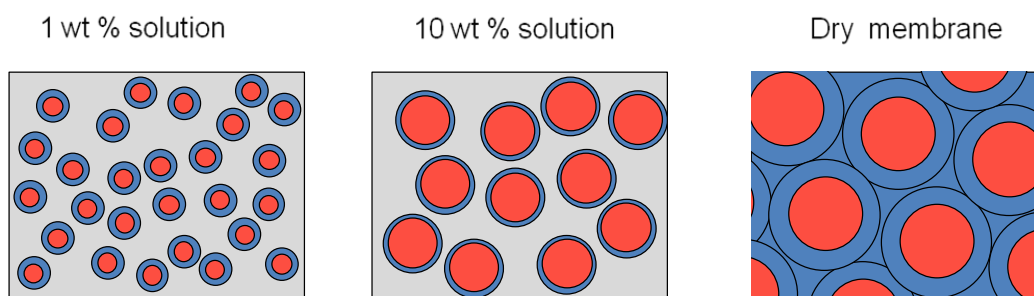


Figure 4.8. The proposed solution to membrane morphology transition is shown from left to right, with snapshots of the 1 wt % solution, the 10 wt % solution, and of the final membrane.

The overall particle size calculated from the model fit is approximately the same size as determined from the TEM images presented earlier. Based on this data from the model fit, we have started to understand the transition from solution to membrane morphology for ion-containing polymers. We believe these TB-1 membranes are kinetically trapped and are therefore not approaching the equilibrium morphology predicted by the phase diagram. Moreover, the high molecular weight and presence of ions precludes annealing these samples. As a case study, a new related diblock and triblock copolymer system was synthesized and functionalized, designed after the model proposed by Matsen and Thompson,²³ with lower molecular weights to promote long-range ordering during the casting process.

The diblock PHMA-*b*-PS and triblock PHMA-*b*-PS-*b*-PHMA, TB-2, used for comparison in this studied were both sulfonated such that the resulting IEC of both PEMs was 1.1 meq·g⁻¹. The dry membranes were characterized using SAXS, and polymer solutions were studied with SANS. The samples will be referred to as DB-1.1-H and TB-1.1-H for this study. The interdomain spacing for the 1, 10, and 20 wt % polymer solutions in d-DMF and the primary and secondary interdomain spacings for the dry membranes are listed in Table 4.2.

Table 4.2. Interdomain spacings of PHMA-*b*-PS and PHMA-*b*-PS-*b*-PHMA (TB-2)

Sample	d_1 (nm)	d_{10} (nm)	d_{20} (nm)	d_{dry} (nm)
DB-1.1-H	71	38	35	23
TB-1.1-H	73	43	41	28

Calculated from the primary scattering peak, q ; $d = 2\pi/q$.

As anticipated, the d-spacing of both diblock and triblock copolymers decreased as the concentration of the polymer solution increased. The d-spacing of the diblock PEM was smaller than the d-spacing of the triblock PEM, due to the lower molecular weight of the diblock copolymer. The interdomain spacings of the $1.1 \text{ meq}\cdot\text{g}^{-1}$ TB-2 can be compared with the interdomain spacings of the $1.2 \text{ meq}\cdot\text{g}^{-1}$ TB-1 PEM, since the ion content is similar in these membranes. From Table 4.1, the 10 wt % and dry interdomain spacings of P-1.2-H were 61 nm and 39 nm, respectively. The equivalent interdomain spacings of the $1.1 \text{ meq}\cdot\text{g}^{-1}$ TB-2 PEM were 43 nm and 28 nm, which is 70-72% of the value for TB-1. The mole fraction of PS does not provide insight into this difference, as TB-1 is 60 mol % PS, and TB-2 is 65 mol % PS. The molecular weight of the PS block and PHMA blocks of TB-2 are 81% and 67% of the PS and PHMA molecular weights of TB-1, so the answer does not lie in examination of the individual blocks. However, the total molecular weight of TB-2 is approximately 74% of the molecular weight of TB-1, which is a reasonable agreement with the discrepancy in the interdomain spacings.

To fit to the SANS data for the diblock and triblock (TB-2) copolymers in solution, the same polydisperse core-shell model with a hard shell structure factor described earlier was used. Calculated values were used as the initial starting values for the volume fraction of polymer and the SLDs. Iterations were performed until there was no change in the chi squared or error. An example of the fit to data of for 1 and 10 wt % solutions and for the dry membrane is shown in Figure 4.9. The dotted line represents the SANS data, and the solid line depicts the model fit.

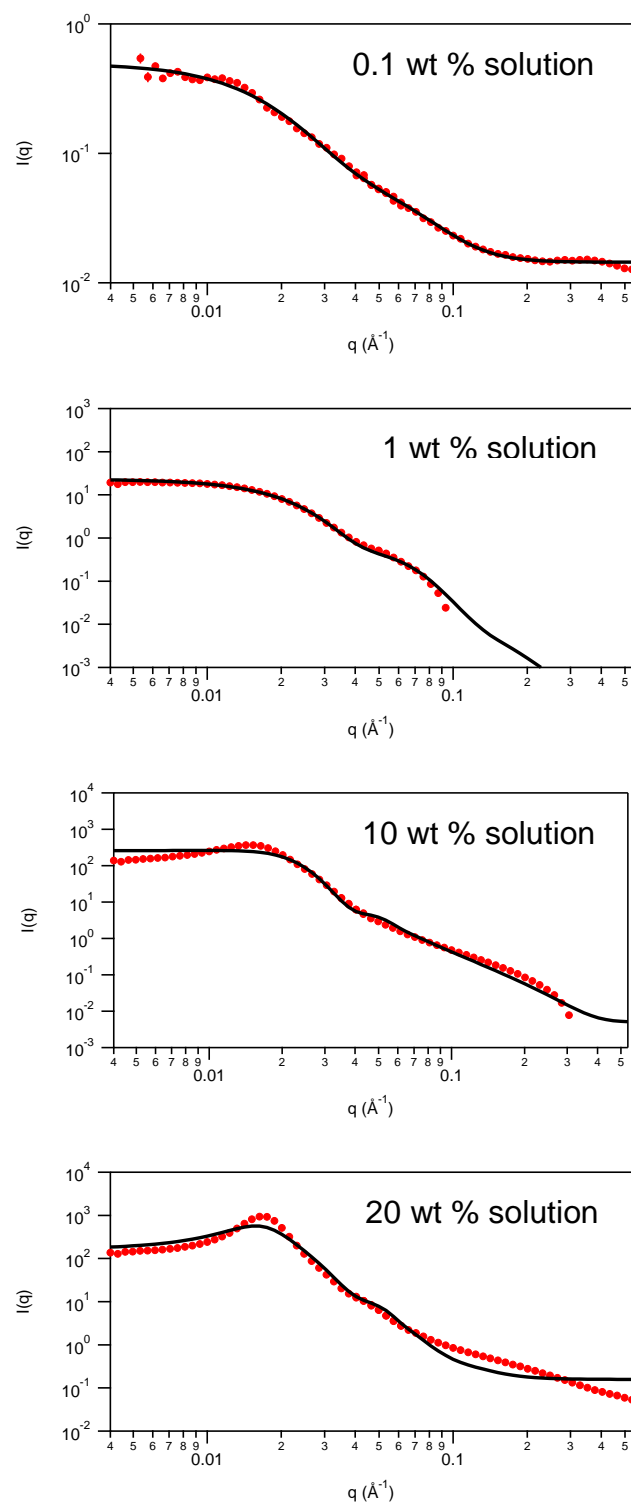


Figure 4.9. Illustration of the model fit (solid black line) to SANS data (dotted colored line) of DB-1.1-H for 0.1, 1, 10, and 20 wt % solutions.

The diblock and triblock copolymer samples were fit using this procedure, which determined values the core radius and shell thickness, depicted in Figure 4.10. Both the diblock and triblock polymer formed small spheres in the 0.1 wt % solutions. The size of the overall polymer spheres increased with polymer concentration. This brief study of the two polymers did not provide substantial additional information on the morphology evolution during the membrane formation, partly due to lack of sufficient time on the neutron scattering equipment.

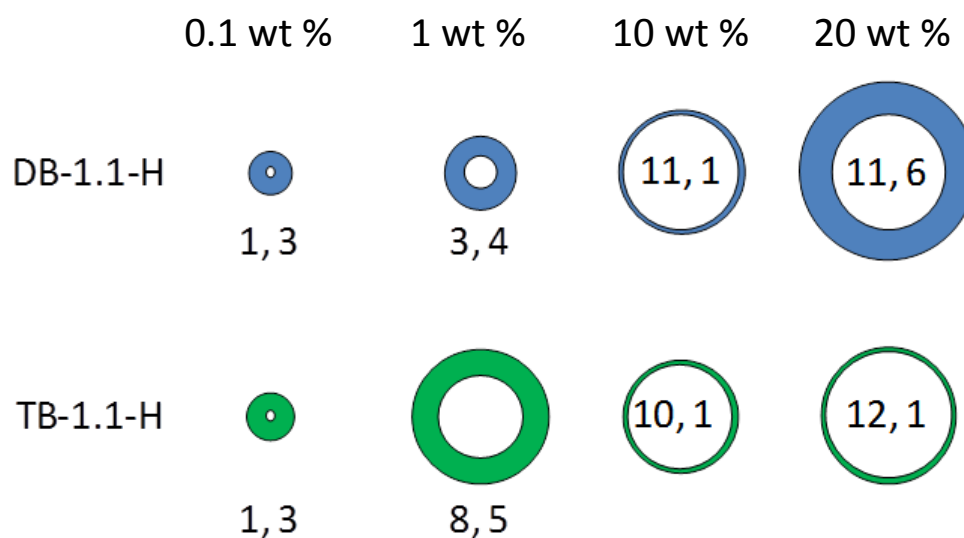


Figure 4.10. Schematic depicting the size (in nm) of the core (white) and shell (blue or green) for the particles in the 0.1, 1, 10, and 20 wt % according to the fit to the NIST polydisperse core-shell model with a hard sphere structure factor.

As with the TB-1 system, the overall polydispersity of the DB-1.1-H and TB-1.1-H polymer cores decreased with increasing polymer concentration, shown in Figure 4.11. Although the diblock copolymer had lower polydispersity than the triblock copolymer at 0.1 wt % polymer, the diblock copolymer exhibited higher polydispersity for the more concentrated solutions. However, the difference in polydispersity between the diblock and triblock copolymers at 10 and 20 wt % polymer was not substantial.

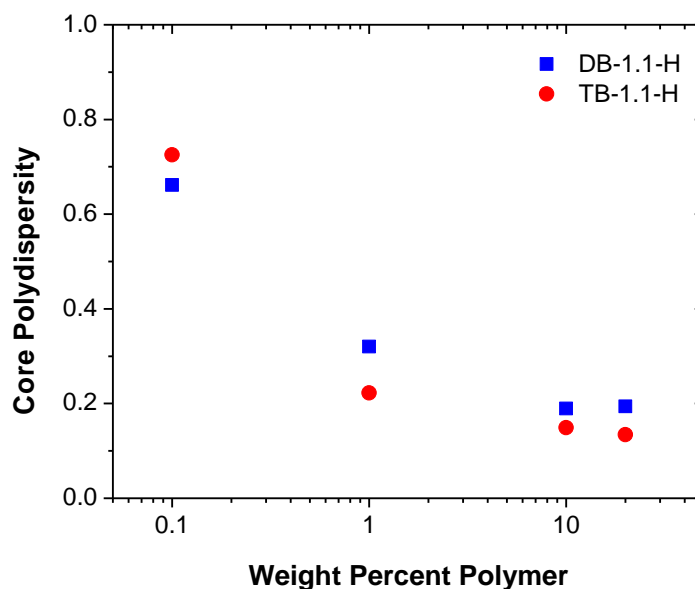


Figure 4.11. The core polydispersity of the diblock and triblock copolymers in solution is plotted as a function of weight percent polymer. As the polymer concentration increases, the particle cores became less polydisperse.

4.5. Conclusions

The solution morphology of PHMA-*b*-PS-*b*-PHMA triblock copolymer PEMs and AEMs were correlated to final membrane morphology through the use of SANS and SAXS experiments. TEM images of membrane cross-sections showed disordered spherical domains on the order of 20 nm in size. SANS experiments were performed on 1 wt % and 10 wt % concentrations of the polymers in solution, and the patterns were fit to a polydisperse core-shell model with a hard sphere structure factor. In conjunction with the TEM images, the ion-containing moiety of the triblock copolymers was believed to form the shell of the core-shell micelles. The overall size of the polymer spheres in solution the uniformity of the polymer cores increased as the polymer

concentration increased from 1 wt % to 10 wt %, and the d-spacing of the 10 wt % solutions was larger than the d-spacings of the dry and hydrated membranes, as expected. The morphology of series of diblock and triblock PHMA-PS PEMs was also investigated. The d-spacing of the second triblock PEM system, TB-2, was about 70-72% of the d-spacing of the TB-1 PEMs, which corresponded to the molecular weight difference between the systems; the molecular weight of TB-2 was about 74% of the molecular weight of TB-1. The solution morphology of the diblock and triblock copolymers was studied to compare with the previous triblock PEM system. Although the polymer concentration of the diblock and triblock copolymers in solution varied from 0.1 wt % to 20 wt %, the overall trends of the diblock and triblock were consistent with the previous study. Differences between the diblock and triblock PEM require further study.

4.6. References

- (1) Elabd, Y. A.; Hickner, M. A. *Macromolecules* **2011**, *44*, 1–11.
- (2) Bates, F. S.; Fredrickson, G. H. *Physics Today* **1999**, *52*, 32–38.
- (3) Ding, J.; Chuy, C.; Holdcroft, S. *Chemistry of Materials* **2001**, *13*, 2231–2233.
- (4) Tanaka, M.; Fukasawa, K.; Nishino, E.; Yamaguchi, S.; Yamada, K.; Tanaka, H.; Bae, B.; Miyatake, K.; Watanabe, M. *Journal of the American Chemical Society* **2011**, *133*, 10646–54.
- (5) Weber, R. L.; Ye, Y.; Banik, S. M.; Elabd, Y. A.; Hickner, M. A.; Mahanthappa, M. K. *Journal of Polymer Science Part B: Polymer Physics* **2011**, *49*, 1287–1296.
- (6) Shi, Z.; Holdcroft, S. *Macromolecules* **2005**, *38*, 4193–4201.
- (7) Park, M. J.; Balsara, N. P. *Macromolecules* **2008**, *41*, 3678–3687.
- (8) Kelley, E. G.; Smart, T. P.; Jackson, A. J.; Sullivan, M. O.; Epps, T. H. *Soft Matter* **2011**, *7*, 7094.
- (9) Kim, B.; Kim, J.; Jung, B. *Journal of Membrane Science* **2005**, *250*, 175–182.

- (10) Wood, D. S.; Koutsos, V.; Camp, P. J. *Soft Matter* **2013**, 3758–3766.
- (11) Tsige, M.; Mattsson, T. R.; Grest, G. S. *Macromolecules* **2004**, 37, 9132–9138.
- (12) Tsige, M.; Grest, G. S. **2005**, 4119.
- (13) Heinzer, M. J.; Han, S.; Pople, J. A.; Baird, D. G.; Martin, S. M. *Macromolecules* **2012**, 45, 3471–3479.
- (14) Dorin, R. M.; Marques, D. S.; Sai, H.; Vainio, U.; Phillip, W. A.; Peinemann, K.; Nunes, S. P.; Wiesner, U. *ACS Macro Letters* **2012**, 1, 614–617.
- (15) Choi, J.-H.; Kota, A.; Winey, K. I. *Industrial & Engineering Chemistry Research* **2010**, 49, 12093–12097.
- (16) Hammouda, B. *European Polymer Journal* **2010**, 46, 2275–2281.
- (17) He, L.; Fujimoto, C. H.; Cornelius, C. J.; Perahia, D. *Macromolecules* **2009**, 42, 7084–7090.
- (18) Saito, T.; Moore, H. D.; Hickner, M. A. *Macromolecules* **2010**, 43, 599–601.
- (19) Disabb-Miller, M. L.; Johnson, Z. D.; Hickner, M. A. *Macromolecules* **2013**, 46, 949–956.
- (20) Painter, P. C.; Coleman, M. M. *Fundamentals of Polymer Science*; Second.; 1997.
- (21) Lu, X.; Weiss, R. A. *Macromolecules* **1996**, 29, 1216–1221.
- (22) Hughes, L. J.; Britt, G. E. *Journal of Applied Polymer Science* **1961**, 5, 337–348.
- (23) Matsen, M. W.; Thompson, R. B. *The Journal of Chemical Physics* **1999**, 111, 7139.
- (24) Knychala, P.; Banaszak, M.; Park, M. J.; Balsara, N. P. *Macromolecules* **2009**, 42, 8925–8932.
- (25) Hamley, I. W.; Castelletto, V. *Progress in Polymer Science* **2004**, 29, 909–948.
- (26) Kline, S. R. *Journal of Applied Crystallography* **2006**.

Chapter 5

Organization and Conductivity of Analogous Diblock and Triblock Ion Conductors

5.1. Introduction

Polymers acting as ion conductors are being investigated for use in devices for energy storage and conversion, such as batteries and fuel cells. In particular, electrolytes for polymer fuel cell membranes such as proton exchange membranes (PEMs) must be robust and demonstrate high conductivity at low levels of hydration.¹⁻⁴ Ion conducting block copolymers are one approach to create the next generation of materials for fuel cell membranes; block copolymers have demonstrated higher conductivity than random copolymers.⁵⁻⁷ The increased conductivity of block copolymer PEMs has been attributed to the microphase separation present in the systems, and the correlations between morphology and conductivity have been extensively studied.^{6,8-11}

However, the mechanical integrity of PEMs must also be carefully monitored. Excessive swelling in polymer electrolyte membranes can lead to ion dilution and polymer disintegration.^{2,12-14} Previously, a series of triblock copolymer PEMs was designed to counteract swelling by functionalization of the mid-block of the polymer instead of the more common end-block functionalization. By using hydrophobic outer blocks of poly(hexyl methacrylate), PHMA, the swelling of the mid-block, sulfonated poly(styrene), PS, could be controlled.^{15,16} The T_g of PHMA and PS are -5 °C and 100 °C, respectively,¹⁷ so addition of the PHMA end blocks were designed to add flexibility to the PHMA-*b*-PS-*b*-PHMA triblock copolymer.^{15,16}

It has been argued that triblock copolymers have greater structural integrity than diblock copolymers due to the interactions between triblock copolymers. Matsen, et al. studied systems of lamellar-forming ABA triblock copolymers and lamellar-forming AB diblock copolymers where the diblock copolymers were formed by “cutting” the triblock copolymer in half. The systems were different in that the chains of the ABA triblock copolymer system formed bridges and loops. Bridges occur when the two A blocks of the triblock copolymer are situated in different A-rich lamellae, with a B block spanning the B-rich lamella, and loops occur when the two A blocks are in the same A-rich lamella, shown in Figure 5.1. Differences in mechanical properties between the two have been attributed to this lack of bridges or loops in diblock copolymers.^{18–20}

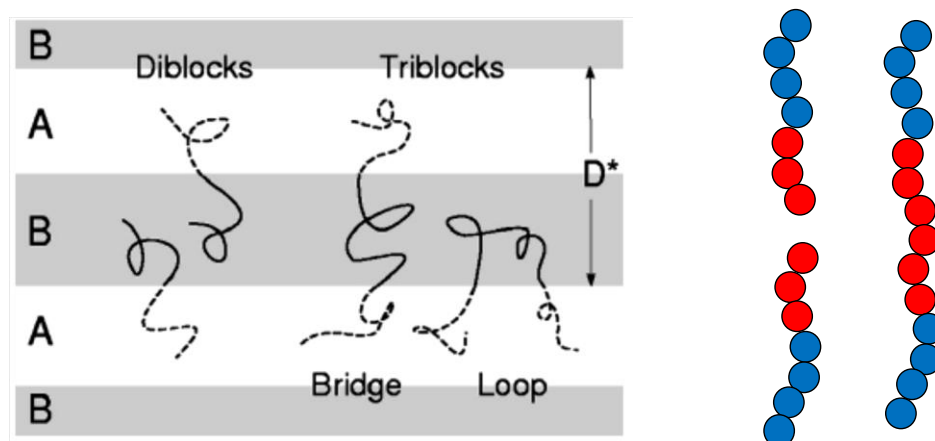


Figure 5.1. A diagram depicting the formation of bridges and loops within a lamellar ABA triblock copolymer and the lack of such formation in an analogous AB diblock copolymer, left;²⁰ a cartoon depicting AB diblock copolymer chains created from “cutting” an ABA triblock copolymer in half, right.

For the ABA triblock copolymer, the number of bridges (compared to loops) formed increases with the degree of polymerization, N , or molecular weight because the A-rich lamellae are less able to be penetrated by the B block, and it is more difficult to form loops. However, for large values of N , the width of the B-rich lamellae increase, and the formation of loops

dominates.¹⁸ The behavior of multiblock copolymer systems has been predicted to be similar to the ABA triblock copolymer system.¹⁹

In terms of ordering, ABA triblock copolymers maintain their order at lower values of χN than the AB diblock copolymers created from “cutting” the ABA triblock copolymer in half. This result was found to be particularly important at large fractions of A, where a disordered structure is more prevalent. If the triblock and diblock copolymers are the same approximate molecular weight, this property has not held. Additionally, for strongly segregating block copolymers, there is little difference in the A-rich domains between the ABA triblock copolymers and the AB diblock copolymer, so the triblock copolymers exhibit larger domain spacings. Although this aspect of the equilibrium behavior of the diblock and triblock copolymers is similar, the mechanical properties of the ABA triblock copolymer are still enhanced compared to the AB diblock copolymer. In the lamellar phase, 40%-45% of the triblock copolymers form bridges, and the fraction of bridges does not strongly depend on the segregation of the polymer or on the copolymer composition.²⁰

The PHMA-PS based diblock and triblock copolymers used in this were designed to have architectures similar to the AB and ABA systems described above; the PHMA-*b*-PS diblock copolymer was targeted to have A and B blocks such that it was as if the PHMA-*b*-PS-*b*-PHMA ABA triblock copolymer was “cut” in half. A cartoon of the AB diblock and ABA triblock copolymers is shown in Figure 5.1. We used analogous diblock and triblock copolymer systems to determine if the triblock copolymers exhibited decreased water uptake (lower swelling) and stronger ordering.

5.2. Experimental

5.2.1 Polymer Synthesis and Membrane Preparation

Styrene and hexyl methacrylate monomers were passed through an activated alumina column to remove inhibitors prior to use. The triblock copolymers were synthesized using atom transfer radical polymerization (ATRP) with the difunctional initiator, α,α' -dibromo-*p*-xylene, copper(I) bromide (CuBr), and 2,2'-bipyridyl (bpy) in the method of Saito, et al.¹⁵ A difunctional poly(styrene) macroinitiator was synthesized in the bulk (45.45 g styrene) in a Schlenk flask in the presence of 0.94 g of CuBr, 2.03 g of bpy, and 0.43 g of α,α' -dibromo-*p*-xylene at 110 °C for 7 h. The reaction target was 50% conversion. The reaction mixture underwent five freeze-pump-thaw cycles under vacuum and Ar before being placed in the oil bath to start the polymerization. After termination of the reaction, approximately 200 mL of THF was added the reaction mixture before the mixture was passed through an activated alumina column and precipitated into methanol. The polymer was filtered and washed with MeOH. The polymer was dissolved in THF before a second precipitation in MeOH. The polymer was filtered and washed again and dried in a vacuum oven at 60 °C for 2 days. This procedure resulted in approximately 20 g of difunctional poly(styrene) ATRP macroinitiator with bromine end groups, Br-PS-Br, with a PDI of 1.19 and a molecular weight of 24.8 kg·mol⁻¹.

To add the poly(hexyl methacrylate) to the macroinitiator, 12 g of the Br-PS-Br was dissolved in 100 mL of toluene with 15 mL of hexylmethacrylate (HMA) in a Schlenk flask. After the addition of 0.28 g of CuBr and 0.61 g of bpy, the flask underwent five freeze-pump-thaw cycles under vacuum and Ar. The flask was placed in an oil bath at 105 °C to start the polymerization of HMA, which proceeded for 24 h. The same post-reaction work-up was used

after termination of the reaction. The reaction produced approximately 16 g of a symmetric ABA triblock copolymer with poly(styrene) as the middle block and poly(hexyl methacrylate) as the end blocks. The poly(hexyl methacrylate)-*b*-poly(styrene)-*b*-poly(hexyl methacrylate) (PHMA-*b*-PS-*b*-PHMA) triblock copolymer had a molecular weight of 11.1-*b*-24.8-*b*-11.1 kg·mol⁻¹ and a PDI of 1.41, as determined by size exclusion chromatography (SEC) and ¹H NMR spectroscopy (see Appendix B). This triblock copolymer was further modified with sulfonate group functionalization.

A poly(hexyl methacrylate)-*b*-poly(styrene), PHMA-*b*-PS, diblock copolymer was synthesized via ATRP with a method similar to the above. However, instead of using a difunctional initiator for synthesis of a difunctional PS macroinitiator, 0.21 g of 1-bromoethyl benzene was added to 22.7 g styrene in the presence of 0.32 g of CuBr and 0.71 g of bpy. The flask was purged under Ar and underwent five freeze-pump-thaw cycles under vacuum and Ar. The reaction proceeded in an oil bath at 110 °C for 7 h and followed the post-reaction work-up described earlier to make approximately 13 g of a monofunctional PS macroinitiator with a PDI of 1.25 and a molecular weight of 10.1 kg·mol⁻¹.

To polymerize the hexyl methacrylate monomer, 10 g of styrene was added to a Schlenk flask with 50 mL of toluene, 0.14 g of CuBr, and 15 mL of HMA. Instead of bpy as the ligand, 0.35 g of N,N,N',N',N''-pentamethyldiethylenetriamine, PMDETA, was used. Again, the flask was purged under Ar and underwent five freeze-pump-thaw cycles under vacuum and Ar. The reaction proceeded in an oil bath heated to 90 °C for approximately 6.25 h and followed the same post-reaction work-up to yield approximately 13 g of PHMA-*b*-PS diblock copolymer. The PHMA-*b*-PS diblock copolymer had a molecular weight of 11.2-*b*-10.1 kg·mol⁻¹ and a PDI of 1.46, as determined by size exclusion chromatography (SEC), calibrated to poly(styrene) standards, and ¹H NMR (refer to Appendix B). The polymer was subsequently functionalized with sulfonate groups.

The sulfonated samples were synthesized by post modification of the PHMA-*b*-PS-*b*-PHMA triblock copolymer and PHMA-*b*-PS using acetyl sulfate to selectively functionalize the PS block. Sulfuric acid (1.3 mL) and acetic anhydride (3 mL) were combined in 20.7 mL of 1,2-dichloroethane at 0 °C to produce 25 mL of 1M acetyl sulfate reagent. The acetyl sulfate was warmed to room temperature and added to a 10 wt/wt % solution of PHMA-*b*-PS-*b*-PHMA in 1,2 dichloroethane. The degree of sulfonation (DS) depended on the reaction time and the molar equivalents of acetyl sulfate (with respect to PS) present in the reaction; refer to Appendix B for details. All reactions were conducted at 50 °C under argon. The chemical structures of the functionalized block copolymers is shown in Figure 5.2

5.2.2 Characterization

¹H NMR spectra of the polymers were obtained on a Bruker DRX-400 spectrometer using *d*-chloroform, *d*₈-tetrahydrofuran, or *d*₆-dimethylsulfoxide (Cambridge Isotope) as a solvent. SEC was performed using a Waters gel permeation chromatography system (GPC), which included Waters Breeze software for analysis, a 1515 isocratic HPLC pump, styrogel columns, and a 2414 RI detector. Tetrahydrofuran was used as the eluent at 35 °C, and the GPC was calibrated to a set of narrow polydispersity index (PDI) poly(styrene) standards.

SAXS patterns were collected on a Rigaku (formerly Molecular Metrology) instrument with a pinhole camera with Osmic microfocus source and parallel beam optic. The instrument was equipped with a Cu target ($\lambda = 1.542 \text{ \AA}$) and a multiwire area detector. Measurements of the dried films were obtained under vacuum at ambient temperature. Typical collection times ranged from 20-40 min, or a minimum of 300,000 photon counts. Scattering intensities were normalized for background scattering and beam transmission.

Conductivity measurements were performed using AC impedance spectroscopy on a Solartron 1260A Impedance/Gain-Phase Analyzer. The conductivity of free-standing films was measured using a two-point, in-plane geometry at frequencies between 1 MHz and 100 Hz.²¹ During the measurements, humidity and temperature were controlled using an Espec SH-241 environmental chamber. The relative humidity varied from 20% to 95% while the temperature was held at 30 °C. The real value of the impedance, where the imaginary response is zero, was used as the membrane resistance. Ion conductivity (σ) was calculated from:

$$\sigma = \frac{L}{R \cdot A} \quad (5.1)$$

where L is the length between electrodes, R is the resistance of the membrane, and A is the cross-sectional area of the membrane. Error in conductivity measurements is believed to be on the order of 1 mS·cm⁻¹.

Water uptake ($wu = (mass_{hydrated} - m_0)/m_0$) was measured using a TA Instruments Q5000SA water vapor sorption microbalance at 30 °C between relative humidities of 20% and 95%, with steps at 35%, 50%, and 75% RH. The hydration number (λ), or the number of water molecules per ionic group, was calculated from:

$$\lambda = \left(\frac{m_{RH} - m_0}{m_0} \right) \times \left(\frac{1000}{M_{H_2O} \cdot IEC} \right) \quad (5.2)$$

where m_{RH} is the sample mass at a given RH, m_0 is the mass of the dry sample, M_{H_2O} is 18.02 g, the molecular mass of water, and IEC is the ion exchange capacity with units of milliequivalents of ions per gram of polymer.

5.3. Results and Discussion

Analogous PHMA-PS based diblock and triblock copolymers were designed after Matsen and Thompson such that the molecular weight of the diblock copolymer was as if the triblock copolymer had been cut in half.²⁰ The diblock copolymer (DB) is 53 wt % PS (60 mol % PS), and the triblock (TB) copolymer is 47 wt % PS (65 mol % PS). The polymers were synthesized and sulfonated for use as PEMs, shown in Figure 5.2.

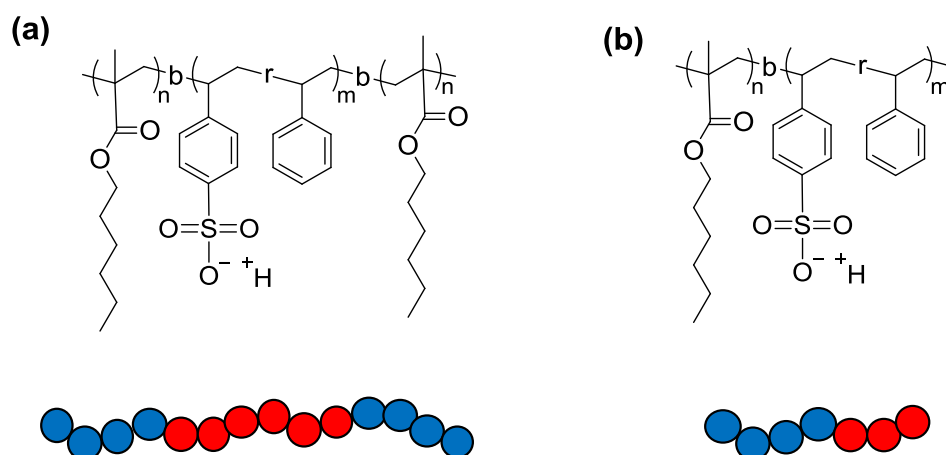


Figure 5.2. Chemical structures of the (a) PHMA-*b*-PS-*b*-PHMA triblock copolymer with tethered sulfonate (PEM) moieties and (b) PHMA-*b*-PS diblock copolymer with tethered sulfonate moieties (PEM). The cartoons depict the diblock copolymer was designed with a molecular weight such that it was as if the triblock copolymer chain had been cut in half.

The degree of functionalization (DF) of the PEMs varied such that low, mid, and high IEC membranes were produced for the DB and TB PHMA-PS based polymers. The conductivity and water uptake of the membranes were measured, and the values are listed in Table 5.1, along with the interdomain spacings calculated from small angle x-ray scattering (SAXS). Both the DB and TB copolymer PEMs exhibited secondary scattering peaks.

Table 5.1. Polymer Membrane Characteristics and Properties

Sample	DF (%)	IEC (meq·g ⁻¹)	wu ^a (%)	λ^a	σ^a (mS·cm ⁻¹)	Interdomain spacing ^b (nm)
DB-1.1-H	26	1.1	33	16	17.7	23
DB-1.7-H	43	1.7	49	16	58.8	27
DB-2.0-H	53	2.0	46	13	35.6	28
TB-1.1-H	23	1.1	26	13	6.3	28
TB-1.6-H	36	1.6	36	13	24.6	27
TB-2.3-H	56	2.3	49	12	36.8	28

DB denotes diblock copolymer PHMA-*b*-PS. TB denotes triblock copolymer PHMA-*b*-PS-*b*-PHMA.

The IEC is the number in the sample name, and the last letter of the sample name is the counter ion.

^aValue for membrane at 95% RH for water uptake (wu), hydration number (λ) and conductivity (σ).

^bDetermined from $d=2\pi/q$.

For the same IEC, the DB copolymers were more hydrated than the TB copolymers, indicated by the larger water uptake and λ values, and illustrated in Figure 5.3. The greater swelling of the DB copolymers is consistent with the findings of Matsen, et al.^{18,20} and supports the design of the polymer by Saito, et al.^{15,16} Due to additional mechanical integrity and by constraining the ion-containing mid-block of the polymer, the water uptake of the PEMs decreased. Also, the sulfonate groups of the DB PEMs might be closer to ion transport channels due to their location near chain ends, allowing for greater water uptake. The water uptake of the TB PEMs increased linearly with IEC, but the DB PEMs did not follow that trend and the mid-IEC DB PEM had the highest water uptake. The λ values for both DB and TB membranes decreased with IEC.

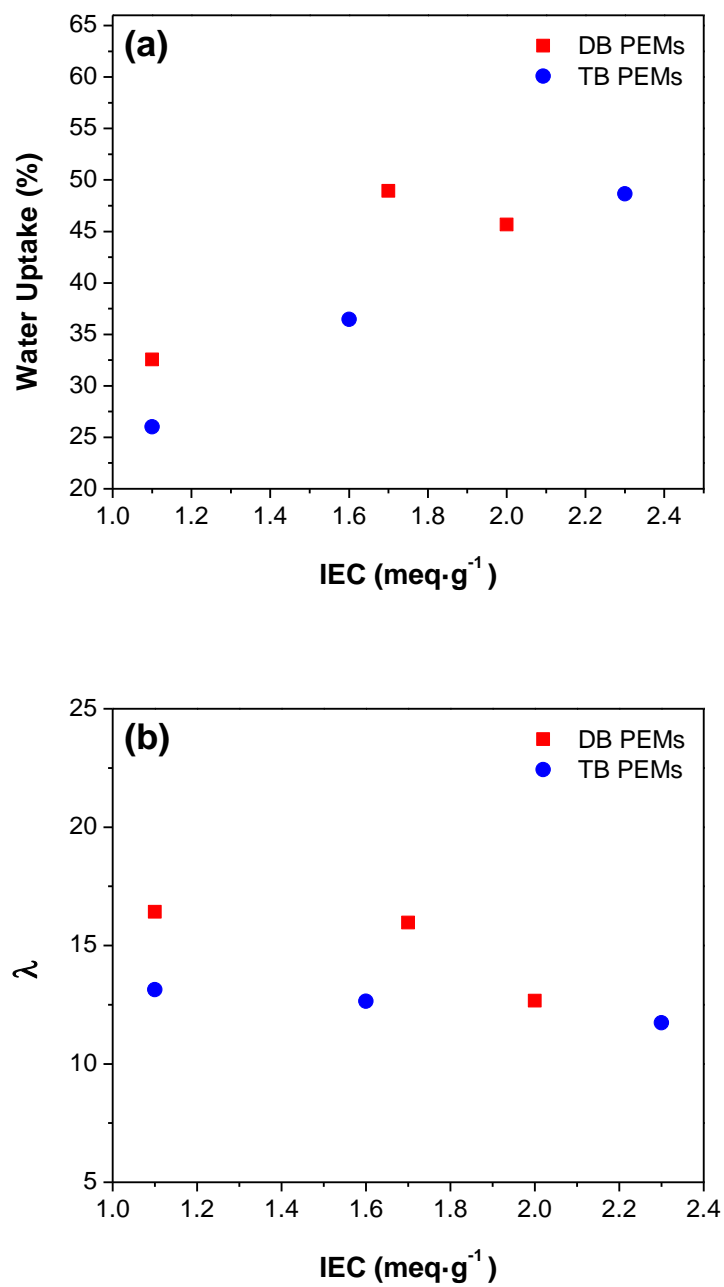


Figure 5.3. Comparison of the (a) water uptake and (b) hydration number of diblock (DB) and triblock (TB) PEMs as a function of ion content.

To directly compare the diblock and triblock copolymers on a membrane-membrane basis, the most straightforward comparison is to examine the $1.1 \text{ meq}\cdot\text{g}^{-1}$ PEMs, where at 95% RH, the DB-1.1-H and TB-1.1-H membranes had w_u of 33% and 26% and λ of 16 and 13, respectively. Similar comparisons between the 1.6 and $1.7 \text{ meq}\cdot\text{g}^{-1}$ DB and TB PEMs can be established and lead to the same conclusion. The most striking example of the swelling of the DB copolymers is the high-IEC PEMs, where the higher $2.3 \text{ meq}\cdot\text{g}^{-1}$ IEC TB copolymer demonstrates similar water uptake and lower hydration than the $2.0 \text{ meq}\cdot\text{g}^{-1}$ IEC DB copolymer. Typically, swelling in ion-containing polymers increases with ion content, so the DB-2.0-H membrane should have demonstrated lower hydration than the TB-2.3-H membrane.

Ion transport relies on adequate transport, and the conductivity of the membranes increased as the RH and hydration number increased as expected, illustrated by Figure 5.4. The conductivity of the triblock copolymer PEMs are consistent with previous work on a PHMA-*b*-PS-*b*-PHMA system,²² but the mid and high-IEC sulfonated diblock copolymers demonstrated higher conductivity than the analogous triblock copolymers, most likely due to the increased hydration of the diblock membranes. Further investigation is required to determine if the high conductivity of the DB-1.6-H membranes is accurate or an artifact of casting conditions. Additionally, after the conductivity measurement at 95% RH, the DB copolymer membranes were extremely fragile, and it was difficult to measure the membrane thickness. It is unlikely that either the of the sulfonated PHMA-PS based membranes could be viable for sustained use at fuel cell operation conditions, and it is doubtful that the conductivity testing of an individual DB copolymer membranes could be performed more than once.

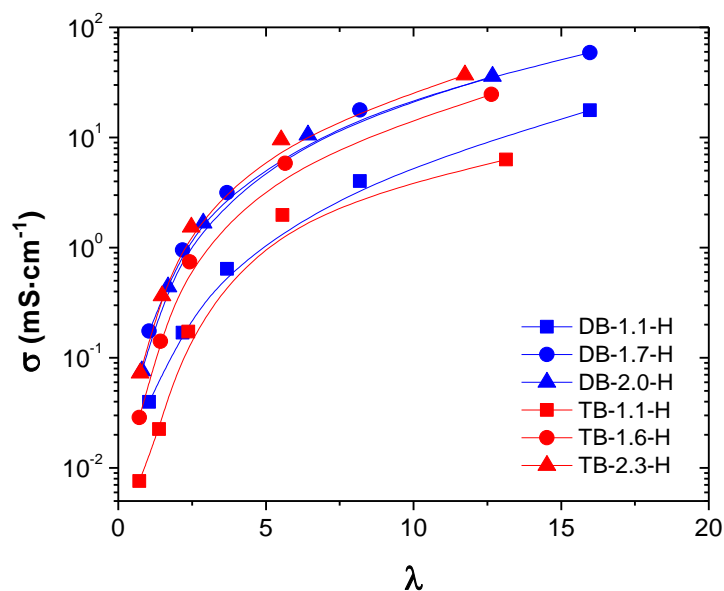


Figure 5.4. The conductivity of the membranes increased with RH and hydration number

The SAXS patterns of the sulfonated PHMA-PS based block copolymer membranes (Figure 5.5) reveal that both the DB and TB copolymers scatter strongly, as secondary scattering peaks were present for all samples. The high-IEC membranes, DB-2.0-H and TB-2.3-H also demonstrated tertiary scattering peaks, but peak maximums could not be defined. The scattering peak ratios for the primary and secondary peaks corresponded to cylindrical morphology.²³ The primary scattering peaks of the DB copolymers moved to lower q values as the degree of sulfonation of the membranes increased. The primary scattering peaks of the TB copolymers did not shift with higher ion content, suggesting the morphology of the TB copolymers is less influenced by the sulfonate groups compared to the DB copolymers.

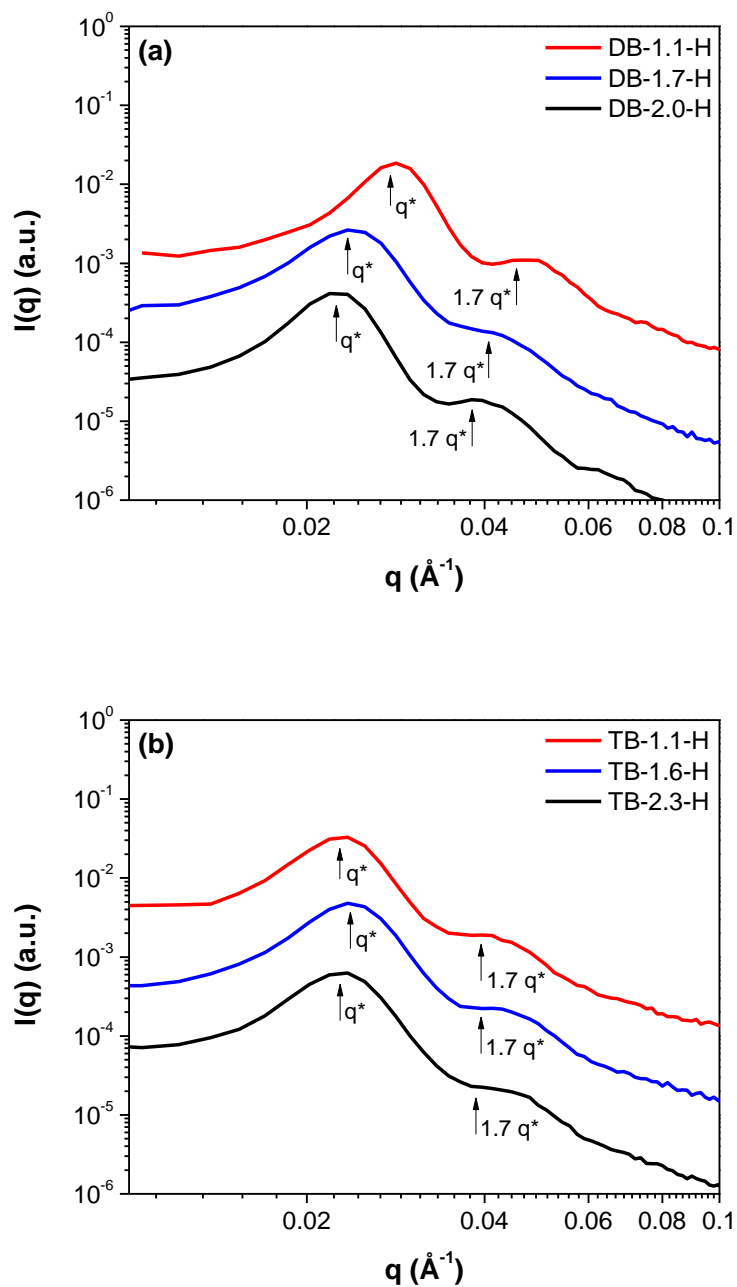


Figure 5.5. Small angle x-ray scattering (SAXS) patterns for (a) diblock and (b) triblock copolymer PEMs. Primary peaks are indicated by q^* .

The similar d-spacings for the sulfonated DB and TB PHMA-PS based copolymers reinforces that the presence of ions can interfere with the Semenov scaling behavior²⁴ of the interdomain spacing as a function of molecular weight and disrupts or alters the morphology of block copolymers.²⁵ According to Semenov, the interdomain spacing is proportional to the number of polymer repeat units to the two-third power, since the interaction parameters for the PHMA-PS based diblock and triblock copolymers should be alike. That calculation would dictate that the diblock copolymer should have interdomain spacings that are 82% of the triblock copolymer interdomain spacings. Subsequently, the diblock copolymer primary scattering peaks should have been 22-23 nm for the entire series, instead of the 23-28 nm observed. In this instance, only the 1.1 meq·g⁻¹ IEC diblock and triblock copolymers obey the Semenov scaling behavior; the interdomain spacing of DB-1.1-H was 23 nm, and the d-spacing of TB-1.1-H was 28 nm.

5.4. Conclusions

Analogous diblock and triblock PHMA-PS based copolymers were designed according to the model presented by Matsen, et al²⁰ to investigate the mechanical integrity (swelling) of diblock and triblock copolymer PEMs. The polymers were synthesized such that the AB diblock copolymer produced was as if the ABA triblock copolymer chains had been “cut” in half. The diblock copolymers exhibited greater water uptake and higher hydration numbers for a given ion exchange capacity, supporting the work by Matsen, et al. The diblock copolymer PEMs demonstrated higher conductivity than the triblock copolymer PEMs, likely due to the greater number of water molecules per ion present in the diblock copolymer membranes.

Although it was outside the scope of this work, it would be interesting to examine hydrated or partially hydrated DB and TB PEMs using density, morphology, and swelling measurements to better quantify the degree of expansion in the polymers with hydration. Care must be taken for these measurements since the sulfonated PHMA-*b*-PS diblock copolymer lost all mechanical integrity after exposure to a RH environment. Additionally, verification of the membrane morphology should be performed using transmission electron microscopy.

5.5. References

- (1) Hickner, M. A. *Mater. Today* **2010**, *13*, 34–41.
- (2) Yee, R. S. L.; Rozendal, R. A.; Zhang, K.; Ladewig, B. P. *Chem. Eng. Res. Des.* **2012**, *90*, 950–959.
- (3) Borup, R.; Meyers, J.; Pivovar, B.; Kim, Y. S.; Mukundan, R.; Garland, N.; Myers, D.; Wilson, M.; Garzon, F.; Wood, D.; Zelenay, P.; More, K.; Stroh, K.; Zawodzinski, T.; Boncella, J.; McGrath, J. E.; Inaba, M.; Miyatake, K.; Hori, M.; Ota, K.; Ogumi, Z.; Miyata, S.; Nishikata, A.; Siroma, Z.; Uchimoto, Y.; Yasuda, K.; Kimijima, K.-I.; Iwashita, N. *Chem. Rev.* **2007**, *107*, 3904–51.
- (4) Zhang, H.; Shen, P. K. *Chem. Rev.* **2012**, *112*, 2780–832.
- (5) Elabd, Y. A.; Hickner, M. A. *Macromolecules* **2011**, *44*, 1–11.
- (6) Ding, J.; Chuy, C.; Holdcroft, S. *Chem. Mater.* **2001**, *13*, 2231–2233.
- (7) Tanaka, M.; Fukasawa, K.; Nishino, E.; Yamaguchi, S.; Yamada, K.; Tanaka, H.; Bae, B.; Miyatake, K.; Watanabe, M. *J. Am. Chem. Soc.* **2011**, *133*, 10646–54.
- (8) Park, M. J.; Balsara, N. P. *Macromolecules* **2008**, *41*, 3678–3687.
- (9) Peckham, T. J.; Holdcroft, S. *Adv. Mater.* **2010**, *22*, 4667–4690.
- (10) Rubatat, L.; Shi, Z.; Diat, O.; Holdcroft, S.; Frisken, B. J. *Macromolecules* **2006**, *39*, 720–730.
- (11) Shi, Z.; Holdcroft, S. *Macromolecules* **2005**, *38*, 4193–4201.

- (12) Ingratta, M.; Jutemar, E. P.; Jannasch, P. *Macromolecules* **2011**, *44*, 2074–2083.
- (13) Lee, M.; Keun, J.; Lee, H.; Lane, O.; Moore, R. B.; McGrath, J. E.; Baird, D. G. *Polymer (Guildf)*. **2009**, *50*, 6129–6138.
- (14) Young, W.-S.; Epps, T. H. *Macromolecules* **2012**, *45*, 4689–4697.
- (15) Saito, T.; Moore, H. D.; Hickner, M. A. *Macromolecules* **2010**, *43*, 599–601.
- (16) Moore, H. D.; Saito, T.; Hickner, M. A. *J. Mater. Chem.* **2010**, *20*, 6316.
- (17) *Polymer Data Handbook*; Mark, J. E., Ed.; Oxford University Press, Inc., 1999.
- (18) Matsen, M. W.; Schick, M. *Phys. Rev. Lett.* **1994**, *72*, 2660–2663.
- (19) Matsen, M. W. *J. Chem. Phys.* **1995**, *102*, 3884–3887.
- (20) Matsen, M. W.; Thompson, R. B. *J. Chem. Phys.* **1999**, *111*, 7139–7146.
- (21) Fujimoto, C. H.; Hickner, M. A.; Cornelius, C. J.; Loy, D. A. *Macromolecules* **2005**, *38*, 5010–5016.
- (22) Disabb-Miller, M. L.; Johnson, Z. D.; Hickner, M. A. *Macromolecules* **2013**, *46*, 949–956.
- (23) Hamley, I. W.; Castelletto, V. *Prog. Polym. Sci.* **2004**, *29*, 909–948.
- (24) Bates, F. S.; Fredrickson, G. H. *Annu. Rev. Phys. Chem.* **1990**, *41*, 525–57.
- (25) Knychala, P.; Banaszak, M.; Park, M. J.; Balsara, N. P. *Macromolecules* **2009**, *42*, 8925–8932.

Chapter 6

Morphology and Conductivity of Poly(styrene)-Based Anion Exchange Membranes

6.1. Introduction

Due to the rising global energy demands, alternative approaches for energy conversion are receiving considerable interest. Polymer electrolyte membrane fuel cells address this need by providing a low-cost, lightweight means of energy conversion, but their current performance, stability, and cost are prohibitive to widespread use of the membranes.¹⁻³ The development of new ion-containing materials are necessary to produce polymer electrolyte membranes that possess high ionic conductivity, good thermally and hydrolytic stability, low fuel crossover, adequate water uptake with minimal swelling, low cost, and easy incorporation into membrane electrode assemblies.⁴⁻⁶ For fuel cell operation, proton exchange membranes (PEMs) currently require precious metal catalysts, such as platinum, for fuel cell operation. Anion exchange membranes (AEMs), the focus of this work, can leverage cheaper catalyst metals, but are less stable and must demonstrate improved conductivity.^{1,4,7}

To produce AEMs, benzyltrimethylammonium (BTMA) and alkyltrimethylammonium cations have been added to poly(arylene ether sulfone),^{8,9} poly(fluorenyl ether ketone sulfone),¹⁰ poly(phenylene oxide),⁹ poly(tetrafluoroethylene),¹¹ poly(ether ketone),¹² and poly(styrene-*b*-ethylene-*co*-butylene-*b*-styrene)¹³ backbones. Since sulfonated block copolymers

A small part of this chapter is adapted from Bryson, K. C.; Hickner, M. A. Synthesis of novel ion-conducting polymers via reversible addition-fragmentation chain transfer polymerization, Pennsylvania State University, 2010, call number: Thesis 2010sBryso,KC.

have exhibited increased conductivity compared to analogous random copolymer PEMs, credited to the morphology present in the block copolymer membranes,¹⁴⁻²¹ block copolymer AEMs merit discussion. Although similar improvement over random copolymers has been observed for quaternary ammonium (QA) functionalized block copolymers used in AEMs,^{4,22,23} further research is necessary to fully validate this occurrence. The ion content, ion exchange capacity (IEC), conductivity (σ), water uptake (wu), and hydration number (λ), the number of water molecules per (mobile) ion are indicators of membrane performance.

QA functionalized poly(styrene-*b*-ethylene-*co*-butylene-*b*-styrene) membranes have demonstrated with an IEC of 0.578 meq·g⁻¹, hydroxide conductivity of 0.69 mS·cm⁻¹, and λ of 5.5.¹³ Hwang and Ohya synthesized block copolymer AEMs with biphasic morphology that showed increased conductivity compared to random copolymers, but the block copolymers also had higher values of IEC. The conductivities of the block copolymer AEMs were high, ranging from 0.15-0.24 S·cm⁻¹, but the measurement was taken with the membranes in a 2 M solution of KCl, so the salt likely played a major role in the conductivity of these materials.^{2,24} Miyatake also demonstrated that block copolymer AEMs have higher conductivity than analogous random copolymers through the synthesis of quaternized multiblock copoly(arylene ether) polymers containing fluorene, shown in Figure 6.1.²³

The random and block copolymers in this work were designed as a systematic study of QA-functionalized poly(vinyl benzyl chloride)-poly(styrene), PVBC-PS, films to determine the effect of ion content and polymer structure on the morphology, water uptake, and conductivity of the AEMs. Both random and block copolymer PVBC-PS systems were synthesized and functionalized for use as AEMs by Kyle Bryson and Professor Michael Hickner at the Pennsylvania State University.²⁵ The materials were used as received in the chloride form.

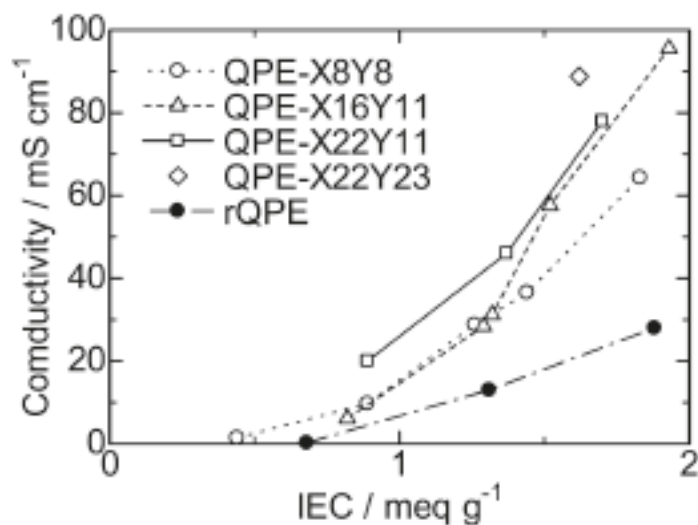


Figure 6.1. Conductivity at 30 °C of block and random QA-functionalized multiblock copoly(arylene ether) AEMs. The block copolymers exhibit higher conductivity than the random copolymers.²³

6.2. Experimental

PS-*b*-PVBC block copolymers were synthesized using reversible addition-fragmentation chain-transfer (RAFT) polymerization, with cumyl dithiobenzoate (CDTB) as the chain transfer agent. The PS-PVBC random copolymers were synthesized by mixing styrene and vinyl benzyl chloride monomers in controlled feed ratios with CDTB. 2,2'-Azobis(2-methylpropionitrile), AIBN, was used as the initiator in both systems. The polymers were dissolved in THF, and trimethylamine was added to convert the benzyl chloride moieties to benzyltrimethylammonium.

The QA PVC-PS polymers were too brittle to form free-standing films. Instead, films were dropcast from solutions, with the mixed solvent system of *n*-propanol and toluene, and left overnight to dry. For morphology characterization, the films were dropcast onto Kapton[®]

substrates, and pieces of these films were then used for water uptake measurements. To measure conductivity, the polymers were dropcast onto electrodes fabricated by Brian Chaloux of the Pennsylvania State University and the US Naval Research Laboratory with the assistance of Holly Ricks-Laskowski of the US Naval Research Laboratory. All dropcast films were allowed to dry overnight in ambient conditions.

Conductivity was measured using AC impedance spectroscopy with a Solartron 1260A Impedance/Gain-Phase Analyzer. The conductivity of free-standing films was obtained using a two-point, in-plane geometry at frequencies between 1 MHz and 100 Hz²⁶ and calculated from equation 1.3. For RH conductivity experiments, the humidity and temperature were controlled using an Espec SH-241 environmental chamber. The temperature was held at 30 °C, and the humidity steps typically used were 20%, 35%, 50%, 75%, and 95%. The real value of the impedance, where the imaginary response was zero, was used as the film resistance. Error in conductivity measurements is believed to be on the order of 1 mS·cm⁻¹.

Small angle x-ray scattering, SAXS, patterns were obtained on a Rigaku (formerly Molecular Metrology) instrument with a pinhole camera with Osmic microfocus source and parallel beam optic. The instrument had a Cu target with a 1.452 Å wavelength and also a multiwire detector. Samples were dried *in vacuo* at ambient conditions before being placed in the SAXS chamber. Spectra of the dried films were collected under vacuum at ambient temperature, and typical collection times were 90-120 minutes, or 1 million photon counts. Scattering intensities were normalized for the Kapton[®] and chamber backgrounds, as well as for the beam transmission.

6.3. Results and Discussion

A range of IEC values were targeted to compare random and block copolymer PVBC-PS based AEMs such that low, mid, and high-IEC copolymers had analogous ion content. However, the molecular weight of the random and diblock copolymers, as determined by SEC and NMR, varied from 15.5-31.4 kg·mol⁻¹ and were not as similar. The structure of the QA-functionalized PVBC-*r*-PS and PVBC-*b*-PS are shown in Figure 6.2. The ratio of the vinyl benzyl chloride to styrene monomers was varied to target the desired IEC values, illustrated in Table 6.1.

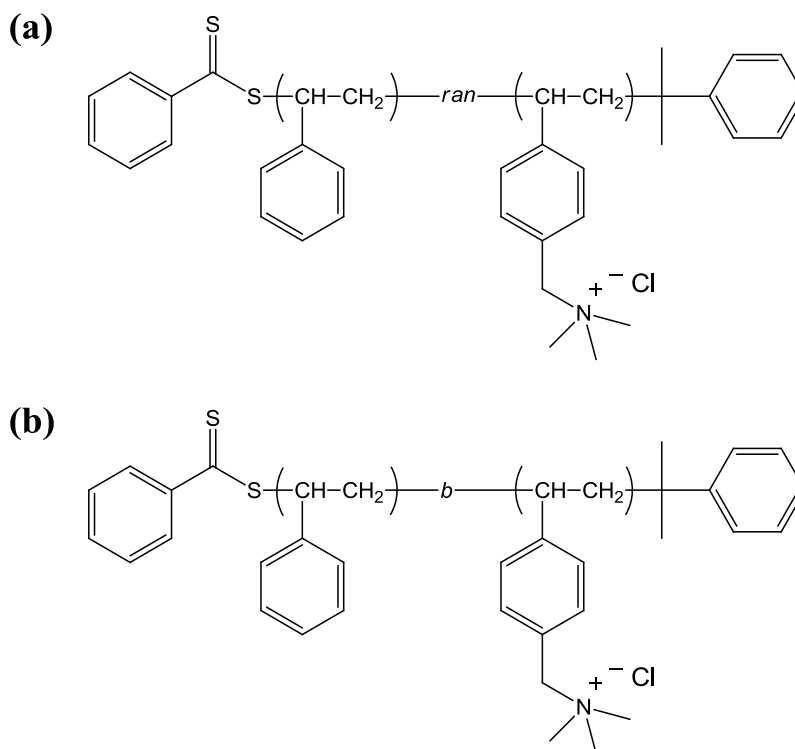


Figure 6.2. Chemical structures of (a) QA PVBC-*ran*-PS, and (b) QA PVBC-*b*-PS.

Table 6.1. Attributes of QA functionalized diblock and random copolymer AEMs

Sample	IEC (meq·g⁻¹)	PS units	QA PVBC units	M_n (g·mol⁻¹)	Solvent system (n-propanol:toluene)
B-1.06	1.06	123	17	15,500	15:85
B-1.41	1.41	130	27	17,600	15:85
B-1.59	1.59	123	31	17,500	15:85
B-1.78	1.78	123	37	18,400	30:70
B-2.09	2.09	123	48	20,100	30:70
R-1.43	1.43	143	31	19,600	30:70
R-1.84	1.84	182	57	27,700	30:70
R-2.05	2.05	193	74	31,400	30:70

B denotes diblock copolymer QA PVBC-*b*-PS in the sample name, and R denotes random copolymer QA PVBC-*ran*-PS. The number in the sample name is the IEC of the polymer.

Both random and copolymer AEM films were too brittle to form free-standing membranes, so films were dropcast from an n-propanol-toluene dual solvent solution onto substrates for water uptake, morphology, and conductivity measurements. The films dried overnight in ambient conditions. The ratio of n-propanol to toluene on a volume:volume basis was either 15:85 or 30:70, as required for polymer dissolution. The low IEC block copolymers required a higher ratio of the less polar toluene. For water uptake measurements, films were scraped from the substrate into the sample pans to prevent the mass of the substrate from interfering with the measurement. The properties are of the AEMs shown in Table 6.2.

Table 6.2. Properties of QA functionalized diblock and random copolymer AEMss

Sample	IEC ($\text{meq}\cdot\text{g}^{-1}$)	wu ^a (%)	λ^a	σ^a ($\text{mS}\cdot\text{cm}^{-1}$)	d-spacing ^b (nm)
B-1.06	1.06	13	7	4.31×10^{-2}	18
B-1.41	1.41	16	6	0.19	22
B-1.59	1.59	33	12	3.21×10^{-2}	28
B-1.78	1.78	27	9	0.82	17
B-2.09	2.09	34	9	0.71	32
R-1.43	1.43	14	6	5.93×10^{-2}	No ordering
R-1.84	1.84	20	6	1.52×10^{-3}	No ordering
R-2.05	2.05	24	7	7.26×10^{-2}	No ordering

B denotes diblock copolymer QA PVBC-*b*-PS in the sample name, and R denotes random copolymer QA PVBC-*ran*-PS. The number in the sample name is the IEC of the polymer.

^a Value for membrane at 95% RH for water uptake (wu), hydration number (λ), and conductivity (σ).

^b Calculated from the SAXS primary scattering peak, q ; $d = 2\pi/q$.

The water uptake of the both the block and random copolymer AEMs were reasonable for low values of IEC, but the water uptake did not increase linearly with IEC for the block copolymer AEMs. Overall, the water uptake of the random copolymers was lower than the water uptake of the block copolymers, and the values for λ followed suit, shown in Figure 6.3. The water uptake of the random copolymers increased linearly with ion content. The water uptake of the block copolymer AEMs almost followed a linear trend with increasing IEC, except for the B-1.59 membrane, which acted as a strong outlier for both wu and conductivity values. For similar IEC values, as IEC increased, the difference in hydration between the two series became more significant.

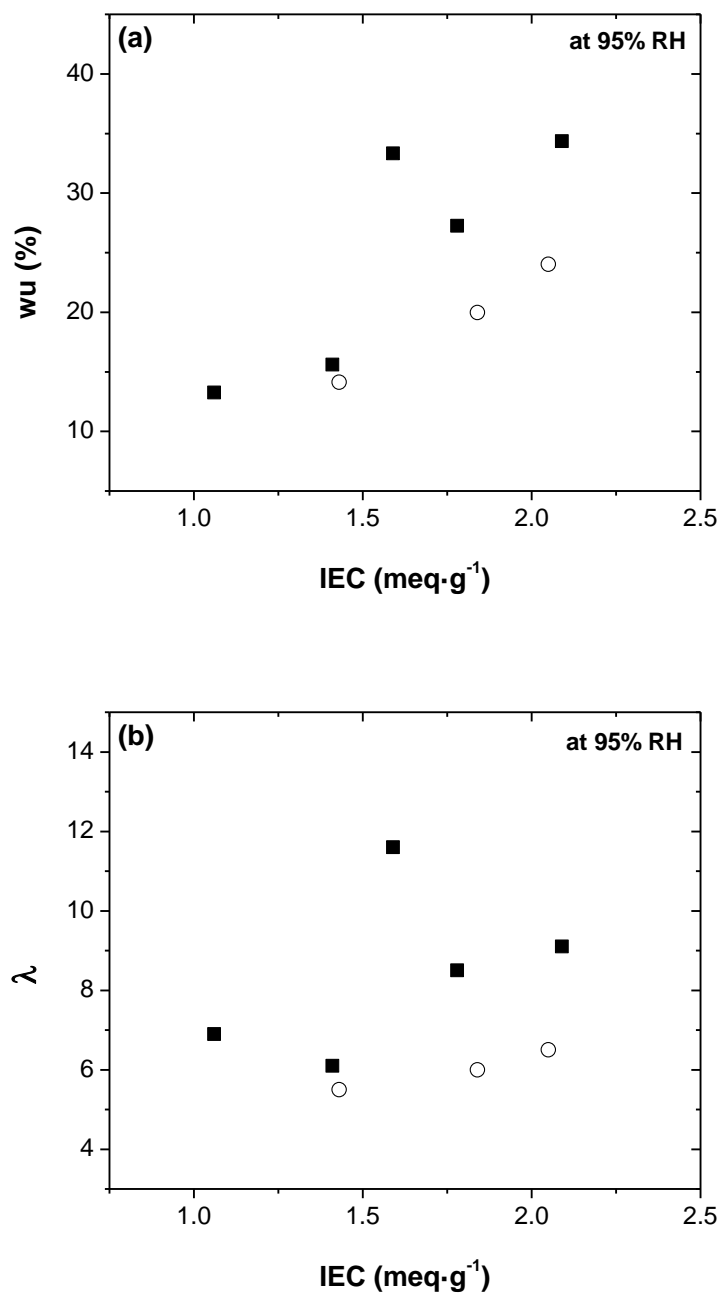


Figure 6.3. For a given IEC, the (■) QA PVBC-*b*-PS copolymers were more hydrated than the (○) QA PVBC-*ran*-PS copolymers at 95% RH, shown by (a) increased water uptake, wu , and (b) increased hydration number, λ , as function of IEC.

Comparing B-1.41 and R-1.43, the w_u was 16% and 14%, and λ values were 6 and 6, respectively, demonstrating only a 15% increase in w_u for the block copolymer AEM. For B-1.78 and R-1.84, these values were 27% and 20% for w_u and 9 and 6 for λ , respectively, which equate to 33% and 50% increases in w_u and λ for the block copolymer AEM. Comparing the highest IEC AEMs, B-2.09 and R-2.05, the values were 34% and 24% for w_u and 9 and 7 for λ , respectively, resulting in 42% and 29% increases in w_u and λ for the block copolymer AEM.

The greater water uptake and hydration values for the block copolymer AEMs should have resulted in higher conductivity values, which appeared to be the case here. However, the conductivity of the random and block copolymers did not increase uniformly with IEC or λ , shown in Figure 6.4. The B-1.78 membrane demonstrated the highest conductivity, $0.81 \text{ mS}\cdot\text{cm}^{-1}$, and the B-2.09 membrane was $0.78 \text{ mS}\cdot\text{cm}^{-1}$. Since there were not clear trends between the conductivity values with either ion content or hydration of the membrane, conclusions cannot be drawn from the conductivity data alone.

The ion diffusion coefficients of the materials as a function of hydration were considered. The measured conductivity values were used to calculate the diffusion coefficients of the mobile chloride ions for each sample using a form of the Nernst-Einstein equation and the number density of charge carriers given by:

$$c = 0.001 \times \frac{\text{IEC} \times \rho}{1 + 0.01 X_{v\text{-H}_2\text{O}}} \quad (6.1)$$

where c is the moles of ion per cm^3 of polymer, IEC is the milliequivalents of ion per gram of polymer, ρ is the polymer density, and $X_{v\text{-H}_2\text{O}}$ is the volume-based water uptake, as opposed to the mass-based water uptake (w_u) presented in Table 3.1.²⁷

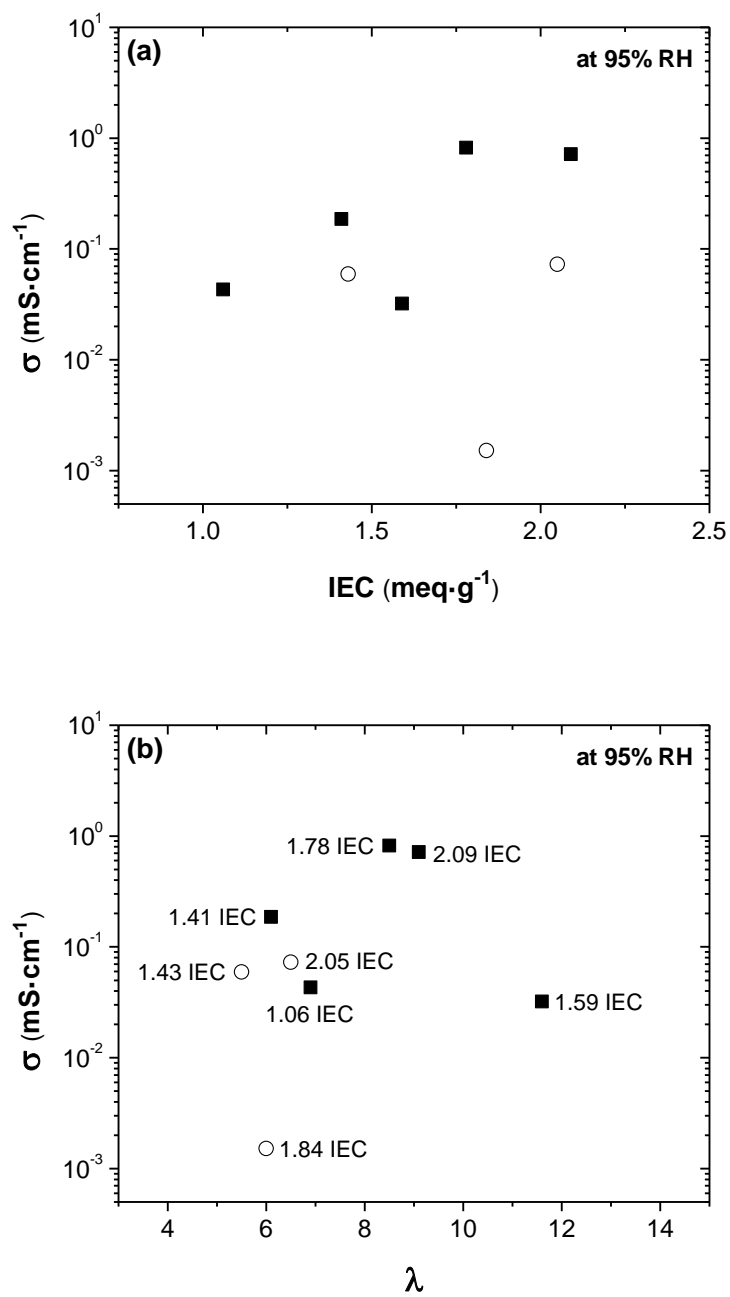


Figure 6.4. The conductivity, σ , of the (■) QA PVBC-*b*-PS and (○) QA PVBC-*ran*-PS copolymers at 95% RH, shown as a function of (a) IEC, and (b) hydration number, λ .

The diffusion coefficients of the mobile chloride ions, shown in Figure 6.5, were calculated from:

$$D = \frac{\sigma RT}{cz^2 F^2} \quad (6.2)$$

where σ is the measured conductivity, R is the ideal gas constant, T is temperature, c is the computed concentration of ions in the hydrated membrane as above, z is valence charge, and F is Faraday's constant.²⁸

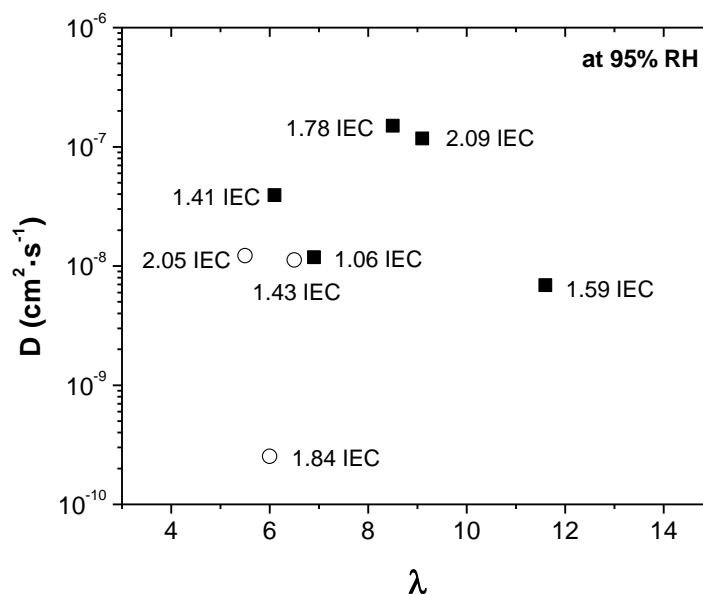


Figure 6.5. Mobile ion diffusivity, D , at 95% RH of the (■) QA PVBC-*b*-PS and (○) QA PVBC-*ran*-PS copolymers.

To understand the relative degree of chloride ion transport in the AEMs, the diffusivity ratio between the Nernst-Einstein calculated diffusivities from conductivity measurements (D)

and the dilute solution diffusivity of the mobile chloride ion (D_0) are shown in Figure 6.6. The dilute solution diffusivities (see Table 6.3) were calculated from the dilute solution mobilities of the mobile ion using:

$$D_0 = \frac{\mu k_B T}{q} \quad (6.3)$$

where μ is the dilute ion mobility, k_B is the Boltzmann constant, T is temperature, and q is the ion charge.²⁹ The diffusivity ratio, D/D_0 , for both block and random copolymer AEMs were well below the ideal value of unity. The polymers were not fully hydrated, accounting for some of the diffusion loss, but the highest D/D_0 values were still two orders of magnitude below unity. This indicates that additional factors prohibited the motion of ions in these systems.

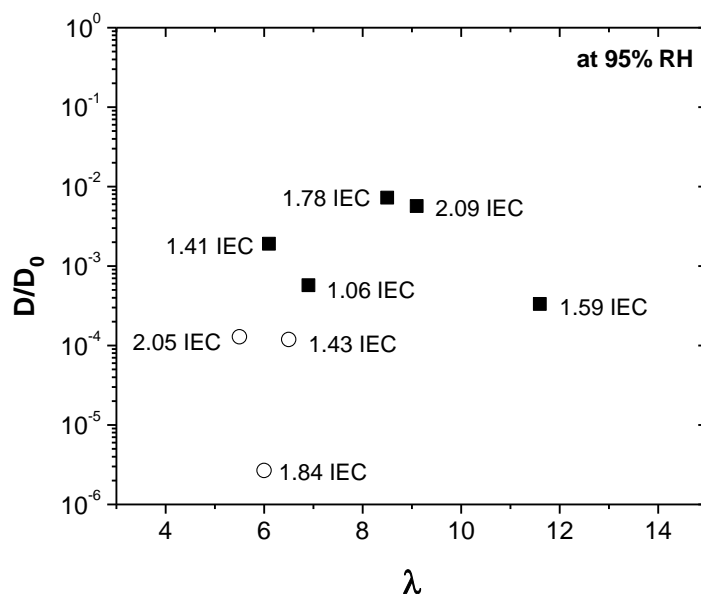


Figure 6.6. The ratio of diffusivity, D , to dilute solution, D_0 , at 95% RH is shown for the (■) QA PVBC-*b*-PS and (○) QA PVBC-*ran*-PS copolymers. Both block and random copolymer AEMs are well below the ideal value of unity for D/D_0 .

Table 6.3. Concentration and Calculated Diffusion Coefficients from Conductivity Measurements and Dilute Solution

Sample	c^a (mol·cm ⁻³)	D^a (cm ² ·s ⁻¹)	D_0 (cm ² ·s ⁻¹)	D^a/D_0
B-1.06	9.86×10^{-4}	1.18×10^{-8}	2.07×10^{-5}	5.72×10^{-4}
B-1.41	1.29×10^{-3}	3.93×10^{-8}	2.07×10^{-5}	1.90×10^{-3}
B-1.59	1.26×10^{-3}	6.89×10^{-9}	2.07×10^{-5}	3.33×10^{-4}
B-1.78	1.48×10^{-3}	1.50×10^{-7}	2.07×10^{-5}	7.25×10^{-3}
B-2.09	1.65×10^{-3}	1.17×10^{-7}	2.07×10^{-5}	5.68×10^{-3}
R-1.43	1.32×10^{-3}	1.22×10^{-8}	2.07×10^{-5}	5.89×10^{-4}
R-1.84	1.62×10^{-3}	2.53×10^{-10}	2.07×10^{-5}	1.22×10^{-5}
R-2.05	1.75×10^{-3}	1.12×10^{-8}	2.07×10^{-5}	5.43×10^{-4}

B denotes diblock copolymer QA PVBC-*b*-PS in the sample name, and R denotes random copolymer QA PVBC-*ran*-PS. The number in the sample name is the IEC of the polymer.

^aValue for membrane at 95% RH.

From the values for conductivity and further examination into ion transport through the use of D/D_0 , it is evident that the QA PVBC-PS block and random copolymer systems do not provide a discrete answer as to the utility of block copolymers in AEMs. The conductivity of the block copolymers was slightly higher, but they did not increase in a logical manner with IEC or with hydration, likely due to morphological differences in the block samples. Although the hydration of the random copolymers increased linearly with water uptake, the trend did not hold for λ or conductivity. The D/D_0 diffusivity ratio indicated that ion transport in these systems is hindered, perhaps due to morphological barriers induced by the co-solvent system or due to the brittle nature of the films. Such low D/D_0 values suggest that perhaps the co-solvent system has led to the formation of non-continuous domains for ion transport. Toluene has a higher vapor

pressure and lower polarity than n-propanol, so it possible that the non-ionic moieties of the polymer chains were constrained during the solvent evaporation and hindered the microphase separation of the PS and PVBC blocks. Additionally, although the wu of the higher IEC polymers seemed adequate, perhaps it did not allow for sufficient solvation of the chloride ions, rendering them immobile. There is also the possibility of counterion condensation in the preparation of thinner films, where the distance between two counterions becomes too small and the free charges adsorb more to the chains than to the water.³⁰ These processes, in conjunction with the possible formation of incomplete networks, could account for the low conductivity and D/D_0 values.

The morphology of the AEMs was of interest as an avenue which might explain the hydration and conductivity properties of the random and block copolymer series. Dropcast QA PVBC-*ran*-PS and QA PVBC-*b*-PS copolymer films were investigated using small angle xray scattering (SAXS), but the overall scattering of the systems was weak. The block copolymer SAXS patterns exhibited primary scattering peaks, but there no ordering was observed from the random copolymer SAXS patterns (Figure 6.7).

The presence of ordering with the block copolymer AEMs may contribute to the slightly increased conductivity of the systems over the random copolymer AEMs, but it is probably a minimal contribution. The ordering in the block copolymers was not strong, indicated by the lack of additional scattering peaks, and there was no relationship between IEC and interdomain spacing of the QA PVBC-*b*-PS films. Additionally, there was no correlation between conductivity and d-spacing; the samples with the highest conductivity values, B-1.78 and B-2.09 exhibited interdomain spacings of 17 and 32 nm, respectively, the smallest and largest interdomain spacings for the system. There did seem to be a slight parallel between large interdomain spacing and increased water uptake. The B-2.09 film with the largest interdomain spacing of 32 nm also

demonstrated the highest water uptake, 34%. The B-1.59 film had next largest interdomain spacing, 28 nm, and the second highest water uptake, 33%. However, the B-1.78 sample had the smallest interdomain spacing, 17 nm, and exhibited the third highest water uptake, 27%, so the relationship is tenuous, at best. The water uptake for the random copolymer films were lower than the block copolymer films, but were covered by the range of the block copolymers, and the random copolymer films showed no ordering. Film morphology variations do not explain the random and block copolymer systems in this study.

By looking more carefully at the block copolymer interdomain spacing, there is one final aspect that can be explored the agreement of the block copolymer systems with theoretical prediction of the d-spacing values. The interdomain spacing in the strongly segregated regime is proportional to the number of repeats units to the two-thirds power, according to the Semenov equation below:

$$D = a \cdot N^{2/3} \chi^{1/6} \quad (6.4)$$

where a is a constant, N is the number of repeat units, and χ is the interaction parameter, calculated from solubility coefficients.³¹

For this study, it was necessary to look at the number of QA PVBC repeat units in the samples, since the number of PS repeat units were either 123 or 130 and the QA PVBC repeat units were ionic. The number of ionic repeat units, $N_{\text{QA PVBC}}$, was raised to the two-thirds power and compared to the interdomain spacing, D , calculated from the SAXS patterns of the block copolymer AEMs, see Figure 6.8. In agreement with the Semenov equation, the relationship between $(N_{\text{QA PVBC}})^{2/3}$ and D was pseudo-linear, with the exception of B-1.78. Interestingly enough, the B-1.78 polymer was the AEM with the highest conductivity.

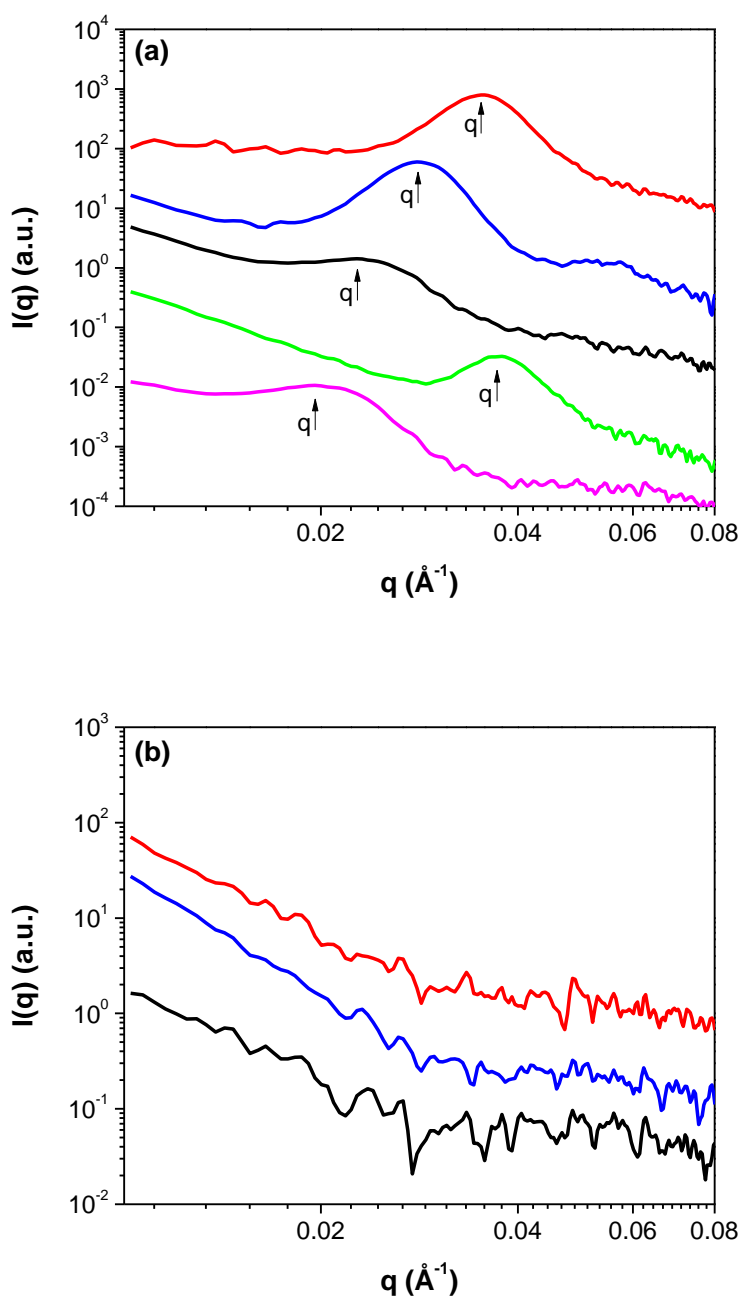


Figure 6.7. Small angle x-ray scattering (SAXS) patterns for (a) QA PVBC-*b*-PS copolymers (—) B-1.06, (—) B-1.41, (—) B-1.59, (—) B-1.78, (—) B-2.09, and (b) QA PVBC-*ran*-PS copolymers (—) R-1.43, (—) R-1.84, and (—) R-2.05. The block copolymers AEMs showed primary scattering peaks, indicated with q^* , while the random copolymer AEMs did not show any ordering.

This relationship could be used to provide valuable information on the interaction parameter between PS and QA PVC since the solubility parameter for QA PVBC is unknown and cannot be accurately calculated from established group contribution values.³² With a large enough sample set and the combination of QA PVC with additional polymers, the group contribution value for a QA group could also be elucidated. This insight would be beneficial to understanding the driving forces behind different AEM morphologies and possibly allow for morphological control of these membranes through polymer design.

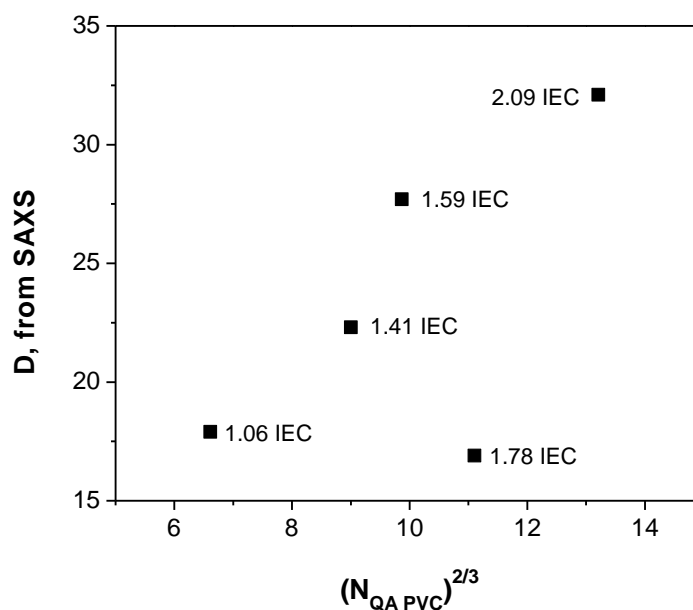


Figure 6.8. Relationship between D, the interdomain spacing calculated from SAXS and $(N_{QA\ PVC})^{2/3}$. The pseudo-linear relationship is in agreement with the Semenov equation, except for the outlier of B-1.78.

6.4. Conclusions

A set of QA PVBC-PS random and block copolymers was designed to establish the effect of block copolymer structure on AEM morphology and performance. The block copolymers demonstrated higher water uptake and hydration numbers, as well as slightly higher conductivity values than the random copolymers, but it was difficult to establish systematic trends for the behavior. In terms of film morphology, the random copolymers showed no order, but had lower water uptake and only mildly lower conductivity values than the block copolymers. The block copolymers showed slightly ordered morphology, but since the SAXS patterns of the block copolymers only had primary scattering peaks, it is doubtful that the ordered morphology significantly contributed to the increased conductivity. Consistent with the Semenov equation, a pseudo-linear relationship between the number of ionic repeat units to the two-thirds power and the interdomain spacing calculated from SAXS was established for four of the five block copolymer AEMs, which could lead to determination of the QA contribution to solubility parameters. However, further research is needed to determine this quantity, as well as to elucidate if using block copolymers is a productive strategy for enhancing AEM performance.

6.5. References

- (1) Hickner, M. A. *Mater. Today* **2010**, *13*, 34–41.
- (2) Couture, G.; Alaaeddine, A.; Boschet, F.; Ameduri, B. *Prog. Polym. Sci.* **2011**, *36*, 1521–1557.
- (3) Yee, R. S. L.; Rozendal, R. A.; Zhang, K.; Ladewig, B. P. *Chem. Eng. Res. Des.* **2012**, *90*, 950–959.
- (4) Merle, G.; Wessling, M.; Nijmeijer, K. *J. Memb. Sci.* **2011**, *377*, 1–35.

- (5) Zhang, H.; Shen, P. K. *Chem. Rev.* **2012**, *112*, 2780–832.
- (6) Zhang, L.; Chae, S.-R.; Hendren, Z.; Park, J.-S.; Wiesner, M. R. *Chem. Eng. J.* **2012**, *204–206*, 87–97.
- (7) Varcoe, J. R.; Slade, R. C. T. *Fuel Cells* **2005**, *5*, 187–200.
- (8) Yan, J.; Hickner, M. A. *Macromolecules* **2010**, *43*, 2349–2356.
- (9) Li, N.; Zhang, Q.; Wang, C.; Lee, Y. M.; Guiver, M. D. *Macromolecules* **2012**, *45*, 2411–2419.
- (10) Chen, D.; Hickner, M. A. *ACS Appl. Mater. Interfaces* **2012**, *4*, 5775–5781.
- (11) Salerno, H. L. S.; Elabd, Y. A. *J. Appl. Polym. Sci.* **2013**, *127*, 298–307.
- (12) Xiong, Y.; Liu, Q. L.; Zeng, Q. H. *J. Power Sources* **2009**, *193*, 541–546.
- (13) Vinodh, R.; Ilakkiya, A.; Elamathi, S.; Sangeetha, D. *Mater. Sci. Eng. B* **2010**, *167*, 43–50.
- (14) Ding, J.; Chuy, C.; Holdcroft, S. *Chem. Mater.* **2001**, *13*, 2231–2233.
- (15) Peckham, T. J.; Holdcroft, S. *Adv. Mater.* **2010**, *22*, 4667–4690.
- (16) Isaacs Sodeye, A. I.; Huang, T.; Gido, S. P.; Mays, J. W. *Polymer (Guildf)*. **2011**, *52*, 3201–3208.
- (17) Rubatat, L.; Shi, Z.; Diat, O.; Holdcroft, S.; Frisken, B. J. *Macromolecules* **2006**, *39*, 720–730.
- (18) Shi, Z.; Holdcroft, S. *Macromolecules* **2005**, *38*, 4193–4201.
- (19) Park, M. J.; Balsara, N. P. *Macromolecules* **2008**, *41*, 3678–3687.
- (20) Elabd, Y. A.; Hickner, M. A. *Macromolecules* **2011**, *44*, 1–11.
- (21) Park, M. J.; Nedoma, A. J.; Geissler, P. L.; Balsara, N. P.; Jackson, A.; Cookson, D. *Macromolecules* **2008**, *41*, 2271–2277.
- (22) Hwang, G.; Ohya, H. *J. Memb. Sci.* **1998**, *140*, 195–203.
- (23) Tanaka, M.; Fukasawa, K.; Nishino, E.; Yamaguchi, S.; Yamada, K.; Tanaka, H.; Bae, B.; Miyatake, K.; Watanabe, M. *J. Am. Chem. Soc.* **2011**, *133*, 10646–54.
- (24) Hwang, G.-J.; Ohya, H. *J. Memb. Sci.* **1998**, *149*, 163–169.

- (25) Bryson, K. C.; Hickner, M. A. Synthesis of novel ion-conducting polymers via reversible addition-fragmentation chain transfer polymerization, Pennsylvania State University, 2010.
- (26) Fujimoto, C. H.; Hickner, M. A.; Cornelius, C. J.; Loy, D. A. *Macromolecules* **2005**, *38*, 5010–5016.
- (27) Kim, Y.; Einsla, B.; Sankir, M.; Harrison, W.; Pivovar, B. *Polymer (Guildf)*. **2006**, *47*, 4026–4035.
- (28) Walls, H. J.; Fedkiw, P. S.; Zawodzinski, T. A.; Khan, S. A. *J. Electrochem. Soc.* **2003**, *150*, E165–E174.
- (29) Muthukumar, M. In *Advances in Chemical Physics*; Rice, S. A., Ed.; 2005; Vol. 131, p. 45.
- (30) Samanta, T.; Mukherjee, M. *Macromolecules* **2011**, *44*, 3935–3941.
- (31) Bates, F. S.; Fredrickson, G. H. *Annu. Rev. Phys. Chem.* **1990**, *41*, 525–57.
- (32) Van Krevelen, D. W.; Te Nijenhuis, K. *Properties of Polymers*; Fourth.; Elsevier: Amsterdam, The Netherlands, 2009.

Chapter 7

Water Uptake and Ion Mobility in Cross-Linked Bis(terpyridine)

Ruthenium-Based Anion Exchange Membranes

7.1. Introduction

To address ever increasing global energy demands, means of alternative energy conversion and storage are needed. New materials are being developed that will drive novel energy technologies, including advanced ion-containing polymers as solid electrolytes for fuel cells and electrolyzers.^{1,2} A fuel cell membrane must demonstrate high ionic conductivity, good thermal and hydrolytic stability, low fuel crossover, adequate water uptake to facilitate ion conductivity with minimal swelling, low cost, and easy incorporation into membrane electrode assemblies.^{3,4} The most popular type of ion-conducting membrane is a proton conducting membrane (PEM) that bears strongly acidic groups to promote water sorption and donate excess protons to solution which facilitate high proton transport rates through the material. PEM fuel cell and electrolyzer technology requires precious metal catalysts, such as platinum, for high cell performance and catalyst stability in the low pH environment of the acidic membrane. Anion exchange membranes (AEMs) with high internal pH can be constructed largely with non-precious metal catalysts, but the polymer membrane must remain stable under alkaline conditions and have high anion conductivity, both of which are current challenges of polymer materials.^{1-3,5}

This chapter is adapted from (1) Zha, Y.; Disabb-Miller, M. L.; Johnson, Z. D.; Hickner, M. A.; Tew, G. N.. *Journal of the American Chemical Society* **2012**, *134*, 4493–4496, and (2) Disabb-Miller, M.L., Zha, Y., Pawar, M., DeCarlo, A., Tew, G.N., Hickner, M.A., in revision.

Benzyltrimethylammonium (BTMA) and alkyltrimethylammonium cations have been employed in AEMs with poly(arylene ether sulfone),^{6,7} poly(fluorenyl ether ketone sulfone),⁸ poly(phenylene oxide),⁷ poly(tetrafluoroethylene),⁹ poly(styrene-*b*-ethylene-*co*-butylene-*b*-styrene),¹⁰ and poly(ether ketone) backbones.¹¹ Of interest in this effort are a membrane's ion exchange capacity (IEC), conductivity (σ), water uptake (wu), and hydration number (λ), the number of water molecules per (mobile) ion. Values for some polymers of interest are shown in Table 7.1. Examples of AEMs include the work by Guiver and coworkers on BTMA poly(arylene ether sulfone) membranes with an IEC of 1.82 meq·g⁻¹, hydroxide conductivity at 20 °C of 35 mS·cm⁻¹, and λ of 12.3; and on BTMA poly(phenylene oxide) membranes with an IEC of 1.39 meq·g⁻¹, hydroxide conductivity at 20 °C of 4 mS·cm⁻¹, and λ of 10.4.⁷ Another series of BTMA poly(arylene ether sulfone) membranes was studied by Yan and Hickner, with IEC ranges of 1.48-2.37 meq·g⁻¹, bicarbonate conductivity at 30 °C ranging from 6.48-27.3 mS·cm⁻¹, and λ of 15-44.⁶ Instead of using a poly(arylene ether sulfone) aromatic backbone, Xiong, et al. synthesized a BTMA poly(ether ketone) with an IEC 0.11 meq·g⁻¹, hydroxide conductivity of 5.06 mS·cm⁻¹, and λ of 16.8.¹¹ In addition to aromatic backbones, polymers with poly(styrene-*b*-ethylene-*co*-butylene-*b*-styrene)¹⁰ have been used for AEMs; the benzyltriethylammonium poly(styrene-*b*-ethylene-*co*-butylene-*b*-styrene) membrane had an IEC of 0.578 meq·g⁻¹, hydroxide conductivity of 0.69 mS·cm⁻¹, and λ of 5.5.¹⁰ These reports have set the landscape for the possible range of properties of AEMs, but more analysis of the effectiveness of ion conductivity in these examples is warranted.

The decoration of aromatic polymers with BTMA cations is synthetically convenient through chloromethylation of aromatic rings, bromination of benzylic groups, or other halomethylation reactions. However BTMA, and especially tetraalkylammonium moieties, have well-known degradation mechanisms at high pH that may limit their ultimate stability in AEM applications.^{5,12-14} Beyond alkyltrimethylammonium cations, different types of organic cations are

being investigated as the fixed charge moiety in AEMs to provide enhanced anion conductivity and stability in these types of polymeric materials. Phosphonium, sulfonium, and imidazolium-functionalized AEMs will be discussed in the following section. Yan and co-workers have been developing tris(2,4,6-trimethoxyphenyl) benzyl quaternary phosphonium poly(sulfone-methylene) anion exchange membranes with reported hydroxide conductivities of 11, 27, 45, and 38 $\text{mS}\cdot\text{cm}^{-1}$ at 20 °C, depending on the water uptake of the membrane.^{15,16} From the reported water uptake values for these materials, we calculated the corresponding λ values to be approximately 24, 33, 53, and 264. Yan and co-workers have also described AEMs consisting of a Udel[®] poly(sulfone) backbone functionalized with triaryl sulfonium groups. The hydroxide conductivity of the sulfonium-containing poly(sulfone) with an IEC of 0.68 $\text{mmol}\cdot\text{g}^{-1}$ was 7.7 $\text{mS}\cdot\text{cm}^{-1}$ at 20 °C (λ or water uptake were not reported). However, the hydroxide conductivity of a similar IEC sample (0.69 $\text{mmol}\cdot\text{g}^{-1}$) more than doubled to 15.4 $\text{mS}\cdot\text{cm}^{-1}$ at 20 °C for a calculated λ of 22 when the poly(sulfone) was functionalized with diphenyl(3-methyl-4-methoxyphenyl) tertiary sulfonium cations.¹⁷

Although imidazolium-functionalized AEMs have been investigated as a more stable alternative to AEMs with BTMA, they have not demonstrated enhanced conductivity over BTMA-based AEMs. A 1-methyl benzylimidazolium-functionalized poly(fluorenyl ether ketone sulfone) membrane with an IEC of 1.64 $\text{meq}\cdot\text{g}^{-1}$ demonstrated bicarbonate conductivity of 3.9 and hydroxide conductivity of 17.1 $\text{mS}\cdot\text{cm}^{-1}$ for λ values of 9.9 and 14.8, respectively. In the same study, this membrane was directly compared to a BTMA-functionalized poly(fluorenyl ether ketone sulfone), which exhibited higher conductivity and water uptake with bicarbonate conductivity of 5.1 $\text{mS}\cdot\text{cm}^{-1}$ and hydroxide conductivity of 22.3 $\text{mS}\cdot\text{cm}^{-1}$ for λ values of 11.1 and 18.2, respectively.⁸ This report demonstrated the usefulness of BTMA cations compared to N-linked 1-methyl imidazolium cations generated from simple synthetic methods. 1,2-dimethyl-3-alkylimidazolium functional groups were also used by Lin, et al. in conjunction with

poly(fluorene) to produce an AEM with an IEC of $0.98 \text{ meq}\cdot\text{g}^{-1}$. The hydroxide conductivity was $23.5 \text{ mS}\cdot\text{cm}^{-1}$ at 30°C , with a calculated λ of 10, which was about twice as much as the bicarbonate conductivity of the same membrane. The conductivity was comparable to that of a similar BTMA-functionalized polymer.¹⁸

In addition to considering different ionic groups for AEM functionalization, another strategy for achieving next-generation AEMs is to cross-link polymers to minimize membrane swelling, even at high IEC. Pan, et al. observed only 3% swelling at 80°C for their BTMA poly(sulfone) polymers that were cross-linked by exposing the chloromethylated polymer to stoichiometric quantities of diethylamine, producing tertiary benzyldiethylamino groups on the polymer backbone. The residual benzylchloride moieties were then further reacted with trimethylamine, resulting in a poly(sulfone) with both tertiary amino groups and BTMA groups. Subsequently, any remaining chloromethyl groups reacted with the tertiary amino groups on the polymer backbone to form cross-links during the membrane casting process.¹⁹ Self-cross-linking quaternary phosphonium tris(2,4,6-trimethoxyphenyl) poly(sulfone-methylene) membranes resulting from the reaction of benzylchloromethyl groups and trimethoxyl benzene rings possessed 5-10 times lower swelling ratio than non-cross-linked membranes with the same IEC.²⁰ The cross-linking was performed at 80°C without a catalyst, allowing for a one-pot process. For quaternary phosphonium functionalized membranes with IEC values of approximately 1.0, 1.17, and $1.23 \text{ meq}\cdot\text{g}^{-1}$ at 60°C , the cross-linked membranes had calculated λ values of 9 (17 wt% wu), 16 (33 wt% wu), and 45 (99 wt% wu), respectively, while the non-cross-linked membranes had much higher calculated λ values of 40 (71 wt% wu), 120 (254 wt% wu), and 1114 (2469 wt% wu), respectively. The hydroxide conductivity was $38 \text{ mS}\cdot\text{cm}^{-1}$ at 20°C for the $1.23 \text{ meq}\cdot\text{g}^{-1}$ cross-linked membrane ($\lambda = 45$), which was consistent with the conductivity of the non-cross-linked membrane in both quaternary phosphonium and BTMA forms.²⁰

Another method of producing cross-linked AEMs was developed by Coates and co-workers, who employed ring-opening metathesis polymerization (ROMP) of a tetraalkylammonium-functionalized norbornene with dicyclopentadiene (DCPD). The resulting cross-linked fully hydrated membrane (λ or water uptake were not reported) demonstrated hydroxide conductivities at 20 °C of 14 and 18 $\text{mS}\cdot\text{cm}^{-1}$ for samples with 2:1 DCPD:monomer (1.0 $\text{meq}\cdot\text{g}^{-1}$ IEC) and 1:1 DCPD:monomer (1.4 $\text{meq}\cdot\text{g}^{-1}$ IEC) ratios, respectively.²¹ Also synthesized using ROMP, a phosphonium-functionalized poly(ethylene) with an IEC of 0.67 $\text{meq}\cdot\text{g}^{-1}$ was found to have hydroxide conductivity of 22 $\text{mS}\cdot\text{cm}^{-1}$ and λ of 43.²² At this point, the key strategies for improved AEM performance are unclear, but by studying the relationships between fixed ion concentration, water diffusion, morphology, and ion conductivity, promising directions in the field can be identified.

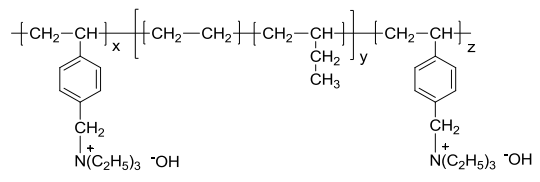
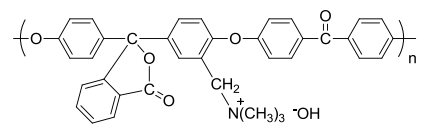
Recently, we introduced bis(terpyridine) Ru (II)-based AEMs, which were the first metal-cation containing AEMs, using the ROMP technique with DCPD cross-linking moieties described above. The use of the metal Ru (II) complex was designed for increased AEM conductivity by allowing for two counterions to be involved in ion transport, instead of the single counterion typically associated tethered cations such as BTMA. The conductivity and hydration values of these membranes were highly dependent on the degree of cross-linking present in the membranes. The hydroxide conductivity at 30 °C ranged from 14-28 $\text{mS}\cdot\text{cm}^{-1}$, for membranes with IEC values of 1.0-2.0 $\text{meq}\cdot\text{g}^{-1}$ and λ values of 30-216, depending on the DCPD:heteroleptic bis(terpyridine) Ru (II) complex ratio in the membrane.²³ These membranes, BTP-R1, were synthesized by Yongping Zha and Professor Gregory Tew of the University of Massachusetts Amherst, and their behavior will be discussed briefly.

A second iteration of these materials, BTP-R2, has been synthesized by Zha and Tew with the addition of cyclooctadiene (COD). The goal of this work is to report optimized compositions and properties for bis(terpyridine) Ru (II)-based AEMs and compare their intrinsic

ion conduction performance to more commonly explored BTMA-based AEMs. Two sets of membranes will be discussed: the first iteration of these membranes, BTP-R1, and the second iteration of these membranes, BTP-R2.

Table 7.1. Chemical structure, conductivity, and hydration number of several BTMA-containing polymers used as AEMs.

Chemical Structure	IEC (meq·g ⁻¹)	σ (mS·cm ⁻¹)	λ	Ref.
<p>PAES HCO₃⁻</p> <p>R=H or N⁺(CH₃)₃ HCO₃⁻</p>	1.48-2.37	6.48-27.3	15-44	Yan and Hickner ⁶
<p>PAES ⁻OH</p> <p>R=H or N⁺(CH₃)₃ ⁻OH</p>	1.82	35	12.3	Li, et al. ⁷
<p>PPO ⁻OH</p> <p>R=H or N⁺(CH₃)₃ ⁻OH</p>	1.39	4	10.4	Li, et al. ⁷
<p>PPO</p> <p>R=H or N⁺(CH₃)₃ ⁻OH or HCO₃⁻</p>	1.8	22.3 OH ⁻ 5.1 HCO ₃ ⁻	18.2 OH ⁻ 11.1 HCO ₃ ⁻	Chen and Hickner ⁸

<p style="text-align: center;">PSEBS ⁻OH</p> 	0.578	0.69	5.5	Vinodh, et al. ¹⁰
<p style="text-align: center;">Poly(etherketone) ⁻OH</p> 	0.11	5.06	16.8	Xiong, et al. ¹¹

7.2. Experimental Methods

7.2.1 Polymer Synthesis and Membrane Preparation

The first heteroleptic bis(terpyridine) Ru (II) complex-functionalized norbornene monomer was synthesized by Yongping Zha and Professor Gregory Tew of the University of Massachusetts Amherst.²³ This previous membrane will be discussed as BTP-R1 and discussed briefly. In order to maintain the same cross-linking density while varying the IEC, a hydrophobic comonomer, 1,5-cyclooctadiene (COD), was introduced to the system in the second iteration of membranes synthesized by Zha, and Tew. COD is inexpensive and highly soluble in the same solvent mixture as the other two components. Its complete polymerization by Grubbs' second generation catalyst (G2) only takes about 10 min at room temperature.²⁴ The Ru (II) complex cationic monomer, COD, and DCPD were dissolved together in a chloroform/methanol solvent mixture at room temperature. After adding G2 and stirring vigorously for 1 min, the homogeneous solution was transferred to a flat, pre-heated aluminum pan where the

polymerization continued at 40 °C for ~1 h. A translucent, ~100-μm-thick membrane was obtained following solvent evaporation. Subsequent ion exchange in sodium bicarbonate solution yielded the final AEM sample in the bicarbonate form. These membranes were studied extensively and will be referred to as BTP-R2.

7.2.2 Characterization

Conductivity measurements were performed using impedance spectroscopy on a Solartron 1260A Impedance/Gain-Phase Analyzer. The impedance of free-standing films was measured using a two-point, in-plane geometry at frequencies between 1 MHz and 100 Hz.²⁵ During the measurements, humidity and temperature were controlled with an ESPEC SH-241 environmental chamber. The relative humidity (RH) was controlled from 20% to 95% while the temperature was held at 30 °C. The real value of the impedance, where the imaginary response was zero, was used as the membrane resistance and the ion conductivity (σ) was calculated from:

$$\sigma = \frac{L}{R \cdot A} \quad (7.1)$$

where L is the length between electrodes, R is the resistance of the membrane, and A is the cross-sectional area of the membrane. Error in conductivity measurements is believed to be on the order of 1 mS·cm⁻¹.

The activation energy for ion conduction, E_a , was calculated from conductivity measurements with the sample immersed in liquid water between 30 °C and 70 °C (in 10 °C steps). The logarithm of conductivity versus 1/T was linearly regressed, and the Arrhenius activation energy was computed from the slope of the best fit regression line.

Bicarbonate conductivities were measured by exchanging the chloride form membranes in 1 M sodium bicarbonate at room temperature for 24 h followed by extensive rinsing to remove excess salt. Hydroxide conductivities were measured by exchanging the bicarbonate form membranes in 1 M KOH solution for 8-12 h. The membranes were then rinsed with degassed, $18.2\text{ M}\Omega\cdot\text{cm}$ water to remove excess ions and placed into conductivity cells and immersed in liquid water that was degassed and blanketed with flowing Ar, as shown in Figure 7.1. The conductivity was measured over a period of 3 h under Ar and then the Ar blanket was removed and the conductivity was measured over a number of days with the water exposed to ambient conditions containing the natural amount of CO_2 , $\sim 395\text{ ppm}$.

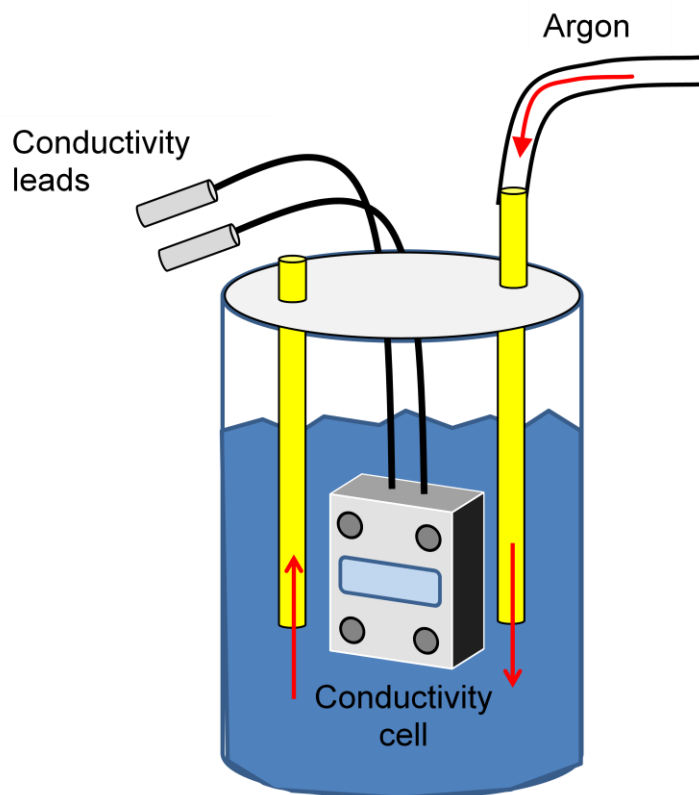


Figure 7.1. Schematic of the argon-purged conductivity setup. Argon is bubbled through water before and during the conductivity measurement.

Water uptake ($wu = (m_{\text{hyd}} - m_0)/m_0$) where m_{hyd} is the hydrated sample mass and m_0 is the dry sample mass, was measured as a function of relative humidity using a TA Instruments Q5000SA water vapor sorption microbalance at 30 °C between relative humidities of 20% and 95%. The hydration number (λ), or the number of water molecules per ionic group, was calculated from:

$$\lambda = \left(\frac{m_{\text{hyd}} - m_0}{m_0} \right) \cdot \left(\frac{1000}{M_{\text{H}_2\text{O}} \cdot \text{IEC}} \right) \quad (7.2)$$

where m_{hyd} is the hydrated sample mass, m_0 is the mass of the dry sample, $M_{\text{H}_2\text{O}}$ is the molecular mass of water (18.02 g·mol⁻¹), and IEC is the ion exchange capacity with units of milliequivalents of ions per gram of polymer.

For liquid water uptake measurements, the fully hydrated anion exchange membranes were removed from liquid water, blotted quickly to remove surface water, and weighed immediately. The measurement was repeated 3-5 times after soaking the membrane in liquid water to rehydrate the membrane and obtain an accurate hydrated sample mass. The membranes were then dried at 80 °C in vacuum for 48 h and at 120 °C in vacuum for 48 h (96 h total) and weighed again to obtain m_0 .

7.3. Results and Discussion of BTP-R1

The chemical structure of the materials used to synthesize the first iteration of the bis(terpyridine) ruthenium-based membranes, BTP-R1, is shown in Figure 7.2.

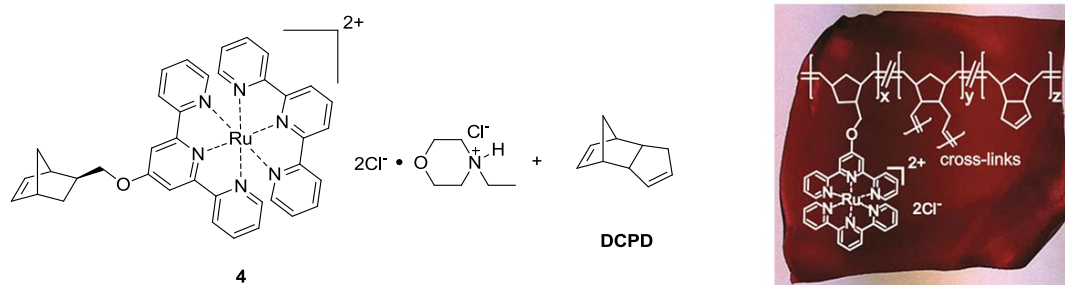


Figure 7.2. First iteration of monomers polymerized by Grubbs' second generation catalyst into resulting chemical structure overlayed on optical image of a membrane, BTP-R1.

As shown in Table 7.2, the molar ratio of bis(terpyridine) ruthenium monomer (M) to DCPD was changed from 1:2 to 1:10 to investigate the impact of increasing the hydrophobic content and cross-linking density on membrane properties. As expected, increasing the DCPD content reduced the theoretical ion exchange capacity (IEC), calculated from the chemical composition of the membrane, resulting in a decrease in the water uptake. On the other hand, the activation energy for ion conduction (E_a) increased (from 14 to 22 kJ·mol⁻¹) with decreasing water uptake which was coupled with a decrease in ionic conductivity from 9.8 to 5.6 mS·cm⁻¹ as a result of lower IEC and water uptake.

Table 7.2. BTP-R1 membrane properties with various M:DCPD ratios

Measurement	M : DCPD		
	1:2	1:5	1:10
theoretical IEC (mequiv·g ⁻¹) ^a	2.0	1.4	1.0
liquid water uptake (wt %) ^b	432	126	30
E_a (kJ·mol ⁻¹) ^c	14	16	22
$\sigma_{30\text{ }^\circ\text{C}}$ (mS·cm ⁻¹) ^d	19.6	28.6	14.1

^aIon exchange capacity calculated based on chemical structures. ^bLiquid water uptake = [(Masswet - Massdry) / Massdry] * 100%. ^cActivation energy for ion conduction. ^dHydroxide ionic conductivity at 30 °C.

The humidity dependence of water uptake and ionic conductivity was also studied. As shown in Figure 7.3, both water uptake and ionic conductivity increased with increasing humidity (in the range of 22 - 95% relative humidity), which is in agreement with results for other reported membranes.^{25,26}

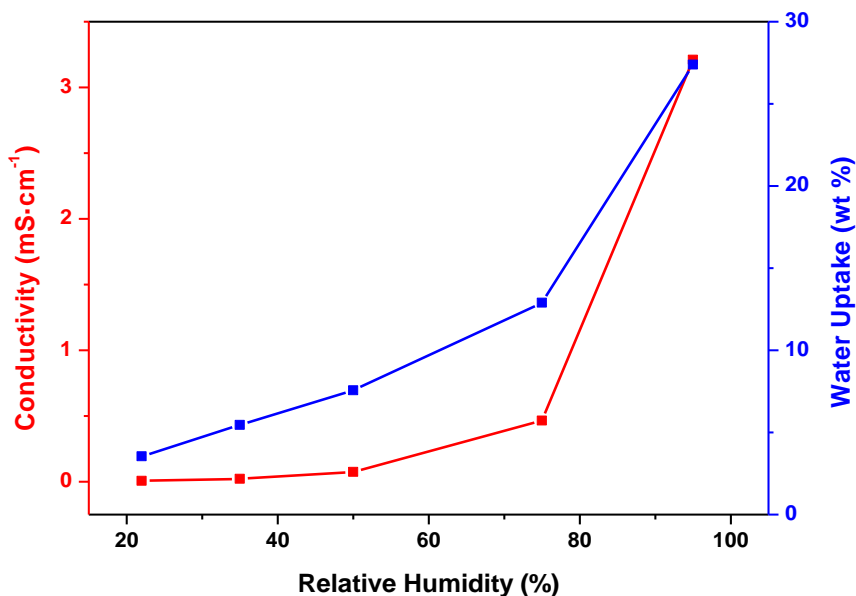


Figure 7.3. Humidity dependence of conductivity and water uptake for the AEM with monomer:DCPD = 1:2.

Bicarbonate conductivities were measured by exchanging the chloride form membranes with sodium bicarbonate followed by extensive rinsing to remove the excess salt. Hydroxide conductivities were measured by exchanging the bicarbonate form membranes in 1 M KOH solution for 1 h. After this ion exchange process, the membranes were kept in as close to carbon dioxide-free conditions as possible. Hickner and coworkers have confirmed conversion of AEMs from the hydroxide to the bicarbonate form, causing a corresponding decrease in ionic conductivity due to the lower dilute solution mobility of bicarbonate ions.⁶

The membranes were then rinsed with degassed, 18.2 MΩ water to remove excess ions and placed into conductivity cells and immersed in liquid water that was degassed and blanketed

with flowing Ar. The conductivity was measured over a period of 3 h under Ar, and then the Ar blanket was removed and the conductivity was measured over a number of days with the water exposed to atmospheric CO₂ as shown in Figure 7.4.

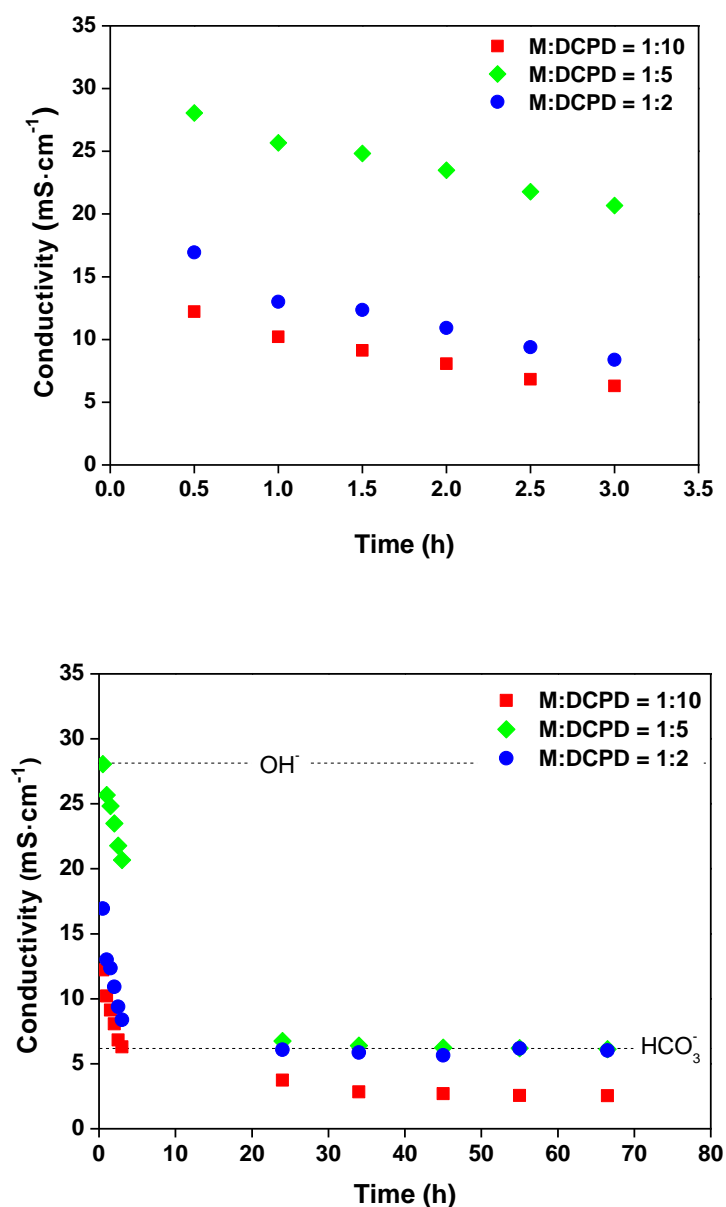


Figure 7.4. Decline in conductivity of the hydroxide form AEMs during conductivity measurements; (top) kept under Ar blanket for up to 3 h, (bottom) left open to atmosphere after 3 h. Conductivities were measured with samples exposed to liquid water at 30 °C.

It is difficult to measure the conductivity of samples in hydroxide form, as revealed by the involved testing procedure described early. In addition to maintaining a CO₂-free environment, multiple ion exchanges can lead to incomplete ion conversion. The mobilities of chloride and bicarbonate ions are lower than the mobility of hydroxide ions,²⁷ so incomplete ion exchange would result in lowered conductivity compared to the conductivity of membranes purely in hydroxide form. This behavior was observed in our study, as shown in Figure 7.5.

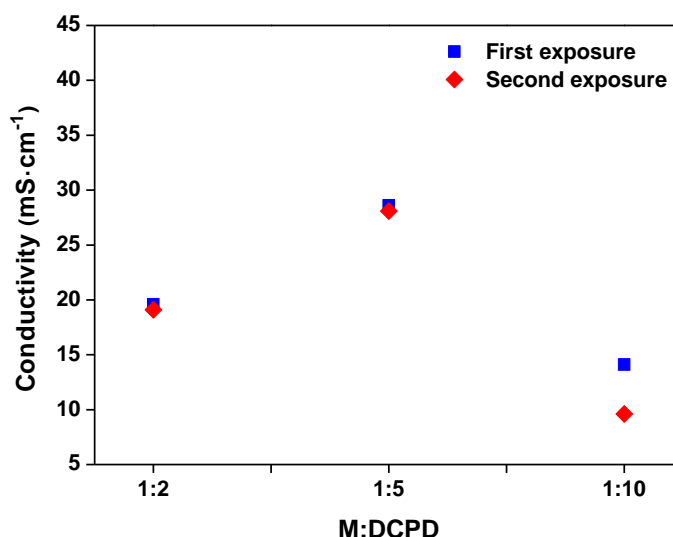


Figure 7.5. Change in hydroxide conductivity upon exposure of the samples to 1 M KOH for 2 h. Conductivities were measured with samples exposed to liquid water at 30 °C.

Temperature is known to have an impact on the conductivity of quaternary ammonium-based AEMs, these Ru complex-based AEMs show similar behavior. As shown in Figure 7.6 (a), the conductivity of all three membranes increased linearly with temperature. The AEMs with M:DCPD = 1:2 and 1:5 possessed similar conductivities over the entire temperature range investigated, while the conductivity of the AEM with M:DCPD = 1:10 was lower. This is most likely due to its high DCPD loading.

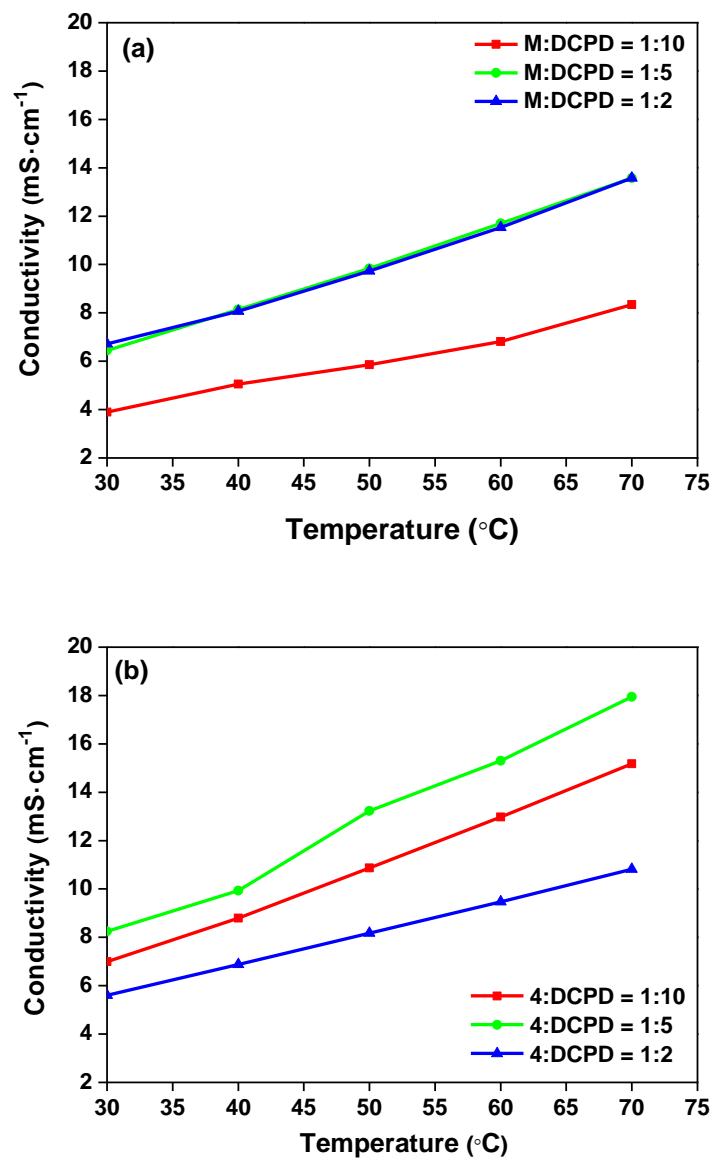


Figure 7.6. Impact of temperature on conductivity for the membranes (a) in the HCO₃⁻ form and (b) in the Cl⁻ form.

At 50 °C, the conductivities of the AEMs with M:DCPD = 1:2 and 1:5 were both around $9.8 \text{ mS}\cdot\text{cm}^{-1}$, which is comparable to the values reported for quaternary ammonium AEMs in the bicarbonate form ($10.1 - 25.7 \text{ mS}\cdot\text{cm}^{-1}$).^{6,28} When factoring in the dilute solution mobility of the ions (0.61 for HCO_3^- and 2.3 for OH^- relative to a mobility of 1 for K^+), the hydroxide conductivity of the membranes was estimated by multiplying their bicarbonate conductivity by 3.8,⁶ giving $37 \text{ mS}\cdot\text{cm}^{-1}$ at 50 °C. For comparison, cross-linked AEMs with a quaternary ammonium monomer and DCPD, reported by Coates and coworkers, exhibited a hydroxide conductivity of $28 \text{ mS}\cdot\text{cm}^{-1}$ at 50 °C,²¹ and the quaternary phosphonium AEM reported by Yan and coworkers had a hydroxide conductivity of $27 \text{ mS}\cdot\text{cm}^{-1}$ at 20 °C.¹⁵ Figure 7.6 (b) shows the temperature dependent conductivity of the membranes in the Cl^- form. While the conductivity of the AEMs in the Cl^- form with M:DCPD = 1:5 and 1:10 increased compared to the membranes in the HCO_3^- form, there was little change in the conductivity of the membrane with the lowest DCPD content. This indicates that as the water uptake decreases, ion mobility plays a greater role in conductivity, as Cl^- ions have higher dilute solution mobility than HCO_3^- ions.

The difference in conductivity at 30 °C between the membranes in the HCO_3^- form and in the Cl^- form as a function of water uptake is shown in Figure 7.7. The AEM with M:DCPD = 1:2, which had the highest water uptake of the three, had a slightly higher conductivity in the HCO_3^- form than in the Cl^- form, with a difference of $0.29 \text{ mS}\cdot\text{cm}^{-1}$. Meanwhile, at the same temperature, the AEMs with M:DCPD = 1:5 and 1:10 had higher conductivities in the Cl^- form, with differences of $1.8 \text{ mS}\cdot\text{cm}^{-1}$ and $3.1 \text{ mS}\cdot\text{cm}^{-1}$, respectively, indicating that water content specifically influences the ion mobility of different species.

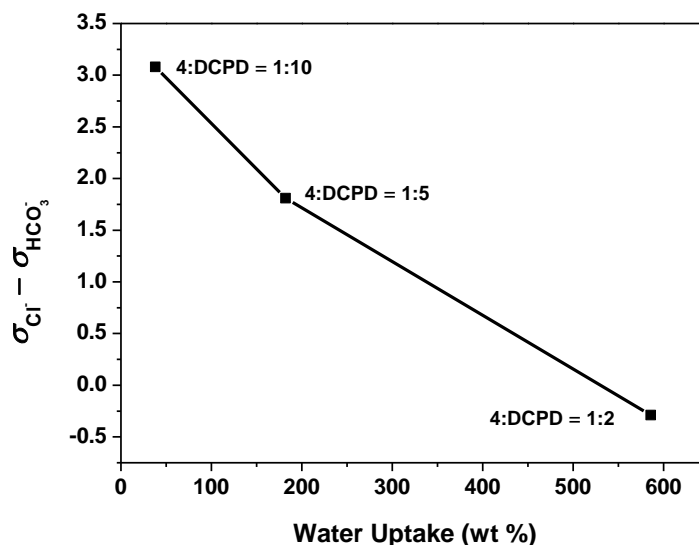


Figure 7.7. The difference in conductivity at 30 °C between membranes in the Cl⁻ form and in the HCO₃⁻ form as a function of water uptake.

7.4. Results and Discussion of BTP-R2

The synthesis scheme for the second iteration of heteroleptic bis(terpyridine) Ru (II) complex-based AEMs with COD and DCPD cross-linking, BTP-R2, is shown in Figure 7.8. Briefly, the bis(terpyridine) Ru (II) complex monomer (M) was combined with COD and DCPD at room temperature to form the BTP-R2 membranes. The ratio of M to COD determined the IEC of the membranes. As in our previous work, the Ru monomer was isolated as a co-salt²³ and extensive soaking after formation of the membrane was used to remove the *N*-ethylmorpholinium chloride from the cross-linked membranes. Compared to the AEMs consisting of only the Ru monomer and DCPD,²³ BTP-R1, addition of COD into the system did not seem to have any significant impact on the alkaline stability of the membranes. The water uptake, conductivity at 30 °C, and activation energy of the membranes studied are listed in Table 7.3.

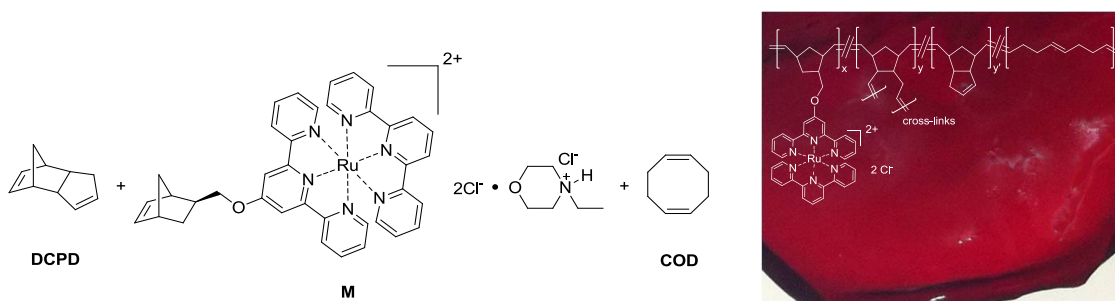


Figure 7.8. Monomers polymerized by Grubbs' second generation catalyst into resulting chemical structure overlaid on optical image of a membrane, BTP-R2.

Table 7.3. BTP-R2 membrane sample parameters and properties

[DCPD]: [M+COD]	1:1	1:1	2:1	2:1	2:1	2:1	5:1
[M]:[COD]	3:7	4:6	3:7	5:5	6:4	8:2	6:4
IEC (meq·g ⁻¹)	1.4	1.6	1.0	1.4	1.6	1.8	1.0
wu _{Cl-} (mass %)	197	417	38	103	148	246	24
λ _{Cl-}	78	145	21	41	51	85	13
σ _{Cl-} (mS·cm ⁻¹)	5.3	3.5	6.1	5.9	7.9	6.8	3.6
wu _{HCO₃⁻} (mass %)	398	461	117	133	260	358	39
λ _{HCO₃⁻}	158	160	65	53	90	124	21
σ _{HCO₃⁻} (mS·cm ⁻¹)	3.5	4.7	3.0	5.5	2.7	6.5	2.4
σ _{OH-} (mS·cm ⁻¹)	8.9	nm	10.0	13.0	10.6	15.2	4.0
E _{a,Cl-} (kJ·mol ⁻¹)	6.4	5.5	19.9	5.9	9.9	14.3	15.6
E _{a,HCO₃⁻} (kJ·mol ⁻¹)	11.4	6.8	17.7	13.5	18.3	11.2	25.9

Water uptake (wu), hydration number (λ), conductivity (σ), and activation energy (E_a) are reported for fully hydrated membranes. Measurements that were not obtained are denoted by nm.

Membranes in bicarbonate form demonstrated higher water uptake and hydration numbers than the corresponding membranes in their chloride form. The highest conductivity values were obtained for membranes in hydroxide form, which we partly attribute to the greater dilute solution mobility of hydroxide ions, $197.6 \times 10^{-5} \text{ cm}^2 \cdot \text{V}^{-1} \cdot \text{s}^{-1}$, compared to the dilute solution mobilities of bicarbonate and chloride ions, 46.4×10^{-5} and $76.3 \times 10^{-5} \text{ cm}^2 \cdot \text{V}^{-1} \cdot \text{s}^{-1}$, respectively.²⁷ Although the conductivity measurements are believed to be accurate within $1 \text{ mS} \cdot \text{cm}^{-1}$ or 20 % in many cases, which would provide some overlap of the membrane conductivity values, we believe the overall trends observed are valid.

For the membranes in the chloride form, the maximum conductivity occurred at a λ value of 51, as shown in Figure 7.9. The cross-linking ratio was critical to both conductivity and water uptake, with 2:1 [DCPD]:[M+COD] yielding the highest conductivity sample. For membranes with the same IEC, the 2:1 [DCPD]:[M+COD] membrane demonstrated higher conductivity and lower water uptake compared to the 1:1 [DCPD]:[M+COD] membrane. We believe the membranes in hydroxide form absorbed more water than the other anion forms due to the thermodynamic driving forces involved with hydration. The Gibbs free energy of hydration for hydroxide ions is $-430 \text{ kJ} \cdot \text{mol}^{-1}$, compared to $-335 \text{ kJ} \cdot \text{mol}^{-1}$ for bicarbonate ions and $-340 \text{ kJ} \cdot \text{mol}^{-1}$ for chloride ions.²⁹ When the membranes were converted to bicarbonate form, the $1.8 \text{ meq} \cdot \text{g}^{-1}$ IEC sample had the highest conductivity of $6.5 \text{ mS} \cdot \text{cm}^{-1}$ at $\lambda = 124$. Such high values for hydration number at maximum conductivity are in stark contrast to PEMs of the perfluorosulfonic acid variety, with maximum conductivity at $\lambda = 22$.³⁰

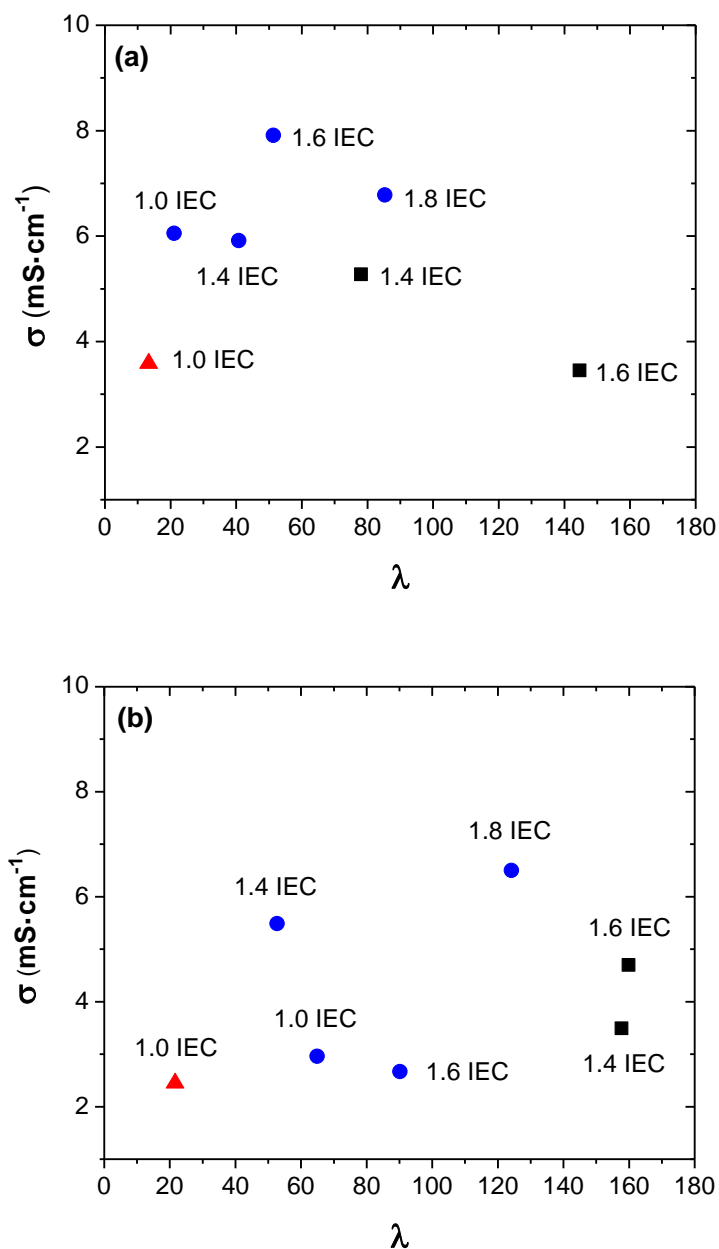


Figure 7.9. Conductivity of membranes as a function of hydration number in the (a) chloride form and (b) bicarbonate form for (■) [DCPD]:[M+COD] = 1:1, (●) [DCPD]:[M+COD] = 2:1, and (▲) [DCPD]:[M+COD] = 5:1. The maximum conductivity occurred at a hydration number of approximately 50 and 125 for membranes in chloride form and bicarbonate form, respectively.

To further study the effect of cross-linking on water uptake and conductivity of the Ru-based AEMs, we calculated the ion concentration for the membranes from the volume-based water uptake using:

$$c = 0.001 \cdot \frac{\rho \cdot \text{IEC}}{1 + 0.01 X_{v-\text{H}_2\text{O}}} \quad (7.3)$$

where c is the moles of ions per cm^3 of polymer, ρ is the polymer density, IEC is the milliequivalents of ion per gram polymer, and $X_{v-\text{H}_2\text{O}}$ is the volume-based water uptake.³¹

As illustrated by Figure 7.10, the membranes with the highest conductivity in the chloride form had between approximately 5×10^{-4} and 7.5×10^{-4} moles of Cl^- per cm^3 of polymer. The maximum conductivity was observed for the sample with $6.5 \times 10^{-4} \text{ mol} \cdot \text{cm}^{-3}$, and there was clear separation between the conductivity values of the samples with a [DCPD]:[M+COD] ratio of 2:1 and those with different cross-linker ratios.

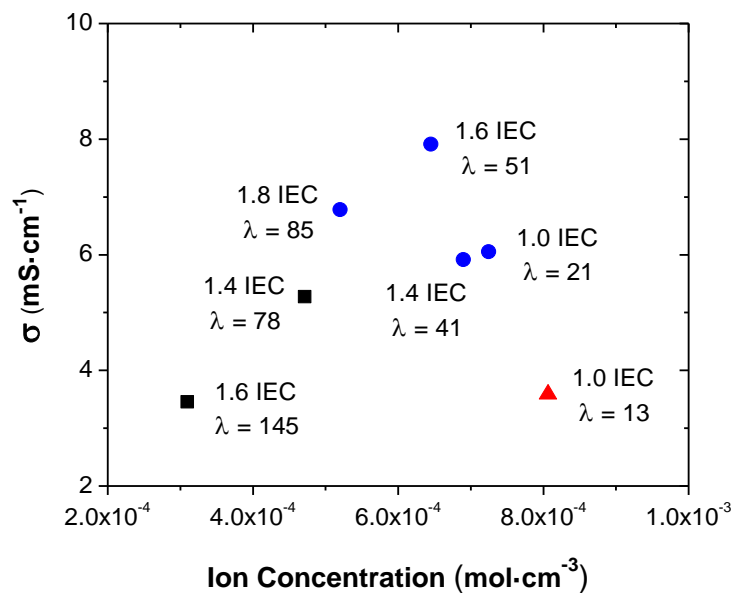


Figure 7.10. The role of ion concentration on membrane conductivity for membranes in the chloride form with [DCPD]:[M+COD] ratios of (■) 1:1, (●) 2:1, and (▲) 5:1. The IEC and hydration number of the membranes are denoted next to the corresponding symbols.

The hydration numbers of the membranes in the chloride form were inversely related to the ion concentration, Figure 7.11. Higher IEC membranes on a gravimetric basis swelled more with liquid water than low IEC membranes and the ion concentration in the hydrated material was lower for the high IEC samples. This swelling behavior, leading to dilution of the fixed charge groups, was dictated by the cross-linking ratio of the material, where the more highly cross-linked samples showed lower water uptakes. For low cross-linking ratios, the samples swelled significantly, even at low IEC. It appears from the data in Figure 7.11 that an intermediate level of cross-linking was required in these samples to balance the water uptake and ion concentration to obtain high conductivity.

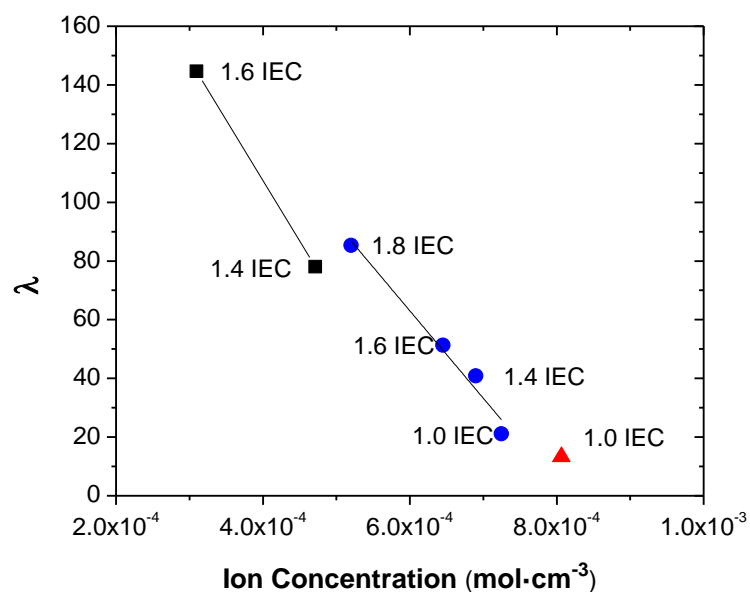


Figure 7.11. Hydration number decreased as ion concentration increases for membranes in chloride form with [DCPD]:[M+COD] ratios of (■) 1:1, (●) 2:1, and (▲) 5:1.

The information obtained from conductivity and water uptake of the polymer membranes can be used to calculate the diffusion coefficients (D) of the mobile ions in PEMs and AEMs. The diffusion coefficients of the mobile ions were calculated from a form of the Nernst-Einstein equation:

$$D = \frac{\sigma \cdot R \cdot T}{c \cdot z^2 \cdot F^2} \quad (7.4)$$

where σ is the measured conductivity, R is the ideal gas constant, T is temperature, c is the computed concentration of ions in moles per cm^3 calculated by eq. 3, z is the valence charge, and F is Faraday's constant.³² For each ion, we determined the barrier to ion transport by comparison of the calculated ion diffusion coefficients to the ion diffusivity in dilute solution (D_0), the maximum diffusivity of an ion in water.

The dilute ion diffusivity is calculated from the dilute solution mobilities of the mobile ion using:

$$D_0 = \frac{\mu \cdot k_B \cdot T}{q} \quad (7.5)$$

where μ is the dilute solution ion mobility, k_B is the Boltzmann constant, T is temperature, and q is the ion charge.³³ The ratio of the diffusion coefficient to the dilute ion diffusivity (D/D_0), shown in Figure 7.12, should approach a value of unity, or the dilute solution limit, at high water uptake where the sample is composed largely of water.^{32,33}

However, although the D/D_0 ratio increased with increasing hydration for membranes in the chloride and bicarbonate forms, the highest D/D_0 ratios obtained were 0.17 at $\lambda = 85$ for the 1.8 meq·g⁻¹ IEC, 2:1 [DCPD]:[M+COD] membrane in the chloride form and 0.37 at $\lambda = 160$ for the 1.6 meq·g⁻¹ IEC, 1:1 [DCPD]:[M+COD] membrane in the bicarbonate form. Despite the fact that bicarbonate anions have lower dilute solution mobilities than chloride anions, we observed that samples in the bicarbonate form had higher intrinsic mobilities compared to their dilute solution limit due to their greater hydration numbers. The larger water uptake led to decreased ion concentration and higher diffusion coefficients for the membranes in the bicarbonate form. The overall higher hydration number of bicarbonate forms, compared to chloride, despite similar free energies of hydration, could be a result of processing to exchange the ions from chloride (as made) to bicarbonate, which causes irreversible swelling and thus increases the water uptake of the bicarbonate form samples. Additionally, based on the Hofmeister effect, bicarbonate ions are more kosmotropic than chloride ions, meaning they are more highly hydrated and thus may draw more water into the sample upon ion exchange.³⁴

To compare the behavior of the bis(terpyridine) Ru (II) complex-based AEMs with other common functional groups used in AEMs, we show in Figure 7.13 the bicarbonate conductivity and D/D_0 ratio with respect to hydration for several membranes from the literature (values are in Table S1). Compared to BTMA, benzyl 1-methylimidazolium, and benzyl tri(methoxyphenyl) phosphonium-based membranes, the bis(terpyridine) Ru (II) membranes demonstrated lower bicarbonate conductivity and greater hydration numbers. Despite the decreased bicarbonate conductivity, the D/D_0 for the metal-complex membranes for cross-linking ratios of 2:1 and 1:1 is similar to the BTMA-based samples.

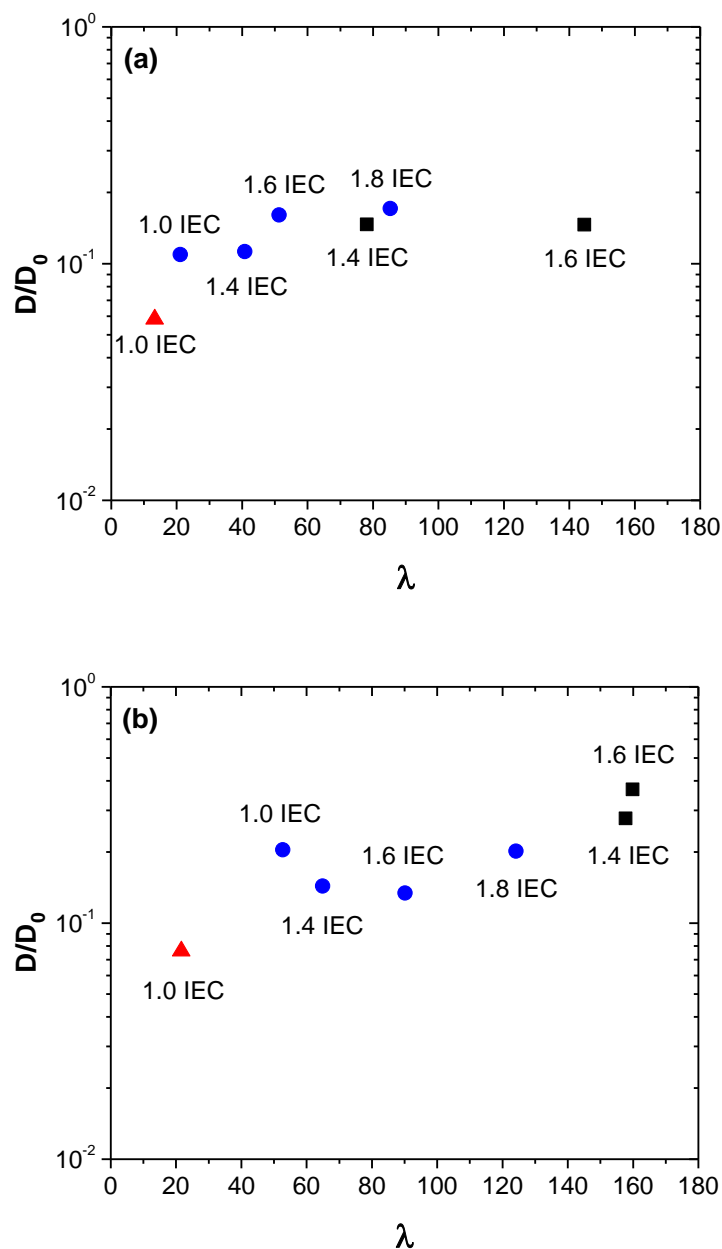


Figure 7.12. Ratio of the diffusion coefficient, D , to the dilute solution diffusivity, D_0 , as a function of hydration number for membranes in the (a) chloride form and (b) bicarbonate form, with DCPD:[M+COD] ratios of (■) 1:1, (●) 2:1, and (▲) 5:1. The higher D/D_0 ratio for the bicarbonate ions signifies that the bicarbonate diffusion coefficient in the samples was closer to the dilute solution diffusivity of bicarbonate ions.

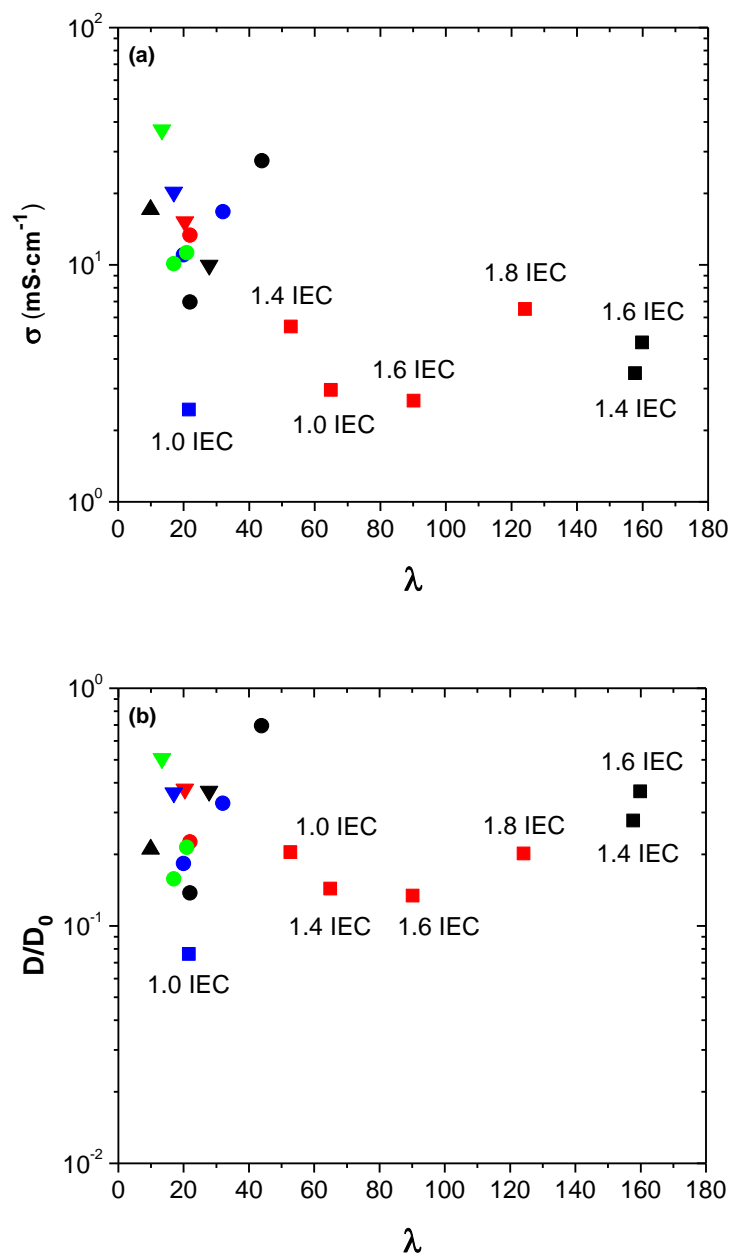


Figure 7.13. Ion transport properties of membranes in the bicarbonate form, for Ru (II) complex-based membranes with [DCPD]:[M+COD] ratios of (■) 1:1, (■) 2:1, and (■) 5:1; BTMA-based tetramethyl bisphenol membranes with (●) 100, (●) 80, (●) 60, and (●) 40 mol % tetramethyl bisphenol;⁶ (▲) imidazolium-based poly(fluorenyl ether ketone sulfone) membrane;⁸ and phosphonium-based bromomethylated poly(2,6-dimethyl-1,4-phenylene oxide) membranes with (▼) 20%, (▼) 34%, (▼) 57%, and (▼) 90% degree of functionalization,³⁵ where (a) depicts bicarbonate conductivity as a function of hydration number, and (b) illustrates the ratio of the diffusion coefficient, D , to the dilute solution diffusivity, D_0 , as a function of hydration number.

7.5. Conclusions

Bis(terpyridine) Ru (II)-based AEMs, BTP-R1, were the first metal-cation containing AEMs, and were synthesized by Zha and Tew of the University of Massachusetts Amherst and evaluated for conductivity and water uptake. The performance of the membranes was subject to the degree of cross-linking present in the membranes. The hydroxide conductivity at 30 °C ranged from 14-28 mS·cm⁻¹, for membranes with IEC values of 1.0-2.0 meq·g⁻¹ and λ values of 30-216.²³ The BTP-R1 materials provided a strong foundation from which new targets for conductivity and hydration could be established.

The conductivity and hydration of the second iteration of bis(terpyridine) Ru (II) complex-based membranes, BTP-R2 were dominated by the cross-linking ratio, [DCPD]:[M+COD]. The IEC played a minor role in the properties of these materials, but it appeared that a balance between sufficient water uptake and ion concentration was critical to promote good conductivity. The maximum conductivity of these membranes in chloride form ($\sigma_{\text{Cl}^-} = 7.9 \text{ mS}\cdot\text{cm}^{-1}$) was observed at a hydration number of 50, which is greater hydration than other AEMs and sulfonated polymers. At high water uptake, the ions in the Ru (II) complex-based membranes did not reach the dilute solution diffusivity limit of the mobile species, indicating the presence of barriers to transport, even in highly hydrated materials. Continued work on these membranes will focus on increasing the mechanical strength of the polymers while maintaining their conductivity and reducing swelling. In addition, understanding the role of the metal within the cation will be essential.

7.6. References

- (1) Hickner, M. A. *Mater. Today* **2010**, *13*, 34–41.
- (2) Couture, G.; Alaaeddine, A.; Boschet, F.; Ameduri, B. *Prog. Polym. Sci.* **2011**, *36*, 1521–1557.
- (3) Merle, G.; Wessling, M.; Nijmeijer, K. *J. Memb. Sci.* **2011**, *377*, 1–35.
- (4) Deabate, S.; Gebel, G.; Huguet, P.; Morin, A.; Pourcelly, G. *Energy Environ. Sci.* **2012**, *5*, 8824–8847.
- (5) Varcoe, J. R.; Slade, R. C. T. *Fuel Cells* **2005**, *5*, 187–200.
- (6) Yan, J.; Hickner, M. A. *Macromolecules* **2010**, *43*, 2349–2356.
- (7) Li, N.; Zhang, Q.; Wang, C.; Lee, Y. M.; Guiver, M. D. *Macromolecules* **2012**, *45*, 2411–2419.
- (8) Chen, D.; Hickner, M. A. *ACS Appl. Mater. Interfaces* **2012**, *4*, 5775–5781.
- (9) Salerno, H. L. S.; Elabd, Y. A. *J. Appl. Polym. Sci.* **2013**, *127*, 298–307.
- (10) Vinodh, R.; Ilakkiya, A.; Elamathi, S.; Sangeetha, D. *Mater. Sci. Eng. B* **2010**, *167*, 43–50.
- (11) Xiong, Y.; Liu, Q. L.; Zeng, Q. H. *J. Power Sources* **2009**, *193*, 541–546.
- (12) Komkova, E.; Stamatialis, D.; Strathmann, H.; Wessling, M. *J. Memb. Sci.* **2004**, *244*, 25–34.
- (13) Edson, J. B.; Macomber, C. S.; Pivovar, B. S.; Boncella, J. M. *J. Memb. Sci.* **2012**, *399–400*, 49–59.
- (14) Chempath, S.; Boncella, J. M.; Pratt, L. R.; Henson, N.; Pivovar, B. S. *J. Phys. Chem. C* **2010**, *114*, 11977–11983.
- (15) Gu, S.; Cai, R.; Luo, T.; Chen, Z.; Sun, M.; Liu, Y.; He, G.; Yan, Y. *Angew. Chemie (International Ed.)* **2009**, *48*, 6499–6502.
- (16) Gu, S.; Cai, R.; Luo, T.; Jensen, K.; Contreras, C.; Yan, Y. *ChemSusChem* **2010**, *3*, 555–558.
- (17) Zhang, B.; Gu, S.; Wang, J.; Liu, Y.; Herring, A. M.; Yan, Y. *RSC Adv.* **2012**, *2*, 12683–12685.

- (18) Lin, B.; Qiu, L.; Qiu, B.; Peng, Y.; Yan, F. *Macromolecules* **2011**, *44*, 9642–9649.
- (19) Pan, J.; Chen, C.; Zhuang, L.; Lu, J. *Acc. Chem. Res.* **2012**, *45*, 473–481.
- (20) Gu, S.; Cai, R.; Yan, Y. *Chem. Commun.* **2011**, *47*, 2856–2858.
- (21) Clark, T. J.; Robertson, N. J.; Kostalik, H. A.; Lobkovsky, E. B.; Mutolo, P. F.; Abruña, H. D.; Coates, G. W. *J. Am. Chem. Soc.* **2009**, *131*, 12888–12889.
- (22) Noonan, K. J. T.; Hugar, K. M.; Kostalik, H. A.; Lobkovsky, E. B.; Abruña, H. D.; Coates, G. W. *J. Am. Chem. Soc.* **2012**, *134*, 18161–18164.
- (23) Zha, Y.; Disabb-Miller, M. L.; Johnson, Z. D.; Hickner, M. A.; Tew, G. N. *J. Am. Chem. Soc.* **2012**, *134*, 4493–4496.
- (24) Bielawski, C. W.; Grubbs, R. H. *Angew. Chemie Int. Ed.* **2000**, *39*, 2903–2906.
- (25) Xu, K.; Oh, H.; Hickner, M. A.; Wang, Q. *Macromolecules* **2011**, *44*, 4605–4609.
- (26) Zhou, Z.; Dominey, R. N.; Rolland, J. P.; Maynor, B. W.; Pandya, A. A.; DeSimone, J. M. *J. Am. Chem. Soc.* **2006**, *128*, 12963–72.
- (27) Voet, D.; Voet, J. G. *Biochemistry*; Fourth.; John Wiley & Sons, 2011; p. 45.
- (28) Robertson, N. J.; Kostalik, H. A.; Clark, T. J.; Mutolo, P. F.; Abruña, H. D.; Coates, G. W. *J. Am. Chem. Soc.* **2010**, *132*, 3400–4.
- (29) Marcus, Y. *Biophys. Chem.* **1994**, *51*, 111–127.
- (30) Suarez, S. N.; Jayakody, J. R. P.; Greenbaum, S. G.; Zawodzinski, T.; Fontanella, J. J. *J. Phys. Chem. B* **2010**, *114*, 8941–8947.
- (31) Kim, Y.; Einsla, B.; Sankir, M.; Harrison, W.; Pivovar, B. *Polymer (Guildf)*. **2006**, *47*, 4026–4035.
- (32) Walls, H. J.; Fedkiw, P. S.; Zawodzinski, T. A.; Khan, S. A. *J. Electrochem. Soc.* **2003**, *150*, E165–E174.
- (33) Muthukumar, M. In *Advances in Chemical Physics*; Rice, S. A., Ed.; 2005; Vol. 131, p. 45.
- (34) Liu, L.; Wang, T.; Liu, C.; Lin, K.; Ding, Y.; Liu, G.; Zhang, G. *J. Phys. Chem. B* **2013**, *117*, 2535–2544.
- (35) Jiang, L.; Lin, X.; Ran, J.; Li, C.; Wu, L.; Xu, T. *Chinese J. Chem.* **2012**, *30*, 2241–2246.

Chapter 8

Scattering of Superacid Proton Exchange Membranes

8.1. Introduction

Controlling the ion domain size of proton exchange membranes (PEMs) is important to fuel cell properties, so research on the morphology of PEM systems is an active area of research.^{1,2} One main avenue for such control is by using synthetic techniques to create block, graft, and star copolymers to drive microphase separation and create the co-continuous domains necessary for ion transport.² The microphase separation in block copolymer PEMs has been extensively studied and is believed to be responsible for the increased conductivity of block copolymers compared to random copolymer PEMs.^{1,3-7} However, there are other approaches for increasing the conductivity of PEMs, especially concerning the character of the polymer-bound acidic group. Carboxylate and phosphonate membranes have not shown great promise as protogenic groups,⁸⁻¹⁰ but superacidic sulfonate groups¹¹ and sulfonimide moieties^{12,13} appear to be promising candidates to boost the conductivity of PEMs.

Random perfluorosulfonic acid-containing polymers, PFSA, such as Nafion[®], Aquivion[®], Flemion[®], and 3M ionomers polymers have served as high-performance fuel cell membranes. In particular, DuPont's Nafion[®] is considered a benchmark fuel cell membrane, especially for PEMs, and the morphology of Nafion[®] has been thoroughly investigated.¹⁴ Nafion[®] has demonstrated wider, more direct and interconnected channels with ions in close proximity compared to sulfonated poly(ether ether ketone), sPEEK, which led to higher

conductivity of the Nafion[®] membrane.¹⁵ In a similar study, the ionic domains of Nafion[®] and sulfonated poly(phenylene), SDAPP, were viewed by transmission electron microscopy; the ionic domains of Nafion[®] were larger than the ionic domains of SDAPP, which correlated to increased water diffusion and transport and increased conductivity in Nafion[®].¹⁶ It appears the perfluorosulfonated nature of Nafion[®] is responsible for the superior membrane performance, but further information is needed to ascertain every contribution to this quality.

The perfluorinated sulfonic acid in PFSA is strongly acidic and is referred to as a “superacid.” It is estimated that the pK_a of this acid is -14.1,¹⁷ compared to the estimated pK_a values of -2.5 for aryl sulfonate, -1 for sulfonated poly(ether ketone), -6 for Nafion[®].¹⁸ Aromatic-based polymers are less expensive than Nafion[®], so there has been a drive to improve the aromatic-based PEMs.¹⁷ Superacid groups were introduced onto poly(arylene ether sulfone) membranes and demonstrated similar conductivity to Nafion[®] at high relative humidity. However, the IEC of the superacid poly(arylene ether sulfone) membranes was higher than the IEC of Nafion[®].^{18,19}

Bae and coworkers compared the functionality of different sulfonic acid groups on PEM performance. Perfluorosulfonate, aryl sulfonate, and alkyl sulfonate moieties have been used to functionalize poly(styrene) and poly(arylene ether sulfone) for use as PEMs, to further the study on superacid behavior. This work has been in collaboration with Bae and coworkers and complements their conductivity measurements.

8.2. Experimental

8.2.1 Random Copolymer PEMs

Poly(sulfone), PSU, and poly(styrene), PS, random copolymers were functionalized by Ying Chang and Chulsung Bae of the Rensselaer Polytechnic Institute for use as PEMs. The polymers were functionalized with perfluorosulfonate, aryl sulfonate, or alkyl sulfonate groups, S₁, S₂, and S₃ functionalities, respectively. Membranes were cast from these polymers and were used as provided.

8.2.2 Triblock Copolymer PEMs

The triblock copolymers were synthesized using atom transfer radical polymerization (ATRP) with the difunctional initiator, α,α' -dibromo-p-xylene, as described by Saito, et al.²⁰ A difunctional poly(styrene) macroinitiator was synthesized in the bulk in a Schlenk flask with copper(I) bromide (CuBr), 2,2'-bipyridyl (bpy), and α,α' -dibromo-p-xylene at 110 °C for 7 h (targeting 50% conversion). The reaction mixture underwent five freeze-pump-thaw cycles under vacuum and Ar before being placed in the oil bath to start the polymerization. After termination of the reaction, ~200 mL of THF was added the reaction mixture before the mixture was passed through an activated alumina column and precipitated into methanol. The polymer was filtered and washed with MeOH. The polymer was dissolved in THF before a second precipitation in MeOH. The polymer was filtered and washed again and dried in a vacuum oven at 60 °C for 2 days. This procedure resulted in difunctional poly(styrene) ATRP macroinitiator Br-PS-Br. Next, the Br-PS-Br was dissolved in toluene with hexyl methacrylate (HMA) in a

Schlenk flask. After the addition of CuBr and bpy, the flask underwent five freeze–pump–thaw cycles under vacuum and Ar. The flask was placed in an oil bath at 105 °C to start the polymerization of HMA, which proceeded for 24 h. The same post-reaction work-up as above was used after termination of the reaction. This strategy resulted in the synthesis of a symmetric ABA triblock copolymer with poly(styrene) as the middle block and poly(hexyl methacrylate) as the end blocks. The poly(hexyl methacrylate)-*b*-poly(styrene)-*b*-poly(hexyl methacrylate) (PHMA-*b*-PS-*b*-PHMA) triblock copolymer.

Two batches of PHMA-*b*-PS-*b*-PHMA triblock copolymer were produced in this manner: the first batch had a molecular weight of 28.3-*b*-25.6-*b*-28.3 kg·mol⁻¹, and the second batch had a molecular weight of 11-*b*-27-*b*-11 kg·mol⁻¹, as determined by size exclusion chromatography (SEC) and ¹H NMR spectroscopy. The batches were approximately 43 mol % PS and 68 mol % PS, respectively, so they were referred to as 43-PS and 68-PS. The polydispersity index, PDI, of the PS macroinitiators was 1.16 for 43-PS and 1.18 for 68-PS. The PDI increased once the PHMA blocks were added to 1.63 for 43-PS and 1.44 for 68-PS, indicative of imperfect end groups on the PS macroinitiator. These triblock copolymers were sent to Chang and Bae for postfunctionalization with perfluorosulfonate groups, and the subsequent PEMs were used as received (with proton counterions) for morphological and water uptake studies.

8.3. Results and Discussion of the Random Copolymer PEMs

To produce PEMs, PSU and PS were sulfonated with perfluorosulfonate, aryl sulfonate, and alkyl sulfonate groups, and the chemical structures of the resulting random copolymers are illustrated in Figure 8.1. The superacid or perfluorosulfonated membranes are denoted as S₁, and the aryl sulfonate and alkyl sulfonated membranes are denoted as S₂ and S₃, respectively. The

degree of functionalization, DF, for these polymers varied, and the PSU and sulfonated PS, sPS, sets of membranes in this study are listed in Table 8.1 along with the ion exchange capacity, IEC, for the membranes determined by Chang and Bae.^{17,21} Two sets of sPS membranes (30 and 40 mol % DF) and three sets of PSU membranes (135, 160, and 200 mol % DF) were studied. All of the membranes were used and received with protons as the counterion.

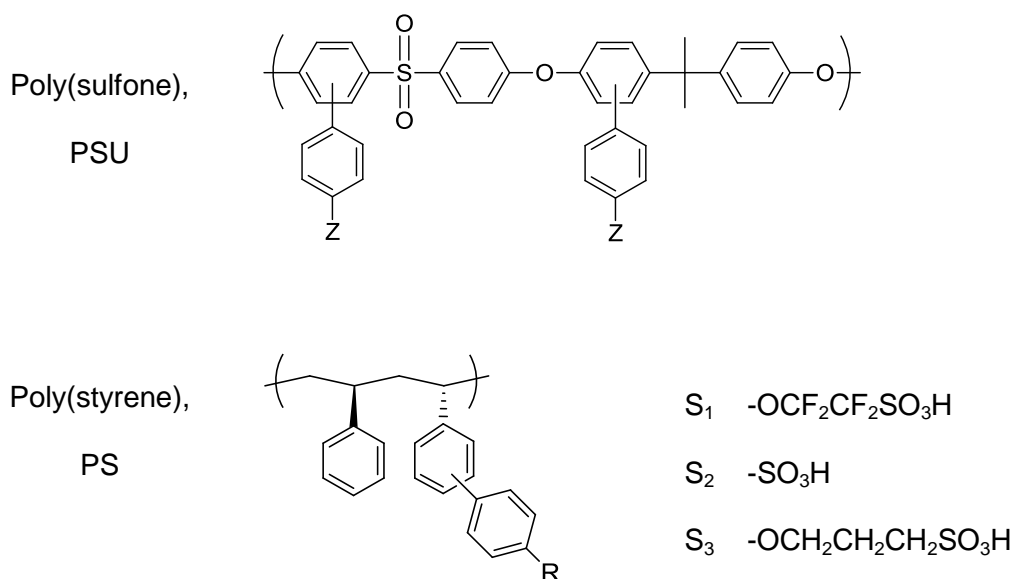


Figure 8.1. Chemical structures of sulfonated poly(sulfone), PSU, and poly(styrene), PS. The perfluorosulfonate, aryl sulfonate, and alkyl sulfonate groups are shown as S₁, S₂, and S₃, respectively.

Table 8.1. Random Copolymer Membrane Parameters and Properties

Sample	DF (mol %)	IEC ^a (meq·g ⁻¹)	IAXS d-spacing ^b (nm)	Hydrated SANS d-spacing ^c (nm)	d _{SANS} -d _{IAXS} due to hydration (%)
30-sPS-S ₁	30	1.33	3.7	4.0	9.5
30-sPS-S ₂	30	1.58	3.5	4.3	21.5
30-sPS-S ₃	30	1.39	3.9	4.3	8.4
40-sPS-S ₁	40	1.64	2.8	4.2	27.8
40-sPS-S ₂	40	2.29	2.6	4.5	35.5
40-sPS-S ₃	40	2.01	2.9	4.3	42.2
135-PSU-S ₁	135	1.48	2.8	3.7	28.6
135-PSU-S ₂	135	2.00	2.6	3.6	35.4
135-PSU-S ₃	135	1.80	2.9	3.5	22.1
160-PSU-S ₁	160	1.58	2.7	3.7	34.3
160-PSU-S ₂	160	2.29	2.5	3.6	41.8
160-PSU-S ₃	160	1.96	2.9	3.6	23.1
200-PSU-S ₁	200	1.94	2.7	4.2	53.8
200-PSU-S ₂	200	2.64	2.0	4.8	139.5
200-PSU-S ₃	200	2.29	2.8	4.2	50.7

^aAs determined by Chang and Bae.^{17,21} ^bCalculated from intermediate angle xray scattering measurements of the dry films, $d = 2\pi/q$. ^cCalculated from small angle neutron scattering measurements of the hydrated films, $d = 2\pi/q$. The assistance of Lilin He of Oak Ridge National Laboratory was used for the 40-sPS and 200-PSU membranes.

The conductivity of 40-sPS-S₁ and 40-sPS-S₂ membranes was comparable to Nafion[®] 112 at 80% and 90% RH, and the sPS membranes exceeded the values of the Nafion[®] 112 conductivity at 100% RH. At 100% RH, the 40-sPS-S₂ membrane demonstrated higher conductivity than the 40-sPS-S₁ membrane, but the λ of the S₂ membrane was also greater.

However, the entire 40-sPS series had lower hydration numbers than Nafion[®] 112.¹⁷ Comparison of the 160-PSU and 200-PSU membranes yielded similar results. At 70% RH, the 200-PSU-S₁ membrane exhibited comparable conductivity to Nafion[®] 112; as the RH humidity increased, other PSU membranes met or exceed the conductivity of Nafion[®] 112. At 100% RH, the 200-PSU-S₁, S₂, and S₃ demonstrated higher conductivity than Nafion[®] 112, and the 160-PSU-S₂ membrane met the Nafion[®] 112 conductivity value. The 200-PSU-S₁ membrane is notable in that it met the conductivity of Nafion[®] 112 at only 80% RH and the membrane's λ was consistently lower than the λ of Nafion[®] 112.²¹

The morphology of the membranes listed in Table 8.1 was of interest to determine if the degree and type (S₁, S₂, or S₃) of functionality of the membranes affected the interdomain spacings, *d*. Intermediate angle xray scattering, IAXS, of the dry membranes and small angle neutron scattering, SANS, of the hydrated membranes experiments were conducted in this effort. The change in *d* due to hydration is reported in Table 8.1 as a percent, while the *d* spacings from IAXS and SANS are reported in nm.

The dry sPS membranes scattered more strongly than did the dry PSU membranes (examples are shown in Figure 8.2), indicating less microphase separation of PSU membranes. This difference can be attributed to the stiffer backbone of the PSU membranes. The polymers with the alkyl sulfonate groups (S₃) demonstrated the largest *d*-spacings; the ether oxygen led to increased flexibility in the acid tether. This idea of flexible tethered acid groups is reinforced by the similar *d*-spacings of the perfluorosulfonated and alkyl sulfonated PEMs (S₁ and S₃). Although the aryl sulfonated PEMs (S₂) often presented similar interdomain spacing, it is bulkier, and the 200-PSU-S₂ membrane had a *d*-spacing of 2.0 nm, compared to 2.7 and 2.8 nm for the 200-PSU-S₁ and 200-PSU-S₃ membranes, respectively.

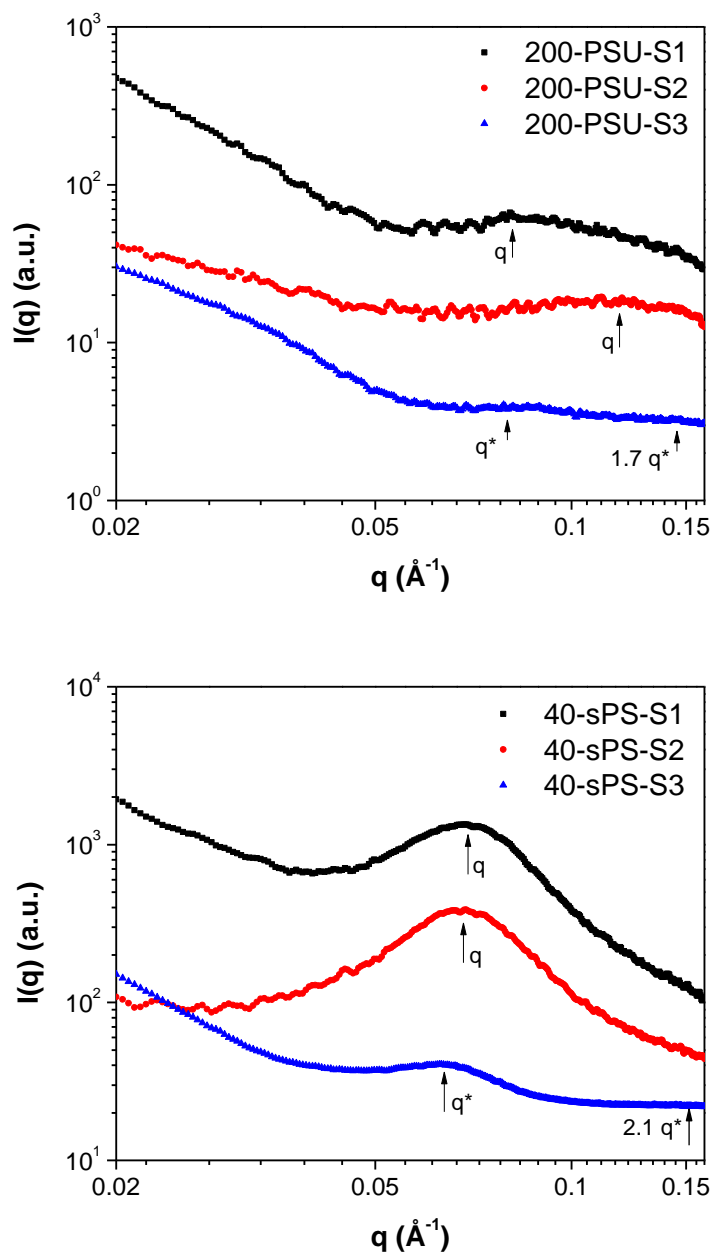


Figure 8.2. Intermediate angle x-ray scattering (IAXS) patterns of dry 200-PSU (top)* and 40-sPS (bottom) membranes. The sPS membranes scatter more strongly than do the PSU membranes.

*Adapted from Chang, Y., et al. *Polymer Chemistry* 2013, 4, 272–281.

SANS spectra of the hydrated PEMs demonstrated that the water interdomain spacings for the PS polymers were slightly larger than the interdomain spacings of the PSU polymers, but the spectra were fairly similar (examples are shown in Figure 8.3). The role of solubility parameters may be of interest to consider the interactions involved with phase separation. In units of $(\text{J}\cdot\text{cm}^{-3})^{1/2}$, the solubility parameters of PS, PSU, poly(ethylene), and poly(tetrafluoroethylene), and water are 18.6,²² 20.3,²³ 17.1,²⁴ 12.7,²⁴ and 48.0,²⁴ respectively. The solubility parameter of sPS is 34 $(\text{J}\cdot\text{cm}^{-3})^{1/2}$, as determined by Lu and Weiss.²² The difference in solubility parameter between PS and water is greater than the difference between PSU and water. This could account for the slightly larger domain spacing of the sPS membranes. Based on the increase in solubility parameter from PS to sPS, we can estimate that the solubility parameter of sulfonated PSU will also increase with functionalization, so both sPS and sulfonated PSU membranes should demonstrate some ion aggregation or phase separation. However, due to the more flexible backbone of PS, there might be more ion clustering in the sPS membranes than the sulfonated PSU membranes.

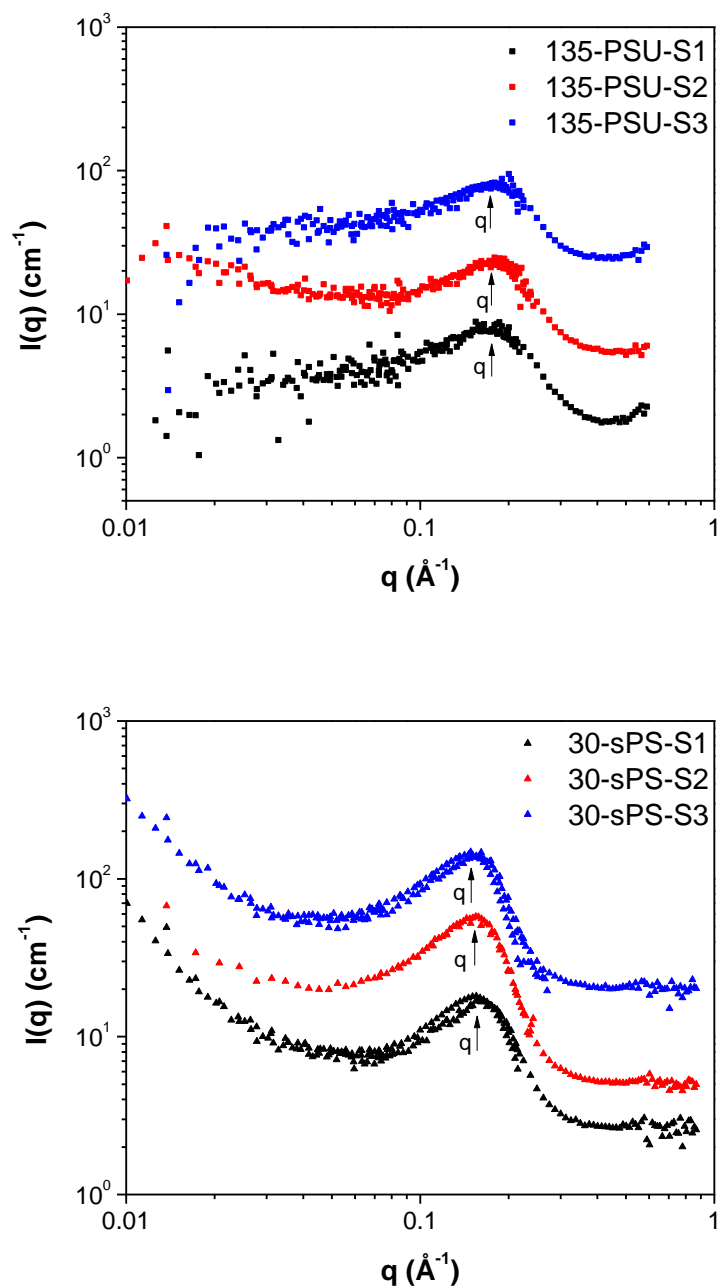


Figure 8.3. Small angle neutron scattering (SANS) patterns of hydrated 135-PSU (top) and 30-sPS (bottom) membranes. The primary scattering peak is denoted by q . The overall scattering of the membranes is similar.

The swelling of the hydrated membranes, calculated from $(d_{\text{SANS}} - d_{\text{IAXS}})/d_{\text{IAXS}}$, is depicted as a function of IEC in Figure 8.4. As expected, increasing ion content led to increased hydration and swelling of the membranes. The PEMs with perfluorosulfonated groups demonstrated greater swelling compared to the S_2 and S_3 polymers for a given IEC. At an IEC near $1.6 \text{ meq}\cdot\text{g}^{-1}$, the 160-PSU- S_1 and 40-sPS- S_1 membranes were approximately 34% and 28% swollen, respectively, compared to the 30-sPS- S_2 membrane, which was only 22% swollen. However, scattering alone does not appear to provide a complete picture of these membranes, and it is not clear that the superacid polymers exhibit morphology that is substantially different than the aryl sulfonated and alkyl sulfonated PEMs. To fully explore the nuances in these membranes, further analysis is required.

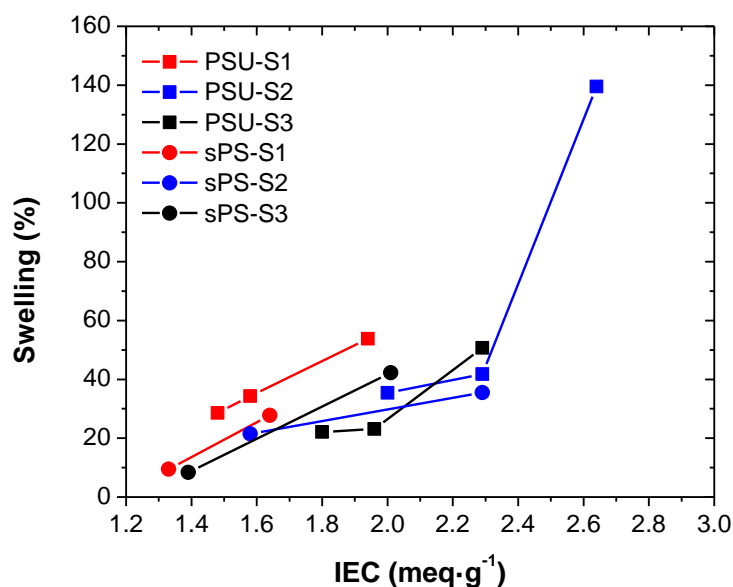


Figure 8.4. The swelling of the membranes calculated from $(d_{\text{SANS}} - d_{\text{IAXS}})/d_{\text{IAXS}}$ increased with the ion content of the membranes.

8.4. Results and Discussion of the Superacid Triblock Copolymer PEMs

Two sets of PHMA-*b*-PS-*b*-PHMA triblock copolymers were perfluorosulfonated by Chang and Bae to produce superacid (S_1) PEMs. The chemical structure of the perfluorosulfonated membranes is shown in Figure 8.5, and the PEMs were used as received with protons as the counterions. The M_n of the base PHMA-*b*-PS-*b*-PHMA triblock copolymers were 82.2 and 48.9 kg·mol⁻¹, with 43 and 68 mol % PS, respectively. Three DFs were achieved for each batch of PHMA-*b*-PS-*b*-PHMA, and the membranes are named after the mol % PS and the DF, as shown in Table 8.2. The IEC, water uptake, wu, hydration number, λ , and primary and secondary interdomain spacings of the membranes are also listed.

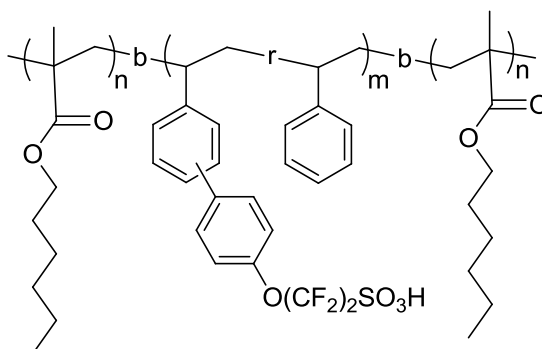


Figure 8.5. Chemical structure of the perfluorosulfonated (S_1) PHMA-*b*-PS-*b*-PHMA triblock copolymers.

The 43-PS series of membranes had lower IEC values than the 68-PS series of membranes due to the mol % PS in the membranes. Due to their greater ion content, the 68-PS superacid membranes exhibited higher wu than the 43-PS series. However, the λ values of the 43-PS were higher than the 68-PS series, meaning that there were more water molecules per ion for the 43-PS series. This may be a result of the higher PHMA content in this series (64 mol %,

compared to 32 mol % for the 68-PS series), since PHMA has a lower T_g than PS. The added flexibility due to the PHMA may allow for additional swelling of the membranes, as well as greater microphase separation, which is shown through the presence of secondary scattering peaks in the 43-PS series.

Table 8.2. Superacid (S_1) Triblock Copolymer Membrane Parameters and Properties

Sample	DF (mol %)	IEC (meq·g ⁻¹)	PS content (mol %)	M_n (kg·mol ⁻¹)	wu ^a (%)	λ^a	d-spacing ^b (nm)
43-PS-50	50	1.1	43	82.2	21	7	42.3
43-PS-75	75	1.5	43	82.2	26	10	41.3
43-PS-87	87	1.6	43	82.2	35	18	40.4
68-PS-44	44	1.5	68	48.9	22	6	30.2
68-PS-83	83	2.0	68	48.9	31	9	30.6
68-PS-92	92	2.1	68	48.9	38	14	30.5

^aCalculated from membranes at 95% RH. ^bCalculated from intermediate angle x-ray scattering measurements of the dry films, $d = 2\pi/q$, where q is the primary scattering peak.

SAXS experiments of the dry membranes (Figure 8.6) revealed that the morphology of the 43-PS series was better ordered than the morphology of the 68-series. The 43-PS membranes demonstrated primary and secondary scattering peaks, but the relationship of the primary and secondary scattering peaks to one another did not correspond to lamellar, hexagonal, or cubic morphologies.²⁵ For both sets of membranes, the interdomain spacings did not vary significantly with the degree of functionalization, which is contrast to other PHMA-*b*-PS-*b*-PHMA PEMs.^{26,27} It is possible that the interactions between perfluorosulfonate groups were weaker than the phase segregation of the PS and PHMA blocks and there was limited ion clustering.

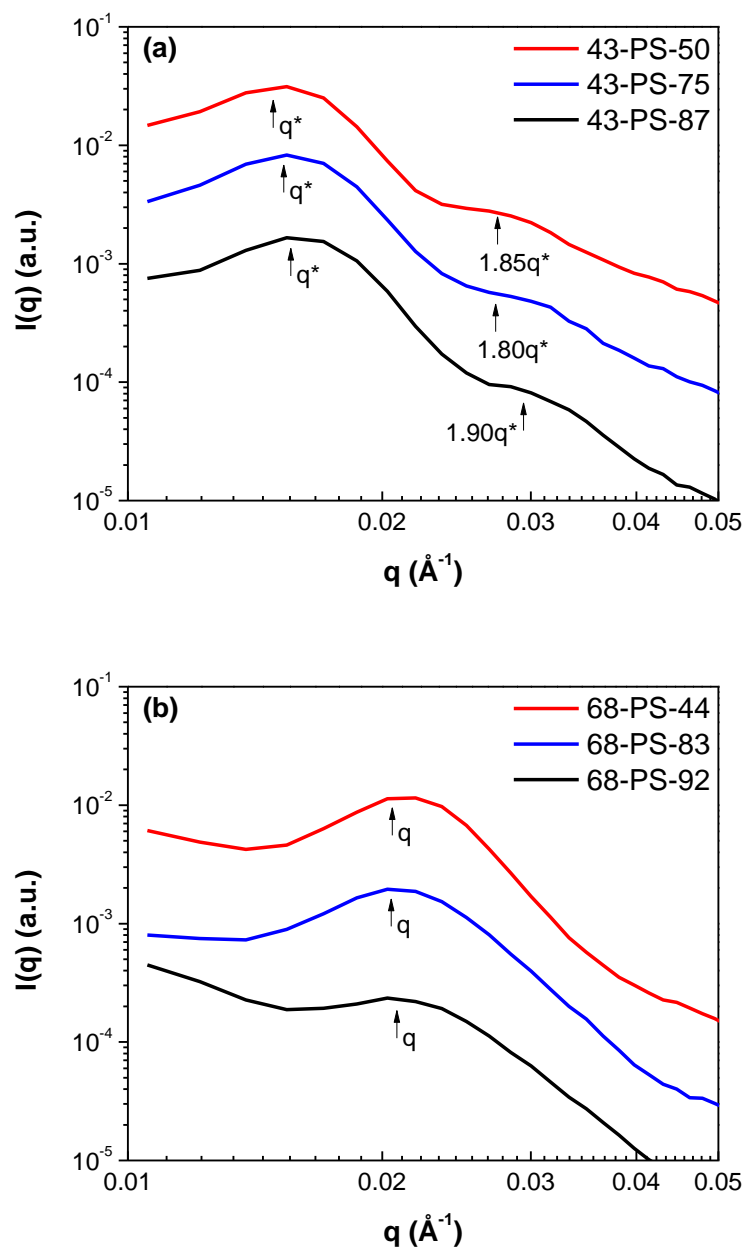


Figure 8.6. Small angle x-ray scattering (SAXS) patterns of (a) 43-PS and (b) 68-PS superacid triblock copolymer PEMs. The primary scattering peak is denoted by q^* or q .

The 68-PS series had smaller interdomain spacing than the 43-PS series, likely due to the difference in molecular weight of the two series. According to the Semenov equation in the strong segregation regime, the interdomain spacing d is proportional to the number of repeat units, N , of the polymer to the two-thirds power, so increasing M_n should lead to increased d -spacing.²⁸ From Table 8.3, calculations of $N^{2/3}$ for N_{PS} , N_{PHMA} , and N_{Total} do not correspond with the interdomain spacings of the polymer. If the PS blocks alone are considered, d_{68-PS} should be greater than d_{43-PS} . However, that is not the case, and other factors such as total molecular weight, ion content, and interaction parameters should be considered in future work.

Table 8.3. Number of Repeat Units and Values of $N^{2/3}$

Sample	N_{PS}	N_{PHMA}	N_{Total}	$N_{PS}^{2/3}$	$N_{PHMA}^{2/3}$	$N_{Total}^{2/3}$	d-spacing (nm)
43-PS	246	332	578	39.3	47.9	69.4	40.4-42.3
68-PS	259	129	388	40.6	25.5	53.2	30.2-30.6

The conductivity of these membranes was measured by Chang and Bae; both sets of membranes demonstrated lower conductivity than Nafion[®] 112 at 40 °C and 60 °C. At 80 °C, the 43-PS-87 membrane (1.6 meq·g⁻¹IEC) approached the conductivity of Nafion[®] 112. The conductivity values for the 68-PS-92 membrane (2.1 meq·g⁻¹IEC) were also below the conductivity of Nafion[®] 112 at lower RH, but they met the value of Nafion[®] conductivity at lower RH than did the 43-PS-87. However, both the conductivity of the 200-PSU-S₁ and 40-sPS-S₁ membranes were higher than Nafion[®] in highly humid environments.^{17,21} The block copolymer design did not appear to enhance the performance of these superacid membranes.

8.5. Conclusions

The effect of perfluorosulfonate groups on the morphology of random copolymers was not clear. The interdomain spacings of the perfluorosulfonated PS and PSU membranes (S_1) were similar to the interdomain spacings of the aryl sulfonated (S_2) and alkyl sulfonated (S_3). Both the S_1 and S_3 PSU membranes swelled more than the S_2 PSU membranes when hydrated for a given degree of functionalization, but that trend did not carry over to the sPS membranes. In addition, for PEMs with similar IEC values, the superacid polymers were more swollen than the S_2 and S_3 membranes. Scattering experiments on superacid block copolymers suggest that the perfluorosulfonate groups do not form significant ion clusters to disrupt the morphology of the PHMA-*b*-PS-*b*-PHMA triblock copolymer since the interdomain spacing did not vary with IEC. The superacid PEMs with lower IEC values, 43-PS, had greater hydration numbers than the 68-PS series, which is attributed to the larger low- T_g PHMA content in the 43-PS series. It was observed that higher molecular weight polymer 43-PS would have larger d-spacing, as expected. However, based on the number of repeat units of the ion-containing block, the 68-PS series should have demonstrated a d-spacing similar to the 43-PS series. It is clear from this work on superacid random and block copolymers that the effects of block architecture on morphology do not enhance membrane performance.

8.6. References

- (1) Elabd, Y. A.; Hickner, M. A. *Macromolecules* **2011**, *44*, 1–11.
- (2) Yang, Y.; Holdcroft, S. *Fuel Cells* **2005**, *5*, 171–186.
- (3) Ding, J.; Chuy, C.; Holdcroft, S. *Chemistry of Materials* **2001**, *13*, 2231–2233.

- (4) Park, M. J.; Balsara, N. P. *Macromolecules* **2008**, *41*, 3678–3687.
- (5) Peckham, T. J.; Holdcroft, S. *Advanced Materials* **2010**, *22*, 4667–4690.
- (6) Rubatat, L.; Shi, Z.; Diat, O.; Holdcroft, S.; Frisken, B. J. *Macromolecules* **2006**, *39*, 720–730.
- (7) Shi, Z.; Holdcroft, S. *Macromolecules* **2005**, *38*, 4193–4201.
- (8) Kreuer, K.-D.; Paddison, S. J.; Spohr, E.; Schuster, M. *Chemical Reviews* **2004**, *104*, 4637–78.
- (9) Steininger, H.; Schuster, M.; Kreuer, K. D.; Kaltbeitzel, A.; Bingöl, B.; Meyer, W. H.; Schauff, S.; Brunklaus, G.; Maier, J.; Spiess, H. W. *Physical chemistry chemical physics : PCCP* **2007**, *9*, 1764–73.
- (10) Noonan, K. J. T.; Hugar, K. M.; Kostalik, H. A.; Lobkovsky, E. B.; Abruña, H. D.; Coates, G. W. *Journal of the American Chemical Society* **2012**, *134*, 18161–18164.
- (11) Ghassemi, H.; Schiraldi, D. S.; Zawodzinski, T. A.; Hamrock, S. *Macromolecular Chemistry and Physics* **2011**, *212*, 673–678.
- (12) Cho, C. G. I.; Kim, Y. U. S.; Yu, X.; Hill, M.; McGrath, J. E. *Journal of Polymer Science Part A: Polymer Chemistry* **2006**, *44*, 6007–6014.
- (13) Hofmann, M. A.; Ambler, C. M.; Maher, A. E.; Chalkova, E.; Zhou, X. Y.; Lvov, S. N.; Allcock, H. R. *Macromolecules* **2002**, *35*, 6490–6493.
- (14) Yee, R. S. L.; Rozendal, R. A.; Zhang, K.; Ladewig, B. P. *Chemical Engineering Research and Design* **2012**, *90*, 950–959.
- (15) Kreuer, K. *Journal of Membrane Science* **2001**, *185*, 29–39.
- (16) Hickner, M. A.; Fujimoto, C.; Cornelius, C. *Polymer* **2006**, *47*, 4238–4244.
- (17) Chang, Y.; Brunello, G. F.; Fuller, J.; Hawley, M.; Kim, Y. S.; Disabb-Miller, M.; Hickner, M. A.; Jang, S. S.; Bae, C. *Macromolecules* **2011**, *44*, 8458–8469.
- (18) Mikami, T.; Miyatake, K.; Watanabe, M. *ACS applied materials & interfaces* **2010**, *2*, 1714–1721.
- (19) Mikami, T.; Miyatake, K.; Watanabe, M. *Journal of Polymer Science Part A: Polymer Chemistry* **2011**, *49*, 452–464.
- (20) Saito, T.; Moore, H. D.; Hickner, M. A. *Macromolecules* **2010**, *43*, 599–601.

- (21) Chang, Y.; Brunello, G. F.; Fuller, J.; Disabb-Miller, M. L.; Hawley, M. E.; Kim, Y. S.; Hickner, M. A.; Jang, S. S.; Bae, C. *Polymer Chemistry* **2013**, *4*, 272–281.
- (22) Lu, X.; Weiss, R. A. *Macromolecules* **1996**, *29*, 1216–1221.
- (23) *Polymer Data Handbook*; Mark, J. E., Ed.; Oxford University Press, Inc., 1999.
- (24) Barton, A. F. M. *CRC Handbook of Solubility Parameters*; CRC Press: Boca Raton, FL, 1983.
- (25) Hamley, I. W.; Castelletto, V. *Progress in Polymer Science* **2004**, *29*, 909–948.
- (26) Moore, H. D.; Saito, T.; Hickner, M. A. *Journal of Materials Chemistry* **2010**, *20*, 6316.
- (27) Disabb-Miller, M. L.; Johnson, Z. D.; Hickner, M. A. *Macromolecules* **2013**, *46*, 949–956.
- (28) Bates, F. S.; Fredrickson, G. H. *Annual Review of Physical Chemistry* **1990**, *41*, 525–57.

Chapter 9

Summary and Future Research Directions

9.1. Summary and Conclusions

The work described in this thesis has increased our understanding of random and block copolymer hydrated ion conductors, the effects of different ionic groups on the properties of proton exchange membranes (PEMs) and anion exchange membranes (AEMs), and how ordering of ionic block copolymers in solution influences order in the solid-state membrane. Many previous studies were missing key elements of considering the mobility of the charge carrier, the hydrated ion density, morphology, or water content in reporting the conductive properties of hydrated membranes. This thesis has not only strived for clarity in these metrics, but has also used novel PEM and AEM materials to gain insight into the wide range of possible structures for next-generation materials and has provided pathways for promising future work on these materials.

9.1.1 Ion Motion in Anion and Proton-Conducting Triblock Copolymers

To investigate the differences in conductivity and water uptake in block copolymer PEMs and AEMs, a series of analogous triblock copolymers were designed and evaluated.¹ Following Saito, et al.² poly(hexyl methacrylate)-*b*-poly(styrene)-*b*-poly(hexyl methacrylate), PHMA-*b*-PS-*b*-PHMA, triblock copolymers were synthesized via atom transfer radical

polymerization (ATRP). A single batch of the triblock copolymer was functionalized with sulfonate or quaternary ammonium (QA) groups for use as PEMs or AEMs. The morphology of the membranes was similar, as determined by transmission electron microscopy (TEM) and small angle x-ray scattering (SAXS), but the PEMs demonstrated higher water uptake and conductivity. To more clearly compare ion transport in PEMs and AEMs, the higher mobility of the proton, compared to the anion, was negated through the development of a new metric. This entailed calculating the ion diffusion coefficient, D , from membrane conductivity values and comparing it to the dilute ion diffusivity, D_0 , the maximum diffusivity of an ion in dilute solution. For a fully hydrated membrane with no morphological barriers to transport and no counterion condensation, D/D_0 should approach unity. However, in both the PHMA-*b*-PS-*b*-PHMA triblock copolymer PEMs and AEMs, this ratio was an order of magnitude lower than the ideal condition indicating there were barriers to both proton and anion transport. The D/D_0 comparison has been extended to additional polymer systems to probe the limits of ion conductivity in water-containing polymers.

This work is the first to compare the conductivity, morphology, and hydration of analogous block copolymer PEMs and AEMs to gain deeper insight into the connection between different types of hydrated polymeric ion conductors. The higher conductivity of the PEMs compared to the AEMs is primarily due to the higher water uptake associated with sulfonate groups and the increased proton mobility, and this conclusion has broad implications. If ion mobility differences are accounted for and the morphology of the membranes are similar, such as the block copolymer system studied here, PEMs and AEMs demonstrate similar ion transport. This conclusion should aid in the development of AEM membranes with increased performance.

9.1.2 Solution Morphology of Triblock and Diblock Copolymers

To explore if solution morphology of the PHMA-*b*-PS-*b*-PHMA triblock copolymer PEMs and AEMs determined the dry membrane morphology, small angle neutron scattering (SANS) experiments were performed as an external user at the National Institute of Standards and Technology (NIST) and at Oak Ridge National Laboratory (ORNL). Triblock copolymer membrane morphology was correlated to 1 wt % and 10 wt % polymer solutions in *d*₇-N,N-dimethylformamide, the deuterated form of the solvent used for membrane casting. The SANS spectra of the functionalized membranes were fit using the NIST polydisperse core-shell model with a hard sphere structure factor, and showed that the core radius of the polymer micelles increased with polymer concentration, due to ion aggregation and polymer interactions. In addition, for the dry membranes with negligible solvent, the shell thickness increased and the core polydispersity decreased. These results were consistent with the disordered spherical morphology observed by TEM, suggesting that controlling solution morphology can lead to targeted membrane morphology. A lower molecular weight PS-PHMA diblock and triblock PEM with the same ion exchange capacity (IEC) were studied as 0.1, 1, 10, and 20 wt % solutions to establish if the lower molecular weight or increased range of polymer concentration influenced the solution morphology. The solution morphology of the lower molecular weight diblock and triblock PEM were consistent with the previous study. Differences in the size of the triblock particles in solution could be correlated to the change in molecular weight.

9.1.3 Organization and Conductivity of Analogous Diblock and Triblock Ion Conductors

Sulfonated PS-PHMA diblock and triblock copolymers were studied to establish if using non-ionic end blocks in a mid-block functionalized triblock copolymer resulted in less swelling during hydration compared to a similar diblock copolymer. Many block copolymer ion-conducting membranes are based on diblocks or ABA functionalized triblock copolymers where the A blocks are ionic. These functionalization strategies may lead to good order in the materials, but poor mechanical properties upon hydration. The work by Matsen, et al. on bridge and loop formation in triblock copolymers was the driving force for this work, as the bridges and loops formed by triblock copolymers add mechanical integrity to the polymer and are absent in diblock copolymers. The polymers were designed according to this work such that the molecular weight of the diblock copolymer was as if the triblock copolymer chains had been “cut” in half.^{3,4} Both sets of polymers were synthesized via ATRP and functionalized for use as PEMs, with low, mid, and high-IEC membranes. The swelling of the polymers was evaluated through water uptake experiments, and the diblock copolymers exhibited greater water uptake and higher hydration numbers for a given IEC, consistent with the prediction from the work of Matsen. The higher hydration translated into increased conductivity for the diblock copolymer PEMs compared to the triblock PEMs, due to the greater number of water molecules per ion present in the membranes. The morphology of the membranes was studied using SAXS, and both sets of polymers showed ordering through the presence of primary and secondary scattering peaks, with the high-IEC membranes demonstrating tertiary scattering peaks, as well. This study provided confirmation of the increased mechanical properties through lower swelling of triblock copolymers, as opposed to diblock copolymers, for ion-containing block copolymers.

9.1.4 Morphology and Conductivity of Poly(styrene)-Based Anion Exchange Membranes

A systematic study of random and block copolymer AEMs was executed to assess the value of block copolymer chemical structure on AEM performance. Quaternary ammonium functionalized poly(vinyl benzyl chloride)-poly(styrene), QA PVBC-PS, random and block copolymers were provided, and the hydration, conductivity, and water uptake of the membranes were evaluated. The polymers were dropcast onto substrates for analysis because they were too brittle to form free-standing membranes. The QA PVBC-*b*-PS copolymers exhibited higher water uptake and larger hydration numbers than the QA PVBC-*ran*-PS copolymers, and the difference in water uptake between the two systems increased with IEC. The block copolymers also demonstrated slightly higher conductivity than the random copolymers, but the values did not increase with ion content or hydration number. Subsequently, the diffusivity ratio, D/D_0 , was calculated for the polymers, and the values were two orders of magnitude below unity, indicating hindered ion transport. The morphology of the polymers was evaluated to determine its role on conductivity and hydration, and SAXS patterns of the films indicated that the random copolymer AEMs did not order. Primary scattering peaks were observed for the block copolymer AEMs, indicating some degree of ordering and a possible contribution to the increase in block copolymer conductivity. However, the interdomain spacing, calculated from SAXS, of the four of the five block copolymers followed a pseudo-linear relationship with the number of ionic repeat units to the two-thirds power, consistent with the Semenov equation,⁵ and offering potential to establish interaction parameters for QA-based systems.

9.1.5 Water Uptake and Ion Mobility in Cross-Linked Bis(terpyridine) Ruthenium-Based Anion Exchange Membranes

Metal-cation-based AEMs are appealing because they offer the ability for increased number counterions to be associated with the cation in the membrane. Bis(terpyridine) ruthenium-based AEMs were provided,⁶ and hydration and conductivity experiments were performed on the membranes. The AEMs were evaluated to ascertain the role of counterion and cross-linker content on water uptake and conductivity of the membranes. The membranes were provided in chloride form, but through ion exchange, the membranes were studied with chloride, bicarbonate, and hydroxide counterions. Since hydroxide ions convert to bicarbonate ions when exposed to carbon dioxide and subsequently have lower ion mobility in water,⁷ the membranes in hydroxide form were measured under an argon blanket and not in ambient conditions. The chloride, bicarbonate, and hydroxide counterion mobility was correlated to the differences in conductivity. The bis(terpyridine) ruthenium-based AEMs demonstrated high water uptake and relatively low conductivity, varying with the degree of cross-linking. It appears there is an optimal range of hydration for maximum conductivity of these membranes, and the degree of cross-linking seems to have greater influence on membrane performance than does the ion concentration. With the new metric described earlier, D/D_0 was calculated from conductivity data of these membranes in bicarbonate and chloride form, and the bicarbonate ions appeared to have a smaller barrier to morphological transport than did the chloride ions. However, the membranes need to uptake less water and exhibit increased conductivity to be considered as a viable alternative to current AEMs.

9.1.6 Scattering of Superacid Proton Exchange Membranes

Perfluorosulfonated membranes, such as the benchmark PEM Nafion[®], are strongly acidic, and are referred to as “superacids” accordingly. To evaluate the effect of the superacid on PEM performance, different sulfonic acid groups were used to functionalize poly(arylene ether sulfone), PSU, and PS. The conductivity and water uptake of the superacid PEMs demonstrated higher conductivity than their aryl and alkyl sulfonic acid counterparts.^{8,9} SAXS and SANS were employed to study the morphology of these membranes, and the interdomain spacing of the superacid membranes were similar to the interdomain spacings of the aryl sulfonated and alkyl sulfonated membranes. The PSU aryl sulfonated membranes were less hydrated than the PSU perfluorosulfonated and alkyl sulfonated membranes, but the same behavior was not observed for the PS-based membranes. For these systems, it appears that morphology does not drive conductivity behavior, as the channels for conductivity are near continuous. As an extension of this work, PHMA *b*-PS-*b*-PHMA triblock copolymers were synthesized via ATRP in house and then functionalized with superacid groups by the collaborator. The interdomain spacing of the superacid PHMA *b*-PS-*b*-PHMA polymers did not vary substantially with IEC, so the presence of ion clusters did not disrupt the morphology of the triblock copolymer membranes. However, scattering experiments alone are insufficient for any significant conclusions to be drawn about the block copolymer system.

9.2. Directions for Future Research

Block copolymers PEMs and AEMs have demonstrated increased conductivity over their random copolymer counterparts, and clear morphology-conductivity relationships have been

established for ion-containing polymers.^{10–17} Continued work in determination of the effect of block copolymer structure on AEM properties is needed, and although there are some efforts in block copolymer AEMs,¹⁸ the lack of fundamental studies should be rectified. Stability of AEMs was not addressed in this work, but design of chemical structure for enhanced conductivity and stability will become increasingly important in this field.^{15,19,20} Recently, comb-shaped AEMs have demonstrated good stability and conductivity,²¹ suggesting that membrane morphology may not only aid conductivity of AEMs, but also decrease AEM degradation.

Additional AEM approaches, such as cross-linking and ion variation must also be pursued. By cross-linking membranes, membrane swelling can be minimized, increasing mechanical integrity and stability. Various cross-linking approaches are being researched across the field,^{22–25} but the polymers chosen must be stable under alkaline conditions.^{26–28} Ionic liquids and alternative tethered ions, such as amino quaternary phosphonium, are being explored for use in AEMs.^{25,29–35} Fundamental and systematic approaches should be taken to compare new materials with cross-linkers and alternative ions to polymers with analogous structures, as well as to established controls.

Although water uptake and hydration number are commonly reported in fuel cell membrane literature, the location of the water and ions within a hydrated membrane are not fully elucidated. Neutron scattering techniques, such as SANS, can be used to quantify the distribution of water and ions in transport domains of both PEMs and AEMs. To characterize the nanostructure of polymer electrolyte membranes, *in situ* SANS techniques can be employed. SANS spectra of hydrated ion-containing membranes can show a marked scattering maximum, the “ionomer peak,” a representation of the spatial distribution of the ionic domains of the membrane, related to the water content of the membrane.³⁶ To increase the scattering contrast, elemental isotopes can be exchanged, such as the replacement of hydrogen with deuterium by modifying the material or the sample environment.³⁷ This exchange could lead to isolation of

water and ionic domains within a hydrated polymer membrane. It is important to further explore water-ion-polymer interactions to determine how water and ion domains change with hydration and the subsequent effects on membrane morphology and conductivity.

The diffusivity ratio D/D_0 established in this work can be extended to both PEM and AEM materials to provide further insight into the ion transport of the materials. It would be interesting to compare the diffusivity ratio of ionic polymers with aromatic and aliphatic backbones to determine if there are substantial differences in mobile ion transport. Within the subset of aromatic backbones, poly(imides), poly(phenylenes), poly(ketones), and poly(sulfones) with comparable ion content could be evaluated. For these experiments, Nafion[®], and other commercial fuel cell membranes should be included. If D/D_0 values correlate with known degrees of network connectivity, it can be used as an additional method of membrane characterization. By truly evaluating ion transport on the basis of the chemical structure of the polymer, new developments may be made to establish targets for PEMs and AEMs.

Understanding solution morphology its relation to final membrane morphology could allow for additional targeting of membrane performance. Simple membrane casting experiments of a given system with variable solvents and evaporation rates could lead to previously unobserved membrane morphology and performance. The solubility parameters of the polymers and chosen solvents should vary to explore the area between theta solvents and non-theta solvents to evaluate the effect of using non-theta solvents. The vapor pressure of the solvents should also be assessed in conjunction with the final membrane performance and properties. It may be desirable to have a co-solvent system in which one solvent evaporates quickly, “locking in” the current polymer morphology. This method is similar to the non-solvent-induced phase separation discussed previously.³⁸

Research on bis(terpyridine) ruthenium-based AEMs is ongoing and will be continued as a model system for tuning cation size. The collaboration is currently focused on methods by

which to reduce water uptake while maintaining or increasing conductivity. The diffusivity ratio comparison of these AEMs to other membranes in the field illuminated the disparity between the current level of ion transport and the desired ion transport. The mechanical integrity of the membranes is also an area for improvement, and changes to the cross-linker structure and ratio, as well as to the co-monomer, are being explored. Each batch of membranes provides another target for the next round of synthesis as new insight on the AEM hydration, conductivity, and cross-linker ratio are discovered. The work will likely be extended to other metal complexes with varying cation size and charge density.

The superacid PEM work is also ongoing, and additional random and block copolymer systems may be studied. It is unclear at this point if the PHMA-*b*-PS-*b*-PHMA triblock copolymer system will continue to be used for further research, but diblock, multiblock, and graft copolymer systems are worth investigation. The comprehensive reasons behind the increased conductivity for the superacid polymers are not established, and it is necessary to gain this information to develop the next generation of high-performance membranes.

9.3. References

- (1) Disabb-Miller, M. L.; Johnson, Z. D.; Hickner, M. A. *Macromolecules* **2013**, *46*, 949–956.
- (2) Saito, T.; Moore, H. D.; Hickner, M. A. *Macromolecules* **2010**, *43*, 599–601.
- (3) Matsen, M. W.; Schick, M. *Physical Review Letters* **1994**, *72*, 2660–2663.
- (4) Matsen, M. W.; Thompson, R. B. *The Journal of Chemical Physics* **1999**, *111*, 7139.
- (5) Bates, F. S.; Fredrickson, G. H. *Annual Review of Physical Chemistry* **1990**, *41*, 525–57.
- (6) Zha, Y.; Disabb-Miller, M. L.; Johnson, Z. D.; Hickner, M. A.; Tew, G. N. *Journal of the American Chemical Society* **2012**, *134*, 4493–4496.

- (7) Yan, J.; Hickner, M. A. *Macromolecules* **2010**, *43*, 2349–2356.
- (8) Chang, Y.; Brunello, G. F.; Fuller, J.; Hawley, M.; Kim, Y. S.; Disabb-Miller, M.; Hickner, M. A.; Jang, S. S.; Bae, C. *Macromolecules* **2011**, *44*, 8458–8469.
- (9) Chang, Y.; Brunello, G. F.; Fuller, J.; Disabb-Miller, M. L.; Hawley, M. E.; Kim, Y. S.; Hickner, M. A.; Jang, S. S.; Bae, C. *Polymer Chemistry* **2013**, *4*, 272–281.
- (10) Elabd, Y. A.; Hickner, M. A. *Macromolecules* **2011**, *44*, 1–11.
- (11) Ding, J.; Chuy, C.; Holdcroft, S. *Chemistry of Materials* **2001**, *13*, 2231–2233.
- (12) Peckham, T. J.; Holdcroft, S. *Advanced Materials* **2010**, *22*, 4667–4690.
- (13) Shi, Z.; Holdcroft, S. *Macromolecules* **2005**, *38*, 4193–4201.
- (14) Tanaka, M.; Fukasawa, K.; Nishino, E.; Yamaguchi, S.; Yamada, K.; Tanaka, H.; Bae, B.; Miyatake, K.; Watanabe, M. *Journal of the American Chemical Society* **2011**, *133*, 10646–54.
- (15) Merle, G.; Wessling, M.; Nijmeijer, K. *Journal of Membrane Science* **2011**, *377*, 1–35.
- (16) Park, M. J.; Balsara, N. P. *Macromolecules* **2008**, *41*, 3678–3687.
- (17) Park, M. J.; Nedoma, A. J.; Geissler, P. L.; Balsara, N. P.; Jackson, A.; Cookson, D. *Macromolecules* **2008**, *41*, 2271–2277.
- (18) Tsai, T.-H.; Coughlin, B. In *242nd National Meeting of the American Chemical Society*; 2011.
- (19) Couture, G.; Alaaeddine, A.; Boschet, F.; Ameduri, B. *Progress in Polymer Science* **2011**, *36*, 1521–1557.
- (20) Varcoe, J. R.; Slade, R. C. T. *Fuel Cells* **2005**, *5*, 187–200.
- (21) Li, N.; Leng, Y.; Hickner, M. A.; Wang, C.-Y. *Journal of the American Chemical Society* **2013**, *135*, 10124–10133.
- (22) Li, N.; Zhang, Q.; Wang, C.; Lee, Y. M.; Guiver, M. D. *Macromolecules* **2012**, *45*, 2411–2419.
- (23) Zeng, Q. H.; Liu, Q. L.; Broadwell, I.; Zhu, A. M.; Xiong, Y.; Tu, X. P. *Journal of Membrane Science* **2010**, *349*, 237–243.
- (24) Clark, T. J.; Robertson, N. J.; Kostalik, H. A.; Lobkovsky, E. B.; Mutolo, P. F.; Abruña, H. D.; Coates, G. W. *Journal of the American Chemical Society* **2009**, *131*, 12888–12889.

- (25) Noonan, K. J. T.; Hugar, K. M.; Kostalik, H. A.; Lobkovsky, E. B.; Abruña, H. D.; Coates, G. W. *Journal of the American Chemical Society* **2012**, *134*, 18161–18164.
- (26) Hibbs, M. R.; Hickner, M. A.; Alam, T. M.; McIntyre, S. K.; Fujimoto, C. H.; Cornelius, C. J. *Chemistry of Materials* **2008**, *20*, 2566–2573.
- (27) Wang, J.; Zhao, Z.; Gong, F.; Li, S.; Zhang, S. *Macromolecules* **2009**, *42*, 8711–8717.
- (28) Nunez, S. A.; Hickner, M. A. *ACS Macro Letters* **2013**, *2*, 49–52.
- (29) Ye, Y.; Elabd, Y. A. *Macromolecules* **2011**, *44*, 8494–8503.
- (30) Ye, Y.; Sharick, S.; Davis, E. M.; Winey, K. I.; Elabd, Y. A. *ACS Macro Letters* **2013**, *2*, 575–580.
- (31) Ye, Y.; Choi, J.-H.; Winey, K. I.; Elabd, Y. a. *Macromolecules* **2012**, *45*, 7027–7035.
- (32) Chen, D.; Hickner, M. A. *ACS Applied Materials & Interfaces* **2012**, *4*, 5775–5781.
- (33) Salerno, H. L. S.; Elabd, Y. A. *Journal of Applied Polymer Science* **2013**, *127*, 298–307.
- (34) Gu, S.; Cai, R.; Luo, T.; Chen, Z.; Sun, M.; Liu, Y.; He, G.; Yan, Y. *Angewandte Chemie (International Edition)* **2009**, *48*, 6499–6502.
- (35) Gu, S.; Cai, R.; Luo, T.; Jensen, K.; Contreras, C.; Yan, Y. *ChemSusChem* **2010**, *3*, 555–558.
- (36) Deabate, S.; Gebel, G.; Huguet, P.; Morin, A.; Pourcelly, G. *Energy & Environmental Science* **2012**, *5*, 8824–8847.
- (37) Manke, I.; Markötter, H.; Tötze, C.; Kardjilov, N.; Grothausmann, R.; Dawson, M.; Hartnig, C.; Haas, S.; Thomas, D.; Hoell, A.; Genzel, C.; Banhart, J. *Advanced Engineering Materials* **2011**, *13*, 712–729.
- (38) Dorin, R. M.; Marques, D. S.; Sai, H.; Vainio, U.; Phillip, W. A.; Peinemann, K.; Nunes, S. P.; Wiesner, U. *ACS Macro Letters* **2012**, *1*, 614–617.

Appendix A

Ion Motion in Anion and Proton-Conducting Triblock Copolymers

A.1 Determination of Triblock Copolymer Molecular Weight

A combination of ^1H NMR spectroscopy and size exclusion chromatography (SEC) was used to measure the molecular weight of the poly(styrene) macroinitiator and the poly(hexyl methacrylate)-*b*-poly(styrene)-*b*-poly(hexyl methacrylate) (PHMA-*b*-PS-*b*-PHMA) triblock copolymer.

The number average molecular weight (M_n) of the styrene macroinitiator was determined from SEC with poly(styrene) standards in THF (see Figure A.1). Subsequently, this value ($32 \text{ kg}\cdot\text{mol}^{-1}$) was used to determine the degree of polymerization of the macroinitiator. The number of aromatic protons from the macroinitiator structure was correlated to the integral of the aromatic region of the ^1H NMR spectrum for the styrene macroinitiator (refer to Figure S2) and used to determine the molar ratio of styrene to methacrylate monomer residues from the ^1H NMR spectrum for the PHMA-*b*-PS-*b*-PHMA triblock copolymer, shown in Figure S3. The total molecular weight of the triblock copolymer could be found from the number of styrene residues from SEC and the molar ratio of styrene residues to methacrylate residues from ^1H NMR. The polydispersity indices of the poly(styrene) macroinitiator and the PHMA-*b*-PS-*b*-PHMA triblock copolymer were 1.14 and 1.39, respectively.

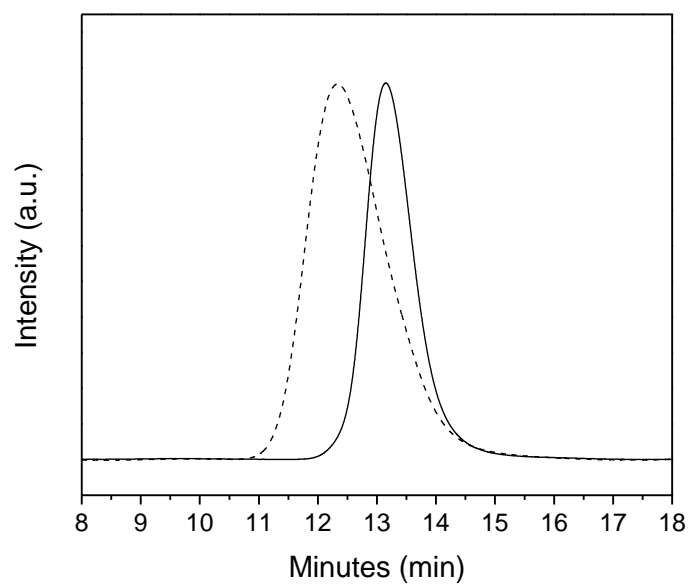


Figure A.1. Size exclusion chromatograph for the styrene macroinitiator (—) and the PHMA-*b*-PS-*b*-PHMA triblock copolymer (---).

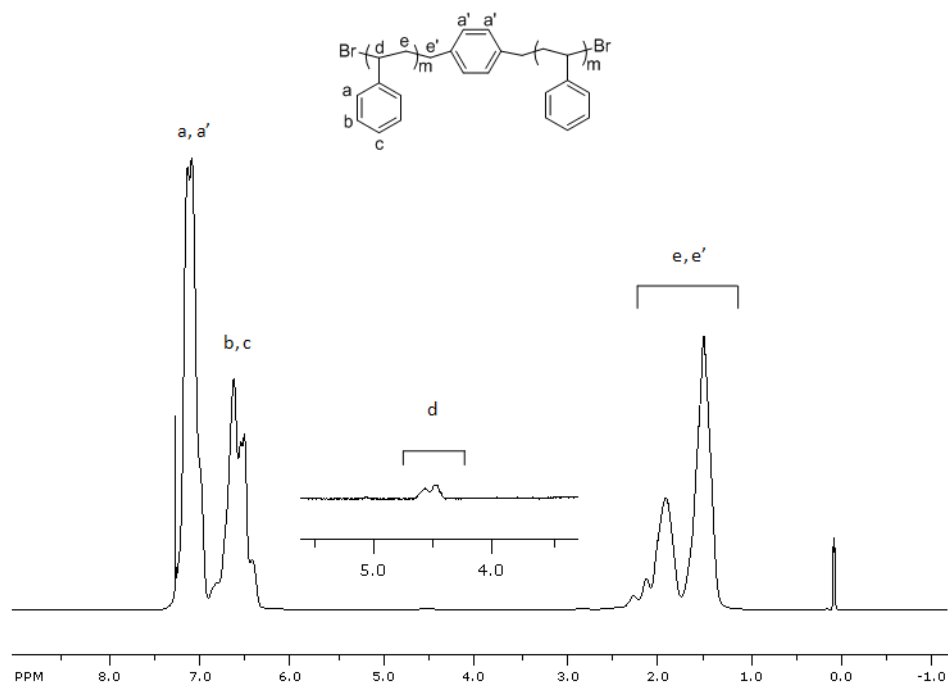


Figure A.2. ¹H NMR spectra for poly(styrene) macroinitiator in deuterated chloroform. The inset shows the peaks associated with the benzyl bromide endgroups.

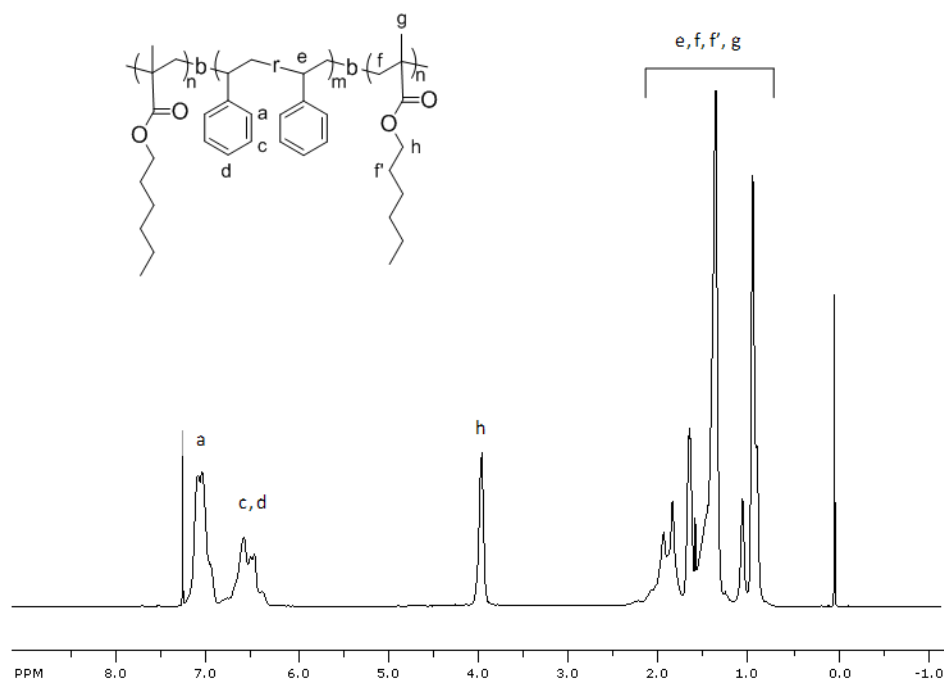


Figure A.3. ^1H NMR spectra for PHMA-*b*-PS-*b*-PHMA in deuterated chloroform.

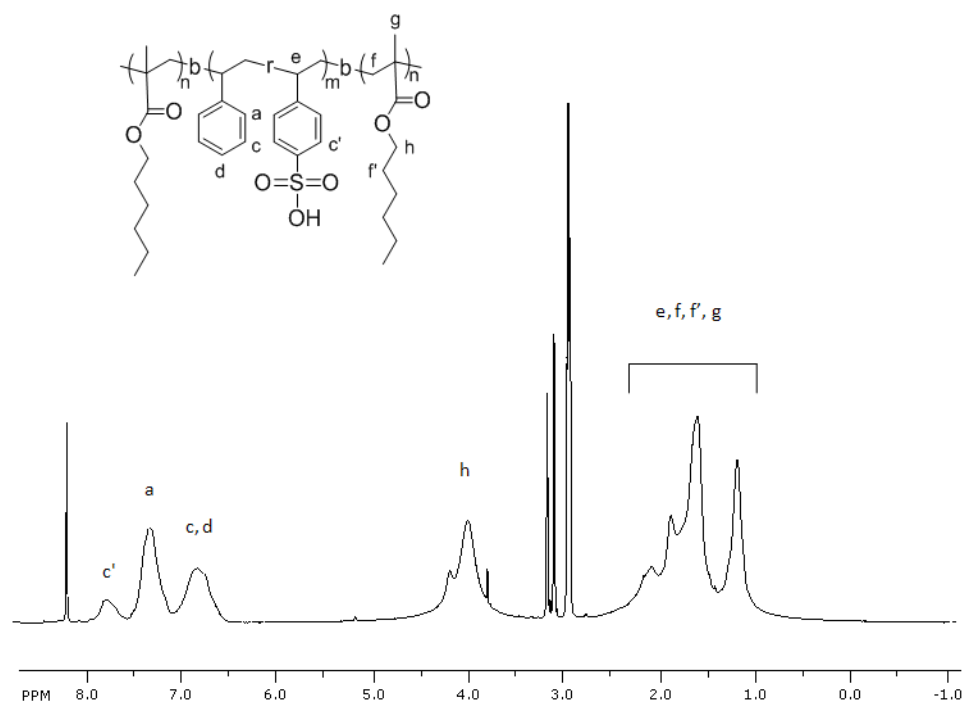
A.2 Polymer Functionalization

A single batch of the PHMA-*b*-PS-*b*-PHMA triblock copolymer was functionalized with sulfonate or quaternary ammonium groups. In order to attain the desired degree of sulfonation, some samples were sulfonated multiple times with acetyl sulfate. The equivalents of reagent and reaction times are described in Table A.1.

Table A.1. Conditions for sulfonation of the PHMA-*b*-PS-*b*-PHMA triblock copolymer.

Initial Degree of Functionalization (%)	End Degree of Functionalization (%)	Equivalents Acetyl Sulfate per mol of styrene monomer residue (mol)	Reaction Time (h)
0	16	0.25	4
16	23	0.25	3
23	27*	0.125	1
0	18	0.50	8
18	38*	0.5	8
0	61*	1.00	3

*Denotes final DF used for sample.

**Figure A.4. ¹H NMR spectra for the sulfonated triblock copolymer, PHMA-*b*-sPS-*b*-PHMA, in deuterated N,N-dimethylformamide.**

Peak broadness in the ^1H NMR spectra of the sulfonated and quaternary ammonium functionalized PHMA-*b*-PS-*b*-PHMA was due to the poor solubility of the ionic form of the triblock copolymer (refer to Figures A.4 and A.5). Although deuterated N,N-dimethylformamide was used as the primary solvent for these spectra, small amounts of deuterated methanol and tetrahydrofuran were added dropwise to aid in solubility of the polymer.

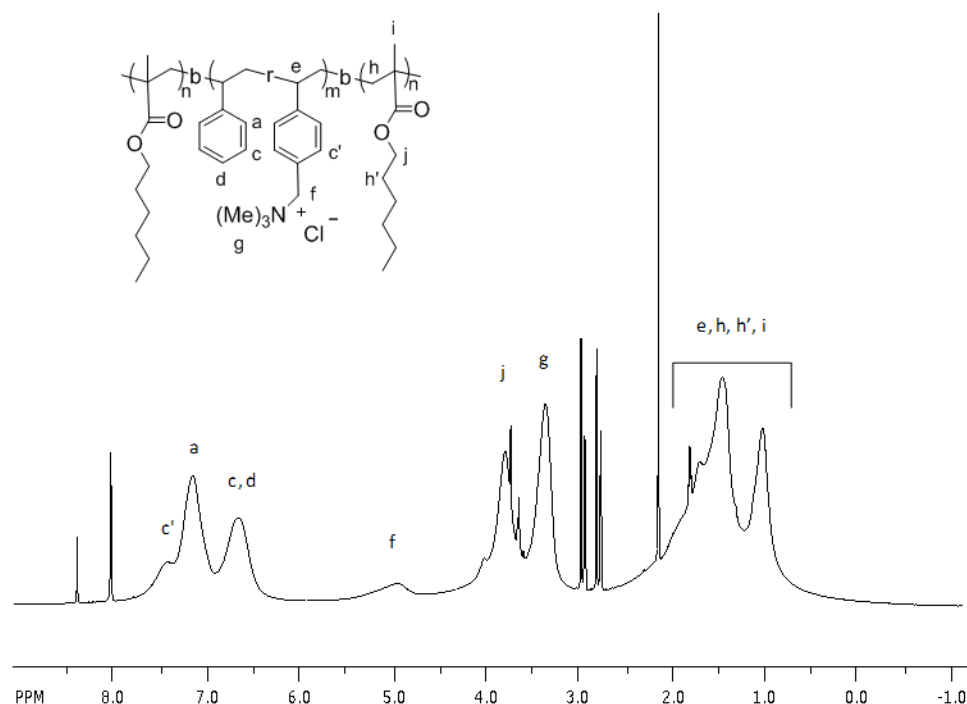


Figure A.5 ^1H NMR spectra for the quaternary ammonium functionalized triblock copolymer, PHMA-*b*-qaPS-*b*-PHMA, in deuterated N,N-dimethylformamide.

A.3 Characterization

Differential scanning calorimetry curves of the PHMA-*b*-PS-*b*-PHMA triblock copolymer showed two distinct T_g values, further validating the block copolymer structure. For the PEMs, the T_g of the PHMA blocks decreased and the T_g of the PS midblock increased with

functionalization (refer to Figure A.6). However, with increasing IEC, the AEMs showed no significant change in T_g .

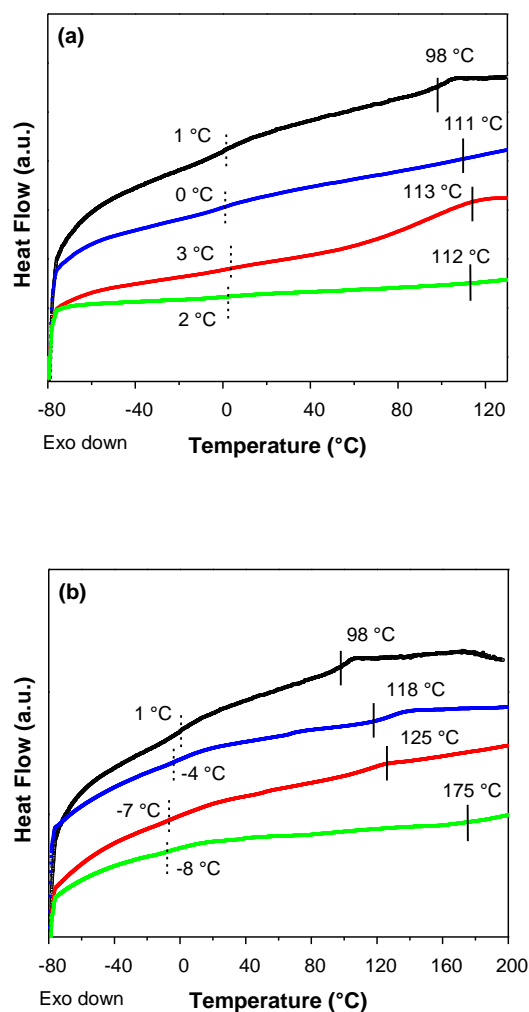


Figure A.6 DSC data for the unfunctionalized triblock copolymer (—), compared to (a) quaternary ammonium functionalized triblock copolymers A-1.2-Cl (—), A-1.7-Cl (—), A-2.0-Cl (—); and (b) sulfonated triblock copolymers P-1.2-H (—), P-1.5-H (—), P-2.3-H (—). The T_g for the PHMA (—) block and the PS block (—) of the polymer were calculated using TA Instruments Universal Analysis software and is marked on the curves.

Appendix B

Organization and Conductivity of Analogous Diblock and Triblock Ion Conductors

B.1 Polymer characterization by SEC and NMR

To measure the molecular weight of the poly(styrene) macroinitiators and the poly(hexyl methacrylate)-*b*-poly(styrene) (PHMA-*b*-PS) and PHMA-*b*-PS-*b*-PHMA diblock and triblock copolymers, ^1H NMR spectroscopy and size exclusion chromatography (SEC) were used.

The number average molecular weight (M_n) of the styrene macroinitiator was determined from SEC with poly(styrene) standards in THF (see Figures B.1 and B.2). This value was used to determine the degree of polymerization of the macroinitiator, and the number of aromatic protons from the macroinitiator structure was correlated to the integral of the aromatic region of the ^1H NMR spectrum for the styrene macroinitiator (refer to Figures B.3 and B.5). Subsequently, these peaks were used to determine the molar ratio of styrene to methacrylate monomer residues from the ^1H NMR spectrum for the PHMA-*b*-PS diblock and PHMA-*b*-PS-*b*-PHMA triblock copolymers, shown in Figures B.4 and B.6. The total molecular weight of the triblock copolymer could be found from the number of styrene residues from SEC and the molar ratio of styrene residues to methacrylate residues from ^1H NMR.

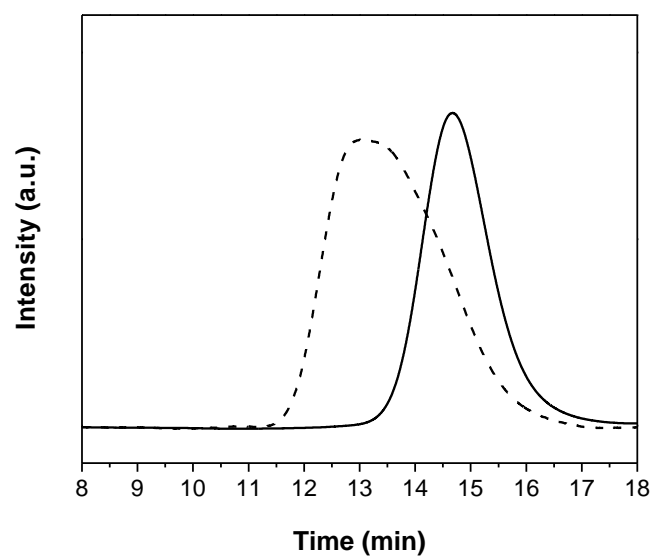


Figure B.1. Size exclusion chromatograph for the styrene macroinitiator (—) and the PHMA-*b*-PS diblock copolymer (---).

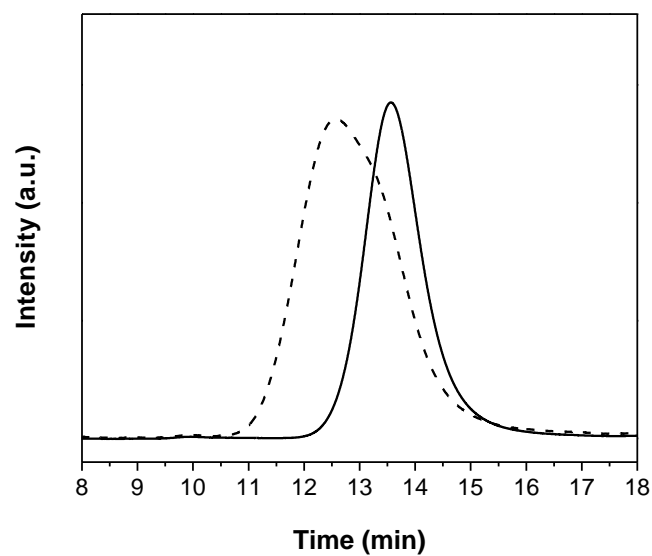


Figure B.2. Size exclusion chromatograph for the styrene macroinitiator (—) and the PHMA-*b*-PS-*b*-PHMA triblock copolymer (---).

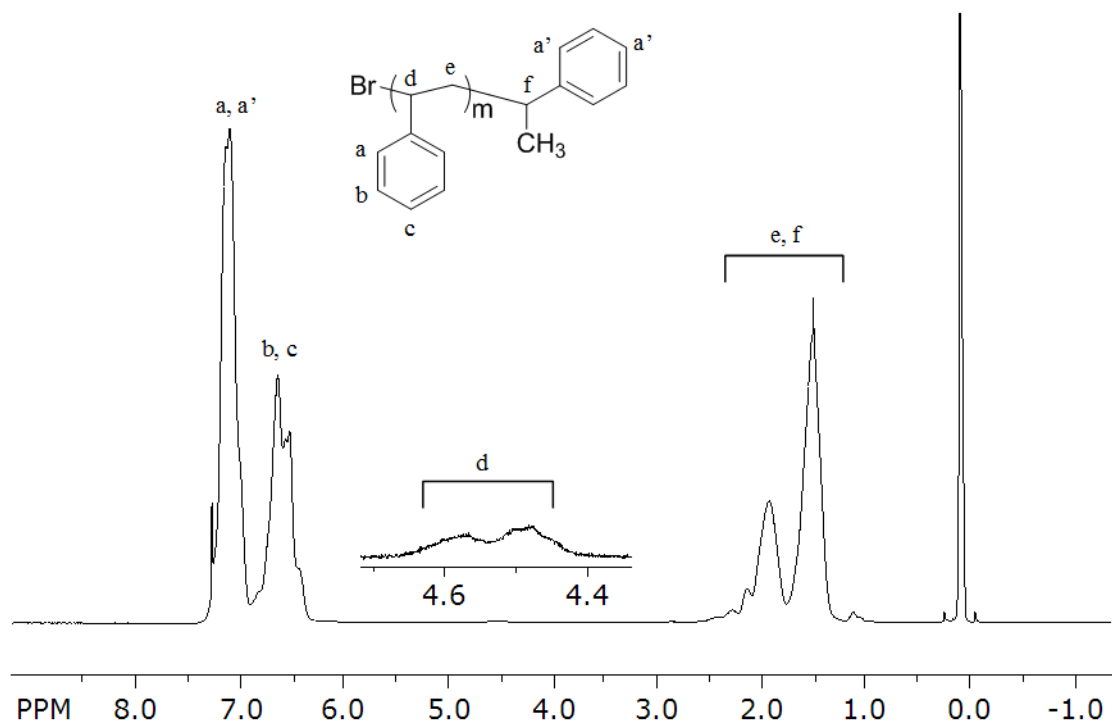


Figure B.3. ^1H NMR spectra for poly(styrene) monofunctional macroinitiator in deuterated chloroform. The inset shows the peaks associated with the benzyl bromide end groups.

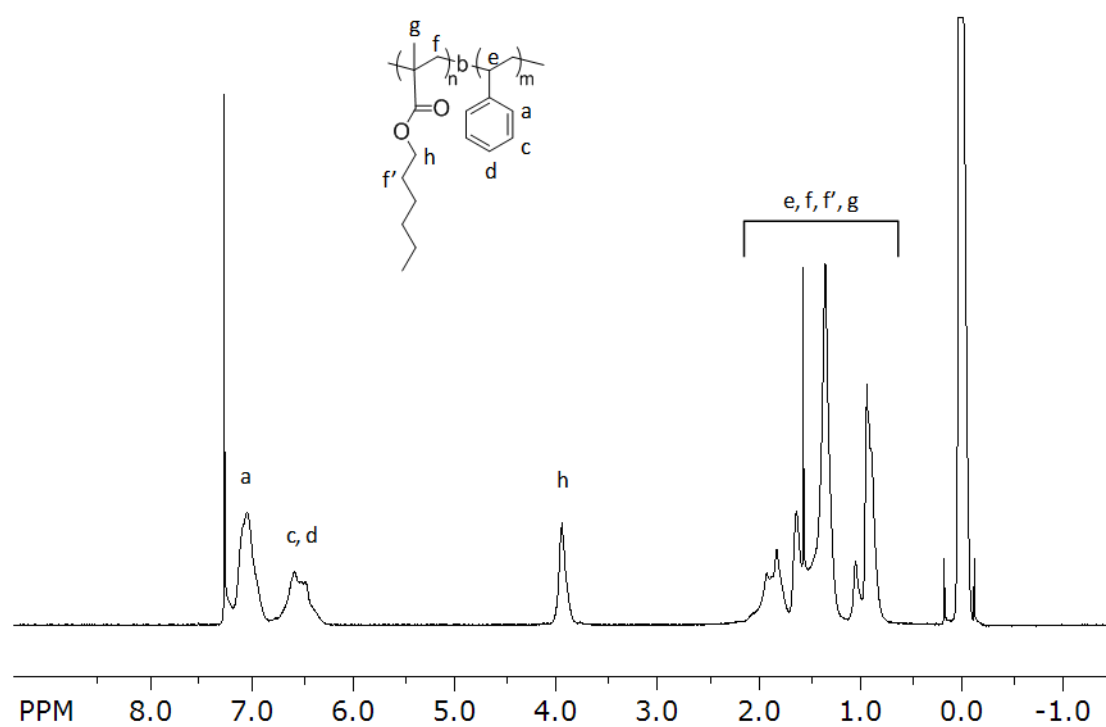


Figure B.4. ^1H NMR spectra for PHMA-*b*-PS in deuterated chloroform.

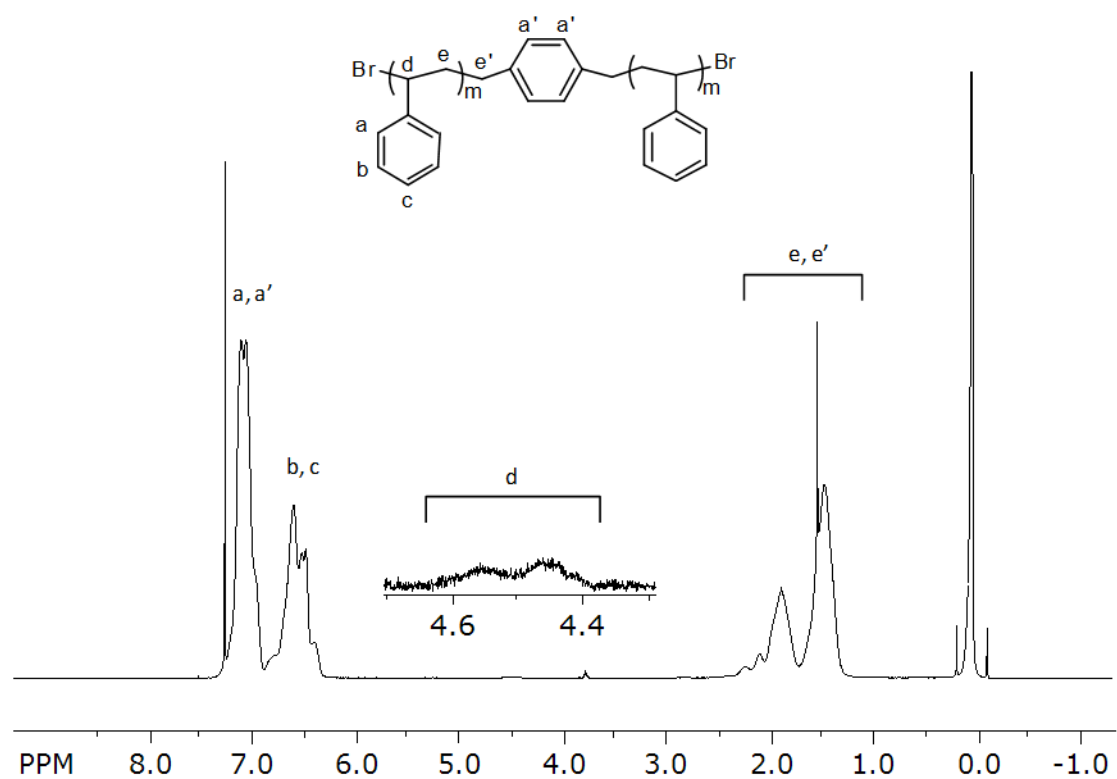


Figure B.5. ^1H NMR spectra for poly(styrene) difunctional macroinitiator in deuterated chloroform. The inset shows the peaks associated with the benzyl bromide end groups.

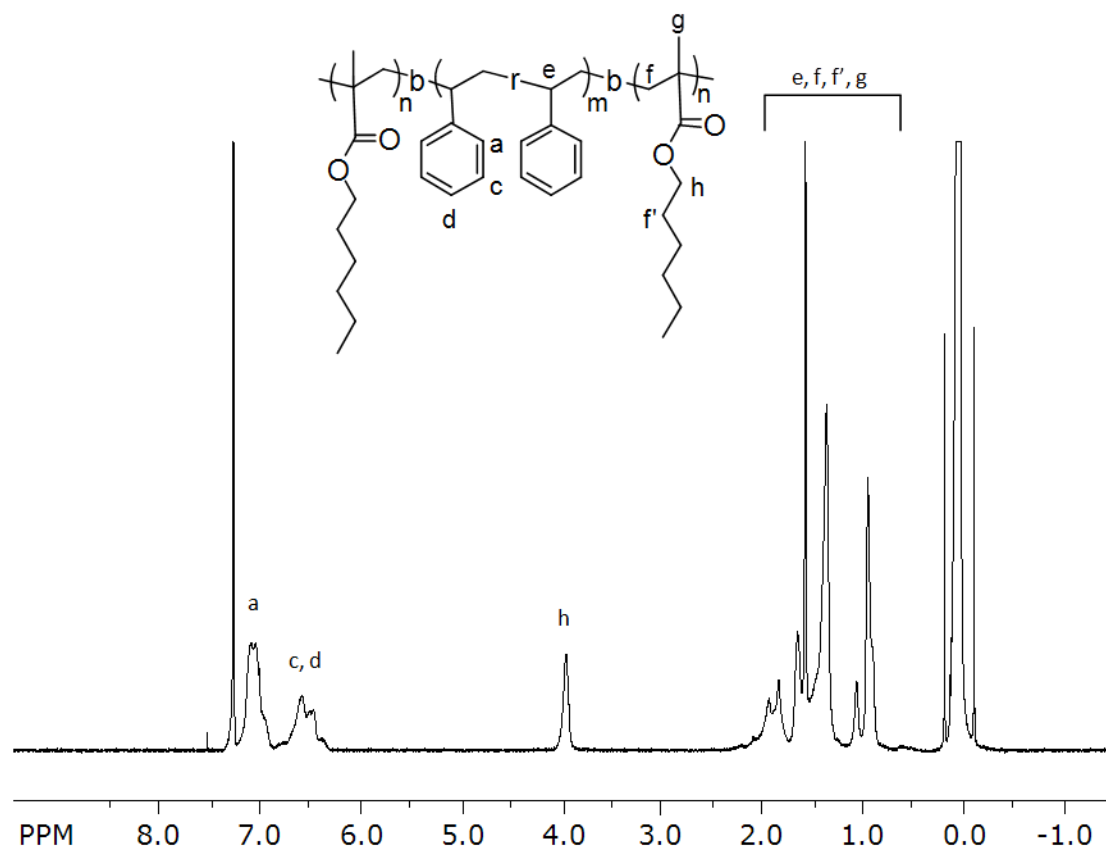


Figure B.6. ^1H NMR spectra for PHMA-*b*-PS-*b*-PHMA in deuterated chloroform.

B.2 Sulfonation of the Block Copolymers

The diblock and triblock copolymers were functionalized with sulfonate groups for use as proton exchange membranes. The molar concentration (with respect to PS) of acetyl sulfate used and the reaction time were varied to target specific degrees of functionalization and ion exchange capacities, shown in Table B.1.

Table B.1. Sulfonation Reaction Conditions

Sample	Acetyl sulfate (mol. equiv.)	Reaction time (h)	DF (%)	IEC (meq·g ⁻¹)
DB-1.1-H	0.88	2.25	26	1.1
DB-1.7-H	1	2.25	43	1.7
DB-2.0-H	1	3.25	53	2.0
TB-1.1-H	1	2	23	1.1
TB-1.6-H	1	3	36	1.6
TB-2.3-H	1	4.3	56	2.3

VITA

Melanie Lisa Disabb-Miller

Melanie Disabb-Miller (née Disabb) was born and raised in Gainesville, Florida. She was part of an International Baccalaureate (IB) program during high school and received her high school and IB diplomas in 2000. Melanie attended the University of Florida in Gainesville, FL, where she pursued Materials Science and Engineering, with a polymers specialty and a French minor. She graduated in 2004 with honors, receiving a Bachelor of Science in Materials Science and Engineering. Melanie furthered her education in Materials Science and Engineering at Northwestern University in Evanston, IL with Professor Samuel I. Stupp. She received a Master of Science in 2007 for her thesis on electronic and photovoltaic properties of self-assembling organic-inorganic hybrids. Melanie then worked as a device processing engineer at MicroLink Devices, Inc. in Niles, IL, where she worked on III-V semiconductor heterojunction bulk transistors and flexible solar cell development. In 2009, Melanie began her graduate studies in Materials Science and Engineering with Professor Michael A. Hickner at The Pennsylvania State University. Her Ph.D. research focused on morphology and transport of ionic membranes.